Precision simulations in Drell-Yan production processes

Robin Linten

A Thesis presented for the degree of
Doctor of Philosophy

Institute for Particle Physics Phenomenology
Department of Physics
Durham University
United Kingdom

October 2018

Precision simulations in
Drell-Yan production processes

Robin Linten

Submitted for the degree of Doctor of Philosophy

October 2018

Abstract: Studies of the Drell-Yan process, $pp \to V + X$ with V a vector boson, have become an important tool to elucidate the fundamental structure of the Standard Model at particle colliders. The precise theoretical understanding of this process is thus paramount to the further success of programs at modern particle colliders. In this thesis, we present the implementation of a method to improve the electroweak accuracy in the description of these processes within the SHERPA framework. This is achieved by including the next-to-leading order electroweak corrections for the leptonic decays of the massive electroweak bosons, Z, W and Higgs, and the next-to-next-to-leading order QED corrections in the case of Z- and Higgs bosons within the framework of the Yennie, Frautschi and Suura resummation formalism. We find small but potentially observable effects on distributions.

Besides the improvement in the theoretical description, phenomenological studies can improve the understanding of the physics at particle colliders. In the second Part of this Thesis we consider b-tagged jets. We study a number of jet shape observables that show good discrimination between a "legitimate", single b-jet and one originating from a gluon splitting, and further show that the combination of these observables already provides good efficiency in rejecting b-jets from gluon splittings.

Contents

List of Figures

List of Tables

Declaration

The work in this thesis is based on research carried out in the Department of Physics at Durham University. No part of this thesis has been submitted elsewhere for any degree or qualification.

Part I is based on research conducted with Prof. Dr. Frank Krauss, Dr. Jonas Lindert and Dr. Marek Schönherr. The content of this Part has been published as a preprint in [1] and is currently under peer review at The European Physical Journal C (EPJC).

Part II of this thesis is based on research conducted in collaboration with Prof. Dr. Frank Krauss and Dr. Dorival Gonçalves-Netto and has been published in [2].

The content of **Appendix A** is based on unpublished research conducted in collaboration with Prof. Dr. Frank Krauss, Dr. Stefan Höche, Dr. Silvan Kuttimalai and Dr. Davide Napoletano.

Acknowledgements

First of all, I would like to thank my supervisor, Frank Krauss, for providing continuous guidance and support throughout the completion of this PhD. Without his patience and occasional nudge in the right direction, this thesis would not exist.

I am very grateful to both Frank, and to Nigel Glover for offering me the opportunity to pursue this PhD and place the trust in me when they did.

Many thanks go to my colleagues in the SHERPA collaboration for providing invaluable help with SHERPA's features. I am particularly indebted to Davide Napoletano for many discussions in trying to elucidate N-Jettiness, to Marek Schönherr for many clarifications regarding the YFS formalism and to Holger Schulz for assistance with software issues, big and small.

I would also like to extend my gratitude to Jonas Lindert for technical support with OPENLOOPS and many helpful discussions regarding electroweak corrections. I am further thankful to Doreen Wackeroth and Alessandro Vicini for support with WZGRAD and clarifications of sometimes subtle issues in the calculational framework for Drell-Yan processes.

Finally, I would like to thank my parents for their continuous support along the way.

Chapter 1

Introduction

Modern particle collider experiments provide a rich environment for the study of the Standard Model (SM) of particle physics and for searches for new physics beyond the SM (BSM). With an unprecedented rate of data taking, the Large Hadron Collider (LHC) has provided and continues to provide avenues to test our understanding, to very high precision, of the fundamental particles and interactions that hold matter together. The outstanding achievement of the LHC's physics program so far has been the discovery of a particle of mass $m = 125.09\,\mathrm{GeV}$ in 2012 [3–5]. The data taken since this discovery shows evidence that this is a scalar particle consistent with the Higgs-boson as predicted by the SM, thereby completing its particle content.

Besides the discovery of the Higgs-boson, the LHC has pushed the precision of many measurements, as well as observing many processes for the first time. Within the collection of SM measurements, the Drell-Yan production process [6], $pp \to V \to f\bar{f}' + X$ with V a vector boson and X further final state particles, plays a major role. At hadron colliders, this process proceeds via the annihilation of a quark and an anti-quark with a large production cross section. The leptonic decay modes of the vector bosons may be used to measure this process with a small background. A non-zero transverse momentum for the lepton system can only be created through the recoil of the system against additional radiation, primarily initial state partonic radiation, but also final state photon radiation. While the high-$p_\perp$ region can be

described in perturbation theory, the region around low $p_\perp$ can be described using resummation. This process thus tests very different aspects of the theory while providing a clean experimental signature. For recent LHC measurements of this process, both inclusively and differentially, see e.g. [7–10].

On the theoretical side, the past decades have seen significant progress in the predictions of SM and BSM processes as well. This progress has in large part been necessitated by the experimental precision achieved and further expected at the LHC. Within the realm of fixed order perturbation theory, next-to-leading order (NLO) calculations in quantum chromodynamics (QCD) have become largely commonplace through the automation of methods to calculate NLO cross sections subject to any experimental cut. This development was sparked by the invention of methods to calculate generic cross sections at NLO, such as phase space slicing [11, 12] and the subtraction method [13–16]. These methods have since been automated and form the perturbative backbone of modern event generators for the LHC [17]. Since these successes, also the calculation of next-to-next-to-leading order (NNLO) calculations has gained traction, with a large number of phenomenologically interesting processes becoming available. Automation of such calculations is still some way off, but there is a large number of methods on the market, including antenna subtraction [18], the CoLoRfulNNLO scheme [19], q_T-subtraction [20], N-Jettiness slicing and subtraction [21], sector-improved residue subtraction [22] and the Projection-to-Born method [23].

In a parallel development, NLO calculations in the electroweak theory and their interplay with calculations in QCD have been investigated as well. For leptonically decaying Drell-Yan processes, the calculation of next-to-leading order EW corrections has been implemented in a large number of codes, including WZGRAD [24–26], HORACE [27, 28], SANC [29], RADY [30, 31], while a combination of NLO initial state QCD and NLO EW corrections is available within the POWHEG framework [32–34] and FEWZ [35]. Efforts to calculate the mixed QCD and EW corrections are underway as well [36]. On a numerical level, one-loop electroweak corrections can be

automatically generated and calculated using programs such as MADGRAPH5 [37,38], OPENLOOPS [39,40] and RECOLA [41,42]. Beyond these efforts, the behaviour of the leptonic final state has to be understood as well. In this case, soft and collinear photon radiation provides the major contributions. The effects of this phenomenon can be resummed to all orders, and if required, also improved order by order in perturbation theory. Implementations of such calculations have been performed via a QED parton shower matching in HORACE [43,44] and in the POWHEG framework, in the structure function approach in RADY, and through a resummation following the approach pioneered by Yennie, Frautschi and Suura (YFS) [45] in particle decays in PHOTOS [46], WINHAC [47], the HERWIG module SOPHTY [48] and the SHERPA module PHOTONS [49]. A recent review of these different approaches in the description of Drell-Yan processes can be found in [50].

1.1   The SHERPA framework

Complete theoretical predictions for collisions at particle accelerators are provided by general purpose event generators [17]. Such generators rely crucially on the factorization of the process into different regimes characterized by a relevant momentum scale. In the hard regime at very high momentum scales, partons interact to produce a small number of energetic particles. This regime can be treated using perturbation theory. In the soft regime, at very low scales, the physics is dominated by non-perturbative effects that cause the confinement of the partons into observable hadrons. This region can thus far only be described using phenomenological models. The hard and the soft regime are connected by an evolution of the partons along the scales which is generally described using a parton shower. Each of these different regimes can be calculated using Monte Carlo techniques, and the combination of the regimes allows one to simulate the full spectrum of a single event. The separation into different regimes also allows, given a properly defined interface, the systematic improvement of each event phase through implementation and use of dedicated cal-

culations. The comparison of several such approaches may be used as an indicator of residual uncertainties in the treatment of the relevant event phase.

SHERPA [51] is a highly modular event generator framework written entirely in C++, providing the complete chain of event generation from the beams into fully hadronic final states that can then be passed on to a detector simulation. Processes included contain all processes of the SM, while BSM models can be implemented either natively or through an interface to the UFO output [52, 53].

SHERPA contains two inbuilt matrix element generators in AMEGIC [54, 55], based on Feynman diagrams, and COMIX [56], based on Berends-Giele recursion relations. These matrix element generators calculate tree-level amplitudes and integrate the squared amplitudes over the relevant phase space, using the phase space generator PHASIC. Both generators can construct dipole subtraction terms following the Catani-Seymour dipole subtraction method [13, 57, 58], and thus can be used for the calculation of events at NLO accuracy. For the calculation of the virtual one-loop amplitudes, native interfaces to OPENLOOPS [39, 40], BLACKHAT [59] and RECOLA [41, 42] are provided as well as the possibility to use an external one-loop generator via the Binoth Les Houches Accord [60, 61].

SHERPA provides two parton showers in the CSS [62] and DIRE [63] implementations. Both showers are based on dipole splitting functions inspired by the subtraction terms of the Catani-Seymour method. Through the use of a symmetric ordering variable, DIRE provides a closer resemblance to an analytic resummation, and can be improved systematically in this regime. Efforts to improve the showers to NLO showers, using NLO splitting kernels, are underway [64, 65]. A key feature of the SHERPA framework is the implementation of matching and merging techniques described in [66–71]. These techniques are used to consistently match higher-order calculations to the parton shower, and to merge a number of exclusive calculations together.

Once evolved to low scales, partonic final states are by default hadronized via a variant of the cluster hadronization model in SHERPA's module AHADIC [72], but an interface to the Lund string fragmentation model [73–75] is also provided. Hadron

decays are handled by the module HADRONS which includes a large number of matrix elements and form factor models. SHERPA further provides, through the PHOTONS module [49], an implementation of the YFS resummation to simulate QED radiation in hard decays. While photon radiation off coloured particles is handled within the parton shower, YFS resummation can be applied to all hadron decays and to leptonic decays of electroweak bosons and leptons. Within this framework, the resummation can also be supplemented with fixed order calculations to increase the accuracy of its predictions.

1.2 Motivation and Structure of this Thesis

The calculation and inclusion of higher-order corrections in the fixed order perturbative expansion and their consistent matching within event generators is one of the most important developments to be undertaken over the further runtime of the LHC. Such developments will help shed light on the fundamental interactions underlying the Standard Model and either provide stringent limits on New Physics contributions or establish a definite deviation in the data.

In the environment of a hadron collider, the corrections due to the strong QCD coupling are most significant. While NLO QCD corrections are by now commonplace and widely automated, and NNLO corrections to all $2 \to 2$ and many $2 \to 3$ processes are available, a general method for calculating processes to such precision is not available yet. One promising method for general NNLO calculations is N-Jettiness phase space slicing [21]. This method originates in soft-collinear effective field theory (SCET) [76–81], and it has been shown that this method can be used to calculate NLO and NNLO QCD corrections using the factorization of the cross section in the soft and collinear limits. Indeed, this method has been used to calculate several processes at NNLO, including colour singlet processes, implemented in a public version of the parton-level event generator MCFM [82], Higgs associated production [83] as well as the production of photons [84], Z- [85, 86], W- [87, 88] and Higgs-bosons

[89, 90] in association with jets, direct photon [91] and diphoton production [92]. We implemented this method within the SHERPA framework, including all ingredients necessary in principle to calculate cross sections at NNLO. We find that already at the NLO in non-trivial processes, establishing the convergence of the cross section integration of this method proves problematic due to the uncertainties present in the numerical integration. These difficulties would require to perform calculations for a large number of cuts and use a fit-based approach to the calculation of the cross section. As the degree of divergence and the complexity of the amplitudes increases, this behaviour is expected to worsen at NNLO, making large scale production of results unfeasible. We thus decided not to pursue the implementation of this method further. Nevertheless, we choose to present the current status and the checks that have been performed at the NLO level in Appendix A for the benefit of the interested reader.

Another avenue for improving the precision of theoretical predictions are electroweak corrections. With the more widespread availability of NNLO QCD calculation, the calculation of NLO electroweak processes has attracted a lot of interest in recent years. The naïve reason for this interest is that the strong and weak coupling constants α_s and α numerically relate as $\alpha_s^2 \approx \alpha$ at typical collision energies, so NLO electroweak effects are expected to have an impact on the same order as NNLO QCD effects. Moreover, for large collision energies, electroweak effects are enhanced by Sudakov logarithms of the form $\log (s/M_V^2)$ [93–98], thus enhancing their effect on tails of distributions. The first Part of this Thesis focusses on such higher-order corrections in the electroweak domain of the SM, presenting an implementation of NLO EW corrections and NNLO QED corrections to particle decays within the YFS formalism. This formalism is used within SHERPA's module PHOTONS [49] to simulate the leading logarithmic effects of photon radiation to all orders within the decays of uncoloured particles, and is set up such that the all-orders calculation can be improved by fixed-order results. In Part I, we will first review the YFS formalism as appropriate for particle decays. We will then discuss an implementation of NLO EW

corrections and NNLO QED corrections for the decays of electroweak bosons into leptons, and compare results from this implementation to the leading logarithmic all-orders results. This implementation extends the accuracy of the final state photon treatment of Drell-Yan processes within SHERPA, and allows for an improved analysis of the associated effects.

Besides the improvement of the perturbative expansion, phenomenological studies can further provide interesting insights into implications of the theory and ultimately lead to better descriptions of nature. Of particular interest are processes involving third generation quarks, top and bottom. Through their Yukawa couplings to the Higgs-boson, these quarks offer a handle on understanding the generation of masses in the Standard Model. In addition, the third generation quarks often appear as (by-)products of the production and decay of particles in BSM models. In this case, a good understanding of both the signal process and the SM background processes is paramount to the discriminatory power of the analysis.

The importance of third generation quarks in a SM context is exemplified by the production of two top quarks in association with a Higgs boson, $pp \to t\bar{t}H$, with the Higgs-boson decaying into a pair of $b\bar{b}$. The analysis strategy for this kind of process heavily relies on the definition of b-jets. Such a definition is achieved through a b-tag, that is an identification of suitable conditions on the jet that make it likely to originate from a b-quark. While the acceptance rates of b-jets and rejection rates of c- or light quark jets in modern tagging algorithms are fairly high, these approaches often lack the ability to reliably identify those jets that contain two b-hadrons originating from a gluon splitting into two b-quarks. In Part II, we present a number of observables that can be used to make a distinction between "genuine" single b-jets and those jets originating from the splitting of a gluon into two b-quarks. Based on the fundamental QCD radiation pattern, we show that the combination of three observables already provides a strong discriminatory power.

Chapter 2

Higher-order corrections

2.1 The QCD factorized cross section

All calculations of cross sections at the LHC rely on the principle of factorization. This principle conjectures that the calculation of an observable can be separated into a high-energy part (corresponding to short distances, at which quarks and gluons are asymptotically free) and a low-energy part (corresponding to long-range interactions). The long-distance part of the calculation is universal and describes how the longitudinal momentum of the colliding hadrons is distributed among their constituent partons. This distribution is commonly described through parton distribution functions (PDFs). The short-distance part of the calculation then contains the cross section of the relevant partonic interaction process and is convoluted into the PDFs via the kinematics, flavour and spins. A proof of an all-orders factorization theorem has only been derived in Deeply Inelastic Scattering processes [99] and Drell-Yan processes [100, 101] through an operator product expansion. It is now understood that more complex processes may show a violation of this factorization in certain configurations [102], but for reasonably inclusive observables and at low orders in the perturbation expansion, factorization is still a valid approximation.

The factorization of a hadronic cross-section for an observable X then reads:

$$\mathrm{d}\sigma\left(X, Q^2\right) = \sum_{a,b \in \{q,g\}} \int_0^1 \mathrm{d}x_1 \int_0^1 \mathrm{d}x_2 f_a\left(x_1, \mu_F^2\right) f_b\left(x_2, \mu_F^2\right) \mathrm{d}\hat{\sigma}_{ab}\left(X; x_1, x_2, \frac{\mu_F^2}{Q^2}\right)$$

$$+ \mathcal{O}\left(\frac{\Lambda_{QCD}^2}{Q^2}\right),$$

$$(2.1.1)$$

where the x_i are the longitudinal momentum fractions carried by parton a and b respectively, f_i are the corresponding PDFs and $\mathrm{d}\hat{\sigma}_{ab}$ denotes the partonic cross section with the incoming partons a and b. The PDFs depend on the factorization scale μ_F that separates the long- and short-distance parts of the calculation. The terms $\mathcal{O}\left(\frac{\Lambda_{QCD}^2}{Q^2}\right)$ break the factorization of the cross section and in an operator product expansion correspond to contributions from higher-twist operators. They are suppressed by powers $\frac{\Lambda_{QCD}^2}{Q^2}$, with Q a hard scale of the process in question and $\Lambda_{QCD} \approx 0.3\,\mathrm{GeV}$ the energy scale at which $\alpha_s\left(\Lambda_{QCD}\right) \approx 1$.

The partonic cross section $\mathrm{d}\hat{\sigma}_{ab}(X)$ is made up of the squared partonic matrix element describing the interaction between partons a and b, and the phase space $\mathrm{d}\Phi_N X\left(\Phi_N\right)$ available for an N-parton final state as required by the matrix element, subject to the cuts and measurements applied in the *measurement function $X\left(\Phi_N\right)$*:

$$\mathrm{d}\hat{\sigma}_{ab} = \mathrm{d}\Phi_N \left|\mathcal{M}\left(p_a, p_b; p_1, \ldots, p_N\right)\right|^2 X\left(\Phi_N\right)$$

$$= \frac{1}{\phi\left(p_a, p_b\right)} \left|\mathcal{M}\left(p_a, p_b; p_1, \ldots, p_N\right)\right|^2 X\left(\Phi_N\right)$$

$$\times (2\pi)^4\, \delta^{(4)}\left(p_a + p_b - \sum_{i=1}^N p_i\right) \prod_{i=1}^N \frac{\mathrm{d}^3 p_i}{(2\pi)^3\, 2E_i}. \qquad (2.1.2)$$

In the following, we will generally incorporate the initial state flux factor $\phi\left(p_a, p_b\right)$ into the phase space measure $\mathrm{d}\Phi_N$, and suppress the functional dependence where appropriate.

2.2 Higher-order corrections in perturbation theory

As noted in the introduction, the inclusion of higher order corrections in calculations of experimental observables is fast becoming mandatory. This necessity is rooted both in the need for theoretical predictions to match the high experimental precision achievable at current and potential future colliders, as well as in the need for a sensibly defined uncertainty estimation due to missing higher-order corrections. Furthermore, the lack of clear signals for physics beyond the SM forces the precision determination of observables in order to be able to detect small deviations from the SM expectation.

The cross section differential with respect to an experimental observable can be calculated order by order in perturbation theory. The basic principle is to expand the partonic cross section as a power series in the relevant coupling constant α:

$$\mathrm{d}\hat{\sigma}_{ab}\left(X; x_1, x_2, \frac{\mu_F^2}{Q^2}\right) = \sum_{m=0}^{\infty} \left(\frac{\alpha\left(\mu_R\right)}{4\pi}\right)^m \mathrm{d}\hat{\sigma}_{ab}^{(m)}\left(X; x_1, x_2, \frac{\mu_F^2}{Q^2}, \frac{\mu_R^2}{Q^2}\right). \qquad (2.2.1)$$

The behaviour at very high energies requires the renormalization of the parameters in the Lagrangian as the original "bare" parameters are related to experimental measurements by potentially divergent terms. The renormalization procedure is performed at the renormalization scale μ_R, upon which each term in the series depends. The all-orders cross section is independent of this unphysical scale; the truncation of the series however will introduce a spurious dependence on this scale. We discuss a particular way of performing renormalization, the so-called on-shell renormalization scheme, further in Appendix B.

Consider now a generic cross section $\sigma(X)$ containing N particles in the final state, where X denotes the kinematic cuts and differential measurements applied at the Born level. When considering cross sections involving coloured particles or photons in the final state, this set of cuts has to be defined in an IR-safe manner, e.g. in the form of an IR-safe jet algorithm or an exclusive photon cut.

The cross section at leading order is schematically given by:

$$\sigma^{\text{LO}}(X) = \int d\sigma^{\text{B}}(X) = \int d\Phi_N B_N\left(\Phi_N\right) X\left(\Phi_N\right). \tag{2.2.2}$$

B_N is the square of the lowest order amplitude for the process being calculated. The lowest order is defined as the order in the coupling constants at which the process first becomes possible. Here we include in the integration over the phase space all sums over helicities, partonic channels, the flux, symmetry and averaging factors.

At the next order in the coupling constant, the *next-to-leading order* (NLO), there are two contributions to the cross section: the virtual corrections contain the corrections due to the emission and subsequent reabsorption of additional particles in the process. These corrections interfere with the leading order amplitude and require renormalization. The real corrections contain all the corrections due to the emission of additional particles into the final state. The NLO cross section can then be written as:

$$\sigma^{\text{NLO}}(X) = \int d\sigma^{\text{V}}(X) + \int d\sigma^{\text{R}}(X)$$
$$= \int d\Phi_N V_N\left(\Phi_N\right) X\left(\Phi_N\right) + \int d\Phi_{N+1} R_{N+1}\left(\Phi_{N+1}\right) X\left(\Phi_{N+1}\right), \tag{2.2.3}$$

where $V_N = 2\text{Re}\left(\mathcal{M}_0^{0*}\mathcal{M}_0^1\right)$ is the interference between the leading order amplitude $\mathcal{M}_0^0$ and the virtual amplitude $\mathcal{M}_0^1$, while $R_{N+1} = \left|\mathcal{M}_1^{\frac{1}{2}}\right|^2$ is the square of the matrix element containing an extra particle in the final state. Here, we have used the notation $\mathcal{M}_{n_R}^{\frac{1}{2}n_R+n_V}$ as the matrix element for the process containing n_V virtual and n_R real particles compared to the LO amplitude. The bottom index then counts the number of real emissions, while the top index denotes the order of this amplitude with respect to the LO amplitude, $\alpha^{\frac{1}{2}n_R+n_V}$.

Note that the two components of this calculation reside in two different phase spaces: the virtual corrections are integrated over the N-particle phase space, the same as the Born level contribution, whereas the real corrections are integrated over the $N+1$-particle phase space.

In gauge theories with massless gauge bosons, of which QCD and QED are examples, both components of the calculation can become separately divergent in the limits in which the additional, virtual or real, particle becomes unresolved. This may be the case if the energy of the additional particle $E \to 0$, i.e. it goes *soft*, or when the additional particle is emitted *collinear* to one of the particles in the Born phase space. It is a general result, proven in the context of QED by Bloch and Nordsieck [103] and more generally by Kinoshita, Lee and Nauenburg (KLN) [104, 105], that for any infrared-collinear safe measurement X these divergences cancel at all orders in the sum of the virtual and real corrections. Such measurements require in particular that in all soft and collinear limits $X(\Phi_{N+1}) \to X(\Phi_N)$, such that the observable values in the unresolved limits end up in the same bin of the measurement to ensure the cancellation of the divergences.

At the second order in the coupling constant, the *next-to-next-to-leading order* (NNLO), three parts appear: the double virtual (VV) contribution $d\sigma^{VV}(X)$, which consists of two-loop amplitudes interfering with Born level amplitudes and the interference of two one-loop amplitudes, the real-virtual (RV) contribution $d\sigma^{RV}(X)$, in which amplitudes with one emitted and one virtual particle interfere with single real amplitudes, and the double real (RR) contribution $d\sigma^{RR}(X)$ that contains the emission of two real particles:

$$
\begin{aligned}
\sigma^{\mathrm{NNLO}}(X) &= \int d\sigma^{\mathrm{VV}}(X) + \int d\sigma^{\mathrm{RV}}(X) + \int d\sigma^{\mathrm{RR}}(X) \\
&= \int d\Phi_N \{VV\}_N (\Phi_N) \, X(\Phi_N) \\
&\quad + \int d\Phi_{N+1} \{RV\}_{N+1} (\Phi_{N+1}) \, X(\Phi_{N+1}) \\
&\quad + \int d\Phi_{N+2} \{RR\}_{N+2} (\Phi_{N+2}) \, X(\Phi_{N+2}) . \quad (2.2.4)
\end{aligned}
$$

Note that now the contributions reside in three different phase spaces: the N-particle phase space for the double virtual contribution, the $N+1$-particle phase space for the real-virtual contribution and the $N+2$-particle phase space for the double real corrections. The possible degree of infrared divergence of these contributions is more

severe than in the NLO case, as now up to two particles can go unresolved at the same time. While the cancellation of divergences in the NLO case meant a straightforward cancellation between terms with the same magnitude but opposite sign in the real and virtual contributions, at NNLO the cancellation is now spread over three terms and the correspondence between the divergences in different contributions is more involved. The KLN theorem however still guarantees that for IRC safe measurements the cross section is free of infrared divergences.

While the overall cancellation of infrared divergences is guaranteed, the divergences still have to be made explicit, using some form of regulator, in intermediate steps of a calculation. Two prominent methods of regularization are to either introduce a small mass m for the massless gauge boson or to analytically continue the number of space time dimensions from $D = 4$ to $D = 4 - 2\epsilon$. In the former approach, the divergences appear as logarithms of the gauge boson mass, $\ln(m)$, while in the latter approach, they appear as poles in the parameter ϵ. Such regularization makes analytical calculations possible and allows for explicit checks of the correctness of the calculation as the final result needs to be independent of the regulator. However, calculating cross sections analytically quickly becomes very difficult as the number of final state particles, and therefore degrees of freedom, increases. In addition, the application of arbitrary phase space cuts may even make an analytical calculation impossible. In these cases, we would like to numerically integrate the cross section. Numerical methods however require finite integrands, as well as an integer number of dimensions. We thus have to deal with the divergences in a different way such that each term is rendered finite and numerically integrable. In the following sections, we will be reviewing the two main procedures for allowing numerical calculations of higher order corrections, namely subtraction and phase space slicing. For simplicity, we will here be sticking with the NLO case, and will use dimensional regularization.

2.3   Subtraction method

One prominent technique for calculating higher-order corrections to cross sections is the subtraction method. The basic idea here is to use the known behaviour of the integrand in the unresolved limits to subtract the divergences from the real contribution at the integrand level, and add the subtracted piece, now integrated over the phase space of the additional particle, to the virtual contribution. This procedure amounts to adding an overall zero, i.e. it does not change the value of the cross section, but it renders each of the integrands finite. This then allows numerical integration of the cross section in four spacetime dimensions.

To elucidate, consider again the NLO correction to the cross section in Eq. (2.2.3). We subtract from the real contribution a term $d\sigma^{S}$ which approaches $d\sigma^{R}$ in all unresolved limits and thus subtracts off all the divergent parts of the real contribution. To the virtual contribution, we add a term $d\sigma^{A}$ containing explicit divergences in the chosen regulator, which exactly cancel the ones contained in $d\sigma^{V}$. $d\sigma^{S}$ and $d\sigma^{A}$ need to satisfy the identity

$$- \int_{N+1} d\sigma^{S}\left(\Phi_{N+1}\right) + \int_{N} d\sigma^{A}\left(\Phi_{N}\right) = 0. \tag{2.3.1}$$

The NLO contribution to the cross section then reads

$$\sigma^{\mathrm{NLO}}(X) = \int_{N}\left(d\sigma^{V}(X) + d\sigma^{A}(X)\right) + \int_{N+1}\left(d\sigma^{R}(X) - d\sigma^{S}(X)\right)$$
$$= \int_{N}\left(d\sigma^{V}(X) + \int_{1} d\sigma^{S}(X)\right)\Big|_{\epsilon=0} + \int_{N+1}\left(d\sigma^{R}(X)|_{\epsilon=0} - d\sigma^{S}(X)|_{\epsilon=0}\right), \tag{2.3.2}$$

where we can now safely take the limit $\epsilon \to 0$ in dimensional regularization, as each bracket is independently finite. While this construction leaves both integrands finite, in the second contribution, the subtracted real contribution, we take the difference of two divergent, hence very large terms. To circumvent numerical problems that may occur as a result of this, the subtraction method will always include a small technical cutoff in one of the integration variables, below which $d\sigma^{R}$ and $d\sigma^{S}$ are assumed to

cancel identically. We can check that the total cross section is independent of this cutoff within the numerical errors, but a residual dependence remains.

An important part of the subtraction method is now to find a way to partition the full phase space Φ_{N+1} into the phase space corresponding to the radiated parton Φ_1 and the remainder Φ_N such that the analytical integration of the subtraction term over the additional parton phase space becomes possible. The limiting behaviour of IRC safe observables is such that $X(\Phi_{N+1}) \to X(\Phi_N)$ in the divergent limits. Therefore, a decoupling of, and integration over, Φ_1 is always possible for such observables. The practicality of the method then hinges on whether one can factorize the phase space and express the subtraction terms $d\sigma^S$ such that:

- $d\sigma^S$ is observable independent. This condition allows a general implementation of the subtraction method.

- $d\sigma^S$ matches the singular limits of $d\sigma^R$ exactly. This renders the real integrand finite.

- $d\sigma^S$ can be integrated exactly over the phase space of the additional parton. This ensures the cancellation of the virtual divergences.

- $d\sigma^S$ is amenable to Monte Carlo integration. This allows to scale up to large phase spaces and arbitrary phase space cuts.

Based on these requirements, a number of different variants of the subtraction method have become established, which can be broadly categorized into two classes: Subtractions based on reduced matrix elements, e.g. Catani-Seymour dipole subtraction [13, 57] or antenna subtraction [14, 106, 107], and residue subtraction, e.g. the FKS method [15]. The subtraction method has also been extended to NNLO, but the complexity in this case grows significantly.

2.4 Phase Space Slicing

Another technique for calculating higher-order corrections to cross section is phase space slicing, originally introduced in [11,12]. The idea behind this method is that the infrared divergences in the real contributions reside in a (possibly disconnected) set of regions of phase space corresponding to the regions in which one or several Lorentz invariants vanish. If one places a lower cut on appropriate invariants (or associated variables approaching that invariant in the relevant limit), the real correction is rendered finite and calculable. For the small phase space region below the cut, it is often possible to write an approximation for the cross section in the divergent limit[1]. This approximation can then be integrated analytically, in a process independent manner, and the divergent terms cancelled against the corresponding terms in the virtual corrections, which reside in the same phase space region. In order for this approximation to the cross section to be justified, the phase space cut has to be very small. However, for very small cuts the cross section has to be evaluated close to the singularity, leading to very large cancellations between separate terms. To minimize any resulting numerical problem, the cut should thus be chosen as large as possible. Finding a balance between these two competing requirements is then crucial for this method.

It is illuminating to illustrate this with a simple toy model. Consider the virtual and real contributions to be given as:

$$
\begin{aligned}
\mathrm{d}\sigma^{\mathrm{V}} &= \frac{V_N}{\epsilon}, \\
\mathrm{d}\sigma^{\mathrm{R}} &= \frac{R_N(x)}{x},
\end{aligned}
\tag{2.4.1}
$$

where the virtual corrections are already dimensionally regularized and renormalized, and the infrared behaviour has been made explicit. The real emission contribution depends in this model on a single phase space parameter $x \in [0, 1]$, and its divergence

---

[1]This may however not be trivial. The simplicity and, ultimately, practicality of such an approximation strongly depends on the choice of variable(s) used for the phase space cut which is one of the major obstacles of this method.

in the limit $x \to 0$ has been made explicit. The essence of an infrared-collinear safe observable is in this model that

$$\lim_{x \to 0} X\left(\Phi_N, x\right) = X\left(\Phi_N, 0\right) \equiv X\left(\Phi_N\right), \tag{2.4.2}$$

and the KLN theorem then states that

$$\lim_{x \to 0} R_N\left(x\right) = R_N\left(0\right) = V_N. \tag{2.4.3}$$

In dimensional regularization, the x^{-1}-pole is replaced by $x^{-1-\epsilon}$. The NLO cross section then reads:

$$
\begin{aligned}
\sigma^{\text{LO+NLO}} &= \lim_{\epsilon \to 0} \left[\int \mathrm{d}\Phi_N \left(\mathrm{d}\sigma^{\text{B}} + \frac{V_N}{\epsilon} \right) X\left(\Phi_N\right) + \int \mathrm{d}\Phi_N \int_0^1 \frac{\mathrm{d}x}{x^{1+\epsilon}} R_N(x) X\left(\Phi_N, x\right) \right] \\
&= \lim_{\epsilon \to 0} \left[\int \mathrm{d}\Phi_N \left(\mathrm{d}\sigma^{\text{B}} + \frac{V_N}{\epsilon} \right) X\left(\Phi_N\right) \right. \\
&\quad \left. + \int \mathrm{d}\Phi_N \int_0^\delta \frac{\mathrm{d}x}{x^{1+\epsilon}} R_N(x) X\left(\Phi_N, x\right) \right] + \int \mathrm{d}\Phi_N \int_\delta^1 \frac{\mathrm{d}x}{x} R_N(x) X\left(\Phi_N, x\right),
\end{aligned}
\tag{2.4.4}
$$

where in the second line, we have split the real region into two regions using the arbitrary cutoff δ. In the contribution above the cut, we can already take the limit $\epsilon \to 0$ as this contribution is not divergent. To first order in δ, this can be approximated as:

$$
\begin{aligned}
\sigma^{\text{LO+NLO}} &= \lim_{\epsilon \to 0} \left[\int \mathrm{d}\Phi_N \left(\mathrm{d}\sigma^{\text{B}} + \frac{V_N}{\epsilon} \right) X\left(\Phi_N\right) + \int \mathrm{d}\Phi_N R_N(0) X\left(\Phi_N, 0\right) \int_0^\delta \frac{\mathrm{d}x}{x^{1+\epsilon}} \right] \\
&\quad + \int \mathrm{d}\Phi_N \int_\delta^1 \frac{\mathrm{d}x}{x} R_N(x) X\left(\Phi_N, x\right) + \mathcal{O}(\delta) \\
&= \lim_{\epsilon \to 0} \left[\int \mathrm{d}\Phi_N \left(\mathrm{d}\sigma^{\text{B}} + \left[1 - \delta^{-\epsilon} \right] \frac{V_N}{\epsilon} \right) X\left(\Phi_N\right) \right] \\
&\quad + \int \mathrm{d}\Phi_N \int_\delta^1 \frac{\mathrm{d}x}{x} R_N(x) X\left(\Phi_N, x\right) + \mathcal{O}(\delta) \\
&= \int \mathrm{d}\Phi_N \left(\mathrm{d}\sigma^{\text{B}} + V_N \log \delta \right) X\left(\Phi_N\right) + \int \mathrm{d}\Phi_N \int_\delta^1 \frac{\mathrm{d}x}{x} R_N(x) X\left(\Phi_N, x\right) + \mathcal{O}(\delta).
\end{aligned}
\tag{2.4.5}
$$

Now each term of the calculation is finite and can be calculated numerically. We show a simple example of the dependence of such a calculation on the cutoff δ for
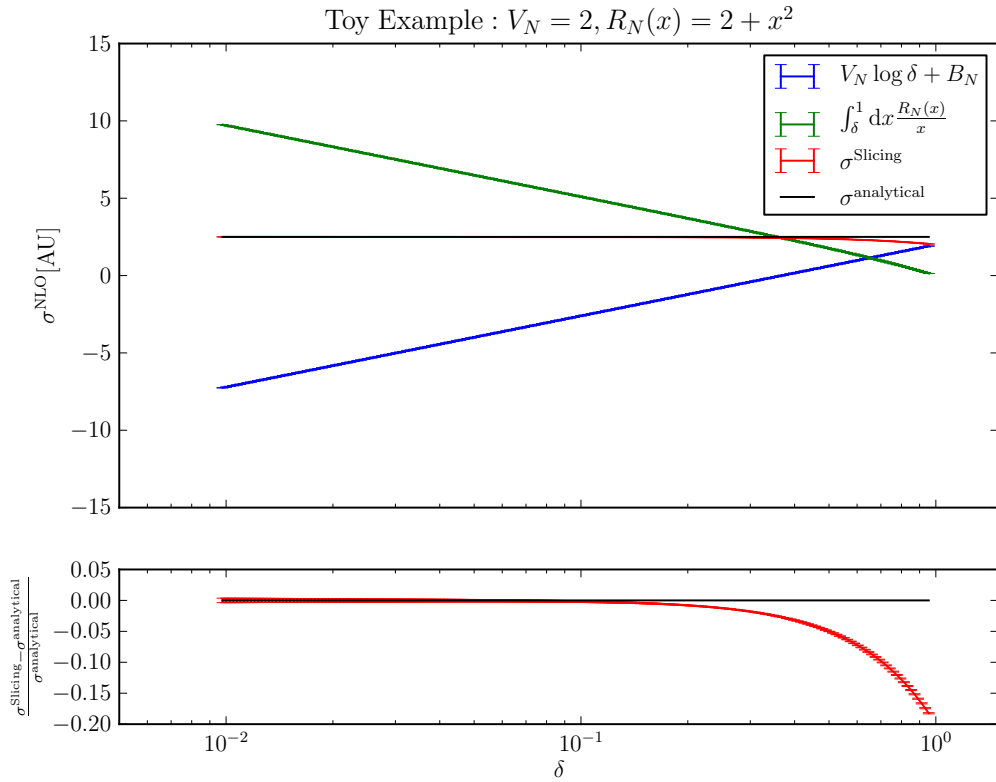
Figure 2.1: Toy example illustrating δ-dependence of the phase space slicing method. In the notation of Eq. (2.4.5), $B_N = 2$, $V_N = 2$ and $R_N(x) = 2 + x^2$ and we assume $\int d\Phi_N = 1$. The analytical result $\sigma^{\text{analytical}} = 2.5$ is shown in black. The result from the phase space slicing is the sum of the virtual and real contributions, shown in blue and green, and approaches the analytical result for low enough cutoffs δ.

$B_N = 2$, $V_N = 2$ and $R_N(x) = 2 + x^2$ in Figure 2.1.

The results of the phase space slicing method can be nicely cross checked, as the calculation should be independent of the cutoff δ. This is evident in Figure 2.1, where below cutoff values of $\delta \approx 0.1$, the result from the slicing method is essentially identical to the analytical result within the integration uncertainties. For higher values of the cutoff, corrections due to the nonsingular terms in the real contributions become visible.

In this form, also the major drawback of this method becomes clear. While the method is simple to implement, there are two requirements that are in major tension: in order to justify the use of the singular approximation, a low cutoff needs to be

chosen. The logarithmic dependence on δ however means low cutoffs are discouraged as they require large cancellations between the separate contributions, and in fact the cutoff should be taken as large as possible to guarantee numerical stability. Therefore this method requires the careful monitoring of the numerical stability, typically necessitating a number of runs at different cutoffs to assess the dependence and stability.

Part I

Accurate simulation of W-, Z-, and Higgs-boson decays in SHERPA

Chapter 3

Introduction

The experiments at the LHC are stress-testing the Standard Model (SM) of particle physics at unprecedented levels of precision. In particular, leptonic standard-candle signatures like charged- and neutral-current Drell-Yan production offer large cross sections together with very small experimental uncertainties, often at or even below the percent level. This allows to extract fundamental parameters in the electroweak (EW) sector of the SM at levels of precision surpassing the LEP heritage. Measurements of the W-boson mass, a key EW precision observable, are already reaching the 20 MeV level [108] based on 7 TeV data alone, with theory uncertainties being one of the leading systematics. Another example for the impressive achievements on the experimental side, challenging currently available theoretical precision, is the recent measurement of the triple differential cross section in neutral current Drell-Yan production based on 8 TeV data [9], the first of its kind at a hadron collider. Furthermore, precision measurements of the Z transverse momentum spectrum [109, 110] have been used to constrain parton distribution functions (PDFs) [111]. In order to fully harness available and future experimental datasets excellent theoretical control of various very subtle effects of higher-order QCD and EW origin is required. For recent reviews and studies on these issues, see e.g. [50, 112, 113]. With this Part we contribute to this effort by investigating higher-order QED/EW effects in the modelling of soft-photon radiation off vector-boson decays.

The demand for (sub-)percent precision in Drell-Yan production has led to formidable achievements in the theoretical description of corresponding collider observables, often pushing boundaries of technical limitations. The pioneering next-to-next-to-leading (NNLO) QCD corrections for differential Drell-Yan production [114–116] are available as public computer codes [117–119] and have recently been matched to QCD parton showers, using the UN^{2}LOPS framework within SHERPA [120], and via a reweighting of a MiNLO improved calculation in DYNNLOPS [121]. Since recently also NNLO corrections to Drell-Yan production at finite transverse momentum are available [85–88, 122–125]. Higher-order EW corrections at the NLO level for inclusive Drell-Yan production have been available for quite some time [126, 127] and are available in a large number of public codes, including WZGRAD [24–26], HORACE [27, 28], SANC [29], RADY [30, 31] and FEWZ [35]. At finite transverse momentum they have been calculated in [128–131]. The combination of higher-order QCD and EW effects is available within the POWHEG framework [32–34, 113, 132, 133] matched to parton-showers. Efforts to calculate the mixed QCD and EW corrections explicitly are underway [134–137]. Their effect has been studied in the pole approximation [36, 138].

At the desired level of precision also QED effects impacting in particular the leptonic final state have to be considered and understood. In this case, soft and collinear photon radiation provides the major contributions. These can be resummed to all orders, and also improved order by order in perturbation theory. Implementations of such calculations have been performed via a QED parton shower matching in HORACE [43, 44] and in the POWHEG framework, in the structure function approach in RADY, and through a YFS-type exponentiation for particle decays in PHOTOS [46], WINHAC [47], the HERWIG module SOPHTY [48] and the SHERPA module PHOTONS [49]. In this Part of the Thesis, we present an extension of the SHERPA module PHOTONS, which provides a simulation of QED radiation in (uncoloured) particle decays. PHOTONS implements the approach of Yennie, Frautschi and Suura (YFS) [45] for the calculation of higher order QED corrections. In the YFS approach,

leading soft logarithms, which are largely independent of the actual hard process involved, are resummed to all orders. Beyond this, the method also allows for the systematic improvement of the description through the inclusion of full fixed-order matrix elements. The present implementation allows for the inclusion of a collinear approximation to the real matrix element using dipole splitting kernels [139]. Furthermore, for several relevant processes, including the decays of electroweak bosons, τ decays as well as generic decays of uncharged scalars, fermionic and vector hadrons, the full real and virtual NLO QED matrix elements are included. This module has also been used for the description of electroweak corrections in the semileptonic decays of B mesons [140]. The aim of this publication is to further enhance the level of precision in the case of the decay of electroweak gauge- and Higgs-bosons bosons by implementing the full one-loop EW corrections, as well as NNLO QED corrections in the case of Z- and Higgs-decays. The electroweak virtual corrections to particle decays have been known for a long time [141, 142] and our implementation will be based on these results. In the case of Z-boson decays, the double virtual corrections in the limit of small lepton masses have been known for about 30 years [143]. We will rely on these results for the virtual corrections.

This Part of the Thesis is organized as follows. In Chapter 4, we review the YFS algorithm, motivating and investigating the procedure to include higher order corrections at a given perturbative order within this framework in Chapter 5. In Chapter 6, we review the results for the decays $Z \to \ell^+\ell^-$, $W \to \ell\nu$ in Drell-Yan production. There we also present results for $H \to \ell^+\ell^-$-decays in hadronic Higgs production. The measurement of the latter is highly challenging due to small leptonic Higgs couplings but potentially achievable at the HL-LHC. We discuss and conclude in Chapter 7.

Chapter 4

The YFS formalism

The results in this Part are obtained from the SHERPA module PHOTONS [49], which simulates QED radiation in particle decays based on the approach pioneered by Yennie, Frautschi and Suura (YFS) [45]. In the work presented here, we implemented the full electroweak next-to-leading order corrections (NLO EW) for the decay of electroweak gauge bosons ($W^{\pm}$- and Z-bosons) into PHOTONS and also included purely electromagnetic next-to–next-to leading order (NNLO QED) corrections for the case of Z-boson and Higgs-boson decays.

4.1 YFS resummation in particle decays

In this section, we will briefly recapitulate the YFS formalism in a form appropriate for the approximate description of photon radiation in particle decays, using the exponentiation of the universal soft limit of matrix elements for real and/or virtual photons and its systematic improvement through exact fixed-order calculations. The decay rate of a decaying particle with mass m and momentum q into a set of decay products with momenta p_f, fully inclusive with respect to the number of real photons n_R, with momenta k_i and phase space Φ_k, and virtual photons n_V reads

$$\Gamma = \frac{1}{2m} \sum_{n_R=0}^{\infty} \frac{1}{n_R!} \int d\Phi_p d\Phi_k (2\pi)^4 \delta\left(q - \sum_f p_f - \sum_{i=0}^{n_R} k_i\right) \left|\sum_{n_V=0}^{\infty} \mathcal{M}_{n_R}^{n_V + \frac{1}{2}n_R}\right|^2 . \quad (4.1.1)$$

Compared to the original, Born-level matrix element M_0^0 describing the decay, the matrix elements $\mathcal{M}_i^j$ include i real photons at the overall order j in the electromagnetic coupling α. This equation for the decay rate describes an unrealistic situation, where we are able to calculate all matrix elements, to all orders, and where we can integrate them over their respective full phase space, while in reality at most the first few orders in perturbation theory can be calculated. The YFS algorithm addresses this by dressing the lowest order matrix elements with exponentiated eikonal factors that capture the leading logarithmic behaviour of the amplitude, thus providing an all-order description of QED radiation correct in this limit. The full result is restored, order by order in perturbation theory, by including the subleading process-dependent parts of the amplitude.

Encapsulating the leading soft behaviour of a single virtual photon in a process-independent factor αB, the full one-loop matrix element can be written as

$$\mathcal{M}_0^1 = \alpha B M_0^0 + M_0^1, \tag{4.1.2}$$

where M_0^1 is an infrared subtracted matrix element including a virtual photon. Note that throughout this paper we assume all charged particles to be massive; consequently the matrix elements do not exhibit collinear singularities. YFS showed that the simple structure at first order above extends also to all further virtual photon corrections. Including the appropriate symmetrization prefactors this generalizes to

$$\mathcal{M}_0^{n_V} = \sum_{r=0}^{n_V} M_0^{n_V-r} \frac{(\alpha B)^r}{r!}. \tag{4.1.3}$$

Upon summing over all numbers of virtual photons n_V, we find that the soft behaviour exponentiates:

$$\sum_{n_V=0}^{\infty} \mathcal{M}_0^{n_V} = \exp\left(\alpha B\right) \sum_{n_V=0}^{\infty} M_0^{n_V}. \tag{4.1.4}$$

In QED, this argument generalises to matrix elements containing any number n_R of real photons. Therefore

$$\left| \sum_{n_V}^{\infty} \mathcal{M}_{n_R}^{n_V + \frac{1}{2}n_R} \right|^2 = \exp\left(2\alpha B\right) \left| \sum_{n_V=0}^{\infty} M_{n_R}^{n_V + \frac{1}{2}n_R} \right|^2, \tag{4.1.5}$$

where the $M_{n_R}^{n_V+\frac{1}{2}n_R}$ are free of virtual soft singularities, but will still contain divergences due to real photons.

In contrast to the virtual amplitudes, the factorization for real photons occurs on the level of the squared matrix elements. For a single photon emission it reads:

$$\frac{1}{2\left(2\pi\right)^3}\left|\sum_{n_V}^{\infty} M_1^{n_V+\frac{1}{2}}\right|^2 = \tilde{S}\left(k\right)\left|\sum_{n_V}^{\infty} M_0^{n_V}\right|^2 + \sum_{n_V=0}^{\infty}\tilde{\beta}_1^{n_V+1}\left(k\right). \tag{4.1.6}$$

The eikonal factor $\tilde{S}\left(k\right)$ contains the soft divergence due to the real photon emission and will be presented later. We denote the complete infrared finite squared matrix element as $\tilde{\beta}_{n_R}^{n_V+n_R}$ and employ the abbreviation

$$\tilde{\beta}_{n_R} = \sum_{n_V=0}^{\infty} \tilde{\beta}_{n_R}^{n_V+n_R} \tag{4.1.7}$$

to write the squared matrix element for the emission of n_R real photons, summed over all numbers of virtual photons n_V, as

$$\left(\frac{1}{2\left(2\pi\right)^3}\right)^{n_R}\left|\sum_{n_V}^{\infty} M_{n_R}^{n_V+\frac{1}{2}n_R}\right|^2$$
$$=\tilde{\beta}_0\prod_{i=1}^{n_R}\left[\tilde{S}\left(k_i\right)\right] + \sum_{i=1}^{n_R}\left[\frac{\tilde{\beta}_1\left(k_i\right)}{\tilde{S}\left(k_i\right)}\right]\prod_{j=1}^{n_R}\left[\tilde{S}\left(k_j\right)\right]$$
$$+\sum_{\substack{i,j=1\\i\neq j}}^{n_R}\left[\frac{\tilde{\beta}_2\left(k_i,k_j\right)}{\tilde{S}\left(k_i\right)\tilde{S}\left(k_j\right)}\right]\prod_{l=1}^{n_R}\left[\tilde{S}\left(k_l\right)\right] + \cdots + \tilde{\beta}_{n_R}\left(k_1,\cdots,k_{n_R}\right). \tag{4.1.8}$$

This expression contains all possible divergences due to real photon emission in the eikonal factors. The first term describes the leading logarithmic behaviour, and contains all virtual insertions to the matrix element without any real photon emission through $\tilde{\beta}_0$. The second term corrects the approximate expression in the $\tilde{S}$ for the real emission of one additional photon to the exact result, and so on. We can now expand the $\tilde{\beta}_i$ in the electromagnetic coupling constant α to get a systematic, perturbative expansion. If we demand agreement with the exact results up to $\mathcal{O}\left(\alpha^2\right)$, this expression reads:

$$\left(\frac{1}{2\left(2\pi\right)^3}\right)^{n_R}\left|\sum_{n_V}^{\infty} M_{n_R}^{n_V+\frac{1}{2}n_R}\right|^2$$

$$= \left(\tilde{\beta}_0^0 + \tilde{\beta}_0^1 + \tilde{\beta}_0^2 \right) \prod_{i=1}^{n_R} \left[\tilde{S}\left(k_i\right) \right] + \sum_{i=1}^{n_R} \left[\frac{\tilde{\beta}_1^1 + \tilde{\beta}_1^2\left(k_i\right)}{\tilde{S}\left(k_i\right)} \right] \prod_{j=1}^{n_R} \left[\tilde{S}\left(k_j\right) \right]$$

$$+ \sum_{\substack{i,j=1 \\ i \neq j}}^{n_R} \left[\frac{\tilde{\beta}_2^2\left(k_i, k_j\right)}{\tilde{S}\left(k_i\right)\tilde{S}\left(k_j\right)} \right] \prod_{l=1}^{n_R} \left[\tilde{S}\left(k_l\right) \right] + \mathcal{O}\left(\alpha^3\right) , \tag{4.1.9}$$

effectively making explicit the terms related to virtual photon corrections[2].

To complete the exponentiation of the leading logarithmic behaviour, we insert this expression into the decay rate and reexpress the momentum conserving δ-functions as exponentials:

$$2m \cdot \Gamma = \int \mathrm{d}y \int \mathrm{d}\Phi_{p_f} \left\{ e^{2\alpha B} \int \mathrm{d}y\, e^{iy\left(q - \sum p_f\right) + \int \frac{\mathrm{d}^3 k}{k^0} \tilde{S}(k) e^{-iyk}} \right.$$

$$\times \left(\tilde{\beta}_0^0 + \tilde{\beta}_0^1 + \tilde{\beta}_0^2 + \int \frac{\mathrm{d}^3 K}{K^0} e^{-iyK} \left(\tilde{\beta}_1^1(K) + \tilde{\beta}_1^2(K) \right) \right.$$

$$\left. \left. + \int \frac{\mathrm{d}^3 K_1}{K_1^0} \frac{\mathrm{d}^3 K_2}{K_2^0} e^{-iy(K_1 + K_2)} \left(\tilde{\beta}_2^2(K_1, K_2) \right) + \mathcal{O}\left(\alpha^3\right) \right) \right\}.$$
$$\tag{4.1.10}$$

In this expression, all virtual infrared singularities are contained in B while all real infrared singularities are contained in the integral over $\tilde{S}(k)$. There, terms diverging in the limit $k \to 0$ can easily be isolated by defining a small soft region Ω that contains the limit $k \to 0$ such that $\Theta(k, \Omega) = 1$ if $k \notin \Omega$:

$$\int \frac{\mathrm{d}^3 k}{k^0} \tilde{S}(k) e^{-iyk}$$

$$= \int \frac{\mathrm{d}^3 k}{k^0} \left\{ \tilde{S}(k) \left[(1 - \Theta(k, \Omega)) + e^{-iyk}\Theta(k, \Omega) + \left(e^{-iyk} - 1 \right)(1 - \Theta(k, \Omega)) \right] \right\}$$

$$= 2\alpha \tilde{B}(\Omega) + D(\Omega). \tag{4.1.11}$$

The two functions $\tilde{B}(\Omega)$ and $D(\Omega)$ are given by

$$2\alpha \tilde{B}(\Omega) = \int \frac{\mathrm{d}^3 k}{k^0} \tilde{S}(k) e^{-iyk} \left(1 - \Theta(k, \Omega) \right) ,$$
$$\tag{4.1.12}$$
$$D(\Omega) = \int \frac{\mathrm{d}^3 k}{k^0} \tilde{S}(k) \left[e^{-iyk}\Theta(k, \Omega) + \left(e^{-iyk} - 1 \right)\left(1 - \Theta(k, \Omega) \right) \right] ,$$

where the former contains the infrared singularities and the latter is infrared regular.

---

[2] For an agreement correct up to order $\mathcal{O}\left(\alpha\right)$, we would need to remove $\tilde{\beta}_0^2$, $\tilde{\beta}_1^2$ and $\tilde{\beta}_2^2$. By far and large this has already been implemented in [49].

This separation allows the re-expansion of the exponentiated integral and the re-instating of explicit momentum conservation through δ-functions, arriving at the master formula for the decay rate in the YFS approach:

$$2m \cdot \Gamma = \sum_{n_R} \frac{1}{n_R!} \int \mathrm{d}\Phi_{p_f} \mathrm{d}\Phi_k \, (2\pi)^4 \, \delta^4 \left(q - \sum_f p_f - \sum_{i=0}^{n_R} k_i \right)$$

$$\times \, e^{Y(\Omega, \{q\})} \prod_{i=1}^{n_R} \tilde{S}(k_i, \{q\}) \, \Theta(k_i, \Omega) \, \tilde{\beta}_0^0(\{q\}) \, \mathcal{C}(\{p\}, \{q\}) \, \mathcal{J}(\{p\}, \{q\}).$$

$$(4.1.13)$$

In the equation above we made the dependence on momenta explicit: the Born-level momenta of the process before QED radiation are denoted by q_i, while the momenta of the full final state including radiation are labelled p_i. The mapping between both sets of momenta is detailed below. The individual terms are

- the YFS form factor

$$Y(\Omega) = \sum_{i<j} Y_{ij}(\Omega) = 2\alpha \left(B_{ij} + \tilde{B}_{ij}(\Omega) \right), \qquad (4.1.14)$$

with the sum running over all pairs of charged particles and the soft factors given by

$$B_{ij} = -\frac{i}{8\pi^3} Z_i Z_j \theta_i \theta_j \int \mathrm{d}^4 k \frac{1}{k^2} \left(\frac{2q_i \theta_i - k}{k^2 - 2(k \cdot q_i)\theta_i} + \frac{2q_j \theta_j + k}{k^2 + 2(k \cdot q_j)\theta_j} \right)^2,$$

$$(4.1.15)$$

$$\tilde{B}_{ij}(\Omega) = \frac{1}{4\pi^2} Z_i Z_j \theta_i \theta_j \int \mathrm{d}^4 k \, \delta\left(k^2\right) \left(1 - \Theta(k, \Omega)\right) \left(\frac{q_i}{q_i \cdot k} - \frac{q_j}{q_j \cdot k} \right)^2.$$

$$(4.1.16)$$

These two terms contain all infrared virtual and real divergences which cancel due to the KLN theorem, guaranteeing the finiteness of $Y(\Omega)$ and of the decay width. Z_i and Z_j are the charges of the particles i and j, and the factors $\theta = \pm 1$ for particles in the final or initial state, respectively. We provide expressions for B_{ij} in final-final and initial-final dipoles in terms of scalar master integrals in appendix D. The calculation of the full form factor can be found in [49];

- the eikonal factor $\tilde{S}(k)$

$$\tilde{S}(k) = \sum_{i<j} \tilde{S}_{ij}(k) = \frac{\alpha}{4\pi^2} \sum_{i<j} Z_i Z_j \theta_i \theta_j \left(\frac{q_i}{q_i \cdot k} - \frac{q_j}{q_j \cdot k} \right)^2 \qquad (4.1.17)$$

describing the soft emission of a photon off a collection of charged particles;

- the lowest order matrix element $\tilde{\beta}_0^0$;

- a correction factor $\mathcal{C}$ to the full matrix element, which we will comment on in more detail in Section 4.3.1;

- and the Jacobian $\mathcal{J}$ capturing the effect of the momenta mapping.

4.2　Momentum mappings

For the purposes of event generation, we need to define the momenta that are used in the master formula Eq. (4.1.13). We will refer to the momenta used in the leading order matrix element, $\tilde{\beta}_0^0$, as the "undressed" momenta, i.e. the momenta before the event is dressed with photons. The undressed momenta are labelled through q_i^μ, and we define as

$$Q_{N/C}^\mu = \sum_{i \in N/CFS} q_i^\mu \qquad (4.2.1)$$

the sums of the final state neutral and charged momenta. After the generation of the additional photon momenta, the undressed momenta have to be mapped to a set of "dressed" momenta to account for momentum conservation. The dressed momenta are labelled through p_i^μ and we define the sums of the neutral and charged final state particles in the same way as for the undressed momenta:

$$P_{N/C}^\mu = \sum_{i \in N/CFS} p_i^\mu . \qquad (4.2.2)$$

In a similar manner, we define the sum of the photon momenta as

$$K^\mu = \sum_{i=1}^{n_R} k_i^\mu . \qquad (4.2.3)$$

The mappings relevant for particle decays of both uncharged and charged initial particles have been outlined in section 3.3 of [49], but we will repeat them here for the benefit of the interested reader. The only condition the mapping has to meet is that in the limit of $K \to 0$, the underlying momenta of the undressed n-parton phase space have to be recovered exactly. QED provides no guiding principle which particle should be taken to balance the momenta of the generated photons. It is therefore sensible to treat all the final state momenta fully democratically and let them all take the recoil. Considering all particles in the rest frame of the multipole responsible for the radiation, this can be achieved by scaling the three-momenta of all final state particles by a common factor u, distributing the photon momenta across and finally enforcing momentum conservation and on-shell conditions.

4.2.1 Neutral initial states

For a neutral particle of mass m decaying into charged particles, such as is the case for the decay of a Z- or a Higgs-boson, the above fixes the mapping to a rescaling of all final state momenta, balancing the photonic momentum by moving the frame of the multipole.

We start with the undressed momenta in the multipole rest frame

$$
q^\mu = \left(\sqrt{m^2 + \vec{Q}_N^2}, \vec{Q}_N \right)
$$
$$
Q_C^\mu = \left(Q_C^0, \vec{Q}_C = \vec{0} \right) \tag{4.2.4}
$$
$$
Q_N^\mu = \left(Q_N^0, \vec{Q}_N \right) .
$$

The outlined procedure maps these momenta onto the final state momenta P_C and P_N:

$$
q'^\mu = \left(\sqrt{m^2 + \left(u\vec{Q}_N + \vec{K} \right)^2}, u\vec{Q}_N + \vec{K} \right)
$$
$$
P_C^\mu = \left(P_C^0, u\vec{Q}_C = \vec{0} \right)
$$
$$
P_N^\mu = \left(P_N^0, u\vec{Q}_N \right) \tag{4.2.5}
$$
$$
K^\mu = \left(K^0, \vec{K} \right) .
$$

We can rewrite the three momentum of the initial state as $u\vec{Q}_N + \vec{K} = u\vec{q} + \vec{K}$ showing that the two vectors q and q' are the same vector in different frames. All momenta now reside in the rest frame of the dressed multipole. We can then determine the scaling parameter u from energy conservation:

$$0 = \sqrt{m^2 + \left(u\vec{Q}_N + \vec{K}\right)^2} - \sum_C \sqrt{m_i^2 + u\vec{q}_i^2} - \sum_N \sqrt{m_i^2 + u\vec{q}_i^2} - K^0. \qquad (4.2.6)$$

4.2.2 Charged initial states

For a charged particle of mass m decaying into a charged particle and a number of neutral particles, such as is the case for the decay of a W-boson, we require a different approach. In order to remain in the rest frame of the dressed multipole, we cannot accomodate the photon momenta purely in the initial state.

Again, we start with the undressed momenta in the multipole rest frame:

$$q^\mu = \left(\sqrt{m^2 + \vec{Q}_C^2}, -\vec{Q}_C\right)$$
$$Q_C^\mu = \left(Q_C^0, \vec{Q}_C\right) \qquad (4.2.7)$$
$$Q_N^\mu = \left(Q_N^0, \vec{Q}_N = -2\vec{Q}_C\right).$$

In the most democratic approach, the photon momenta are accomodated equally by all particles in the final state and the undressed momenta will be mapped onto:

$$q'^\mu = \left(\sqrt{m^2 + \left(-u\vec{Q}_C + n_C\vec{\kappa}\right)^2}, -u\vec{Q}_C + n_C\vec{\kappa}\right)$$
$$P_C^\mu = \left(P_C^0, u\vec{Q}_C - n_C\vec{\kappa}\right)$$
$$P_N^\mu = \left(P_N^0, u\vec{Q}_N - n_N\vec{\kappa}\right) \qquad (4.2.8)$$
$$K^\mu = \left(K^0, \vec{K}\right).$$

All momenta now reside in the rest frame of the dressed multipole. The n_C and n_N denote the number of charged and neutral final state particles, and $\vec{\kappa}$ is defined as:

$$\vec{\kappa} = \frac{1}{2n_C + n_N}\vec{K}. \qquad (4.2.9)$$

One can however also choose to let only the charged particles or only the neutral

particles in the process accomodate the photon momenta, in which case $\vec{\kappa} = \vec{K}/(2n_C)$ or $\vec{\kappa} = \vec{K}/(n_N)$, respectively, and corresponding terms in the mapping vanish. The default option in PHOTONS, and the one that we will choose for the results in this work, is the choice of letting only the neutral particles take the recoil.

Again, the scaling parameter u can be determined from energy conservation:

$$0 = \sqrt{m^2 + \left(-u\vec{Q}_C + n_C\vec{\kappa}\right)^2} - \sum_C \sqrt{m_i^2 + (u\vec{q}_i - \vec{\kappa})^2} - \sum_N \sqrt{m_i^2 + (u\vec{q}_i - \vec{\kappa})^2} - K^0.$$
(4.2.10)

4.3 The algorithm

Having mapped the momenta, including a transformation into the multipole centre of mass frame, the full decay rate can be written as:

$$2M\Gamma = \sum_{n_\gamma} \frac{1}{n_\gamma!} \int d\Phi_q d\Phi_k (2\pi)^4 \delta^3 \left(\vec{Q}_M\right) \delta \left(Q_M^0 - Q_C^0 - p_C^0\right) \tilde{\beta}_0^0 e^{Y(\Omega)} \mathcal{C}$$

$$\times \prod_{i=1}^{n_\gamma} \left[\tilde{S}(k_i)\Theta(k_i, \Omega)\right] \frac{m_{M,p}^3 u^{3n-4}}{M^2 \left(P_C^0 + P_N^0 + K^0\right)} \frac{\frac{\vec{p}^2}{p^0} - \sum_{C,N} \frac{\vec{q}_i^2}{q_i^0}}{\frac{\vec{p}'\vec{p}}{p'^0} - \sum_{C,N} \frac{\vec{p}_i\vec{q}_i}{p_i^0}} \prod_{i=1}^{n} \left[\frac{q_i^0}{p_i^0}\right], \quad (4.3.1)$$

where Q_M denotes the momentum of the multipole centre of mass, and we have written out the Jacobian $\mathcal{J}$. This formula can be simplified by factoring out the leading order differential decay rate $d\Gamma_0$:

$$\Gamma = \sum_{n_\gamma} \frac{1}{n_\gamma!} \int d\Gamma_0 d\Phi_k e^{Y(\Omega)} \mathcal{C} \prod_{i=1}^{n_\gamma} \left[\tilde{S}(k_i)\Theta(k_i, \Omega)\right]$$

$$\times \frac{m_{M,p}^3 u^{3n-4}}{M^2 \left(P_C^0 + P_N^0 + K^0\right)} \frac{\frac{\vec{p}^2}{p^0} - \sum_{C,N} \frac{\vec{q}_i^2}{q_i^0}}{\frac{\vec{p}'\vec{p}}{p'^0} - \sum_{C,N} \frac{\vec{p}_i\vec{q}_i}{p_i^0}} \prod_{i=1}^{n} \left[\frac{q_i^0}{p_i^0}\right]. \quad (4.3.2)$$

In order to generate events using a hit-or-miss Monte Carlo method, we need to overestimate this integral. The maximum of all Jacobians is obtained when the sum of photon momenta vanishes, i.e. for the leading order phase space. Furthermore, the dressed momenta are replaced by the undressed versions and $\mathcal{C} = 1$ is chosen.

Then the distribution reduces to:

$$\Gamma_{\mathrm{cr}} = \sum_{n_\gamma} \frac{1}{n_\gamma!} \int \mathrm{d}\Gamma_0 \mathrm{d}\Phi_k e^{Y(\Omega)} \prod_{i=1}^{n_\gamma} \left[\tilde{S}(k_i)\Theta(k_i, \Omega) \right]$$
$$\approx \Gamma_0 \sum_{n_\gamma}^{\infty} \left[\frac{1}{n_\gamma!} e^{-\bar{n}} \bar{n}^{n_\gamma} \right], \tag{4.3.3}$$

where the YFS form factor has been estimated by $Y(\Omega) \approx -\bar{n}$. Eq. (4.3.3) has the form of a Poissonian distribution with mean photon number $\bar{n}$. This expression allows us to generate the photons once the underlying, zeroth order decay rate, has been generated. For this purpose, we apply the following steps:

1. Generate the number of photons in the event following the above Poisson distribution.

2. Generate energies and angles of the photons according to $\tilde{S}(q, k)$:

   - The energy is distributed according to $\rho(E) \sim \frac{1}{E}$,

   - the angles are distributed according to

   $$\rho(\theta, \phi) \sim \sum_{i<j} \left(\frac{q_i}{q_i \cdot n_k} - \frac{q_j}{q_j \cdot n_k} \right)^2, \tag{4.3.4}$$

   with n_k a light-like unit vector in the direction of the photon.

   Veto the event if the sum of the photon energies exceeds the available energy in the decay.

3. Map the momenta following the mappings given in Section 4.2.

4. Calculate and apply a reweighting using the total weight

   $$W = W_{\mathrm{dip}} \times W_{\mathrm{YFS}} \times W_{\mathrm{J,L}} \times W_{\mathrm{J,M}} \times W_{\mathcal{C}} = \mathcal{J} \times W_{\mathcal{C}}, \tag{4.3.5}$$

   the separate weights being given by:

   $$W_{\mathrm{dip}} = \prod_{i=1}^{n_\gamma} \frac{\tilde{S}\left(p_C, P_C, k_i\right)}{\tilde{S}\left(p_C, Q_C, k_i\right)},$$
   $$W_{\mathrm{YFS}} = e^{Y(p_C, P_C, \Omega) + \bar{n}},$$

$$W_{\mathrm{J,L}} = \frac{m_{M,p}^3}{m_{M,q}^3} \frac{Q_C^0 + Q_N^0}{P_C^0 + P_N^0 + K^0},$$

$$W_{\mathrm{J,M}} = u^{3n-4} \frac{\frac{\vec{p}^2}{p^0} - \sum_{C,N} \frac{\vec{q}_i^2}{q_i^0}}{\frac{\vec{p}'\vec{p}}{p'^0} - \sum_{C,N} \frac{\vec{p}_i \vec{q}_i}{p_i^0}} \prod_{i=1}^{n_\gamma} \left(\frac{q_i^0}{p_i^0} \right),$$

$$W_{\mathcal{C}} = \mathcal{C}.$$

The first of these, W_{dip}, corrects the dipole used in the generation from the unmapped momenta q_i to the mapped momenta p_i, the second weight, W_{YFS}, corrects the YFS form factor, the third and fourth weight account for the Jacobians associated with the Lorentz transformation into the dipole centre of mass frame and the mapping of the momenta respectively, and $W_{\mathcal{C}}$ contains the corrections due to the exact matrix elements.

Applying this algorithm, including the reweighting in the fourth step, means that the distribution of the photons is now correctly described following the distribution of the full YFS method.

4.3.1 The correction factor $W_{\mathcal{C}}$

The correction $W_{\mathcal{C}}$ factor due to the full matrix elements reads:

$$\mathcal{C} = 1 + \frac{1}{\tilde{\beta}_0^0} \left(\tilde{\beta}_0^1 + \sum_{i=1}^{n_\gamma} \frac{\tilde{\beta}_1^1(k_i)}{\tilde{S}(k_i)} \right)$$

$$+ \frac{1}{\tilde{\beta}_0^0} \left(\tilde{\beta}_0^2 + \sum_{i=1}^{n_\gamma} \frac{\tilde{\beta}_1^2(k_i)}{\tilde{S}(k_i)} + \sum_{\substack{i,j=1 \\ i \neq j}}^{n_\gamma} \frac{\tilde{\beta}_2^2(k_i, k_j)}{\tilde{S}(k_i) \tilde{S}(k_j)} \right) + \frac{1}{\tilde{\beta}_0^0} \mathcal{O}\left(\alpha^3 \right). \qquad (4.3.6)$$

The terms in the first bracket describe the *next-to-leading order* (NLO), i.e. the $\mathcal{O}\left(\alpha \right)$ term of the expansion, and the terms in the second bracket describe the *next-to-next-to-leading order* (NNLO), the $\mathcal{O}\left(\alpha^2 \right)$ term of the expansion. Terms of $\mathcal{O}\left(\alpha^3 \right)$ or higher are beyond the scope of this work and will be neglected. Our primary concern in this Part of the Thesis will lie with this correction factor, in particular with the virtual corrections at NLO, i.e. $\tilde{\beta}_0^1$, which we extend to an expression at NLO in the full electroweak theory for the decays of the weak bosons, as well

as the complete NNLO bracket which we will be calculating for the decays of the neutral electroweak bosons. Any further corrections are of at least third order in the electromagnetic coupling constant in comparison to the other terms.

For completeness, we list here the full expressions of the $\tilde{\beta}_{n_R}^{n_R+n_V}$ that will be important in this publication:

$$\tilde{\beta}_0^0 = M_0^0 M_0^{0*},$$

$$\tilde{\beta}_0^1 = M_0^0 M_0^{1*} + M_0^1 M_0^{0*},$$

$$\tilde{\beta}_1^1 = \frac{1}{2(2\pi)^3} M_1^{\frac{1}{2}} M_1^{\frac{1}{2}*} - \tilde{S}(k) M_0^0 M_0^{0*} = \frac{1}{2(2\pi)^3} M_1^{\frac{1}{2}} M_1^{\frac{1}{2}*} - \tilde{S}(k) \tilde{\beta}_0^0,$$

$$\tilde{\beta}_0^2 = M_0^0 M_0^{2*} + M_0^1 M_0^{1*} + M_0^2 M_0^{0*},$$

$$\tilde{\beta}_1^2 = \frac{1}{2(2\pi)^3} \left(M_1^{\frac{3}{2}} \mathcal{M}_1^{\frac{1}{2}*} + \mathcal{M}_1^{\frac{1}{2}} M_1^{\frac{3}{2}*} \right) - \tilde{S}(k) \left(M_0^0 M_0^{1*} + M_0^1 M_0^{0*} \right)$$

$$= \frac{1}{2(2\pi)^3} \left(M_1^{\frac{3}{2}} \mathcal{M}_1^{\frac{1}{2}*} + \mathcal{M}_1^{\frac{1}{2}} M_1^{\frac{3}{2}*} \right) - \tilde{S}(k) \tilde{\beta}_0^1,$$

$$\tilde{\beta}_2^2 = \left(\frac{1}{2(2\pi)^3} \right)^2 M_2^1 M_2^{1*} - \sum_{\substack{i,j=1 \\ i \neq j}} \tilde{S}(k_i) \tilde{\beta}_1^1(k_j) - \tilde{S}(k_i) \tilde{S}(k_j) \tilde{\beta}_0^0. \qquad (4.3.7)$$

We note here that throughout this work, we use dimensional regularization to regulate both the UV and IR divergences that occur at intermediate steps of the calculation.

4.3.2　Momenta in higher order corrections

Having discussed the momentum mappings necessary to map from undressed to dressed momenta, it is worth briefly discussing which set of momenta is to be used in each component of Eq. (4.1.13).

Every part of this formula apart from the correction factor, $\mathcal{C}$, is calculated using the undressed momenta q_i, with the Jacobian $\mathcal{J}$ accounting for the mapping from undressed to dressed momenta. This in particular includes the factors $\tilde{S}$ that implement the soft approximation to the real matrix elements.

The correction factor $\mathcal{C}$ amounts to a reweighting of this approximation to the required order. This means that the correction factor improves upon the approxim-

ation by taking its place. Practically, for the real matrix element corrections, the eikonal factors $\tilde{S}$ have to be cancelled out. Thus, the eikonals in the denominators in Eq. (4.3.6) have to be calculated using the undressed momenta.

All matrix elements containing no additional photon, $\tilde{\beta}_0^i$, are calculated in the n-particle Born phase space, i.e. using the undressed momenta. The terms describing real matrix element corrections are then calculated in the phase space appropriate to the number of photons they contain: In the $n+1$-particle phase space for the single real matrix elements $\tilde{\beta}_1^i$, in an $n+2$-particle phase space for double real matrix elements, $\tilde{\beta}_2^i$, and so on. In order to define the momenta in these phase spaces, we repeat the mapping procedure described previously, but now only taking into account the photons that are taken to be hard in the matrix element correction. This procedure is repeated for every photon or set of photons that have been created. For the single real matrix elements, this means there are in total n_γ calls to the mapping and the matrix elements, while for the double real matrix elements, there are $n_\gamma(n_\gamma - 1)/2$ calls to the mapping and the matrix element. If no photon has been generated, no real weights are calculated, if only one photon is generated, then the double real matrix elements are not calculated.

Chapter 5

NLO EW and NNLO QED corrections within PHOTONS

5.1 Motivation for higher order corrections

The previous chapter dealt with the procedure for dressing the lowest order matrix element with soft radiation to all orders. This basic procedure, in which $\mathcal{C} = 1$, yields photon distributions that are correct in the limit of soft radiation. For the remainder of this Part, we will call this the *soft approximation*. Away from the soft limit, exact matrix elements are necessary to describe observables at the required accuracy, and we described the procedure for their systematic incorporation. Hard photon radiation occurs predominantly collinear to the emitter and more frequently in processes with large energy-to-mass ratios of the involved particles. With this in mind, generic collinear corrections for the real matrix element, based on the splitting functions developed in [139], were employed in [49] to account for hard QED radiation in the *soft-collinear approximation*. While this approximation correctly describes radiation in the limits of soft and collinear radiation, it does not account for either interference effects or hard wide-angle radiation. In order to capture these effects correctly, full matrix elements for real and virtual photon radiation must be added, some of which have already been included in [49].
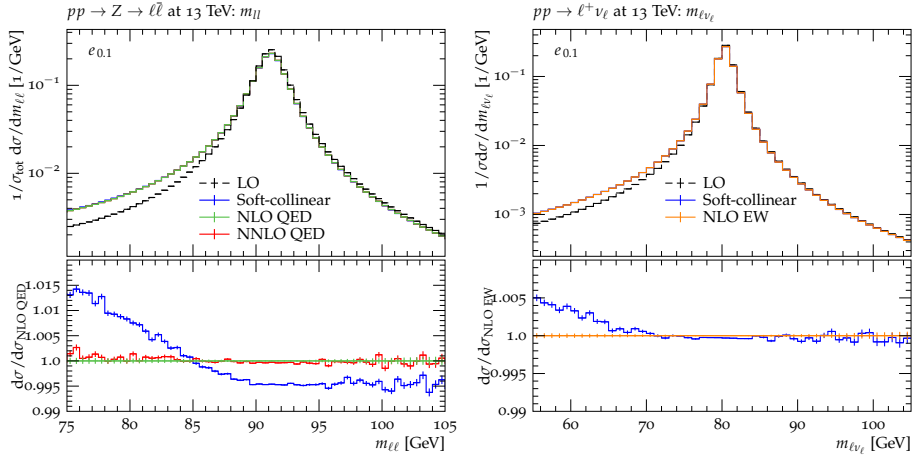
Figure 5.1: The invariant mass $m_{\ell\ell}$ of the two leptons in Z-boson decays on the left and the invariant mass $m_{\ell\nu}$ of the charged lepton and the neutrino in W-boson decays on the right are shown for the processes $pp \to Z \to e^+e^-$ and $pp \to W^+ \to e^+\nu_e$ respectively. Different levels of fixed order accuracy are compared. The electrons in both cases are dressed with collinear photons within $dR = 0.1$.

In Fig. 5.1 we compare the soft-collinear, the full NLO-correct results and the NNLO-correct results for the invariant mass $m_{\ell\ell}$ of the electrons produced in Z-boson decays, as well as the soft-collinear and full NLO-correct results for the invariant mass $m_{\ell\nu}$ of the charged electron and the neutrino in W-boson decays. To guide the eye we also show the leading-order result for both distributions. The NLO result represents the maximal accuracy of the implementation in PHOTONS as described in [49].

These distributions clearly show the necessity to include photon radiation in the first place. Photon radiation causes a significant shape difference, shifting events from large to lower $m_{\ell\ell}$ or $m_{\ell\nu}$. This effect is a lot more striking in the decay into the lighter leptons, such as the electrons exhibited here, which are much more likely to radiate photons. We can also appreciate that while the soft-collinear approximation does a good job of describing the distribution near the peak, it predicts a harder spectrum at lower values of $m_{\ell\ell}$ or $m_{\ell\nu}$. The peak region corresponds to the limit of soft photon radiation, while the latter region corresponds to hard photon radiation. This observation thus suggests that in order to capture the behaviour of the distribution over its entirety, we need to employ full matrix elements. It is then natural to ask whether higher order corrections beyond the NLO in QED are required as well. The

description of these higher order corrections will be the focus of the next sections.

5.2 NLO Electroweak correction

The discussion in Chapter 4 was restricted to QED corrections only. Since the exponentiation relies on the universal behaviour of the amplitudes in the soft limit only, additional fixed-order corrections can easily be added, as long as they are *not* divergent in the soft limit and thus do not spoil the soft-photon exponentiation. This is, in fact, the case for the weak part of the corrections in the full electroweak theory, where the masses of the weak bosons regulate the soft divergence that is plaguing the massless photon. In this work, we will be concerned with the decays of weak bosons; consequently, there is no phase space available for the emission of a real, massive weak boson, and the additional electroweak corrections contribute only to the virtual corrections $\tilde{\beta}_0^{n_V}$.

The known one-loop virtual corrections for the decays of the electroweak bosons [141, 144] have been implemented in a number of programs dedicated to electroweak precision calculations already mentioned in the introduction. They can be calculated analytically with programs such as FEYNCALC [145, 146], FORMCALC [147] or *Package*-X [148], and numerically with programs such as GOSAM [149, 150], MADGRAPH5 [37, 38], OPENLOOPS [39, 40] or RECOLA [41, 42]. The two-loop virtual electroweak corrections are not fully known yet, with only partial results for particular observables available, see for example [151, 152].

We implemented the electroweak corrections for the decays $Z \to \ell\bar{\ell}$, $H \to \ell\bar{\ell}$ and $W \to \ell\nu$. In doing so, we also reimplemented, and revalidated, the QED corrections in a more straightforward way. We retain the full dependence on the lepton masses in the decay $H \to \ell\bar{\ell}$, while we only retain the lepton masses in the QED part of the corrections in the other two decays, where they are required to regularize the collinear singularities, and neglect them in the other contributions. To this end we used the vertex form factors found in [142] to describe the virtual corrections to the vertices.

We renormalize the theory using the on-shell renormalization scheme, following the treatment described in [141]. The choice of this renormalization scheme means the corrections to the external legs are absorbed into renormalization constants so that we do not need to consider self-energy corrections to the external legs in the amplitude. The renormalization in the on-shell scheme is discussed in Appendix B. We validated the amplitudes and the implementation of the higher order corrections in a number of ways presented in Appendix G.

For the decays of Z- and Higgs-bosons, we further implement an option to consider only QED corrections. In the decay of neutral bosons, this choice forms a gauge-invariant subset of the full electroweak corrections and can thus be considered independently. Practically, this amounts to turning off the purely weak vertex form factors as well as turning off those parts of the renormalization constants that are of weak origin. This option is not available in the case of a W-boson decay as the W itself couples to the photon. We list the relevant form factors, renormalization constants and the necessary modifications in the pure QED case in Appendix C.

As mentioned at the start of this section, there are no real corrections due to the weak part of the theory, so the only contribution here remains the real radiation of an additional photon. We approach these contributions by splitting the fermion propagators into spin sums and writing the helicity amplitudes in terms of X-, Y- and Z-functions [54, 153–155]. We give a more detailed discussion of this approach in Appendix F.

5.3 NNLO QED corrections

We will now turn to the discussion of the NNLO QED corrections to Z- and Higgs-boson decays, which represent the next step up in accuracy. These corrections are particularly interesting in the context of providing better predictions in those distributions, or parts thereof, that are not accessible kinematically in the NLO corrections. As discussed in Section 2, the NNLO QED corrections consist of double-

virtual, real-virtual and real-real corrections. The NNLO QED corrections can be combined with the full NLO EW corrections, and we will label that combination "NNLO QED $\oplus$ NLO EW".

5.3.1 Double virtual corrections

The two-loop QED corrections to the form factor for the Z-boson decay have been known in the limit of small lepton masses since the LEP era [143, 156]. To the best of our knowledge, there are no such results for the decay of Higgs bosons in QED. Including the full mass dependence, at the moment only the two-loop form factor for the decay of a virtual photon is known analytically in QED [157].

Furthermore, in a series of papers, the two-loop QCD corrections including the full mass dependence to the vector [158], the axial vector [159], the anomaly contributions [160] and the scalar and pseudo-scalar form factors [161] have been obtained, which have recently been extended to also include the $\mathcal{O}(\epsilon)$ contributions [162]. From these, the full two-loop form factors in QED can in principle be obtained by considering only the abelian contributions to the QCD form factors and replacing the respective group factors by the appropriate ones in QED. We have however not been able to successfully reproduce the two-loop QED form factor as cited in [143] from these results. Thus for the description of the decays of Higgs-bosons, we rely on the leading logarithmic behaviour, $\tilde{\beta}_0^2 = \frac{1}{2} \log^2 \left(\frac{s}{m^2} \right)$. We find that for the decays into muons, this is a sufficient approximation and we only start to see appreciable effects that may root in the missing two-loop terms when considering the decay into τ's.

For the decay of the Z-boson, we can use the results in Eqs. (2.15) and (2.22) from [143], together with the subtraction term B expanded in the limit $s \gg m^2$, to find the infrared subtracted double virtual corrections in this limit. The results for the form factors given in [143] are sufficient as we only require $\text{Re}(M_0^2 M_0^{0*})$ in the double virtual correction. The two-loop amplitude M_0^2 reduces here to a simple factor multiplying the leading order matrix element, so that only the real part of

M_0^2 is necessary for the calculation of $\tilde{\beta}_0^2$.

The double virtual corrections can be decomposed, following the procedure described in Chapter 4, as

$$\mathcal{M}_0^2 = M_0^2 + \alpha B M_0^1 + \frac{(\alpha B)^2}{2!} M_0^0, \tag{5.3.1}$$

so that the infrared subtracted matrix element reads:

$$M_0^2 = \mathcal{M}_0^2 - \alpha B M_0^1 - \frac{(\alpha B)^2}{2!} M_0^0 = \mathcal{M}_0^2 - \alpha B \mathcal{M}_0^1 + \frac{(\alpha B)^2}{2!} M_0^0. \tag{5.3.2}$$

In the second step we used the decomposition $M_0^1 = \mathcal{M}_0^1 - \alpha B M_0^0$.

Using the results in [143] and the form of the subtraction term given in Eq. (D.1.2), we can then use this result to get $\mathrm{Re}M_0^2$:

$$\begin{aligned}
\mathrm{Re}M_0^2 = \frac{\alpha^2}{\pi^2} \Bigg[& \frac{1}{8} \log^2 \left(\frac{s}{m_l^2} \right) + \log \left(\frac{s}{m_l^2} \right) \left(-\frac{5}{32} - \frac{\pi^2}{8} + \frac{3}{2} \zeta(3) \right) \\
& - \frac{9}{4} \zeta(3) - \frac{\pi^4}{15} + \frac{3}{2} + \pi^2 \left(\frac{13}{32} - \frac{\log 2}{2} \right) \Bigg] M_0^0,
\end{aligned} \tag{5.3.3}$$

where m_l denotes the lepton mass and $\zeta(n)$ is the Riemann Zeta function, with $\zeta(3) \approx 1.202056903159594$.

Then the correction term $\tilde{\beta}_0^2$ becomes:

$$\begin{aligned}
\tilde{\beta}_0^2 = & M_0^2 M_0^{0*} + M_0^1 M_0^{1*} + M_0^0 M_0^{2*} \\
= & \frac{\alpha^2}{\pi^2} \Bigg[\frac{1}{2} \log^2 \left(\frac{s}{m_l^2} \right) + \log \left(\frac{s}{m_l^2} \right) \left(-\frac{13}{16} - \frac{\pi^2}{4} + 3\zeta(3) \right) \\
& - \frac{9}{2} \zeta(3) - \frac{2\pi^4}{15} + \frac{13}{4} + \pi^2 \left(\frac{17}{16} - \log 2 \right) \Bigg] \tilde{\beta}_0^0.
\end{aligned} \tag{5.3.4}$$

5.3.2 Real-virtual corrections

The real-virtual corrections contain the virtual corrections to the process $X \to f \bar{f}^{(\prime)} \gamma$, with one real, hard photon. We can write the infrared subtracted, squared real-virtual matrix elements as:

$$\tilde{\beta}_1^2 (k_1) = \frac{1}{2 (2\pi)^3} \sum_{s_i, \lambda_j} \left(M_1^{\frac{3}{2}*} \mathcal{M}_1^{\frac{1}{2}} + \mathcal{M}_1^{\frac{1}{2}*} M_1^{\frac{3}{2}} \right) - \tilde{S} (k_1) \tilde{\beta}_0^1, \tag{5.3.5}$$

where k_1 denotes the momentum of the hard photon, and the sum in the first term runs over the spins s_i of the leptons and the polarizations λ_j of the vector bosons. The factor $\tilde{S}(k_1)$ is calculated using the momenta mapped to the single photon final state taking k_1 as the hard photon momentum. For consistency, $\tilde{\beta}_0^1$ contains only the one-loop QED corrections.

The expression above, Eq. (5.3.5), includes one-loop corrections to the vertices, the internal propagators, and, new at this level, box diagrams as well, all of which can be dealt with using the Passarino-Veltmann reduction scheme. This scheme reduces the rank of the tensor integrals encountered in the calculation of the loop corrections, returning an expression containing rational factors multiplying a number of lower rank integrals. Through successive application of this reduction, the entire amplitude can be written in terms of a set of standard matrix elements multiplied by expressions involving scalar master integrals. To reduce the time spent in function calls, we use FEYNCALC's implementation of the Passarino-Veltmann reduction scheme to perform this reduction to an expression containing only scalar integrals. We have encoded the neccessary master integrals using [141, 142, 163]. These are listed in Appendix E. To this end, we also implemented the algorithm proposed in [164] for the evaluation of the complex dilogarithm occuring in the master integrals.

In the somewhat lengthy expressions, we have confirmed the analytical cancellation of the UV divergences upon including the renormalization terms as well as the cancellation of the virtual IR divergences upon inclusion of the infrared subtraction term. However, the very nature of the expressions involved increases the likelihood of numerical instabilities in the evaluation of particular phase space points: while strictly finite, separate terms in the expression may grow beyond the limits of the `double` precision employed in our implementation. Such cases cause incomplete cancellations between different terms and thus may upset the accuracy of our result. The reasons are twofold, and connected with the collinear regime of the emissions:

- The YFS formalism relies on fermion masses to regularize the collinear singularities, which in the case of small fermion masses may amount to the evaluation

of expressions very close to this shielded singularity, of the type $\log(s_{ij}/m^2)$, where $s_{ij} = (p_i + p_j)^2$ is the invariant mass of two momenta. We find that in our implementation the amplitudes for the decays into electrons and to some extent also into muons are affected by numerical instabilities while the amplitudes for the decays into τ's are well-behaved.

- In addition, the Passarino-Veltmann reduction may lead to the appearance of small Gram determinants in denominators. The reduction amounts to solving systems of equations relating higher rank tensor integrals to lower order ones. This procedure is repeated until every tensor integral has been expressed in terms of scalar master integrals, which can then be calculated using Feynman parameterization. Common to each reduction step is the inversion of a Gram matrix, the matrix containing all permutations of scalar products between the external momenta p_i flowing into the loop, $G_{ij} = p_i \cdot p_j$. In the inversion, the expression is divided by the determinant of this matrix, the Gram determinant, such that a small value of this determinant may lead to a very large overall expression. As an example, take the case of bubble integrals with just two momenta flowing into the loop. For on-shell external lines, the Gram determinant is then $\det G = (p_1 \cdot p_2)^2 - p_1^2 p_2^2 = (p_1 \cdot p_2)^2 - m_1^2 m_2^2$. In the case of small masses m_i, this expression can become very small when $p_1 \cdot p_2 \to 0$.

  One way to circumvent this issue is by employing an expansion in the Gram determinant for the problematic tensor integrals rather than the full reduction, as is implemented in the Collier library [165]. Since this requires the implementation of a significant number of expressions for different combinations of arguments in the tensor integrals, such an implementation carries a large overhead and is not pursued in this work.

To cure both problems, we instead use the following algorithm: We call a phase space point "collinear" when $s_{ik} < a \cdot m_i^2$, where s_{ik} is the invariant mass between the photon and one of the fermions in the process and a is some predefined cutoff. Such

a phase space point will not be evaluated using the full matrix element but rather using the quasi-collinear limit of the amplitude. Using this limit, the calculational complexity of the amplitude is significantly reduced and numerical instabilities are avoided.

As an additional rescue system, in case a bad phase space point should still pass to be evaluated using the full matrix element, we also check the scaling behaviour of the amplitude under a rescaling of all dimensionful quantities. The expressions for the coefficients of the master integrals can be rewritten using reduced quantities, i.e. all dimensionful quantities are divided by the centre of mass energy of the decay. In this way, dimensionful quantities only survive in the master integrals themselves as well as in a single factor multiplying the master integral[3]. The mass dimension of a four point function in four dimensions is 0, such that upon rescaling all scales in the master integrals and the coefficients by a common factor $\xi \neq 1$, the full expression should remain unchanged, $\mathcal{M}(\xi) = \mathcal{M}(1)$. Different terms in the matrix elements scale differently due to the different scaling behaviours of the master integrals, so a deviation from the expected scaling behaviour indicates numerical instabilities in the expression. If we find $\left| \frac{\mathcal{M}(1)}{\mathcal{M}(\xi)} - 1 \right| > c$, with c some predefined cutoff, we decide to set the real-virtual matrix element to 0. It would be possible to try and cure such problematic phase space points by reevaluating them using `quad` precision, as is done e.g. in OPENLOOPS, but SHERPA does not have the facility to use this option presently.

Only once a point passes through these two checks, it is evaluated using the full matrix element. The introduction of two in principle arbitrary cutoffs mandates a check of the behaviour of the results upon variation of this cutoff. We will comment on this in Appendix G.

---

[3]In four dimensions, the tadpole diagrams A_0 have mass dimension 2, the bubble integrals B_0 are dimensionless, the triangle integrals C_0 have mass dimension -2 and the box integrals D_0 have mass dimension -4. Thus the scale is raised at most squared in all expressions.

5.3.3 Real-real corrections

The real-real corrections stem from the emission of two hard photons. In the case
of Z- or Higgs-boson decays, these corrections involve the repeated emission of two
photons from either the lepton or the antilepton and the emission of one photon off
the lepton and the other off the anti-lepton. For the implementation, we choose the
same strategy as in the case of single real corrections, using helicity amplitudes and
building blocks already present in SHERPA. We detail the amplitudes in Appendix
F and the strategy used to calculate them.

After setting up the amplitude like this, we can calculate the infrared subtracted
matrix element squared that enters into the correction factor $\mathcal{C}$:

$$\tilde{\beta}_2^2\left(k_1, k_2\right) = \left(\frac{1}{2\left(2\pi\right)^3}\right)^2 \sum_{s_i, \lambda_j} \mathcal{M}_2^{1*}\mathcal{M}_2^1 - \tilde{S}\left(k_1\right)\tilde{\beta}_1^1\left(k_2\right) - \tilde{S}\left(k_2\right)\tilde{\beta}_1^1\left(k_1\right) - \tilde{S}\left(k_1\right)\tilde{S}\left(k_2\right)\tilde{\beta}_0^0.$$

$$(5.3.6)$$

In this formula, the k_1 and k_2 denote the momenta of the two hard photons, the
sum in the first term runs over the spins s_i of the leptons and the polarizations λ_j
of the vector bosons. The $\tilde{S}\left(k_i\right)$ are calculated using the momenta in the mapped
$(n+2)$-dimensional phase space, using the pair k_1, k_2 as the hard photons.

Chapter 6

Results

6.1 Setup

In this section we present the numerical effects induced by the NLO EW and NNLO QED corrections presented in the previous section, focussing on the decays $Z \to \ell\bar{\ell}$, $W \to \ell\nu$ and $H \to \ell\bar{\ell}$ with $\ell = \{e, \mu, \tau\}$ following hadronic neutral-current and charged-current Drell-Yan and Higgs production respectively.

The results presented here are based on an implementation in the PHOTONS module [49] of the SHERPA Monte Carlo framework (release version 2.2.4). We consider hadronic collisions at the 13 TeV LHC for the production of Z-, W- and Higgs-bosons and their subsequent decays. In the neutral-current Drell-Yan case we require $65\,\text{GeV} < m_{\ell\ell} < 115\,\text{GeV}$, while for the other modes no generation cuts are applied. Since we aim to purely focus on the effects of photon radiation in the decays, we turn off the QCD shower, fragmentation and underlying event simulation. We use RIVET 2.5.4 [166] for the analysis. For the case of electrons in the final state, we perform the analysis either using bare leptons or using dressed leptons with a radius parameter $dR = 0.1$ or $dR = 0.2$. For the case of muon and τ final states only bare results are shown. We focus our results on a few key distributions and always normalize to the respective inclusive cross section. Overall, we choose to focus on

	Mass [GeV]	Width [GeV]
Z	91.1876	2.4952
W	80.385	2.085
H	125	0.00407
e	$0.511\,\mathrm{MeV}$	-
μ	$0.105\,\mathrm{GeV}$	-
τ	$1.777\,\mathrm{GeV}$	-
ν_i	$0\,\mathrm{GeV}$	-
$1/\alpha\,(0)$	137.03599976	

Table 6.1: Electroweak input parameters: gauge- and Higgs-boson masses and widths, lepton masses and the EW coupling in the $\alpha(0)$ scheme.

ratios between different predictions, in order to highlight small subtle differences relevant for precision Drell-Yan and Higgs physics.

Input parameters for the numerical results are chosen as listed in Tab. 6.1. The weak coupling α is defined in the on-shell $\alpha(0)$ scheme. This choice is sensible as we are explicitly also investigating distributions in resolved final-state photons. At the same time, the YFS formalism is strictly only defined in the limit of soft photon emissions. In this input scheme, the sine of the weak mixing angle is a derived quantity $s_W^2 = 1 - \frac{M_W^2}{M_Z^2}$. Gauge- and Higgs-boson widths are taken into account in a fixed-width scheme.

In the decays of W- and Z-bosons, we apply an IR technical cutoff in the YFS formalism of $E_{\gamma,\mathrm{cut}} = 0.1\,\mathrm{GeV}$, while in the Higgs-decay we reduce this value to $E_{\gamma,\mathrm{cut}} = 0.01\,\mathrm{GeV}$ in order to improve the resolution near the resonance[4]. In both cases, we keep an analysis cut of $E_\gamma > 0.1\,\mathrm{GeV}$ for observables involving photons.

---

[4]It should of course be noted that the SM Higgs has a resonance width of only $\sim 4\,\mathrm{MeV}$, which is smaller than this photon cut, suggesting that we still do not resolve the resonance well with this cut. However, from the results of Appendix G we see that a cut of the order $10\,\mathrm{MeV}$ is necessary in order to guarantee a good performance of the method in both decay channels. In any case, this smaller choice of the cutoff still allows a closer investigation of the regions close to the resonance in plots generated from the lepton momenta, as long as the binning is not chosen too fine. In particular the regions that will be populated through the radiation of photons from leptons in the resonance region will be included in this description.
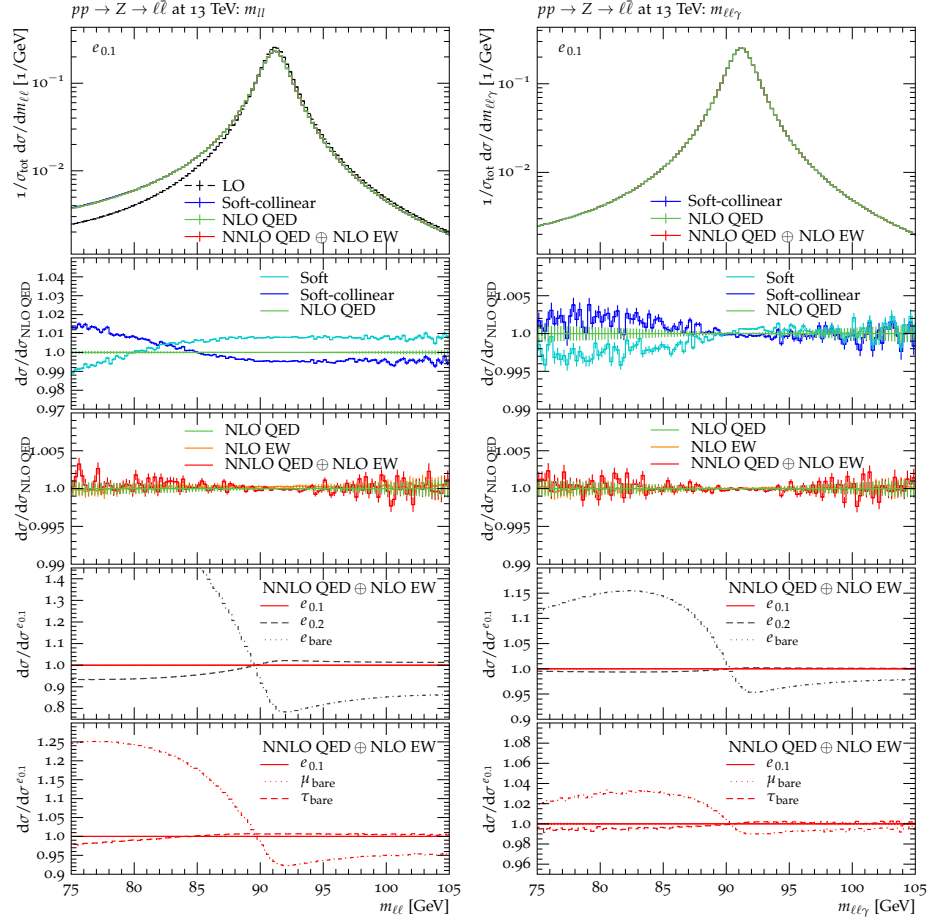
Figure 6.1: On the left the invariant mass of the two leptons, $m_{\ell\ell}$, and on the right the invariant mass of the system of the two decay leptons and the closest photon, $m_{\ell\ell\gamma}$, is shown for $pp \to Z \to \ell^+\ell^-$ production. Nominal predictions are shown for $pp \to Z \to e^+e^-$ at LO, in soft-collinear NLO approximation, at NLO QED and at NNLO QED $\oplus$ NLO EW, where electrons are always dressed with collinear photons within $dR = 0.1$. The ratio plots highlight the effect of the considered higher-order corrections and the effect due to different photon dressing or lepton identity. See text for details.

6.2 Neutral Drell-Yan lepton pair production

In Figs. 6.1-6.3 we present several key observables in neutral-current Drell-Yan production including higher-order QED corrections up to NNLO and EW corrections up to NLO. All distributions are normalized and the effects of the higher-order corrections typically manifest themselves as very subtle shape distortions in the considered observables. All figures are identically structured and we show nominal predictions for dressed di-electron production, i.e. collinear photon–electron pairs with $dR < 0.1$ are combined, at LO (black), considering soft-collinear QED corrections (blue), NLO QED corrections (green), and our best predictions at NNLO QED $\oplus$ NLO EW (red). In the first two ratio plots we compare the predictions at NLO QED against the soft and soft-collinear approximations and against the NLO EW and NNLO QED $\oplus$ NLO EW predictions respectively. In the third ratio plot we investigate different dressing prescriptions of the electrons, considering $dR = 0.2$ and undressed bare electron. Finally, in the last ratio plot we compare predictions for dressed electron with corresponding ones for bare muons and τ's. In the latter two ratios plots all predictions correspond to the most accurate level, i.e. NNLO QED $\oplus$ NLO EW.

In Fig. 6.1, we present the distributions of the invariant mass of the two leptons, $m_{\ell\ell}$, (left) and of the invariant mass of the system made up of the decay leptons and the photon closest to either of them, $m_{\ell\ell\gamma}$ (right).

Already from the plots in Section 5.1, it is clear that the inclusion of photon radiation is crucial for a reliable description of the dilepton invariant mass. All higher-order corrections significantly differ from the LO prediction, which fails to describe the lineshape below the peak. At the NLO QED level corrections beyond the soft and soft-collinear approximations induce distortions up to the 1% level. In fact, the soft approximation does not generate enough hard radiation, while the soft-collinear approximation produces about 1% too many events at low $m_{\ell\ell}$, i.e. it seems to generate too much hard photon radiation. In this observable both the NLO EW and NNLO QED corrections provide only a marginal effect on the order of permille, and
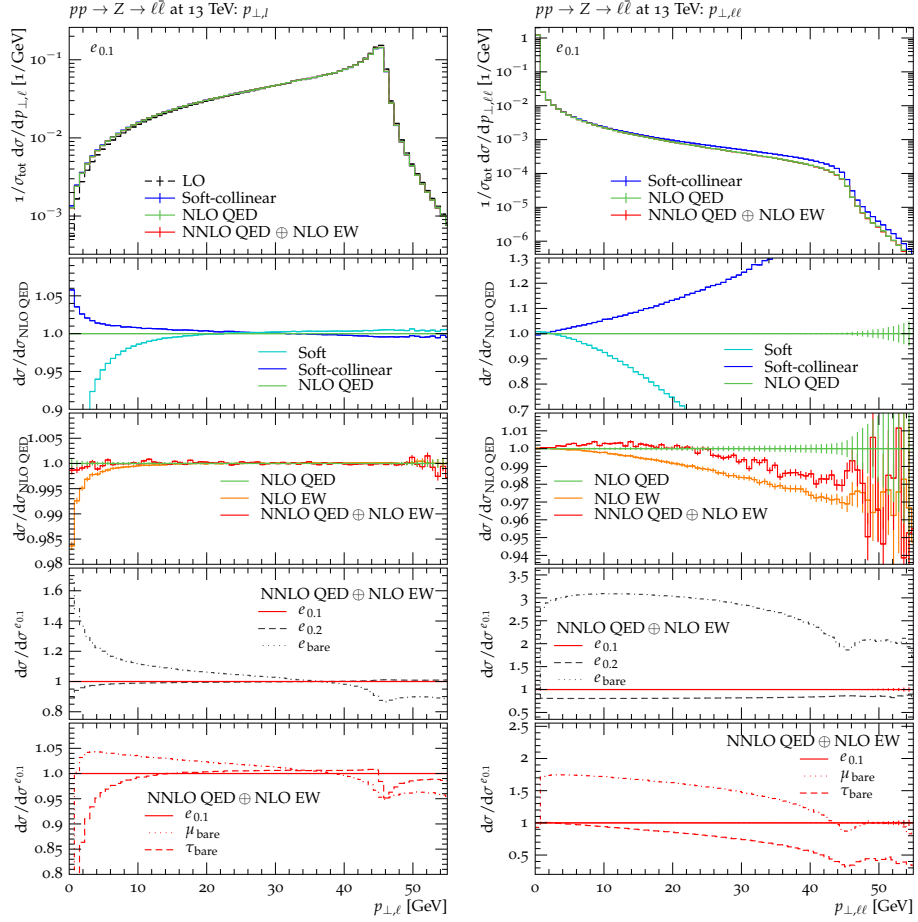
Figure 6.2: Plots of the transverse momentum of the leptons, $p_{\perp,\ell}$, on the left and the transverse momentum of the system of the two decay leptons, $p_{\perp,\ell\ell}$, on the right. Predictions and labels as in Fig. 6.1.

neither of these corrections provides a significant shift of the peak of the distribution.

Clearly, the dressing of the electrons has a significant effect on this distribution, reflecting the sensitivity to QED radiation. Bare electrons show a significant shape difference compared to dressed electrons. The results based on different dressing parameters however differ by at most a few %, suggesting that much of the photon radiation occurs close to the electron. Comparing different lepton species, we see that muons, in comparison to the dressed electrons, radiate significantly more, yielding up to 25% more events at low $m_{\ell\ell}$. In contrast, the heavier τ's radiate less in comparison, resulting in differences with respect to dressed electrons of only a few %.

A very similar behaviour can be found in the invariant mass of the dilepton system

combined with the closest photon. As this observable requires the emission of at least one photon, the NLO QED curve corresponds effectively to a LO prediction. However, also the soft and soft-collinear approximations describe this observable reasonably well and higher order NNLO QED or NLO EW corrections are negligible. Comparing the dressing parameters, we find much smaller differences here: bare electrons only differing by about 15% from the dressed versions. There is barely a difference between the two dressings. In the same manner, the difference between lepton species is subdued as well: muons differing up to 2% at most from dressed electrons.

In Figure 6.2, we present the distribution of the transverse momentum of the lepton, $p_{\perp,\ell}$, alongside the transverse momentum of the system of the two leptons, $p_{\perp,\ell\ell}$.

The transverse momentum of the leptons, $p_{\perp,\ell}$, receives small corrections from the inclusion of higher order corrections beyond NLO QED into the YFS formalism. Only the phenomenologically irrelevant region of very low $p_{\perp,\ell}$ receives corrections at the permille level at NLO EW. Both the soft and soft-collinear approximations agree at the permill level with NLO QED for $p_{\perp,\ell} > 20$ GeV.

Correspondingly, also the dressing of the electrons has a small effect on this distribution, with bare electrons carrying significantly less transverse momentum than the dressed versions. The difference between lepton species is marginal, up to about 5% at very low $p_{\perp,\ell}$ and above the Jacobi peak.

In contrast, the transverse momentum of the system of leptons, $p_{\perp,\ell\ell}$, shows significantly larger effects. Of course this distribution is not defined at LO and correspondingly it is very sensitive to the modelling of photon radiation.

This can be appreciated when comparing the NLO QED prediction with the soft and soft-collinear approximations. Only at small $p_{\perp,\ell\ell}$ the approximations agree. In this observable also the inclusion of NLO EW effects shows a significant impact, with differences reaching up to 5%. The NNLO QED effects provide a competing effect to the NLO EW corrections, lifting the distributions by about 2% across the entire

Figure 6.3: Plots of the sum of the photon energies in the decay rest frame, $\sum_{n_\gamma} E_\gamma$, on the left and the ϕ_η^* variable on the right. Predictions and labels as in Fig. 6.1.

distribution.

The effects of the dressing on the distribution is unsurprisingly very large as well. Bare electrons show significantly more events at non-vanishing values of $p_{\perp,\ell\ell}$, while a different dressing parameter leads to an almost flat decrease across the spectrum. The comparison of the different lepton species shows that the muons again radiate a lot more, with up to 75% more events at medium $p_{\perp,\ell\ell}$. τ's in comparison show a reduction in the number of events at large $p_{\perp,\ell\ell}$ of up to 50%.

Finally, in Figure 6.3, we show the distribution of the sum of the photon energies in the decay rest frame, $\sum_{n_\gamma} E_\gamma$, and the distribution of the so-called ϕ_η^*-variable.

The sum of the photon energies is largely correlated with the $p_{\perp,\ell\ell}$, as discussed before. This distribution shows a distinct edge at about half the Z-boson mass,

which is being washed out by multiple radiation. The kinematics of the decay restrict the energy of a single radiated photon to be smaller than $E^1_{\gamma,\max} = \frac{\hat{s}-4m_\ell^2}{2\sqrt{\hat{s}}}$, which is roughly equal to half the boson mass near the resonance. For an event to have a total photon energy beyond this edge, two hard photons need to recoil at least partly against each other. The region above the kinematical edge is then only described approximately, as long as no NNLO corrections are considered.

The NLO EW prediction mildly increases the number of events without photon radiation, leading to a decrease at the kinematic edge of about 3%. The NNLO QED corrections again provide a competing effect, leading to a difference of about 1% to the NLO QED predictions near the edge. Beyond it, the NNLO QED corrections show a significant departure from the shape of the previous predictions as this region is for the first time described correctly at fixed order.

The behaviour of different dressings and lepton species is very similar to the case of the $p_{\perp,\ell\ell}$. The bare electrons show a significantly larger number of hard photons, while another dressing only leads to an approximately flat decrease. Muonic decays contain a larger number of events with hard photons, while τ's radiate significantly less.

The ϕ^*_η-variable [167] can be seen as an alternative to $p_{\perp,\ell\ell}$, with the aim of being easier measurable. It is defined purely in terms of lepton directions as:

$$\phi^*_\eta = \tan\left(\frac{\phi_{\text{acop}}}{2}\right)\sin\left(\theta^*_\eta\right), \tag{6.2.1}$$

where the acoplanarity angle ϕ_{acop} is defined in terms of the difference in azimuthal angles $\Delta\phi$ between the two leptons as $\phi_{\text{acop}} = \pi - \Delta\phi$, and $\theta^*_\eta = \tanh\left(\frac{\eta^- - \eta^+}{2}\right)$ in terms of the lepton pseudorapidities η^i. In this observable, the soft region corresponds to the region of low ϕ^*_η.

In comparison to the NLO QED predictions, the soft approximation predicts too many events with low ϕ^*_η, the difference quickly reaches beyond 10%. The soft-collinear approximation shows the opposite behaviour, predicting too many events
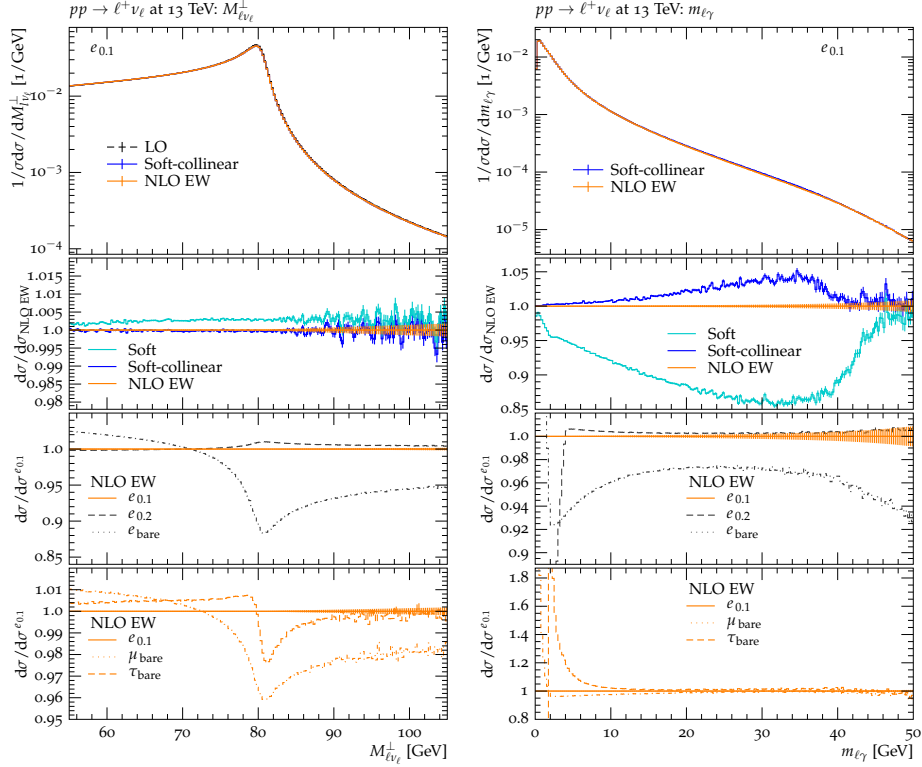
Figure 6.4: Transverse mass of the lepton-neutrino system $M_{\ell\nu}^{\perp}$ (left) and the invariant mass of the system of the charged lepton and the nearest photon, $m_{\ell\gamma}$ (right) in $pp \to W^+ \to \ell^+\nu_\ell$. Nominal predictions are shown for $pp \to W^+ \to e^+\nu_e$ at LO, in soft-collinear NLO approximation and at NLO EW, where electrons are always dressed with collinear photons within $dR = 0.1$. The ratio plots highlight the effect of the considered higher-order corrections and the effect due to different photon dressing or lepton identity. See text for details.

with large ϕ_η^*. The NLO EW prediction provide corrections of a few percent, while the NNLO QED corrections compensate the NLO EW corrections almost completely. The dressing shows effects of up to 25% at medium value of ϕ_η^*.

6.3   Charged Drell-Yan lepton-neutrino pair production

In Figs. 6.4-6.6, observables crucial for the study of charged-current Drell-Yan dilepton production are investigated. We present results for the decay $W^+ \to \ell^+\nu_\ell$, as the charge conjugate case behaves practically identically. All figures are similar to
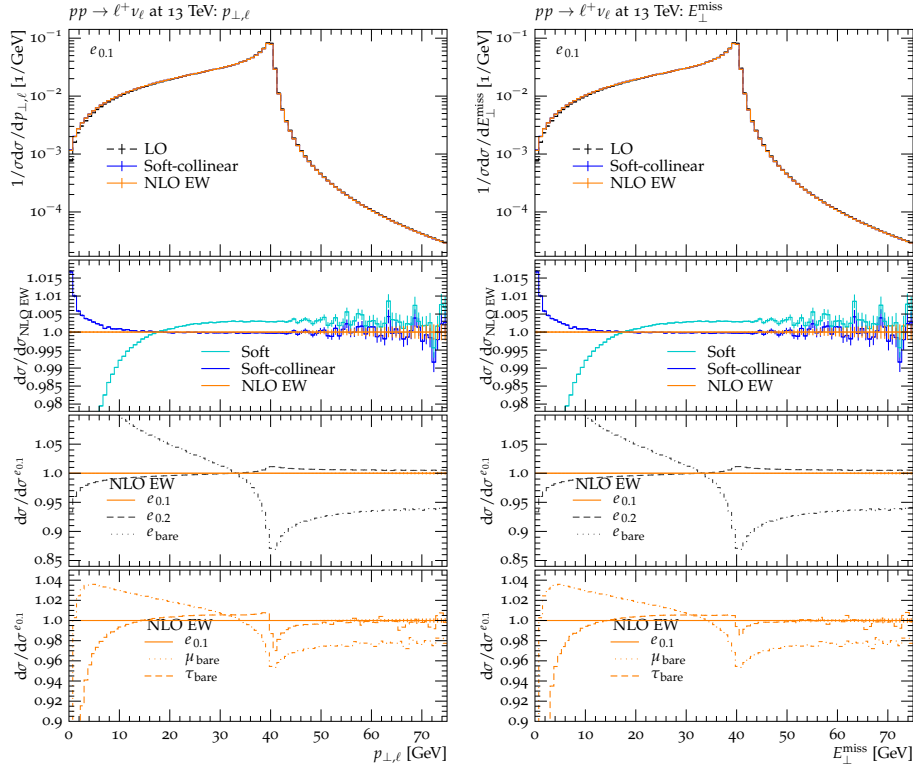
Figure 6.5: Plots of the transverse momentum of the charged leptons, $p_{\perp,\ell}$, on the left and the missing transverse E, $E_\perp^{\mathrm{miss}}$, on the right. Predictions and labels as in Fig. 6.4.

the neutral-current case presented in Section 6.2. However, here the best prediction is of NLO EW, as pure QED corrections cannot be defined in a gauge-invariant way. As before all nominal predictions correspond to dressed electrons.

In Figure 6.4, we start with the transverse mass of the lepton neutrino system, $M_{\ell\nu}^\perp$, and the invariant mass of the charged lepton and the nearest photon, $m_{\ell\gamma}$.

The $M_{\ell\nu}^\perp$ observable is barely affected by the NLO EW corrections. In fact the soft-collinear approximation agrees with NLO EW at the permille level.

The dressing of the electrons has a rather large impact, with differences with respect to a bare treatment reaching up to 10% at the edge. A slight shift of the edge is observed when comparing different lepton species with one another, affecting the distribution to up to a few %.

The invariant mass of the charged lepton and the closest photon, $m_{\ell\gamma}$ shows significantly larger corrections. Compared to the NLO EW corrections, the soft approx-
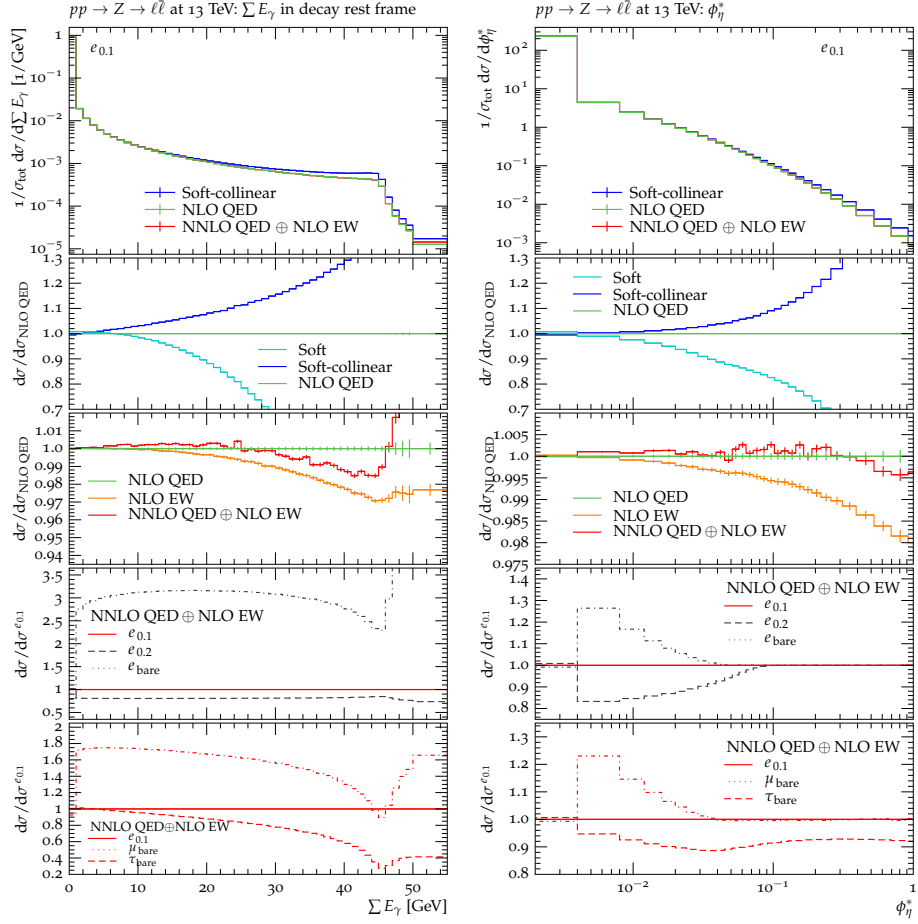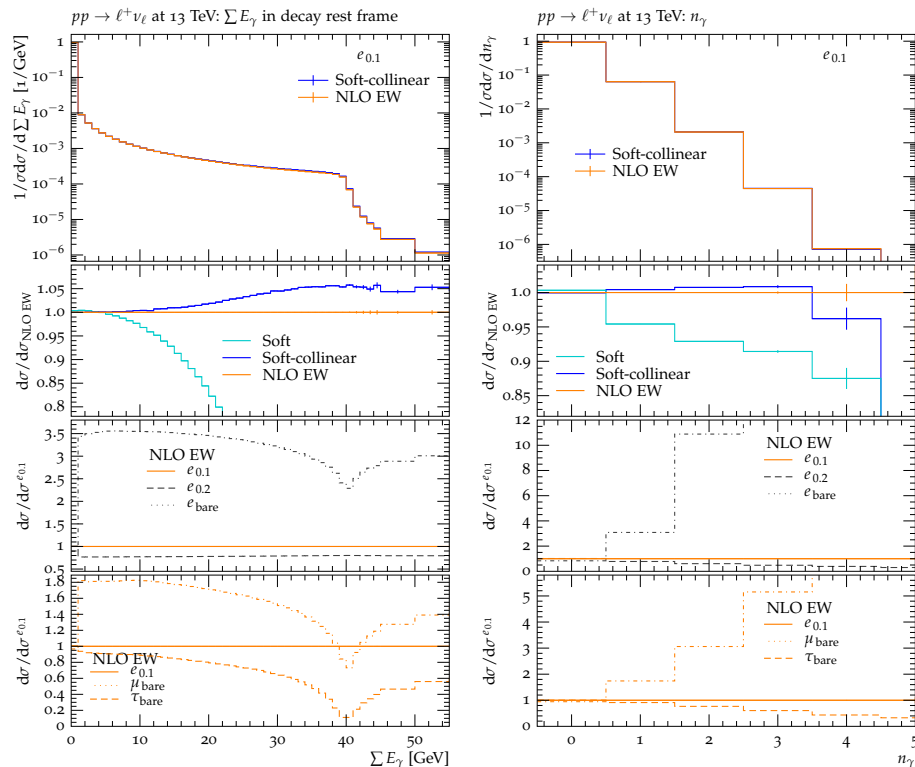
Figure 6.6: Plots of the sum of the photon energies in the decay rest frame, $\sum_{n_\gamma} E_\gamma$, on the left and the number of photons with $E_\gamma > 0.1\,\text{GeV}$, n_γ, on the right. Predictions and labels as in Fig. 6.4.

imation predicts a spectrum that is too soft, while the soft-collinear approximation produces up to 5% more events with large $m_{\ell\gamma}$.

Bare electrons have a lot more events at low $m_{\ell\gamma}$ coming from those photons that have not been clustered in comparison to the dressed cases. On the other hand, those electrons dressed with $dR = 0.2$ have a reduced number of events at low $m_{\ell\gamma}$. The comparison between lepton species shows significant differences close to low $m_{\ell\gamma}$, illustrating the differing size of the dead cone.

In Figure 6.5, we show the transverse momentum of the charged lepton, $p_{\perp,\ell}$, alongside the missing transverse energy, $E_\perp^{\text{miss}}$. The latter corresponds in our simple setup to the transverse energy that the neutrino carries away.

Both distributions are related and indeed they behave very similarly. As in the neutral-current case, the transverse momentum of the charged lepton is barely affected by NLO EW corrections, with corrections only becoming appreciable for very

low values of $p_{\perp,\ell}$.

The dressing affects the distributions by up to about 10% in the peak region, while different lepton species differ by up to 4% in the peak region and at low $p_{\perp,\ell}$.

In Figure 6.6, we present the sum of photon energies in the decay rest frame, $\sum_{n_\gamma} E_\gamma$, and the number of photons with energy $E_\gamma > 0.1\,\mathrm{GeV}$, n_γ.

The sum of photon energies shows a kinematic edge just as in the neutral current case. While the soft approximation predicts too soft a spectrum of photon energies, the soft-collinear approximation does a much better job in W-decays as the effects coming from NLO EW corrections reach at most 5% at the kinematic edge. The reason for this behaviour can be read from the distribution of the n_γ. The soft approximation is shown to produce too few photons, while the soft-collinear approximation predicts more events with 1-3 photons.

Analyses using bare electrons show a significantly larger number of photons, with already 4 times more events with 1 photon. At the same time, for $dR = 0.2$ electrons, the number of photons is suppressed significantly. A similar picture presents itself when comparing lepton species. Muonic decays contain significantly more photons, while decays into τ's end up with a lot less events with at least one photon.

As a noteworthy observation we want to point out a difference between neutral-current and charged-current processes: the soft-collinear approximation is more reliable in the charged-current case. This can be understood from the fact that here collinear radiation predominantly originates from just one particle, the lepton, rather than two competing particles as in the Z-boson case. Any error due to the missing interference contributions in the soft-collinear approximation is thus significantly diminished.
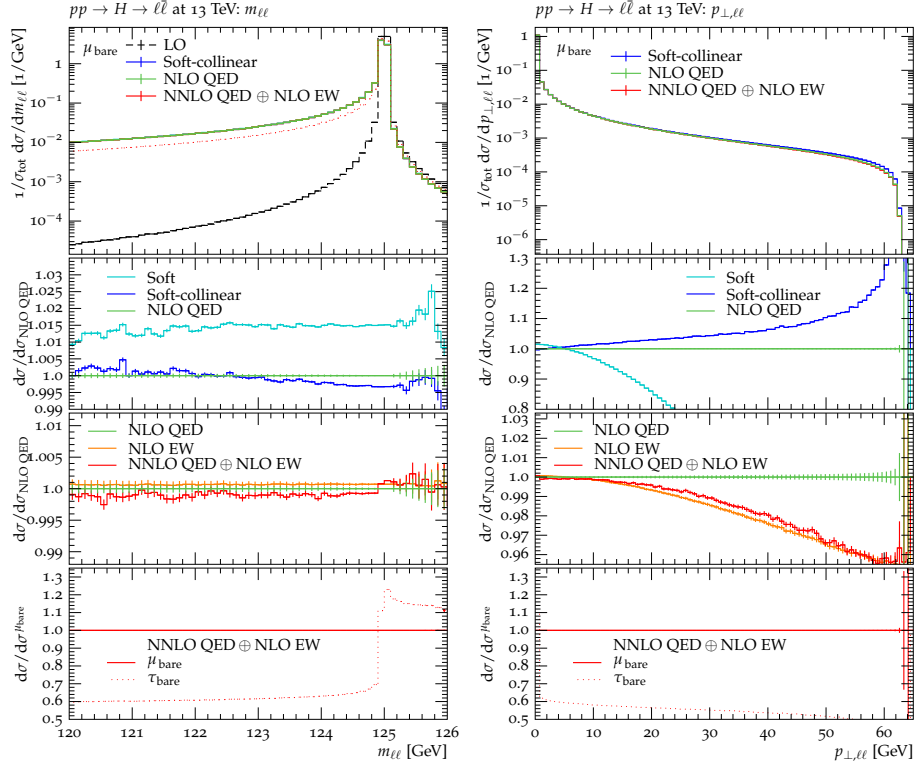
Figure 6.7: Plots of the invariant mass of the two decay leptons, $m_{\ell\ell}$, on the left and the transverse momentum of the system of the two leptons, $p_{\perp,\ell\ell}$, on the right in the process $pp \to H \to \ell^+\ell^-$. Nominal predictions are shown for $pp \to H \to \mu^+\mu^-$ at LO, in soft-collinear NLO approximation, at NLO QED and at NNLO QED $\oplus$ NLO EW. The ratio plots highlight the effect of the considered higher-order corrections and lepton identity. See text for details.

6.4   Leptonic Higgs-boson decays

Finally we highlight the effect of higher-order corrections in photon radiation off leptonic Higgs decays. Numerical results are shown in Fig. 6.7, where the nominal distribution corresponds to $H \to \mu^+\mu^-$ with bare muons. Here we focus on the dilepton invariant mass $m_{\ell\ell}$ and the recoil of the lepton system, $p_{\perp,\ell\ell}$. As for neutral-current Drell-Yan we consider higher-order corrections at the level of soft and soft-collinear approximations, full NLO QED, NLO EW and also combining NLO EW with NNLO QED. The LO prediction clearly fails to describe the invariant mass distribution. Yet, the soft and soft-collinear approximations provide a quite reliable description with corrections smaller than 1-2% with respect to full NLO QED. The weak corrections are slightly larger compared to the neutral-current Drell-Yan

case, still they alter the invariant mass distribution only at the permille level and are overcompensated by NNLO QED effects of the same order. As mentioned in Section 6.1 we are unable to resolve the sharp mass peak of the Higgs-boson with the lowest energy photons we generate. However, investigating the low energy tail of the invariant mass distribution, we observe that the NLO QED corrections provide a mostly flat contribution in the peak region.

Comparing decays into bare muons with decays into bare τ's, we can appreciate a significantly smaller sensitivity of the τ distribution to QED radiation.

The distribution of the transverse momentum of the di-lepton system shows similar effects as in the case of the Z-boson decay. The soft approximation predicts a distribution that is far too soft, while the soft-collinear approximation predicts too many events with large $p_{\perp,\ell\ell}$. The NLO EW corrections increase the number of events by about a permille at low $p_{\perp,\ell\ell}$, and decrease them at high values up to about 5%. The NNLO QED corrections in this case do not provide a large competing effect, and the NNLO QED $\oplus$ NLO EW prediction agrees with the NLO EW one at the permille level.

Decays into τ's show about 40% less events with non-vanishing $p_{\perp,\ell\ell}$, the effect being close to constant across the entire distribution.

Chapter 7

Conclusions

In this Part, we have presented an implementation of NLO EW and NNLO QED corrections to the decays of the weak bosons within the YFS formalism. For this purpose, we extended SHERPA's module PHOTONS to include the relevant matrix elements, renormalized in the on-shell scheme, and subtractions needed within this formalism. In our numerical results we find that observables relating to the leptons in the process are only marginally affected by the corrections, up to the level of a few per cent. In particular, the outstanding features of important distributions, such as the peak of the invariant mass distribution are practically not affected. Distributions that relate to the energies of the generated photons themselves, or can be related to them, such as the transverse momentum of the pair of the leptons $p_{\perp,\ell\ell}$, naturally receive larger corrections. The electroweak corrections increase the likelihood of hard photon radiation by up to 2-3% for very hard radiation. The NNLO QED corrections compete with these corrections by reducing the likelihood of hard radiation, albeit to a smaller extent. At the same time, some regions of phase space are only described at leading order in α upon the inclusion of the double real radiation, such that in these regions the corrections can be significantly larger. Examples for such regions are the region when the sum of the photon energies exceeds half the boson mass or regions of large ϕ^*. Angular distributions of the photons are not affected by higher order contributions confirming the general radiation pattern of QED radiation. The

results give us confidence that the inclusion of the full EW corrections to particle decays within the YFS formalism in SHERPA are sufficient to achieve precise results for most leptonic observables. Beyond the corrections implemented in this work, it is interesting to consider the YFS formalism also including initial state effects.

The implemented NNLO QED and NLO EW corrections provide high precision also in extreme phase space regions and can be seamlessly added to standard precision QCD simulations. This provides an important theoretical input to future precision determinations of fundamental parameters of the EW theory at hadron colliders and beyond.

Part II

Distinguishing b-quark and gluon

jets with a tagged b-hadron

Chapter 8

Introduction

Jets containing a bottom quark play a significant role in many analyses at the LHC, both in searches for new physics and in further studies of the Standard Model (SM).

As an illustrative example, consider the measurements of the phenomenologically relevant Yukawa couplings of the newly found Higgs boson to quarks of the third generation, top and bottom quarks. One of the processes central to this measurement is the production of a Higgs boson in association with top-quarks, $pp \to t\bar{t}H$, where the Higgs boson decays into a $b\bar{b}$ pair. This has recently been observed by both ATLAS and CMS collaborations, drawing partly on the decay of the Higgs boson into two b-quarks [168, 169]. For this study, both the signal and the dominant background processes are understood at next-to leading order in QCD [170–175]. More modern fixed-order calculations, performed with automated tools such as OPENLOOPS + SHERPA [39, 51, 176] or MADGRAPH5 [37, 177], have successfully been embedded in hadron-level simulations based on MC@NLO [178], for the signal process $t\bar{t}H$ [179], and the dominant irreducible background $t\bar{t}b\bar{b}$ [180]. Multijet merging technologies at NLO [71, 181–183] have successfully been applied to the production of $t\bar{t}$ pairs in conjunction with jets [184, 185], thereby also providing a handle on this background. Combined, this work represents an amazing technological development. However, following the analysis strategy employed by both ATLAS and CMS, it becomes clear that the experimental cuts shape the background and the signal to

look relatively similar, rendering them hard to distinguish. The analysis is thus ultimately reduced to the counting of events with a suitable number of b-jets – 3 or 4 – within certain acceptance regions [186–189]. In a very similar manner, the recent observation of the Higgs decay $H \to b\bar{b}$ when produced in association with a W or a Z also relies heavily on the identification of b-tags to define their event samples [190, 191].

One of the problems arising from this kind of analysis is related to the fact that they rely on the identification of b-quarks through jets with a b-tag. This identification is realised by b-tagging conditions [192–195]. Examples include criteria based on displaced vertices with a certain impact parameter significance, the presence of soft muons inside the jet, which may stem from such a displaced vertex, or criteria based on the further decay chain and their possible impact on the intrinsic shape of the tagged jet [196]. Recently, machine learning methods have received more attention to combine and improve upon these different approaches [197–202]. Usually, the acceptance rate of jets including a b-hadron based on such tags is relatively high, between 60% and 70%, while the rejection rate of light jets containing no such hadron reaches well beyond 90% at typical working points. However, this simple tagging technology may fail to reliably identify jets containing two b-hadrons, which can originate from a $g \to b\bar{b}$ splitting. This translates into limitations in distinguishing "legitimate" b-jets, stemming from a b-quark coming out of a hard interaction, from gluon (or other light) jets, thereby hampering analyses of processes with b's produced in the hard interaction. This is further exarcerbated by the absence of very precise theory estimates of the gluon splitting: Its description by the parton shower is possibly not quite as reliable as one would naïvely assume. Earlier analyses by the LEP collaborations measured this splitting probability with large statistical and systematic errors in the range of (0.21%-0.31%)±0.1%, while parton shower programs usually arrived at rates of just below 0.2% [203–206]. This immediately translates into the need to measure the $g \to b\bar{b}$ transition such that the modern parton shower algorithms can be compared and, if necessary, improved through direct comparison.

It also motivates the construction of robust and reliable observables discriminating the "real" b-jets from those where a $b\bar{b}$ pair emerges from gluon splitting.

Some early attempts at this identification were performed by CDF [207] by trying to identify two secondary vertices in the jet consistent with two b-hadrons from a sample of already tagged events. Both ATLAS [208] and CMS [209] are also working on this identification, with varying levels of success. Due to the intrinsic difficulty of finding two separate secondary vertices belonging to b-hadrons, these searches are typically combining observables related to the jet and the vertex. Both collaborations use sophisticated multivariate analysis tools to define their discriminators.

This Part of the Thesis aims to further explore the very same problem. Using well-established features in the QCD radiation pattern and simple geometric considerations motivates the use of a combination of jet shapes and secondary vertex finding to distinguish b-jets from what will be called $b\bar{b}$-jets in the rest of this Part. This Part is organised as follows: in Section 9.1 the most sensitive jet shape observables are reviewed and possible improvements when combining them with a reconstruction of fragmentation function observables are discussed. Since the last observable is a new discriminant in the context of single vs. double b-tag jets, we devote special emphasis to it. An analysis of samples of pure QCD jets produced by the SHERPA event generator is performed in Section 9.2 and results for the efficiencies of discriminating between b- and $b\bar{b}$-jets presented in Chapter 10.

Chapter 9

Shaping b-jets

9.1 Kinematic observables

It is well-known that the fragmentation function $F(x)$ of b-quarks is relatively hard, peaking close to $x \approx 1$. Here, x denotes the b-hadron energy or momentum fractions x_E or x_p with respect to the underlying b-quark jet. This behaviour is due to the fact that the finite masses of the b-quarks shield the collinear divergence in gluon emissions off the quark, thereby effectively suppressing the emission of energetic secondary partons. This phenomenon is also known as the "dead cone effect", and we have already encountered it in the first Part of this work when considering the emission angle of photon radiation off massive leptons, see Section G.1.2. As a result, b-quarks tend to retain most of their energy – in contrast to light partons – and thus the b-hadrons created during the hadronization of the partonic final state more or less have energies and momenta very similar to the b-quark when it was produced in the hard process. Conversely, b-quarks originating from a gluon splitting tend to have a fairly symmetric share in the energy of the original gluon, which they retain during fragmentation. As a result the emerging b-hadrons, and in particular also the harder of the two, tend to have an energy fraction well below unity, closer to $x \approx 0.5$.

A somewhat independent observable is related to the shape of the actual jet. Based
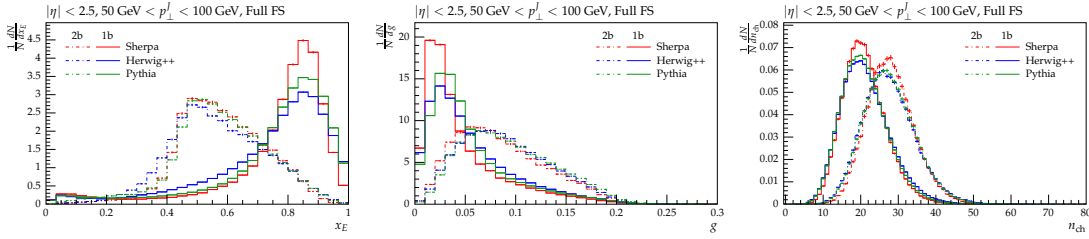
Figure 9.1: Comparison of x_E, g, n_{ch} from different event generators for jets within 50 GeV $< p_\perp^J <$ 100 GeV, based on the full hadronic final state. The left panel shows results for x_E. The little enhancement at small values of x_E stems from light jets, where a single b-quark was captured, either through gluon splitting, with the other b-quark radiated outside the jet, or from the underlying event. The central panel shows results for g, where the b-hadron(s) were set stable - this was only done for the purpose of this plot and none of the rest of the thesis. The right panel shows the number of final state particles inside the jet (including uncharged ones). A vertex is defined as having at least 3 tracks.

on the reasoning above, b-jets tend to be relatively narrow, with only small amounts of radiation roughly following the direction of the colour connection of the b-quark to the rest of the event. In contrast, $b\bar{b}$-jets tend to originate from hard gluons, which may not only radiate more due to the larger colour charge of $C_A = 3$ vs. $C_F = 4/3$ before they split, but which also have an intrinsic size related to the relative distance of the two b-quarks inside the jet. This effect could be captured by using the mean of the energy distribution $\rho(r)$ inside the jet, where $r < R$ is the radial distance of a hadron or similar to the centroid of the jet with radius R. It turns out, however, that a good observable is provided by the first $p_\perp$-moment of this distribution

$$g = \frac{1}{p_\perp^{(J)}} \sum_{i \in \text{Jet}} p_\perp^{(i)} \Delta R_{iJ} \,, \tag{9.1.1}$$

an observable also known as "girth" g, or jet width. Here $p_\perp^{(J)}$ is the transverse momentum of the jet, $p_\perp^{(i)}$ the transverse momentum of the hadron, track, or energy cell (i) inside the jet $(i \in \text{Jet})$, and ΔR_{iJ} is its radial distance with respect to the jet vector.

Many more observables can be used with different distinguishing powers and robustness. A prime example is the number of charged tracks n_{ch}. Despite possibly

presenting a poor Monte Carlo modelling, highly depending on the details of hadronization modelling and underlying event implementation, this observable is still extensively used by experimental analyses. Hence, we also inspect its impact in the following section.

The typical behaviour of these observables is exemplified in Fig. 9.1; in this figure all jets have a transverse momentum $p_\perp^J$ between 50 and 100 GeV and their pseudorapidity $|\eta_J| < 2.5$. To provide an idea of modelling uncertainties, the results of different event generators, HERWIG++ [210], PYTHIA 8 [211] and SHERPA [51] are exhibited.

There are other observables that aim to scrutinize the colour connection and 2-dimensional shape of the jet, e.g. planar flow, pull or differential jet shape, that were also inspected. However, in this study only the most powerful observables will be investigated, namely fragmentation fractions x_E, girth g and number of charged tracks n_{ch}. Additional observables could be used in the construction of more advanced discriminators based on boosted decision trees or neural networks, which is beyond the scope of this study. It is worth noting that there are interesting similarities between the investigations here and studies aiming at distinguishing gluon and light quark jets, see for instance Ref. [212, 213]. Due to the significantly different gluon and light quark fragmentation fraction profiles, induced by the smaller mass of the light quarks, they present sensibly weaker efficiencies in comparison to the single vs. double b-tag case. An exception might be found for c-quarks, which through their mass share some characteristics with b-quarks, but the effect is still expected to be smaller in this case.
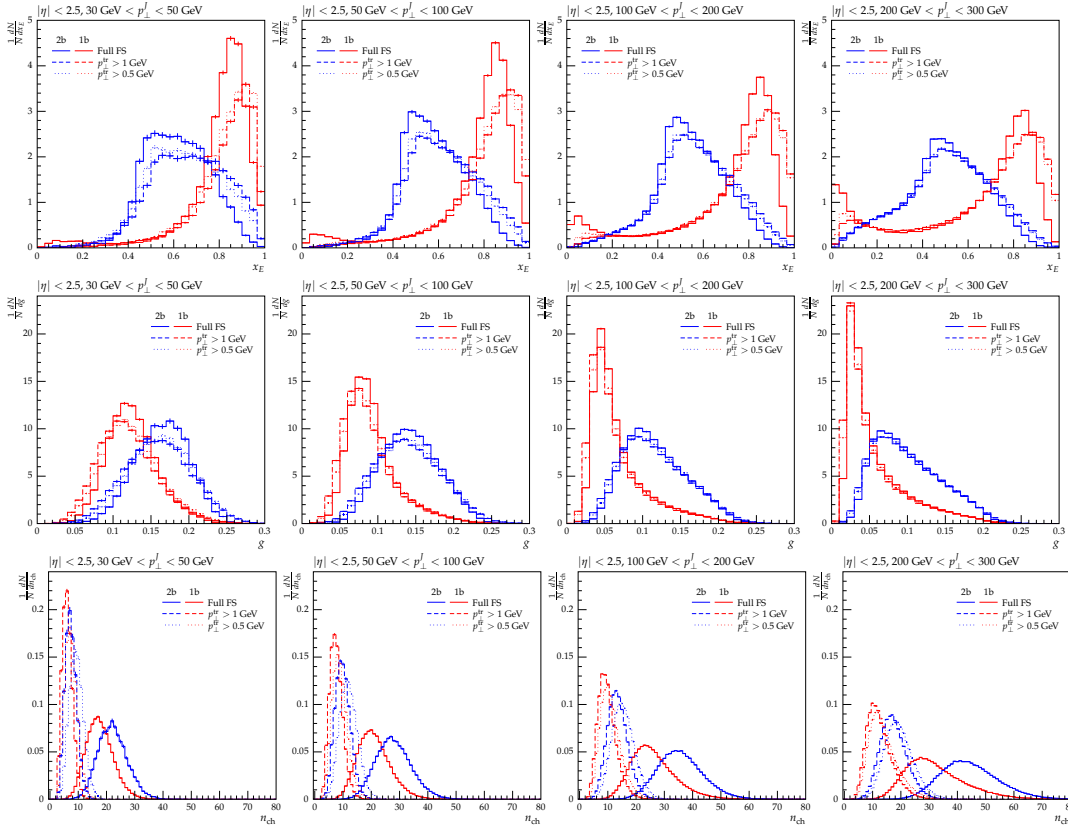
Figure 9.2: x_E (top row), girth (central row) and number of charged tracks (bottom row) distributions for jets within different $p_\perp$ slices: $30 \text{ GeV} < p_\perp^J < 50$ GeV (first column) $50 \text{ GeV} < p_\perp^J < 100$ GeV (second column), $100 \text{ GeV} < p_\perp^J < 200$ GeV (third column) and $200 \text{ GeV} < p_\perp^J < 300$ GeV (fourth column). Red curves correspond to jets with one b-hadron and blue with two b-hadrons. Solid lines are based on the full hadronic final state, including uncharged particles, dashed lines on charged tracks with a minimum $p_\perp^{\text{tr}}$ of 1 GeV and dotted with a minimum $p_\perp^{\text{tr}}$ of 0.5 GeV. A vertex is defined as having at least 3 tracks.

9.2   Analysis

As a test case, a pure QCD $pp \to$ jets sample at the $\sqrt{s} = 13$ TeV LHC is considered. The event sample was generated with SHERPA [51] in a very basic setup, using $2 \to 2$ matrix elements at leading order, supplemented with the default parton shower based on Catani–Seymour subtraction [62], and accounting for hadronization and underlying event effects. Since different event generators differ in their approximations and implementation details of the parton shower evolution and non-perturbative models it is important to quantify the resulting uncertainties and to access the robustness

of the results. To this end, event samples with the same specifications have been generated and analysed, using HERWIG++ [210] and PYTHIA 8 [211]. Where relevant, the results from these different simulation tools are contrasted; overall, however, they do not impact on the results and conclusions of this study.

The analysis is performed using RIVET [214]. Jets are defined by the anti-k_T algorithm, using FASTJET [215], with $R = 0.4$, requiring $p_\perp^J > 30$ GeV and $|\eta_J| < 2.5$. Charged tracks are defined with a minimum transverse momentum $p_\perp^{\mathrm{tr}} \geq 0.5$ or 1 GeV. The different cutoffs are used to probe the stability of the observables. Lowering the threshold would of course lead to more statistics, however, it also increases the dependence on the MC modelling. In addition, a realistic experimental analysis uses cutoffs in this range as well.

Jets are categorized as containing one or two b-hadrons, with other values rejected, by counting their number inside the jet radius. For our purposes, the b-hadrons are "reconstructed" from the event record, taking into account the choice of observable final state particles. A b-hadron is reconstructed if at least three particles, subject to the constraints of the observable final state, originate from it. In case of two different b-hadrons in the jet, by default the harder one is selected for the calculation of x_E.

In Fig. 9.2 (top row), the x_E distributions are displayed. It is observed that in the case of one b-hadron in the jet, the b-hadron carries most of the energy content with the distribution peaking between 0.8 and 1, depending on the $p_\perp$ slice. On the other hand, in the case of two b-hadrons in the jet, the energy fraction for the most energetic b-hadron tends to be near $0.5 - 0.6$. This effect does not diminish when considering only charged tracks, rather it improves slightly, e.g., the distribution for one b-quark in the jet narrows near $x_E \approx 1$. Similar observables built out of the 3-momentum, the transverse momentum or weighted with the cosine of the angle to the jet axis are qualitatively and quantitatively similar to x_E. Therefore, only the latter is considered for simplicity.

The girth distributions g are displayed in Fig. 9.2 (central row). This observable presents a good separation between the single and double b-tagging case. The
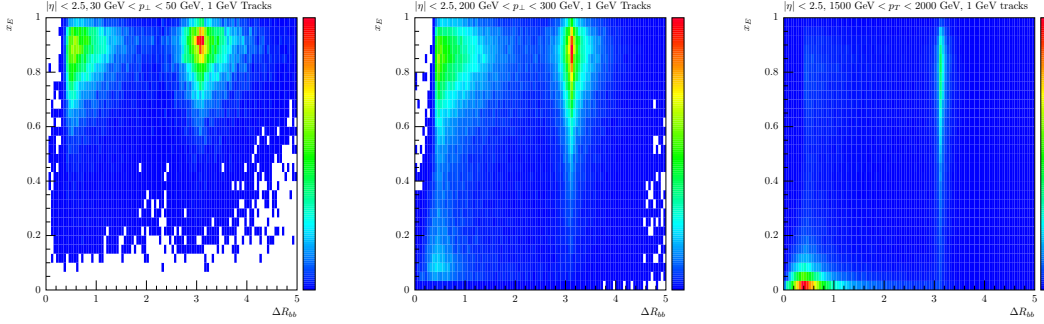
Figure 9.3: Normalised $(x_E, \Delta R_{bb})$ distributions for jets containing one b-hadron. The jets are considered in three momentum slices: $p_\perp^J$ of 30 to 50 GeV (left panel), 200 to 300 GeV (centre panel) and 1500 to 2000 GeV (right panel). The results here are based on charged tracks with a minimum $p_\perp^{tr}$ of 1 GeV.

double b-tag sample leads to broader jets with respect to the single b-tag case. This observable presents useful results at either low or high $p_\perp^J$. Moreover, the charged tracks present qualitatively similar results and only a subleading dependence on the threshold energy, $p_\perp^{tr} > 0.5$ GeV or 1 GeV, is observed.

The dependence on the charged track multiplicity n_{ch} is inspected in Fig. 9.2 (bottom row). The jets with two b-hadrons present a much higher multiplicity than the single b-tagged jets. This is a result of the longer decay chain of the b-hadron and the different emission pattern described by the parton shower. These differences are enhanced at higher $p_\perp^J$ where the n_{ch}^{2b}/n_{ch}^{1b} slowly converges to C_A/C_F.

Despite n_{ch} not being an infrared safe observable and therefore highly dependent on the parton shower, hadronization and underlying event modelling, the disagreement with the MCs is usually suppressed via an appropriate tuning to the LHC data. Hence, its applications have to account for these limitations and/or should be taken with a grain of salt.

Notice that in the boosted kinematics, the x_E distribution displays an enhancement at low x_E for the single b-hadron case, see Fig. 9.2 (top-right panel). Again, QCD radiation in the form of $g \rightarrow b\bar{b}$ splittings accounts for the observed feature. It appears in the boosted regime because the larger initial energy of the jets leads to an enhanced emission phase space with more gluons being produced during the

perturbative part of their fragmentation. These gluons may split into $b\bar{b}$-pairs which may spill into other, potentially harder, jets.

This behaviour is exemplified by three $x_E - \Delta R_{bb}$ correlation plots, in Fig. 9.3. These plots correlate the x_E of the b-hadrons inside single-b tagged jets with their spatial distance ΔR_{bb} with respect to the nearest b-hadron outside the jet. In the left panel, for low transverse momentum jets with 30 GeV$\leq p_\perp^J \leq$ 50 GeV, we find that most events reside in a region around $x_E \approx 0.8$, with the nearest b-hadron a distance $\Delta R_{bb} \approx \pi$ away. This corresponds to a configuration with the two b-hadrons produced close to back-to-back as might be expected in a hard QCD production process. In the centre panel, referring to the boosted regime, with 200 GeV$\leq p_\perp^J \leq$ 300 GeV, a second hot spot in the correlation plot emerges, for low values of x_E close to 0. For these events, the nearest b-hadron resides within a distance $\Delta R_{bb} \lesssim 0.6$, such that they lie fairly close to the jet boundary. This further suggests that these b-hadrons "leaked" into a hard, light jet, their appropriate partner falling just outside that particular jet. In fact, such b-tags should therefore probably not be identified with "legitimate" b-jets originating from a primary hard b-quark. This observation can be driven to the extreme: in the right panel we show the same correlation for jets with 1500 GeV$\leq p_\perp^J \leq$ 2000 GeV. In this case, most of the events are contained within this low-x_E region, with small ΔR_{bb} values to their nearest b-hadron, reflecting the dense environment in such an event.

Chapter 10

Double and Single b-tagging Efficiencies

The observables x_E, g and n_{ch} provide good sensitivity towards the single and double b-tagging samples when considered independently. As most of the b-tagging algorithms resort to Multivariate Analysis (MVA) with the combination of the most significant distributions, it is important to ensure that these observables do not present the same correlation pattern and could therefore generate improved constraints through their combination. In Fig. 10.1, the 2-dimensional correlations between the fragmentation fraction, girth and charged track multiplicity are displayed, showing only the case for charged tracks of $p_\perp^{\text{tr}} > 1$ GeV for jets in the $p_\perp^J$-bin between 50 and 100 GeV. The behaviour seen in these plots is qualitatively observed also for higher transverse momenta. While the observables considered so far show some correlation, it seems clear that the combination may enhance the discriminatory power.

Tagging efficiencies are defined based on the so-called ROC curve that uses a simple cut argument. For the 1-dimensional distributions, as shown in Fig. 9.2, the efficiency curve is obtained by sliding a cut along the value of the observable. Each point of the cut leads to a corresponding efficiency for keeping b-jets (ϵ_{1b}) and $b\bar{b}$-jets (ϵ_{2b}). The ROC curve is the interpolation of all possible cuts - due to the discrete nature
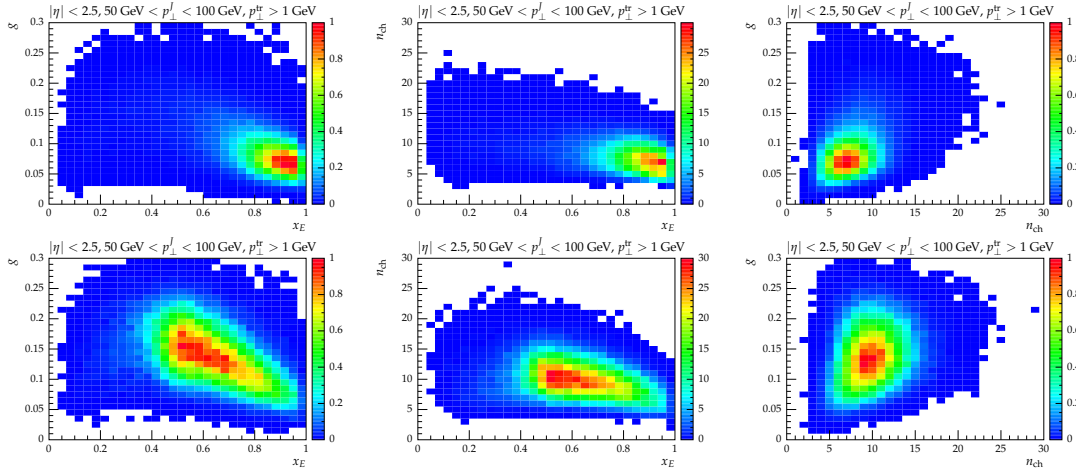
Figure 10.1: Correlations between the fragmentation fraction with the girth (x_E, g) (left column), fragmentation fraction with charged tracks (x_E, n_{ch}) (central column) and charged tracks with girth (g, n_{ch}) (right column). The colours represent the normalized weight of the particular bin. The top plots are for one b-hadron in the jet, the bottom ones for two b-hadrons in the jet. The jets considered here have a $p_\perp^J$ of 50 to 100 GeV. The objects considered in the analysis in this case are charged tracks of at least 1 GeV $p_\perp^{tr}$. A vertex is defined as having at least 3 tracks.

of the histogrammed distributions, this amounts to a finite number of cuts. For instance, for the girth and multiplicity, a jet is tagged as containing two b-hadrons, if the value of the observable is above the cut, whereas for the fragmentation fractions it is tagged as such when the observable is below the cut. The efficiency to tag a jet containing one b-hadron is defined analogously. The region $x_E < 0.3$ is removed to avoid the lower peak in the boosted regime to maximize the performance of this method. This region could be efficiently included via an MVA, but this was not done in this letter to retain the simplicity of our strategy. One way to generalize this approach to combine two observables, based on the behaviour of the correlations in Figure 10.1, is the following: carrying out a Principal Component Analysis on the 2-dimensional correlation plots for two b-hadrons in the jet, we can define a cut line perpendicular to the largest eigenvector along the correlation. Jets falling into the region above this cut line are then defined as double b-jets, while those to the bottom of the cut line are defined as single b-jets. Sliding this cut line along the eigenvector, we can then determine efficiencies as for the 1-dimensional ROC curve.
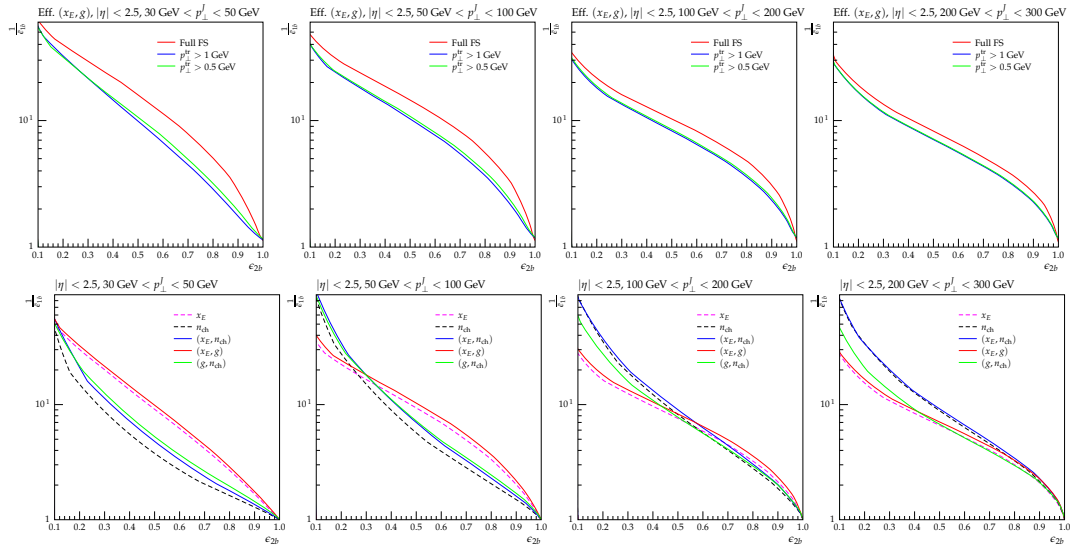
Figure 10.2: Efficiency for tagging a b-jet as containing two b-hadrons ϵ_{2b} against the rejection of jets containing one b-hadron $1/\bar{\epsilon}_{1b}$ from combining x_E and girth. The plots are again shown in different $p_\perp^J$ bins as in Fig. 9.2. Top row: the red curves refer to an analysis using the full final state, whereas the blue and green consider only charged tracks with minimum $p_\perp^{\mathrm{tr}}$ of 1 GeV and 0.5 GeV, respectively. Bottom row: efficiencies for different combinations of observables (red: (x_E, g), blue: (x_E, n_{ch}), green: (g, n_{ch})). The displayed results refer to charged tracks with minimum $p_\perp^{\mathrm{tr}}$ of 1 GeV.

This approach works in this case as the correlations for single b-jets lie along the large eigenvector of the correlation for double b-jets. This may not always be the case, and depends on the exact definition of the observables used for the analysis. It would thus be preferable to use multivariate algorithms to enable the determination of efficiencies in this case. Again, we refrained from such an analysis here to retain the simplicity of our approach.

These efficiencies are shown in Fig. 10.2 (top row) as the efficiency of tagging a b-jet as a jet containing two b-hadrons, ϵ_{2b}, against the rejection of single b-jets, $1/\bar{\epsilon}_{1b}$. The combination of observables proves to be robust against the choice of charged tracks or the fully hadronic final state. Lowering the threshold $p_\perp^{\mathrm{tr}}$ to 0.5 GeV produces only mild improvements in respect to 1 GeV.

In Fig. 10.2 (bottom row), different combinations of observables are compared with the discrimination from n_{ch} or x_E only. A visible improvement in using the combination of two observables is found. For low transverse momenta the combination
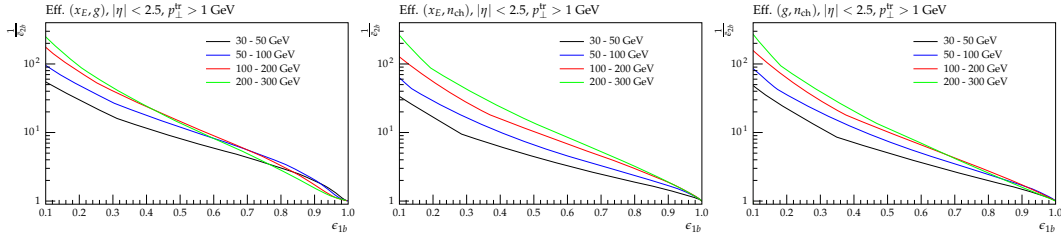
Figure 10.3: Efficiency for tagging a b-jet as containing one b-hadron ϵ_{1b} against the rejection of jets containing two b-hadrons $1/\bar{\epsilon}_{2b}$ as a function of $p_\perp^J$ for different combinations of observables. Left: (x_E, g), centre: (x_E, n_{ch}), right: (n_{ch}, g).

(x_E, g) outperforms the other combinations, while for larger transverse momenta of the jet, the combination of (x_E, n_{ch}) is most sensitive. In both cases, however, the fragmentation fraction is involved, an observable that hitherto has not been documented for this discrimination.

In Fig. 10.3, the different combinations are displayed for distinct transverse momenta slices. Here, in contrast to the previous Figure, we show the efficiency of correctly identifying a single b-hadron jet versus the rejection efficiency for $b\bar{b}$-jets. This way of looking at the efficiencies may be of interest in a search for b-quark initiated jets coming from the hard interaction. The $b\bar{b}$-jet rejection efficiency $(1/\bar{\epsilon}_{2b})$ significantly improves for the phenomenologically interesting boosted topologies in all cases. The (x_E, g) produces robust results through all the transverse momentum slices. This suggests that the combination of these two observables contains complementary and relevant information not found in the single observables or the other combinations. In contrast, the combinations containing the number of charged tracks show a significant dependence on the transverse momentum of the jets. This behaviour is driven by the number of charged tracks, suggesting that the importance of this observable grows with the available energy in the jet. We note in passing that in the boosted regime a sizable fraction of b-tags correspond to b-hadrons with a low x_E, stemming predominantly from the splitting of secondary gluons into the jets. A simple cut on x_E will remove such unwanted b-tags.

Chapter 11

Conclusions

Studies that require multiple b-jets will become increasingly frequent at the LHC in the years to come. These studies range from SM precision analyses to searches for beyond the SM physics, such as resonance searches. One of the problems encountered is related to discriminating the "legitimate" b-jets, containing only one, typically hard b-hadron, from jets containing two b-hadrons, usually emerging from a gluon splitting. In this Part of the Thesis a phenomenological attempt at a more coherent strategy of discriminating b- and $b\bar{b}$-jets has been presented, based on possible kinematic handles, in particular combinations of jet shapes with the fragmentation fraction.

Several observables were considered and the most powerful encountered were the girth g, the number of charged tracks n_{ch}, and b-hadron jet energy fraction x_E. Especially when combining either of the former two with the latter, a considerable improvement was found. A significant improvement for the $b\bar{b}$-jet rejection is observed at the boosted regime for all variable combinations.

An interesting development in the analysis of events at the LHC is presented by the use of machine learning methods, such as boosted decision trees and neural networks. These methods are particularly interesting for the categorization of events, and thus could find good application in the tagging of jets. Such methods can be set out with little knowledge of the intrinsic behaviour of the physics, with the machine "learning" the typical radiation patterns present in the training data. We refrained

from using such an approach in this Part as it was beyond the scope of the study. In addition, we could show that the knowledge of the underlying radiation pattern can drive the choice of strong discriminatory observables. For a practical application, the combination of these observables, with others already in place, into a multivariate algorithm would of course be desirable.

Appendix A

N-Jettiness

In this appendix, we will be presenting the results of an implementation of N-Jettiness phase space slicing, following the method outlined in [21]. We will first review the definition of the N-Jettiness variable and the associated factorization of the cross section before presenting our implementation and results.

A.1 Definition of N-Jettiness

N-Jettiness, denoted τ_N in the following, was introduced as an event shape observable in [216]. As an event shape it can be interpreted as an inclusive measure of how much the event "looks like" an event with N jets. As such, it may be used as a criterion for requiring a fixed number of jets, interpolating smoothly between the fully exclusive limit of exactly N infinitely narrow jets in the limit $\tau_N \to 0$ and the fully inclusive limit $\tau_N \to 1$ [5]. Its usefulness in a phase space slicing method was worked out in [21]. A similar and somewhat parallel development introduced a jet shape N-Subjettiness [217] which can be interpreted as measuring how much a jet looks like it is made up of N subjets.

_____

[5]Note that the normalization, as shown in the following, may be chosen to limit $\tau_N \in [0, 1]$, but this is not a necessary requirement.

A.1.1 Notation

Before considering the definition of *N*-Jettiness, let us first define our notation[6]. Consider a process that at LO contains N final state partons, labelled $1, \ldots, N$, and a number of unspecified, non-QCD final state particles. The initial state partons will be labeled a, b. The Born phase space is then the collection of the parton momenta $\{q_a, q_b; q_1, \ldots, q_N\}$ together with their flavour, helicity and spin information $\{\kappa_a, \kappa_b; \kappa_1, \ldots, \kappa_N\}$ and the phase space for the non-QCD particles $\Phi_L(q)$ with a total momentum q[7]:

$$\Phi_N = \{(q_a, \kappa_a), (q_b, \kappa_b); (q_1, \kappa_1), \ldots, (q_N, \kappa_N); \Phi_L(q)\}. \tag{A.1.1}$$

For the use of the *N*-Jettiness method in higher-order corrections, the non-partonic particles are only relevant in that they are required to enforce momentum conservation:

$$q_a + q_b = q_1 + \cdots + q_N + q. \tag{A.1.2}$$

The complete phase space measure $\mathrm{d}\Phi_N$ then reads:

$$\int \mathrm{d}\Phi_N \equiv \frac{1}{2E_{\mathrm{cm}}^2} \int \frac{\mathrm{d}x_a}{x_a} \frac{\mathrm{d}x_b}{x_b} \int \mathrm{d}\Phi_N \left(q_a + q_b; q_1, \ldots, q_N; q\right) \frac{\mathrm{d}q^2}{2\pi} \mathrm{d}\Phi_L(q) \sum_\kappa s_\kappa, \tag{A.1.3}$$

where $\mathrm{d}\Phi_N(\ldots)$ is the usual Lorentz invariant phase space appropriate for N final state particles, E_{cm} is the center of mass energy of the collision, x_i are the momentum fractions of the initial states carried by the partons involved in the collision and s_κ is the symmetry factor appropriate to the respective partonic channel κ.

In the following, we will denote final state particles as p_k. Light-like vectors denoting jet directions, as defined in the following section, will be denoted with q_i. Let us further define the unit vector n_i in the direction of q_i as $q_i = E_i n_i$. We then use the shorthand $x_{ij} \equiv n_i \cdot n_j$ to denote the scalar product of these directions.

---

[6]We emphasize this point here since several different conventions are found in the literature. Naming conventions may be the exact opposite of other conventions. In addition, this choice may also lead to differing explicit factors of 2.

[7]Momenta of non-partonic incoming particles, as in *ep* and *ee* collisions, will be considered part of $\Phi_L(q)$.

A.1.2 N-Jettiness definition

For any final state with $M \geq N$ partons, the N-Jettiness variable is then defined as follows [216]:

$$\tau_N = \sum_{k \in FS} \min_{i \in \{a,b,1,...,N\}} \left(\frac{2p_k \cdot q_i}{Q_i} \right) = \sum_{k=1}^{M} \min_{i \in \{a,b,1,...,N\}} \left(\frac{2p_k \cdot q_i}{Q_i} \right). \qquad (A.1.4)$$

The sum in this expression runs over all partons k in the final state. The light-like vectors q_i denote N jet directions and the beam directions a and b, if the beams are hadronic. The minimization in this expression is performed over these jet directions. The Q_i are normalization factors specific to each jet direction, which may be chosen arbitrarily as long as they do not upset the behaviour of the variable in the limit of soft or collinear radiation. Different normalizations will lead to different characteristics in the behaviour of $\tau_N \neq 0$. Each term in the minimization can be interpreted as the distance of p_k to jet direction q_i, the lowest value of which contributes to the overall sum. The bracket thus determines a distance measure akin to the distance measures in jet algorithms.

We observe that if $M = N$, corresponding to the fully exclusive case, we find $\tau_N = 0$ while for any $M > N$, $\tau_N \geq 0$. The scalar product in the above expression reads for massless partons $p_k \cdot q_i = E_k E_i \left(1 - \cos \theta_{i,j} \right)$. In the limit of soft, $E_k \to 0$, or collinear radiation, $\theta_{i,j} \to 0$, the scalar product $p_k \cdot q_i \to 0$. Thus in the limit of soft or collinear radiation, we have $\tau_N \to 0$. N-Jettiness therefore fulfills exactly the requirements placed on an N-jet resolution variable, namely:

$$\tau_N \left(\Phi_N \right) = 0, \qquad \tau_N \left(\Phi_{>N} \right) \geq 0, \qquad \tau_N \left(\Phi_{>N} \to \Phi_N \right) \to 0. \qquad (A.1.5)$$

A.1.3 The normalization factors Q_i

The normalization factors Q_i represent a choice which affects not only the structure of the singular spectrum of the cross section, but also the dimensionality of the N-Jettiness variable. The only requirement on the Q_i is that they do not spoil the behaviour in the singular limits. Two classes of normalizations are common:

- A common hard scale Q related to the full event. This leads to a minimization of the invariant masses in each of the regions defined by the jet directions.

- A scale related to the hardness of the jet, e.g. the jet energy E_i. This creates a geometric measure.

A number of other distance measures, some of which can be represented in the way we have chosen here, have been discussed in the context of using the minimization of an N-jet resolution observable as a jet defining algorithm [218].

Relation to known measures

An interesting observation is the relation of N-Jettiness to other observables which may be used for validation. For processes with only two partons at Born level, a large number of similar observables have been studied and used for resummations.

In electron positron collisions, 2-Jettiness is related to the thrust observable $T = \max_{\hat{t}} \sum_i |\hat{t} \cdot \vec{p}_i|/E_{\mathrm{CMS}}$ with thrust axis $\hat{t}$ and E_{CMS} the centre of mass energy of the event. In the two-jet limit, the jet directions are back-to-back and align with the thrust axis. In this case, we have for the 2-Jettiness value:

$$\tau_2^{ee} = \frac{1}{Q} \sum_k E_k \min\{1 - \cos\theta_k, 1 + \cos\theta_k\}. \tag{A.1.6}$$

This is in fact equivalent to $\tau_2^{ee} = 1 - T$. Due to the light-like nature of all momenta involved, the minimization of the scalar product between four-momenta p_k and q_i in Eq. (A.1.4) can be rewritten as a maximization over the scalar product of the three-momenta $\vec{p_k}$ and $\vec{q_i} \equiv \hat{t}$. This observable has been known for a long time [219], and resummations of $1 - T$ have been performed as well in [220, 221].

Similarly, 2-Jettiness with a dimension-two normalization factor $Q_i = E_{\mathrm{CMS}}^2$ is equal to the original JADE algorithm measure $y_{ij} = 2E_i E_j (1 - \cos\theta_{ij})/E_{\mathrm{CMS}}^2$ [222] and also the same as the variable $y_{13;2}$ used in the Catani-Seymour dipole subtraction method. This latter equivalence allows for a number of computational cross-checks

between our N-Jettiness implementation and the Catani-Seymour implementation within SHERPA.

A.1.4   The jet directions q_i

The jet directions q_i are defined through a minimization procedure. For the fixed order (N)NLO corrections that we are interested in in this work, we will only be concerned with final states that include up to two extra partons compared to the number of jets N. In this case, we can use a simple brute-force algorithm for determining the jet directions that give the minimum N-Jettiness values[8].

In order to be as general as possible, we consider a process with two fixed hadronic beam directions $q_{a,b} = E_{a,b}\,(1,0,0,\pm1)$. Any process with fewer than two partons in the initial state can then be obtained by removing the respective number of beam directions from the algorithm.

The minimization procedure employed in the definition of the N-Jettiness measure defines N jet sectors and two beam sectors. Each parton is then clustered into one of these sectors depending on the direction q_i that it is "closest" to. Let us define as τ_N^i the contribution due to the i-th sector:

$$\tau_N^i = \sum_{k=1}^{M} \left[\frac{2q_i \cdot p_k}{Q_i} \prod_{j \neq i} \theta \left(\frac{q_j \cdot p_k}{Q_j} - \frac{q_i \cdot p_k}{Q_i} \right) \right], \qquad (A.1.7)$$

with $i \in \{a, b, 1, \ldots, N\}$. The product of θ-functions is non-vanishing only if the particle k is closest to direction i, thereby ensuring the clustering into this region. The total N-Jettiness value is then just the sum of all these contributions, $\tau_N = \sum_i \tau_N^i$. For convenience of the presentation let us define a combined four-momentum of the momenta denoted by $1, \ldots, r$,

$$q_{\widetilde{1 \ldots r}} = \sum_{i=1}^{r} E_i \begin{pmatrix} 1 \\ \sum_{j=1}^{r} \vec{n}_j \end{pmatrix}, \qquad (A.1.8)$$

---

[8]The general problem of finding N-Jettiness axes through minimization for a large number of final state particles poses a difficult computational problem. An algorithm based on a one-pass minimization can be used to solve this problem and forms the basis of the XCONE jet algorithm [218].

where $\vec{n}_i$ is the three-vector in which momentum i is pointing. One could also recombine the partons by adding their three-momenta and assigning the energy component as $|\sum_{i=1}^{r} E_i \vec{n}_i|$. In the soft and collinear limits, the choice of recombination procedure does not make a difference.

One additional parton

For $N + 1$ partons, $N - 1$ jet axes must be aligned with $N - 1$ partons in the final state to find the global minimum of τ_N. There will thus only be one sector that contributes to the total value of τ_N, determined by a single optimal axis. This axis may now be one of a choice of two possibilities: either it is aligned with one of the remaining final state partons, in which case the other parton is clustered into one of the beam sectors, or the final direction lies along the sum of the two final state partons, along $q_{\widetilde{ij}}$. We can formalize this algorithm as follows:

1. Choose a pair $\{i, j\}$ from all the partons in the event. Skip the pair if both partons are in the initial state, as the beam directions are fixed.

2. Choose the optimal jet axis $q_{\{i,j\}}$ related to these partons:

   (a) if one of the $\{i, j\}$ is in the initial state, $q_{\{i,j\}} = q_{\text{IS}}$.

   (b) if both $\{i, j\}$ are in the final state, $q_{\{i,j\}} = q_{\widetilde{ij}}$.

3. Calculate the contribution of this sector to $\tau_N^{\{i,j\}} = \frac{2(p_i + p_j) \cdot q_{\{i,j\}}}{Q_{\{i,j\}}}$.

4. Repeat steps 1-3 for all possible pairs of partons $\{i, j\}$.

5. Keep the lowest value as the value of τ_N for this event.

Two additional partons

For a final state with $N + 2$ partons, we can proceed similarly, but are faced with a larger number of possibilities. $N - 2$ jet directions will now be aligned with $N - 2$ partons, with four additional partons left to be clustered into two additional jet axes:

1. Choose a pair of partons $\{i, j\}$ in the final state. Let all other partons define a sector.

2. Choose two, not necessarily distinct, sectors $\{a_1^{\{i,j\}}, a_2^{\{i,j\}}\}$:

   (a) if $a_1^{\{i,j\}} = a_2^{\{i,j\}}$, both $\{i, j\}$ fall into the same sector. Choose the optimal axis as:

      - if $a_1^{\{i,j\}}$ is a beam direction, $q_{a_1 ij} = q_{a_1}$.
      - if $a_1^{\{i,j\}}$ is in the final state, $q_{a_1 ij} = q_{\widetilde{a_1 ij}}$.

   (b) if $a_1^{\{i,j\}} \neq a_2^{\{i,j\}}$, both partons fall into different sectors. Consider, without loss of generality, i falling into sector $a_1^{\{i,j\}}$, j into sector $a_2^{\{i,j\}}$. Choose optimal axes for each sector:

      - if $a_1^{\{i,j\}}$ is a beam direction, $q_{a_1 i} = q_{a_1}$.
      - if $a_1^{\{i,j\}}$ is in the final state, $q_{a_1 i} = q_{\widetilde{a_1 i}}$.
      - if $a_2^{\{i,j\}}$ is a beam direction, $q_{a_2 j} = q_{a_2}$.
      - if $a_2^{\{i,j\}}$ is in the final state, $q_{a_2 j} = q_{\widetilde{a_2 j}}$.

3. Calculate the contribution to N-Jettiness in this case as $\tau_N = \sum \tau_N^k$.

4. Repeat step 2-3 for all possible sectors $\{a_1^{\{i,j\}}, a_2^{\{i,j\}}\}$, keeping the lowest value of τ_N as the contribution if $\{i, j\}$ are unclustered.

5. Repeat steps 1-4 for all possible pairs of partons $\{i, j\}$, keeping the lowest contribution to τ_N as the overall value of τ_N.

A.2   Factorization in the singular limits

As already alluded to, the choice of an N-jet resolution variable is in principle arbitrary as long as it respects the conditions on resolving the number of jets. However, for implementing a phase space slicing, it must also be possible to separate the cross

section into its singular and finite parts whilst allowing for a simple calculation of this contribution in the singular region.

We define the singular spectrum of an N-jet resolution variable as

$$\frac{\mathrm{d}\sigma^{\mathrm{sing}}(X)}{\mathrm{d}\tau_N} = \mathcal{C}_{-1}(X)\delta(\tau_N) + \sum_{n\geq 0} \mathcal{C}_n(X)\mathcal{L}_n(\tau_N). \tag{A.2.1}$$

Here, the $\mathcal{C}_n$ are singular coefficients defining the singular spectrum. The calculation of these coefficients defines the contribution to the cross section below the cut. The $\mathcal{L}_n(\tau_N)$ are +-distributions, which are defined for a test function $f(\tau_N)$ as:

$$\mathcal{L}_n(\tau_N) = \left[\frac{\theta(\tau_N)\ln^n(\tau_N)}{\tau_N}\right]_+,$$

$$\int_{-\infty}^{\tau_{N,\mathrm{cut}}} \mathrm{d}\tau_N \mathcal{L}_n(\tau_N)f(\tau_N) = \int_0^{\tau_{N,\mathrm{cut}}} \mathrm{d}\tau_N \frac{\ln^n(\tau_N)}{\tau_N}\left[f(\tau_N) - f(0)\right] + f(0)\frac{\ln^{n+1}(\tau_{N,\mathrm{cut}})}{n+1}. \tag{A.2.2}$$

This structure follows from the infrared structure of QCD amplitudes for infrared safe observables. The singular cross section differential in τ_N can be written in terms of pieces differential in the contributions τ_N^i due to the sectors $i \in \{a, b, 1, \ldots, N\}$:

$$\frac{\mathrm{d}\sigma^{\mathrm{sing}}(X)}{\mathrm{d}\tau_N} = \int \mathrm{d}\Phi_N \frac{\mathrm{d}\sigma^{\mathrm{sing}}(\Phi_N)}{\mathrm{d}\tau_N} X(\Phi_N), \tag{A.2.3}$$

$$\frac{\mathrm{d}\sigma^{\mathrm{sing}}(\Phi_N)}{\mathrm{d}\tau_N} = \int \left(\prod_i \mathrm{d}\tau_N^i\right) \frac{\mathrm{d}\sigma^{\mathrm{sing}}(\Phi_N)}{\mathrm{d}\tau_N^a \mathrm{d}\tau_N^b \ldots \mathrm{d}\tau_N^N} \delta\left(\tau_N - \sum_i \tau_N^i\right). \tag{A.2.4}$$

Note that the singular limits of the cross section only depend on the underlying Born phase space, hence the separation of $\mathrm{d}\sigma^{\mathrm{sing}}(X)/\mathrm{d}\tau_N$ into $\mathrm{d}\sigma^{\mathrm{sing}}(\Phi_N)/\mathrm{d}\tau_N$ is justified. For the cross section differential in the individual contributions, a factorization theorem has been proven in [216, 223, 224] using the formalism of Soft-Collinear Effective Theory (SCET). The factorized cross section reads:

$$\frac{\mathrm{d}\sigma^{\mathrm{sing}}(\Phi_N)}{\mathrm{d}\tau_N^a \mathrm{d}\tau_N^b \ldots \mathrm{d}\tau_N^N} = \int \mathrm{d}t_a B_a(t_a, x_a, \mu) \int \mathrm{d}t_b B_b(t_b, x_b, \mu) \left[\prod_{i=1}^N \int \mathrm{d}s_i J_i(s_i, \mu)\right]$$

$$\times \vec{H}^\dagger(\Phi_N, \mu) \hat{S}_\kappa \left(\tau_N^a - \frac{t_a}{Q_a}, \ldots, \tau_N^N - \frac{s_N}{Q_N}, \{\hat{q}_i\}, \mu\right) \vec{H}(\Phi_N, \mu). \tag{A.2.5}$$

There are several components to this factorization theorem:

- The beam functions B_a and B_b: these functions contain the contributions from radiation collinear to the respective beam direction. The beam functions depend on the flavour κ of the parton from the beam and the light-cone momentum fraction x of the proton momentum it carries. These functions also contain the PDFs.

- The jet functions J_i, $i \in \{1, \ldots, N\}$: these functions contain the contributions due to radiation collinear to the jet direction q_i. The jet functions depend on the flavour κ of the jet.

- The soft function $\hat{S}_\kappa$: this function encodes the contributions due to soft radiation. $\hat{S}_\kappa$ depends on all normalized jet directions $\hat{q}_i \equiv \frac{q_i}{Q_i}$ in the process, and acts as a matrix in the colour space of the process.

- The hard Wilson coefficients $\vec{H}$[9]: these coefficients contain the QCD amplitude of the N-parton process, i.e. the Born and hard virtual amplitudes. In SCET, these coefficients arise as the matching coefficients from QCD onto SCET. They are vectors in the same colour space as the soft function.

The first set of arguments of B_a, J_i and $\hat{S}_\kappa$ are the contributions to the τ_N^i from the respective sectors. All functions have an explicit dependence on the unspecified scale μ, which cancels exactly between them at each order, with the remaining μ dependence contained in the running $\alpha_s(\mu)$.

Whilst it is possible to keep the entire cross section differential in all contributions to the different sectors, we are ultimately interested in slicing the phase space into a singular and a non-singular region. We therefore consider the projection of the factorized cross section onto the singly differential $d\sigma^{\mathrm{sing}}(\Phi_N)/d\tau_N$:

$$\frac{d\sigma^{\mathrm{sing}}(\Phi_N)}{d\tau_N} = \int dt_a B_a(t_a, x_a, \mu) \int dt_b B_b(t_b, x_b, \mu) \left[\prod_{i=1}^{N} \int ds_i J_i(s_i, \mu) \right]$$

---

[9] Note that we choose to denote these coefficients through $\vec{H}$. In other literature, the coefficients are usually denoted $\vec{C}$, and the symbol H reserved for the hard function $\vec{C}^\dagger \vec{C}$. We choose this representation to prevent confusion with other C's floating around in the expressions.

$$\times \vec{H}^\dagger \left(\Phi_N, \mu \right) \hat{S}_\kappa \left(\tau_N - \frac{t_a}{Q_a} - \frac{t_b}{Q_b} - \sum_{i=1}^N \frac{s_i}{Q_i}, \{\hat{q}_i\}, \mu \right) \vec{H} \left(\Phi_N, \mu \right).$$

(A.2.6)

The single differential soft function is obtained by integrating using the delta-functions in Eq. (A.2.4):

$$\hat{S}_\kappa \left(k, \{\hat{q}_i\}, \mu \right) = \int \left[\prod_i k_i \right] \hat{S}_\kappa \left(\{k_i\}, \{\hat{q}_i\}, \mu \right) \delta \left(k - \sum_i k_i \right).$$

(A.2.7)

We now expand this cross section as we did in Eq. (A.2.1) into singular coefficients:

$$
\begin{aligned}
\frac{\mathrm{d}\sigma^{\mathrm{sing}}}{\mathrm{d}\tau_N} &= \mathcal{C}_{-1} \left(\Phi_N, \xi \right) \delta \left(\tau_N \right) + \sum_{n \geq 0} \mathcal{C}_n \left(\Phi_N, \xi \right) \frac{1}{\xi} \mathcal{L}_n \left(\frac{\tau_N}{\xi} \right) \\
&= \sum_{m \geq 0} \left(C_{-1}^{(m)} (\Phi_N, \xi, \mu) \delta(\tau_N) + \sum_{n=0}^{2m-1} C_n^{(m)} (\Phi_N, \xi, \mu) \frac{1}{\xi} \mathcal{L}_n \left(\frac{\tau_N}{\xi} \right) \right) \left(\frac{\alpha_s(\mu)}{4\pi} \right)^m.
\end{aligned}
$$

(A.2.8)

where in the second line we expanded the singular coefficients as a series in the coupling constant α_s. At LO, only $\mathcal{C}_{-1}^{(0)} = B_N \left(\Phi_N \right)$ contributes. Note that the Born level amplitude may already include couplings α_s, which are not included in the counting m in above equation. At NLO $\mathcal{C}_{-1,0,1}$ are non-zero, at NNLO we need to consider $\mathcal{C}_{-1,0,1,2,3}$. The parameter ξ is an arbitrary dimension-one parameter that cancels among the different contributions. It can be taken equal to the normalization of the jet directions, but its cancellation for other values is a non-trivial cross check of the implementation.

To find the coefficients $\mathcal{C}_n$, we expand all the functions in Eq. (A.2.6) in terms of $\alpha_s(\mu)$ and then assemble the respective orders. The expanded functions read:

$$
\begin{aligned}
J_i(s, \mu) &= \delta(s) + \sum_{m \geq 1} J_i^{(m)}(s, \mu) \left(\frac{\alpha_s}{4\pi} \right)^m, \\
B_a(t, x, \mu) &= \delta(t) f_a \left(x, \mu_F \right) + \sum_{m \geq 1} B_a^{(m)}(t, x, \mu, \mu_F) \left(\frac{\alpha_s}{4\pi} \right)^m, \\
\hat{S}_\kappa \left(k, \{\hat{q}_i\}, \mu \right) &= \mathbf{1}_\kappa \delta(k) + \sum_{m \geq 1} \hat{S}_\kappa^{(m)} \left(k, \{\hat{q}_i\}, \mu \right) \left(\frac{\alpha_s}{4\pi} \right)^m, \\
\vec{H} \left(\Phi_N, \mu \right) &= \vec{H}^{(0)} \left(\Phi_N, \mu \right) + \sum_{m \geq 1} \vec{H}^{(m)}(\Phi_N, \mu) \left(\frac{\alpha_s}{4\pi} \right)^m.
\end{aligned}
$$

(A.2.9)

In $\hat{S}_\kappa$, $\mathbf{1}_\kappa$ denotes the identity operator in colour space.

A.2.1   The leading order cross section

At leading order, the factorized cross section has to reduce to the QCD Born level cross section of the underlying process. At this level, we then have

$$J_i^{(0)}(s,\mu) = \delta(s),$$

$$B_a^{(0)}(t,x,\mu) = \delta(t) f_a(x,\mu_F),$$ (A.2.10)

$$\hat{S}_\kappa(k_a,\ldots,k_N,\{\hat{q}_i\},\mu) = \mathbf{1}_\kappa \prod_i \delta(k_i).$$

We then get for the differential cross section:

$$\frac{d\sigma^{\text{sing}}(\Phi_N)}{d\tau_N} = f_a f_b \vec{H}^{\dagger(0)}(\Phi_N) \mathbf{1}_\kappa \vec{H}^{(0)}(\Phi_N) \prod_i \delta(\tau_N^i)$$

$$= B_N(\Phi_N) \prod_i \delta(\tau_N^i),$$ (A.2.11)

with $B_N \equiv f_a f_b \vec{H}^{\dagger(0)}(\Phi_N) \mathbf{1}_\kappa \vec{H}^{(0)}(\Phi_N)$. Upon integration, this reproduces the leading order cross section as required.

A.2.2   NLO coefficients

For the below-the-cut contributions at NLO, we need, for a pure slicing approach, the coefficient $\mathcal{C}_{-1}^{(1)}$:

$$C_{-1}^{(1)}(\Phi_N,\xi,\mu) = f_a(x_a,\mu_F) f_b(x_b,\mu_F) \left(\vec{H}^{\dagger(1)}\vec{H}^{(0)} + \vec{H}^{\dagger(0)}\vec{H}^{(1)}\right)(\Phi_N,\mu)$$

$$+ \left|\vec{H}^{(0)}(\Phi_N,\mu)\right|^2 \Bigg[f_a(x_a,\mu_F) f_b(x_b,\mu_F) \sum_{i=1}^N J_{i,-1}^{(1)}\left(\frac{Q_i\xi}{\mu^2}\right)$$

$$+ B_{a,-1}^{(1)}\left(x_a,\mu,\mu_F,\frac{Q_a\xi}{\mu^2}\right) f_b(x_b,\mu_F) + f_a(x_a,\mu_F) B_{b,-1}^{(1)}\left(x_b,\mu,\mu_F,\frac{Q_b\xi}{\mu^2}\right) \Bigg]$$

$$+ f_a(x_a,\mu_F) f_b(x_b,\mu_F) \vec{H}^{\dagger(0)}(\Phi_N,\mu) \hat{S}_{\kappa,-1}^{(1)}\left(\{\hat{q}_i\},\frac{\xi}{\mu}\right) \vec{H}^{(0)}(\Phi_N,\mu).$$ (A.2.12)

In the first line, $\left(\vec{H}^{\dagger(1)}\vec{H}^{(0)} + \vec{H}^{\dagger(0)}\vec{H}^{(1)}\right)(\Phi_N,\mu)$ is the virtual contribution to the cross section, which corresponds to the term $V_N(\Phi_N)$ in Eq. (2.2.3). The further

lines contain the contributions due to the below-the-cut contributions in SCET.

For the coefficients at NNLO, we also need the coefficients $\mathcal{C}_n^{(1)}$ with $n = 0, 1$:

$$C_n^{(1)}(\Phi_N, \xi, \mu) = \left|\vec{H}^{(0)}(\Phi_N, \mu)\right|^2 \left[f_a(x_a, \mu_F)\, f_b(x_b, \mu_F) \sum_{i=1}^{N} J_{i,n}^{(1)}\left(\frac{Q_i\xi}{\mu^2}\right) \right.$$

$$\left. + B_{a,n}^{(1)}\left(x_a, \mu, \mu_F, \frac{Q_a\xi}{\mu^2}\right) f_b(x_b, \mu_F) + f_a(x_a, \mu_F) B_{b,n}^{(1)}\left(x_b, \mu, \mu_F, \frac{Q_b\xi}{\mu^2}\right) \right]$$

$$+ f_a(x_a, \mu_F)\, f_b(x_b, \mu_F)\, \vec{H}^{\dagger(0)}(\Phi_N, \mu)\, \hat{S}_{\kappa,n}^{(1)}\left(\{\hat{q}_i\}, \frac{\xi}{\mu}\right) \vec{H}^{(0)}(\Phi_N, \mu).$$

$$(\text{A.2.13})$$

There is no contribution from the hard Wilson coefficients here as these contributions are all contained in the single point that corresponds to the Born configuration, i.e. in the $\delta(\tau_N)$ contribution.

NNLO coefficients

At NNLO, the different terms become more convoluted. To reduce clutter, we omit the functional dependencies. They are the same as in Eq. (A.2.12).

All coefficients, apart from $\hat{S}_{-1}^{(2)}$, the two-loop soft constant, and the $\vec{H}^{(2)}$, the hard two-loop coefficients, are known exactly. $\hat{S}_{-1}^{(2)}$ is known analytically for processes involving two external partons at Born level, and can be calculated numerically for a larger number of partons in the process [225]. We will perform such a calculation in the next chapter.

We can further write the m-loop, below-the-cut, SCET contributions as

$$X_n^{(m)} = \left|\vec{H}^{(0)}\right|^2 \left(f_a f_b \sum_i J_{i,n}^{(m)} + B_{a,n}^{(m)} f_b + f_a B_{b,n}^{(m)} \right)$$

$$+ f_a f_b \vec{H}^{\dagger(0)} \hat{S}_n^{(m)} \vec{H}^{(0)}.$$

$$(\text{A.2.14})$$

The cross-terms between the one-loop SCET contribution and the one-loop virtual amplitudes can be collected as

$$X_n^{(1+1)} = \left|\vec{H}^{\dagger(1)} \vec{H}^{(0)} + \vec{H}^{(1)} \vec{H}^{\dagger(0)}\right| \left(f_a f_b \sum_i J_{i,n}^{(1)} + B_{a,n}^{(1)} f_b + f_a B_{b,n}^{(1)} \right)$$

$$+ f_a f_b \left(\vec{H}^{\dagger(0)} \hat{S}_n^{(1)} \vec{H}^{(1)} + \vec{H}^{\dagger(1)} \hat{S}_n^{(1)} \vec{H}^{(0)} \right), \tag{A.2.15}$$

and the cross terms between two different SCET contributions, stemming from different $\mathcal{L}_n \otimes \mathcal{L}_m$ convolutions can be written as

$$X_{n,m}^{(1+1)} = \left| \vec{C}^{(0)} \right|^2 \left(f_a f_b \sum_{i \leq j} J_{i,n}^{(1)} J_{j,m}^{(1)} + B_{a,n}^{(1)} f_b \sum_i J_{i,m}^{(1)} + f_a B_{b,n}^{(1)} \sum_i J_{i,m}^{(1)} + B_{a,n}^{(1)} B_{b,n}^{(1)} \right)$$
$$+ f_a f_b \sum_i J_{i,n}^{(1)} \vec{C}^{\dagger(0)} \hat{S}_n^{(1)} \vec{C}^{(0)} + B_{a,n}^{(1)} f_b \vec{C}^{\dagger(0)} \hat{S}_n^{(1)} \vec{C}^{(0)} + f_a B_{b,n}^{(1)} \vec{C}^{\dagger(0)} \hat{S}_n^{(1)} \vec{C}^{(0)}.$$
$$\tag{A.2.16}$$

Using all of these abbreviations, we can finally collect together the NNLO, below-the-cut contributions into the coefficient $\mathcal{C}_{-1}^{(2)}$:

$$C_{-1}^{(2)} = f_a f_b \left(\vec{H}^{\dagger(2)} \vec{H}^{(0)} + \vec{H}^{\dagger(0)} \vec{H}^{(2)} + \vec{H}^{\dagger(1)} \vec{H}^{(1)} \right)$$
$$+ X_{-1}^{(2)} + X_{-1}^{(1+1)} - \frac{\pi^2}{6} X_{0,0}^{(1+1)} + \zeta_3 \left(X_{1,0}^{(1+1)} + X_{0,1}^{(1+1)} \right) - \frac{\pi^4}{360} X_{1,1}^{(1+1)}. \tag{A.2.17}$$

The coefficients in front of the $X_{n,m}^{(1+1)}$ are coefficients V_k^{mn} arising from the convolution of two plus distributions:

$$(\mathcal{L}_m \otimes \mathcal{L}_n) \equiv \int d\tau' \mathcal{L}_m (\tau - \tau') \mathcal{L}_n(\tau) = V_{-1}^{mn} \delta(\tau) + \sum_k^{m+n+1} V_k^{mn} \mathcal{L}_k(\tau), \tag{A.2.18}$$

which are listed in appendix B of [226].

A.2.3 Power corrections

The factorization theorem in Eq. (A.2.4) is strictly only valid in the limit of soft or collinear radiation. This, in principle, necessitates the calculation of the contribution above and below the cut in the limit $\tau_N \to 0$. Taking this limit exactly is not possible due to the limited precision of numerical calculations, so we have to use small, but finite, cutoffs $\tau_{N,\mathrm{cut}}$. The total cross section is then the sum of the result found assuming strict factorization of the cross section and so-called power corrections caused by deviations from the strict limit.

The leading behaviour of these power corrections in the total cross section is

$$\sigma^{\text{nonsing}} \propto \tau_{N,\text{cut}} \alpha_s^m \log^{2m}\left(\tau_{N,\text{cut}}\right) \tag{A.2.19}$$

for a process calculated up to order m in the slicing. Owing to the logarithmic enhancement, we expect a larger deviation of the phase space slicing results from the true cross section for larger values of the cut. The exponent of the logarithm also means that the power corrections become more important relative to the singular spectrum at higher orders in the coupling constant. In the absence of a calculation of these power corrections, an extrapolation into the region $\tau_N \to 0$ of the cross section evaluated at multiple values of the cut can be used to extract the true cross section. At NLO a differential fit function

$$f^{\text{NLO}}(\tau_{N,\text{cut}}) = c_1 + c_2 \tau_{N,\text{cut}} \log \tau_{N,\text{cut}} + c_3 \tau_{N,\text{cut}}, \tag{A.2.20}$$

can be used to extract the NLO cross section. This procedure has been advocated and used in the programs MCFM [82] and in MATRIX [119] in the context of q_T slicing.

The potential size of the power corrections has led to increased efforts to understand and calculate these corrections [227–231]. In SCET, power corrections originate in universal sub-leading Lagrangian insertions, non-universal sub-leading corrections in the hard scattering operators, and in sub-leading terms in the expansion of the measurement function and the phase space. Power corrections are thus non-universal and have to be calculated for each process separately.

The combination of power corrections with the below-the-cut contributions improves the convergence of the phase space slicing by providing subleading corrections to the cross section. Beyond this, the inclusion of power corrections also allows one to use larger values of the cut parameter to achieve the same precision, substantially reducing computation time and increasing the numerical stability. The implementation presented in this work does not include such power corrections, however their inclusion would improve the computational efficiency and allow a larger cut to be used.

A.3 N-Jettiness slicing within the SHERPA framework

Having introduced the ingredients necessary for the implementation of N-Jettiness slicing, we will now present their incorporation into the SHERPA framework. The framework has been reviewed in Section 1.1. As noted there, SHERPA, alongside the input from an external loop generator, already allows for automated NLO calculations both in QCD and the full electroweak theory. The method of choice for these calculations is the Catani-Seymour subtraction method . The framework however also provides the infrastructure necessary for a phase space slicing calculation.

The formulation of the below-the-cut contribution in Eq. (A.2.12), with the exception of the virtual contribution, is written in exactly the form of a differential K-factor. The Born amplitude squared is multiplied by a phase-space-dependent factor which also carries information about the flavour, helicity and colour of the external partons. The SHERPA framework provides a facility within its PHASIC module to calculate such a differential K-factor and apply it to the process in question.

The above-the-cut contribution in an NLO calculation amounts to a LO calculation of the process $X + j$ above the N-Jettiness cut. Such a calculation can be achieved straightforwardly within SHERPA using a custom-built selector to apply a τ_N phase space cut.

A.3.1 NLO: the above-the-cut contribution

At NLO, the contribution above the τ_N cut is the simplest to implement. We use the algorithm described in Section A.1.4 to determine the value of N-Jettiness from a LO process with $N + 1$ partons, as generated by one of SHERPA's matrix element generators, COMIX and AMEGIC. If a generated phase space point has a value $\tau_N < \tau_{N,\mathrm{cut}}$, it is vetoed.

There is an interesting point to consider when trying to simulate processes involving more than 2 partons at leading order. While in those processes (e.g. Drell-Yan, $e^+e^- \to q\bar{q}$), the kinematics are fixed, with three partons at the Born level we need to use a jet algorithm. Such a definition can be done using any exclusive jet algorithm, including a cut on τ_{N-1}. The number of jets that are generated can be affected by hard radiation, which can also lead to a reduction in the number of jets. In this sense, it would seem the most sensible choice to define the N jets using a cut on τ_{N-1} as the minimization in this variable includes the same minimization required in the evaluation of τ_N. In the limit of collinear radiation however, where most of the cross section sits, the choice of jet algorithm should not make a big difference. The effect of using different types of jet algorithms to define the underlying Born event in N-Jettiness slicing has, to the best of our knowledge, not been discussed before and may be an issue to be kept in mind, in particular in cases in which N-Jettiness cuts are chosen large. Here, we indiscriminately use a FASTJET implementation of an exclusive k_T-algorithm, as appropriate for either hadron collider processes and e^+e^--collisions.

The above-the-cut contribution affords a number of cross checks with other parts of SHERPA as well as external codes. As noted in A.1.3, using the normalization factor $Q_i = E_{\text{CMS}}^2$ in a process involving two partons at Born level makes N-Jettiness equivalent to y as used in Catani-Seymour subtraction. In this method, we have two parameters that play a part in the real-subtracted contribution:

- The parameter α_{cut} is a technical cutoff, below which the cancellation between the real contribution $\mathrm{d}\sigma^{\text{R}}$ and the subtraction terms $\mathrm{d}\sigma^{\text{S}}$ is assumed to be exact. This cutoff is normally set very low[10] and applied in order to prevent numerical miscancellations in the regions that are close to the singularities.

- The parameter α_{dip} is used to restrict the available phase space for the subtraction terms S, providing an upper cutoff. Such a restriction is typically

---

[10]The default setting in SHERPA is $\alpha_{\text{cut}} = 10^{-9}$.

chosen in order to improve the performance of the integration of the *RS* part of the calculation as a lowering of α_{dip} requires less evaluations of the dipole terms, and can be tuned to reduce large cancellations between real and virtual contributions.

One possible, choice is to set $\alpha_{\text{cut}} = \alpha_{\text{dip}}$. In this case, the subtraction terms are not evaluated at all as the phase space over which they are integrated vanishes. The real contribution then takes exactly the form found in a slicing method, with the real matrix element integrated down to a cutoff in a 2-jet resolution observable.

A.3.2   NLO: the below-the-cut contribution

The terms below the cut are applied as a *K*-factor to the Born amplitude. This amplitude is provided by one of the inbuilt matrix element generators, COMIX or AMEGIC, alongside flavour, spin and PDF information.

The Jet function J_i

The jet function J_i is conceptually the easiest of the integrated contributions as each parton in the Born level final state contributes exactly one such function. All coefficients are known analytically and only depend on whether the parton is a gluon or a quark. The coefficients are given in Appendix A.4. The implementation of the J_i runs over all final state partons in the Born amplitude and calculates the relevant coefficients, see Eq. (A.4.12); their sum amounts to the total jet function contribution.

The Beam function B_a

The coefficients for the beam function are also all known analytically, again depending on the incoming flavour. In addition however, the beam function contains a convolution over the PDFs relevant to the parton a. Since the Born amplitude

already comes with a factor $f_a(x_a)$, this requires us to divide out this factor in the calculation. The implementation then sets up all the relevant beam function coefficients, including the relevant convolutions. Since the beam function coefficients contain plus-distributions, care has to be taken that the contributions from the endpoints are taken into account properly.

The Soft function $\hat{S}_\kappa$

The N-Jettiness soft function was calculated at NLO for the first time in [232]. For two partons at Born level, $\hat{S}_\kappa$ can be calculated analytically but beyond this, the angular integrals have to be solved numerically.

The calculation of the soft function amounts to an integral over the contraction of two soft-gluon emission currents. In SCET, the soft virtual integrals are scaleless and vanish in dimensional regularization. The contraction of two soft emission currents originating from the same Wilson line n_i again vanishes as this contribution is proportional to $n_i^2 = 0$. The surviving expression is thus:

$$
\begin{aligned}
\hat{S}_N^{\text{bare},(1)}\left(\{k_i\}\right) &= -\sum_{i\neq j} \mathbf{T}_i \cdot \mathbf{T}_j \left(\frac{e^{\gamma_E}\mu^2}{4\pi}\right)^\epsilon g^2 \int \frac{d^d p}{(2\pi)^d} \frac{n_i \cdot n_j}{(n_i \cdot p)(n_j \cdot p)} \\
&\quad \times 2\pi\delta\left(p^2\right)\theta\left(p^0\right) X\left(\{k_i\},\{n_i\cdot p\}\right) \\
&= \sum_{i\neq j} \mathbf{T}_i \cdot \mathbf{T}_j S_{ij}^{\text{bare},(1)}\left(\{k_i\}\right),
\end{aligned}
\tag{A.3.1}
$$

where for simplicity, we have assumed a normalization $Q_i = 2E_i$. The full expression can be restored by replacing $n_i \to 2E_i n_i$.

The measurement function X takes the form:

$$
\begin{aligned}
X\left(\{k_i\},\{n_i\cdot p\}\right) &= \delta\left(p^i - k_i\right)\delta\left(k_j\right)\theta\left(p^j - p^i\right) \prod_{m\neq i,j}\delta\left(k_m\right)\theta\left(p^m - p^i\right) \\
&\quad + \delta\left(k_i\right)\delta\left(p^j - k_j\right)\theta\left(p^i - p^j\right)\prod_{m\neq i,j}\delta\left(k_m\right)\theta\left(p^m - p^i\right) \\
&\quad + \sum_{m\neq i,j}\delta\left(p^m - k_m\right)\delta\left(k_i\right)\delta\left(k_j\right)\theta\left(p^i - p^m\right)\theta\left(p^j - p^m\right)\prod_{n\neq i,j,m}\delta\left(k_n\right)\theta\left(p^n - p^m\right),
\end{aligned}
$$
$$\tag{A.3.2}$$

where we used the abbreviation $p^i = n_i \cdot p$. The first line corresponds to the case in which the gluon is clustered with parton i, the value of N-Jettiness then becoming p^i in this region. The second line corrresponds to the gluon clustering into the region around parton j, while the last line denotes all clusterings with partons $m \neq i, j$. The calculation in [232] proceeds by expressing this measurement function in terms of two so-called hemisphere contributions by extending the regions around partons i, j such that their union covers the whole phase space. The subtraction of the added piece from the regions around the other partons m means that all divergences are contained within the hemisphere contributions. These contributions can be calculated analytically, and the UV divergences cancelled explicitly through the renormalization of SCET. The other contributions are fully finite, but have to be calculated numerically as no closed analytical form can be found for the angular integrals.

We propose here a calculation that circumvents the rearrangement of the measurement function into hemispheres and rather calculates each coefficient of the Laurent expansion $\hat{S}_\kappa$ in ϵ numerically. This approach can easily be extended to the calculation of the soft function at NNLO, and has since been published by other authors in [225].

Phase space

In order to perform this calculation, let us first rewrite the phase space. Let us define as $S_{ij;k}^{\mathrm{bare},(1)}(\{k_i\})$ the contribution to the bare soft function from the soft gluon connecting the Wilson lines i and j, clustered with the jet direction k. For each of these contributions, we will use a lightcone decomposition of the additional gluon momentum p in terms of two of the jet directions, here generically denoted m, n:

$$p^\mu = p^+ \frac{n_m^\mu}{x_{mn}} + p^- \frac{n_n^\mu}{x_{mn}} + p_\perp^\mu, \tag{A.3.3}$$

with $n_n \cdot p_\perp = n_m \cdot p_\perp = 0$ and the lightcone components:

$$
\begin{aligned}
p^+ &= n_n \cdot p = \frac{x_{ij} (E + p_z)}{2}, \\
p^- &= n_m \cdot p = \frac{x_{ij} (E - p_z)}{2}.
\end{aligned}
\tag{A.3.4}
$$

The decomposition of one of the other jet directions $r \neq m, n$ is given by:

$$
n_r^\mu = n_m^\mu \frac{x_{rn}}{x_{mn}} + n_n^\mu \frac{x_{rm}}{x_{mn}} + n_{r\perp}^\mu.
\tag{A.3.5}
$$

The scalar product of the additional gluon momentum with this decomposition is:

$$
n_r \cdot p = p^- \frac{x_{rn}}{x_{mn}} + p^+ \frac{x_{rm}}{x_{mn}} - 2 \left| n_{r\perp} \right| \left| p_\perp \right| \cos \phi_{pr},
\tag{A.3.6}
$$

with ϕ_{pr} the angle in the transverse plane between the momenta p and n_r. From the mass-shell requirement, it follows that

$$
\begin{aligned}
p_\perp^2 &= \frac{2 p^+ p^-}{x_{nm}}, \\
n_{r\perp}^2 &= \frac{x_{rn} x_{rm}}{2 x_{nm}}.
\end{aligned}
\tag{A.3.7}
$$

For what follows, we also define the following ratio:

$$
\frac{n_r \cdot p}{n_m \cdot p} = \frac{x_{rn}}{x_{mn}} + \frac{n_n \cdot p}{n_m \cdot p} \frac{x_{rm}}{x_{mn}} - 2 \sqrt{\frac{n_n \cdot p \ x_{rm} x_{rn}}{n_m \cdot p x_{mn}^2}} \cos \phi_{pr} \equiv A_{nm;r} \left(\frac{n_n \cdot p}{n_m \cdot p}, \phi_{pr} \right).
\tag{A.3.8}
$$

The phase space in this parameterization reads:

$$
\begin{aligned}
\int \mathrm{d}\Phi_1 &= \int \frac{\mathrm{d}p^d}{(2\pi)^{d-1}} \delta \left(p^2 \right) \Theta \left(p^0 \right) \\
&= \int \frac{\mathrm{d}E \ \mathrm{d}p_z \ \mathrm{d}p_\perp^{d-2}}{(2\pi)^{d-1}} \delta \left(p^2 \right) \Theta (E) \\
&= \frac{1}{(2\pi)^{d-1}} \int \mathrm{d}p^+ \mathrm{d}p^- \mathrm{d}^{d-2} p_\perp \delta \left(\frac{2 p^+ p^-}{x_{mn}} - p_\perp^2 \right) \frac{1}{x_{mn}} \Theta \left(x_{mn} \left(p^+ + p^- \right) \right) \\
&= \frac{1}{(2\pi)^{d-1}} \int \mathrm{d}p^+ \mathrm{d}p^- \frac{\mathrm{d}p_\perp^2}{2} \left(p_\perp^2 \right)^{\frac{d-4}{2}} \mathrm{d}\Omega_{d-3} \delta \left(\frac{2 p^+ p^-}{x_{mn}} - p_\perp^2 \right) \frac{1}{x_{mn}} \Theta \left(\left(p^+ + p^- \right) \right) \\
&= \frac{1}{(2\pi)^{d-1}} \int \mathrm{d}p^+ \mathrm{d}p^- \left(\frac{x_{mn}}{2 p^+ p^-} \right)^\epsilon \mathrm{d}\Omega_{d-3} \frac{1}{2 x_{mn}} \Theta \left(p^+ p^- \right) \Theta \left(p^+ + p^- \right) \\
&= \frac{1}{(2\pi)^{d-1}} \int \mathrm{d}p^+ \mathrm{d}p^- \left(\frac{x_{mn}}{2 p^+ p^-} \right)^\epsilon \mathrm{d}\Omega_{d-3} \frac{1}{2 x_{mn}} \Theta \left(p^+ \right) \Theta \left(p^- \right),
\end{aligned}
\tag{A.3.9}
$$

where $\mathrm{d}\Omega_{d-3}$ is the infinitesimal solid angle describing the direction of transverse momentum in the $(d-2)$-dimensional subspace which it spans. If the amplitude does not depend on this solid angle, it can be integrated out. The solid angle subtended by a d-dimensional sphere is given by[11]:

$$\Omega_d = \frac{2\pi^{\frac{d+1}{2}}}{\Gamma\left(\frac{d+1}{2}\right)}. \tag{A.3.10}$$

The soft function

There are two major cases to be distinguished in the calculation of the soft function. If $k = i$, i.e. the gluon is clustered with the emitting Wilson line i, we choose $m = i$, $n = j$. The case with $k = j$ can be obtained by letting $i \leftrightarrow j$. Combining this with the amplitude, we get for $S_{ij;i}^{\mathrm{bare},(1)}$:

$$
\begin{aligned}
S_{ij;i}^{\mathrm{bare},(1)}\left(\{k_i\}\right) = &- \left(\frac{e^{\gamma_E}\mu^2}{4\pi}\right)^{\epsilon} g^2 \int \mathrm{d}p^+ \mathrm{d}p^- \left(\frac{x_{ij}}{2p^+p^-}\right)^{\epsilon} \mathrm{d}\Omega_{d-3} \frac{1}{2x_{ij}} \frac{x_{ij}}{(n_i \cdot p)(n_j \cdot p)} \\
&\times \Theta\left(p^+\right) \Theta\left(p^-\right) \Theta\left(p^+ - p^-\right) \delta\left(k_i - p^-\right) \prod_{m \neq i,j} \Theta\left(p^m - p^-\right) \\
= &- \frac{\alpha_s(\mu)}{2\pi} \left(\frac{e^{\gamma_E}\mu^2 x_{ij}}{2}\right)^{\epsilon} \frac{1}{\Gamma(1-\epsilon)} \int \mathrm{d}p^+ \mathrm{d}p^- \frac{1}{(p^+p^-)^{\epsilon}} \\
&\times \Theta\left(p^+\right) \Theta\left(p^-\right) \Theta\left(p^+ - p^-\right) \delta\left(k_i - p^-\right) \prod_{m \neq i,j} \Theta\left(p^m - p^-\right).
\end{aligned}
\tag{A.3.11}
$$

We now do a further change of variables, inspired by sector decomposition. Let

$$
\begin{aligned}
p^+ &= \frac{\tau_N \xi}{s}, \\
p^- &= \tau_N \xi.
\end{aligned}
\tag{A.3.12}
$$

In terms of these variables, we find:

$$
S_{ij;i}^{\mathrm{bare},(1)}\left(\{k_i\}\right) = -\frac{\alpha_s(\mu)}{2\pi} \left(\frac{e^{\gamma_E}\mu^2 x_{ij}}{2}\right)^{\epsilon} \frac{\tau_N^{-1-2\epsilon}}{\Gamma(1-\epsilon)} \int_0^1 \mathrm{d}\xi \mathrm{d}s
$$

---

[11]Note that another common convention denotes the solid angle subtended by the d-dimensional sphere as Ω_{d+1} since the d-dimensional sphere is the full sphere that can be embedded in a $d+1$-dimensional space. We choose to denote this solid angle Ω_d. Both conventions are used in the literature, and should be noted carefully.

$$\times \, \xi^{-1-2\epsilon} s^{-1+\epsilon} \delta \left(1 - \xi\right) \prod_{m \neq i,j} \Theta \left(A_{ij;m}\left(s, \phi_{pm}\right) - s\right)$$

$$= -\frac{\alpha_s(\mu)}{2\pi} \left(\frac{e^{\gamma_E} \mu^2 x_{ij}}{2}\right)^{\epsilon} \frac{\tau_N^{-1-2\epsilon}}{\Gamma(1-\epsilon)} \int_0^1 \mathrm{d}s \, s^{-1+\epsilon} \prod_{m \neq i,j} \Theta \left(A_{ij;m}\left(s, \phi_{pm}\right) - s\right).$$

$$(\text{A.3.13})$$

The poles in ϵ now occur in the limits $\tau_N \to 0$ and $s \to 0$. An analytic integration is made more difficult by the theta functions keeping the contribution in the region around parton i. The poles can however be extracted through the use of plus distributions. For this purpose, we use the general expansion:

$$x^{-1+a\epsilon} = \frac{1}{a\epsilon} \delta(x) + \sum_{n=0} \frac{(a\epsilon)^n}{n!} \left[\frac{\Theta(x) \log^n x}{x}\right]_+ = \frac{1}{a\epsilon} \delta(x) + \sum_{n=0} \frac{(a\epsilon)^n}{n!} \mathcal{L}_n(x). \quad (\text{A.3.14})$$

Having performed this expansion, the coefficients in the Laurent expansion can now be integrated numerically.

For the contribution $S_{ij;k}^{\text{bare},(1)}$, it is more convenient to choose $m = k$ and $n = i$ in the parameterization of the phase space. Here we find, using the same change of variables:

$$S_{ki;j}^{\text{bare},(1)}\left(\{k_i\}\right) = -\frac{\alpha_s(\mu)}{2\pi} \left(\frac{e^{\gamma_E} \mu^2 x_{ij}}{2}\right)^{\epsilon} \left(\frac{x_{ij}}{x_{ki}}\right)^{1-\epsilon} \frac{\tau_N^{-1-2\epsilon}}{\Gamma(1-\epsilon)} \int_0^1 \mathrm{d}\xi \mathrm{d}s \mathrm{d}\phi$$

$$\times \, \xi^{-1-2\epsilon} s^{\epsilon} \frac{\sin^{-2\epsilon}\phi}{A_{ki;j}\left(x_{ki}, \phi_{pj}\right)} \delta\left(1-\xi\right) \prod_{m \neq i,k} \Theta\left(A_{ki;m}\left(x_{ki}, \phi_{pm}\right) - s\right)$$

$$= -\frac{\alpha_s(\mu)}{2\pi} \left(\frac{e^{\gamma_E} \mu^2 x_{ij}}{2}\right)^{\epsilon} \left(\frac{x_{ij}}{x_{ki}}\right)^{1-\epsilon} \frac{\tau_N^{-1-2\epsilon}}{\Gamma(1-\epsilon)} \int_0^1 \mathrm{d}s \mathrm{d}\phi$$

$$\times \, \frac{\sin^{-2\epsilon}\phi}{A_{ki;j}\left(x_{ki}, \phi_{pj}\right)} \prod_{m \neq i,k} \Theta\left(A_{ki;m}\left(x_{ki}, \phi_{pm}\right) - s\right). \qquad (\text{A.3.15})$$

Again, the poles in ϵ can be extracted by expanding out the $\tau_N^{-1-2\epsilon}$.

Upon renormalization, only the $\mathcal{O}\left(\epsilon^0\right)$ terms survive, and the sum of all possible contributions represents the soft function contribution to the integrated virtual subtraction terms. The calculations performed here agree with the results found in [225, 233].

The hard virtual contribution

The hard virtual contribution contains all finite effects from the full virtual diagrams. Such a calculation is, in general, performed by a one-loop provider specializing in quick and reliable evaluations of loop amplitudes, such as OPENLOOPS, RECOLA or BLACKHAT, all of which are natively supported in SHERPA. At NLO, the hard virtual contribution is not affected by the SCET coefficients and can thus be added on top of the soft-collinear pieces. There is however one caveat in doing this: most one-loop programs provide the IR-finite one-loop amplitudes after the subtraction of Catani's IR-divergent operator $\boldsymbol{I}(\epsilon)$. The SCET amplitudes used in this work are calculated in the $\overline{\text{MS}}$-scheme, and in order to have the correct matching between the SCET amplitudes and the one-loop contribution, we have to include a conversion term [234]:

$$
\mathbf{C}^{(0)} = \sum_{(i,j)} \frac{\mathbf{T}_i \cdot \mathbf{T}_j}{16} \left[\gamma^0_{\text{cusp}} \log^2 \frac{\mu^2}{-s_{ij}} - \frac{4\gamma^i}{C_i} \log \frac{\mu^2}{-s_{ij}} \right] - \frac{\pi^2}{96} \Gamma'_0, \tag{A.3.16}
$$

where $\gamma^0_{\text{cusp}} = 4$, $\gamma^q = -3C_F$, $\gamma^g = -\beta_0$, $\Gamma'_0 = -\gamma^0_{\text{cusp}} \sum_i C_i$ and μ is the renormalization scale. As this term depends on the colours of the partons in the process, it is in practice most simply included in the calculation of the soft function.

A.3.3 Results

In this section, we present results for the implementation of the *N*-Jettiness slicing at NLO. In the results presented here, we will consider the full cross section at NLO including the Born cross section.

A.3.4 $e^+e^- \to 2\,\text{jets}$

The production of two jets in e^+e^--collisions provides a good testing ground for the components of the calculation, in particular those of the quark jet functions. The soft function is completely fixed, since the kinematics of the final state is completely

Figure A.1: Plot of the contributions above, in blue, and below, in green, the
N-Jettiness slicing cut in the process $e^+e^- \to 2\,\text{jets}$. The red line
denotes their sum, while the cyan band corresponds to the NLO
cross section calculated using Catani-Seymour dipole subtraction.
The quadratic dependence on the cut parameter is visible in the
separate contribution and their cancellation in the sum is clear. The
two predictions for the total cross section are barely distinguishable.
A close-up of this region can be found in Figure A.2.

fixed. To the best of our knowledge, no public implementation of this process using

N-Jettiness phase space slicing is available, but a componentwise comparison with

Sherpa's Catani-Seymour method is possible.

Throughout this section, we consider the process $e^+e^- \to 2\,\text{jets}$ at a centre of

mass energy of 91.2 GeV. In Figure A.1, we show the contribution above the cut,

$\sigma\left(\tau_N > \tau_{N,\text{cut}}\right)$, the integrated contributions below the cut, $\sigma^{\text{sing}}\left(\tau_{N,\text{cut}}\right)$, and their

sum. Overlaid is the total cross section at NLO found using Catani-Seymour dipole

subtraction, in its default setup, i.e. using $\alpha_{\text{dip}} = 1$ and $\alpha_{\text{min}} = 10^{-9}$. Clearly

visible is the strong cancellation between the large positive contribution from the
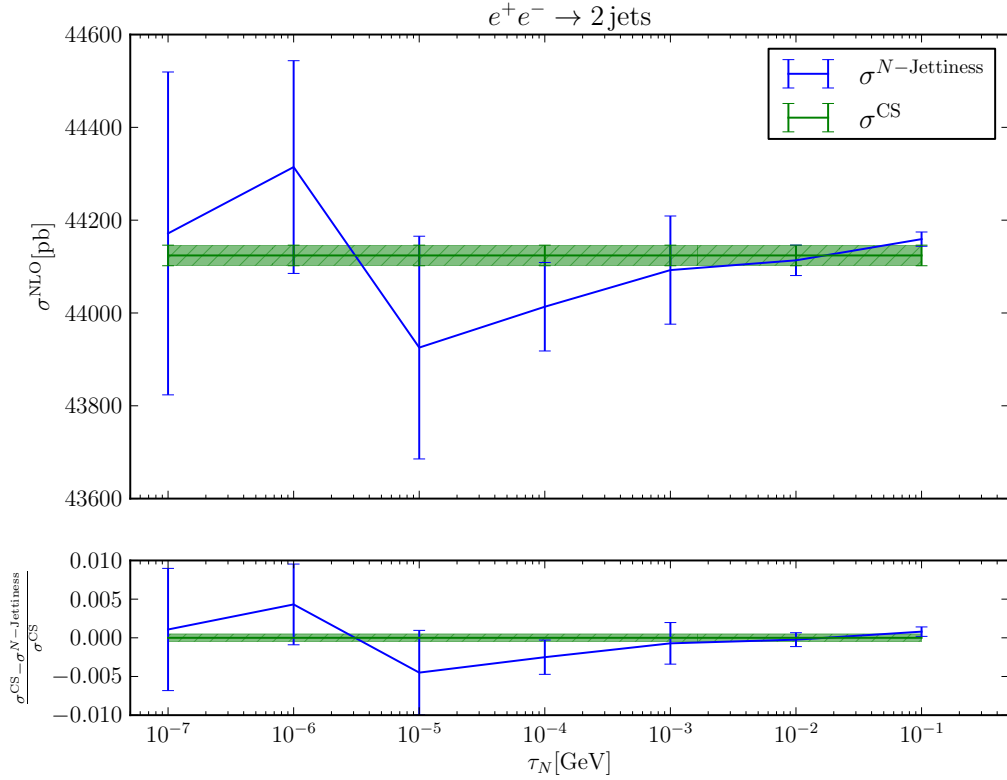
Figure A.2: Close-up of Figure A.1 in the region of the total cross section. The error bars and envelope denote the statistical uncertainty of the integration. The cross sections from the two different methods are found to agree within statistical uncertainties, as evidenced also by the ratio plot in the lower panel.

contribution above the cut and the large negative contribution due to the integrated terms below the cut. In Figure A.2, we zoom into the region of the total cross section. We observe that the NLO cross section found from *N*-Jettiness phase space slicing, $\sigma^{N-\text{Jettiness}}$, agrees with the result from Catani-Seymour subtraction, σ^{CS}, within the statistical uncertainties of the integration. For large values of the cut we can see a mild deviation starting to appear between the result from the slicing and the subtraction, which may be the first indication that power corrections become important in this region.

The integration time for a full *N*-Jettiness calculation is significantly larger than the time taken with Catani-Seymour subraction. All parameters being equal, the integration of the cross section for one particular value of $\tau_{N,\text{cut}}$ takes about as long as

for Catani-Seymour subtraction. This calculation has to repeated a number of times, however, in order to establish the independence of $\tau_{N,\text{cut}}$ and the convergence of the cross section. An N-Jettiness calculation thus needs significantly more resources for the same calculation.

The integration performance is worse overall in the slicing method, which is unsurprising as the slicing, being entirely non-local, suffers from significantly larger cancellations than a local subtraction method such as Catani-Seymour dipole subtraction. Moreover, the fluctuating behaviour of the cross section at low cuts suggests that the quoted statistical uncertainty may be underestimating the true error. Further fluctuation is observed upon changing parameters of the integration, e.g. the number of phase space points in each optimization step, also suggesting that the quoted uncertainty may be underestimating the true error. We will comment on this point in more detail for the process $e^+e^- \rightarrow 3\,\text{jets}$, where this effect is more pronounced. It should be noted that custom scale variations applied to the Catani-Seymour calculation give residual uncertainties of the order of the statistical uncertainty in the N-Jettiness calculation. This does not however alleviate the difficulty of finding a central value from the N-Jettiness method.

Comparison with Catani-Seymour ingredients

As mentioned before, if instead of normalizing N-Jettiness by $Q_i = 2E_i$, we choose to normalize by $Q_i = E_{\text{CMS}}^2$, 2-Jettiness in e^+e^--collisions reproduces the Catani-Seymour variable $y_{ij,k}$. We can then directly compare the two implementations if we set both α_{min}, the technical cutoff below which the real and subtracted contributions are assumed to cancel, and α_{dip}, the parameter restricting the phase space over which the subtraction terms are integrated, equal to the N-Jettiness cut $\tau_{N,\text{cut}}$. The implementation of the Catani-Seymour method in Sherpa is completely independent from the N-Jettiness implementation presented here. The comparison of these two methods is thus a highly non-trivial check of our implementation.
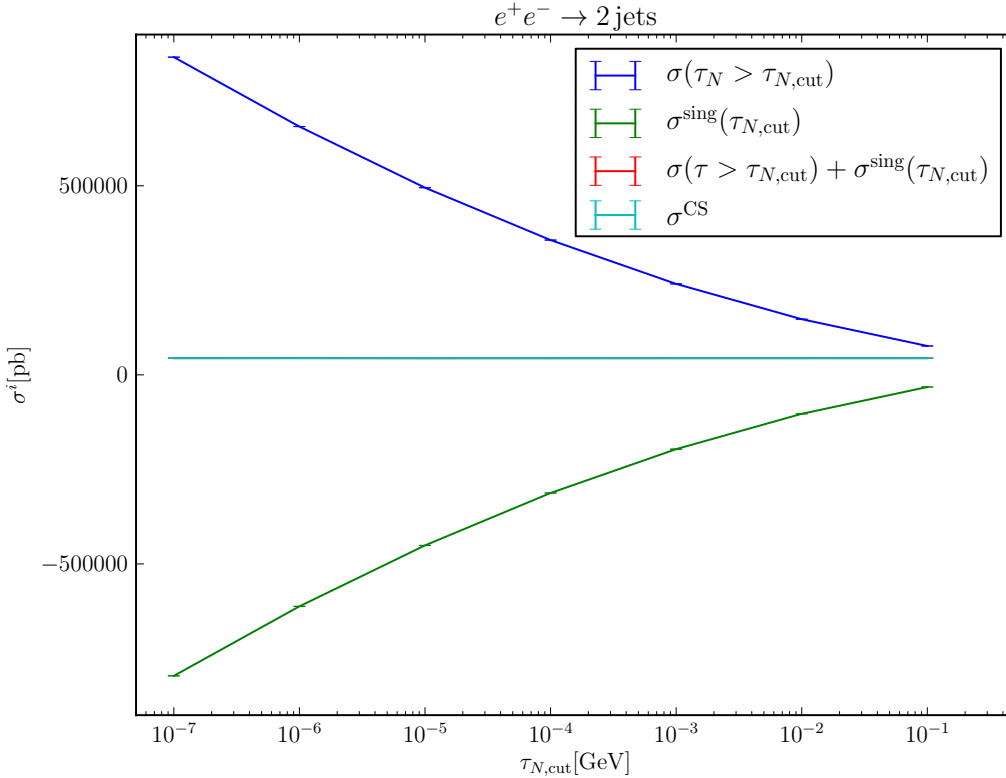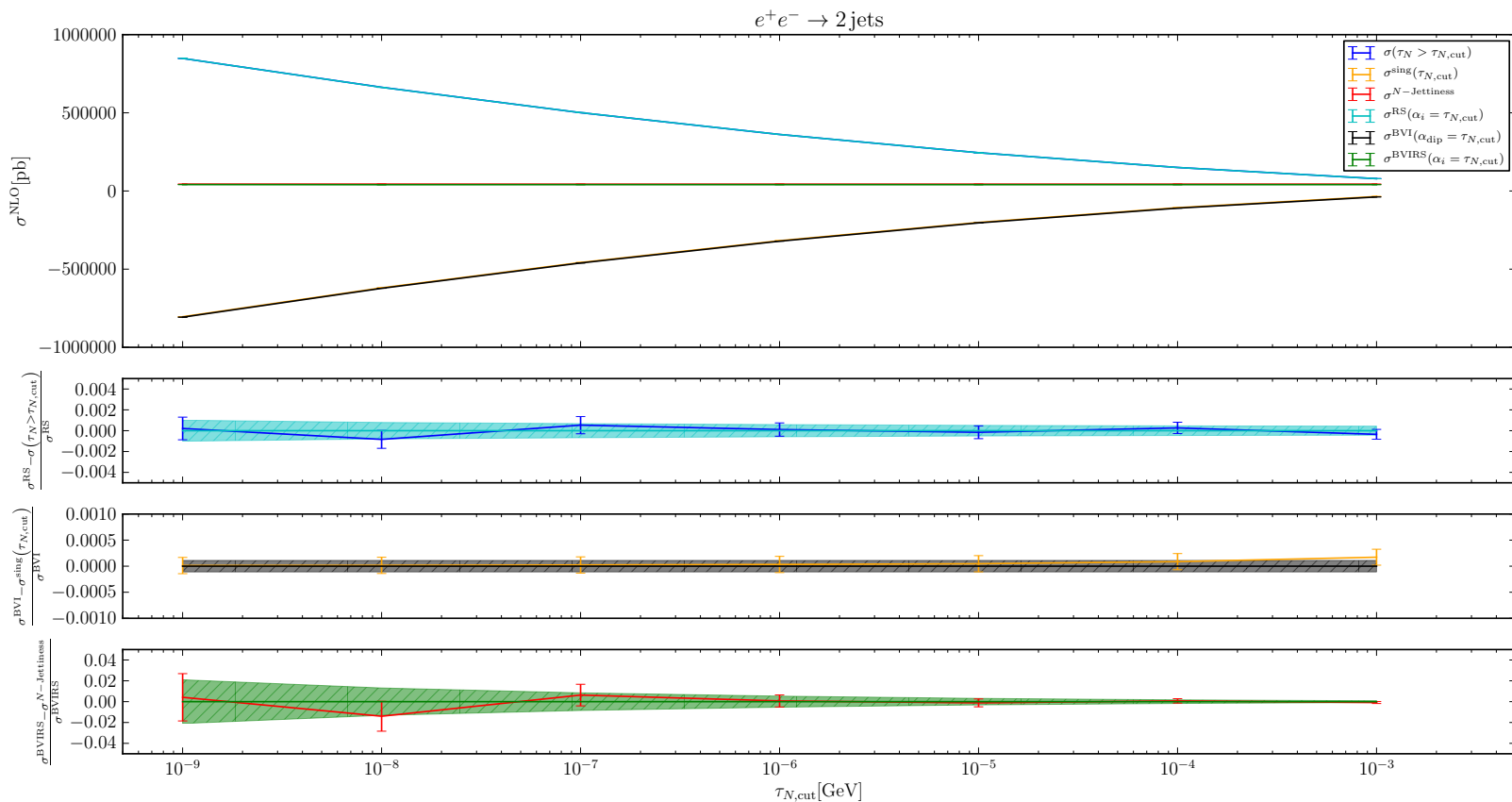
Figure A.3: Plot of the contributions above, in blue, and below, in orange, the *N*-Jettiness slicing cut in the process $e^+e^- \to 2\,\text{jets}$, using $Q_i = Q^2$. The red line denotes their sum. Also shown are the RS contributions, in cyan, and the BVI contribution, in black, in the Catani-Seymour subtraction method with $\alpha_{\text{dip}} = \alpha_{\text{min}} = \tau_{N,\text{cut}}$. Their sum is given by the green line. The differences normalized with respect to the respective result from the CS method, are shown in the panes below the main plot. Both the separate contributions and their sum are found to agree within the statistical uncertainty for low enough values of $\tau_{N,\text{cut}}$.

We run the same setup as before and show the results in Fig. A.3. For low values of the cut parameter, we observe very good agreement between the two methods, while for large values (with this normalization, $\tau_N \in [0, 1]$) we start to see very mild deviations in the behaviour between the two methods. These deviations are due to the inclusion of different finite terms at different stages of the procedures.

A.3.5 $e^+ e^- \to 3\,\text{jets}$

The calculation of the cross section for $e^+ e^- \to 3\,\text{jets}$ is the first calculation we present that contains a non-trivial soft function. In addition, this process contains for the first time a gluon jet at Born level, thus allowing us to test the gluon jet function.

We again consider $e^+ e^-$-collisions at a centre of mass energy of 91.2 GeV. In order to define the 3 jets at the Born level, we use FASTJET's implementation of the k_T-algorithm to require at least 3 jets with $k_T > 15\,\text{GeV}$ and radius parameter $dR = 0.4$. In Figure A.4, we show the separate contributions in the slicing together with their sum and the result obtained using Catani-Seymour subtraction. In Figure A.5, we zoom in on the sum of the contributions. We observe here that while the dependence on the cut parameter mostly cancels, we still find a mild dependence on the cut for high values of $\tau_{N,\text{cut}}$. In addition, we find a discrepancy with the result from Catani-Seymour subtraction. This example illustrates one of the main difficulties of phase space slicing methods: finding a plateau in the dependence on the cut parameter is paramount, as the region of high cut parameters is affected by the onset of power corrections, while regions of low cut parameters are plagued by numerical miscancellations and thus bad integration performance. There is, however, no guidance from the theory to suggest where this plateau lies, and when it is safe to say that the integration has converged to the true cross section. A reliable implementation would thus require the calculation of the cross section for a large number of cuts and a subsequent fit to establish the stability and accuracy of the

Figure A.4: Plot of the contributions above, in blue, and below, in green, the N-Jettiness slicing cut in the process $e^+e^- \to 3\,\mathrm{jets}$. The red line denotes their sum, while the cyan band corresponds to the NLO cross section calculated using Catani-Seymour dipole subtraction. The two predictions for the total cross section are barely distinguishable. A close-up of this region can be found in Figure A.5.

result.

Echoing a statement from the process $e^+e^- \to 2\,\mathrm{jets}$, we show in Figure A.6 the variation of the integrated cross section found upon varying parameters of the integration. SHERPA uses adaptive integration based on the VEGAS algorithm [235]. Both the target integration error as well as the number of evaluated phase space points per optimization cycle can be adjusted. An appropriate increase in the latter may be necessary to ensure that the entirety of the phase space is covered and optimized for. This becomes more important the more complex the integrand structure is, i.e. the more possibilities there are for particles to go unresolved. In Figure A.6, we fix $\tau_{N,\mathrm{cut}} = 10^{-5}\,\mathrm{GeV}$ and, for definiteness, $\sigma^{\mathrm{sing}}\left(\tau_{N,\mathrm{cut}}\right) = -132029 \pm 40.8939\,\mathrm{pb}$. We then vary the number of phase space points evaluated per optimization step
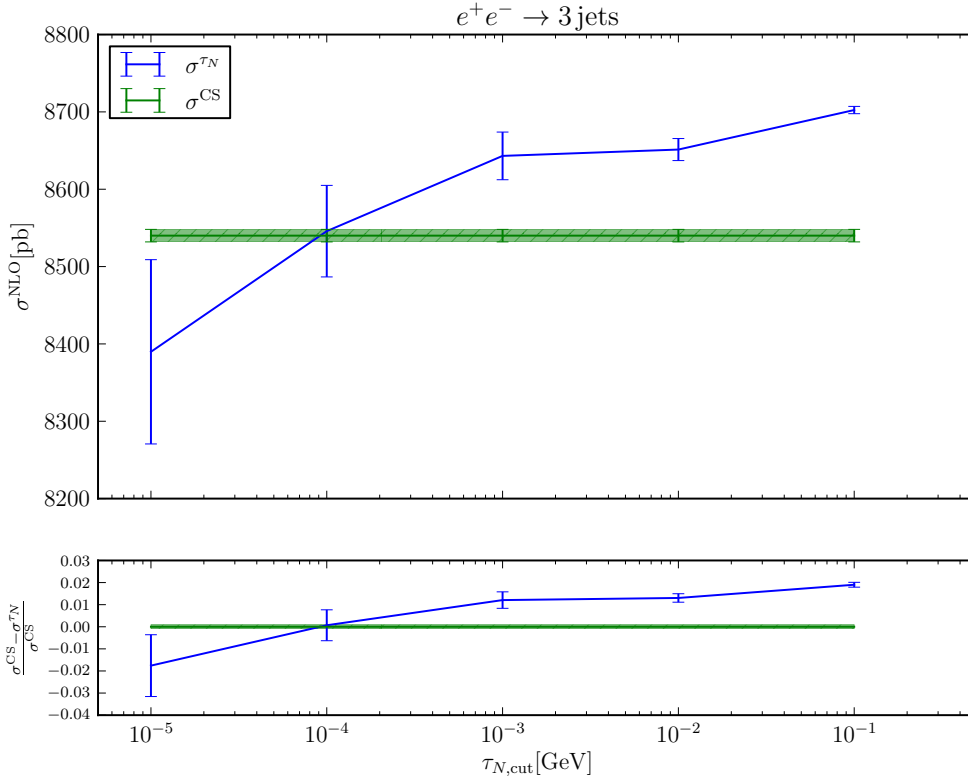
Figure A.5: Close-up of Figure A.4 in the region of the total cross section. There
is a small difference between the cross section found from the slicing
and the subtraction methods. Also visible is a possible dependence
on the cut parameter for high values of $\tau_{N,\text{cut}}$.

in $\sigma\left(\tau_N > \tau_{N,\text{cut}}\right)$. We find that while the results of the integrations agree within
their uncertainties, the mean value fluctuates significantly. This can be traced to the
behaviour of the above-the-cut contributions, which tend to have a larger associated
error. When the below- and above-the-cut contributions are summed, the fluctuation
of the mean value of the total cross section can become problematic. Because of
the large cancellations between the two contributions, a simple combination of the
statistical uncertainties of the two contributions underestimates the uncertainty of
the sum. Conversely, this means that in order to achieve uncertainties equivalent
to those in Catani-Seymour subtraction, the components of the slicing calculation
have to be performed to higher accuracy, thus leading to a significant increase in the
amount of resources needed.
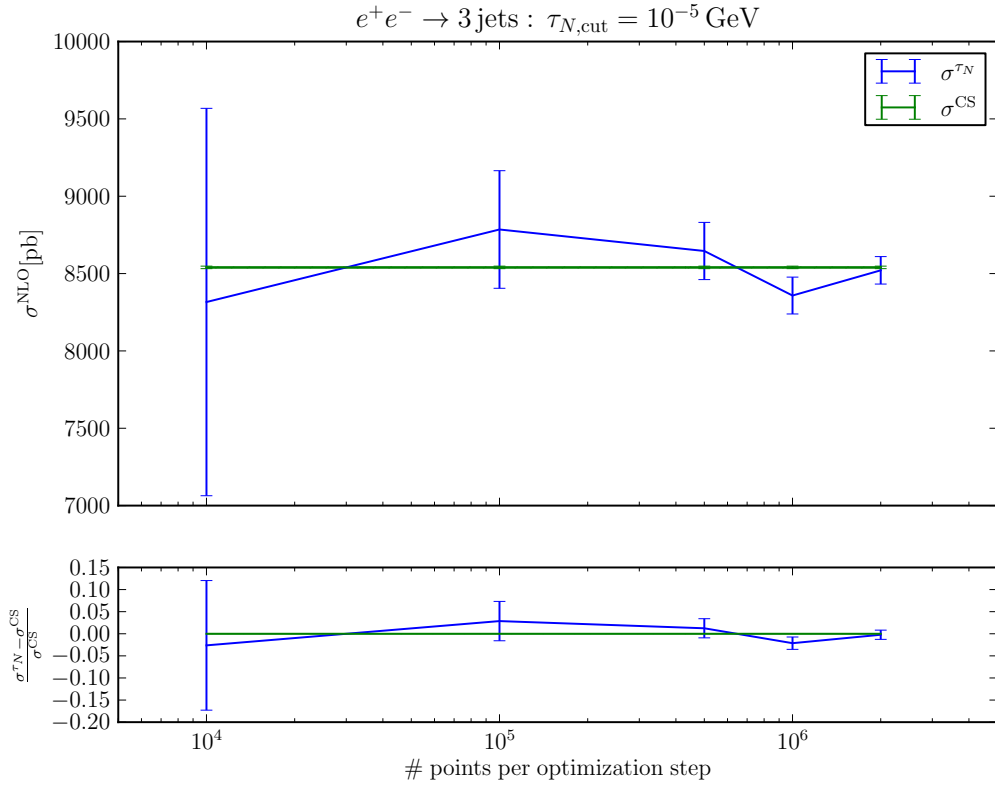
Figure A.6: Variation of the total integrated cross section σ^{τ_N} for the process $e^+e^- \to 3\,\text{jets}$ with the number of phase space points used per optimization step in the integration of the above-the-cut contribution. $\tau_{N,\text{cut}} = 10^{-5}\,\text{GeV}$ and $\sigma^{\text{sing}}(\tau_{N,\text{cut}}) = -132029 \pm 40.8939\,\text{pb}$ have been fixed.

A.3.6 Drell-Yan

Our next process is the Drell-Yan process, $pp \to \gamma^*/Z \to l^+l^-$. For this case, all terms in the integrated virtual contributions can be written analytically, making it an ideal testbed for the ingredients of the quark beam function and the main contribution to the soft function. In addition, there is a publicly available implementation of this process as part of the parton-level Monte Carlo program MCFM [82].

In the setups used in this section, we consider the process $pp \to e^+e^-$ at the 13 TeV LHC, with the restriction that the dilepton invariant mass be in the range $m_{ll} \in [50, 150]\,\text{GeV}$. In Figure A.7, we show the contribution above the cut, $\sigma(\tau_N > \tau_{N,\text{cut}})$, the integrated contributions below the cut, $\sigma^{\text{sing}}(\tau_{N,\text{cut}})$, and their sum. Overlaid is the total cross section at NLO found using Catani-Seymour dipole subtraction, in its
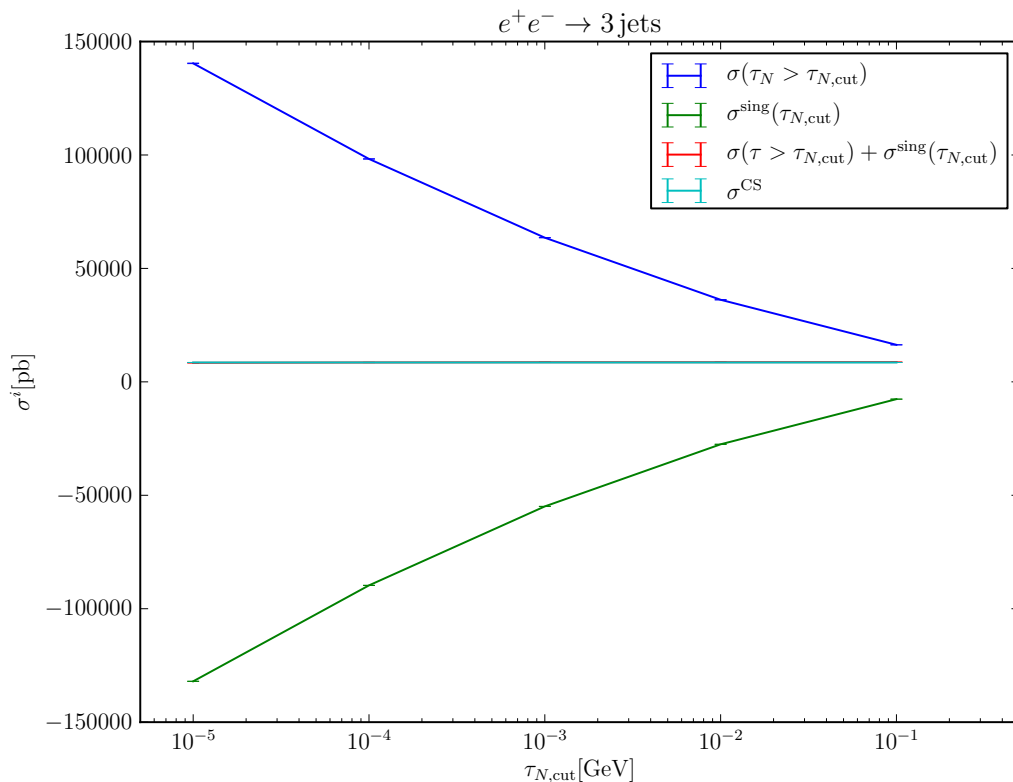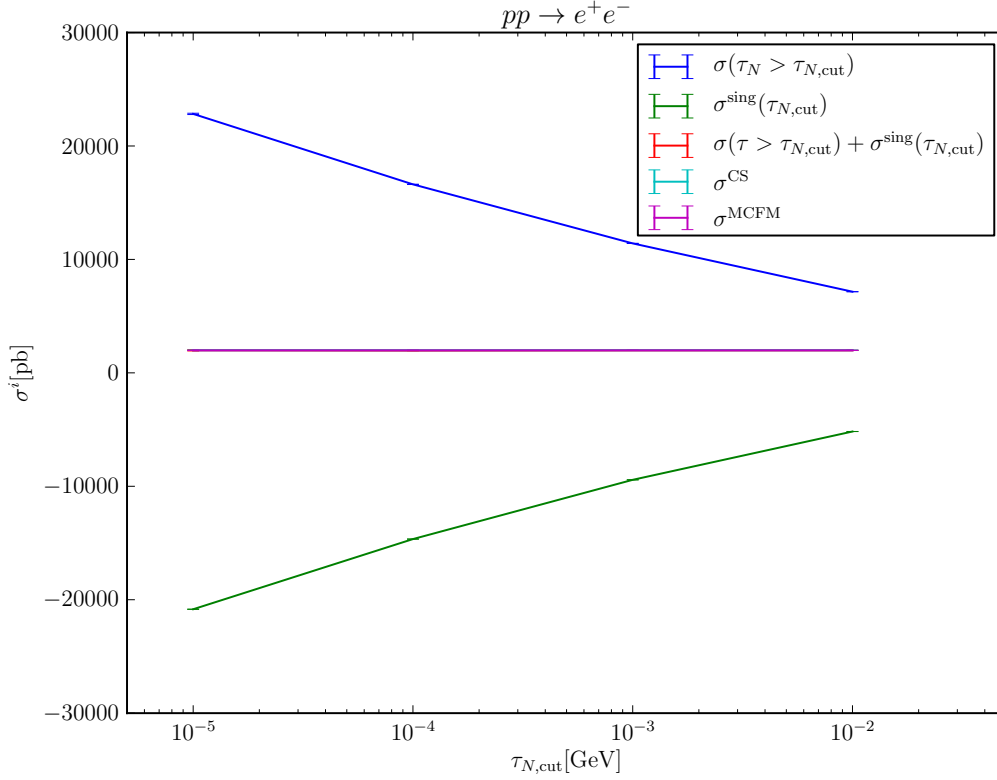
Figure A.7: Plot of the contributions above, in blue, and below, in green, the
N-Jettiness slicing cut in the process $pp \to e^+e^-$. The red line
denotes their sum, while the cyan band corresponds to the NLO
cross section calculated using Catani-Seymour dipole subtraction,
and the purple line is the result obtained from using MCFM. These
three lines are barely distinguishable, and we provide a close-up of
this region in Figure A.8.

default setup, as well as the result obtained using an implementation within MCFM.
For the plots in this section, we do not include the hard virtual contributions, which
do not affect the dependence on the cut parameter. In Figure A.8, we zoom into the
region of the total cross section. We observe a small constant difference of about 1%
between the result found from the slicing in comparison with the Catani-Seymour
result, while our slicing agrees with the result found using MCFM's implementation.
Unlike the case of jet production at an electron positron collider, we do not find a
systematic deviation for large values of the cut parameter. Just as in that case, we
observe poor integration performance at low values of the cut parameter.
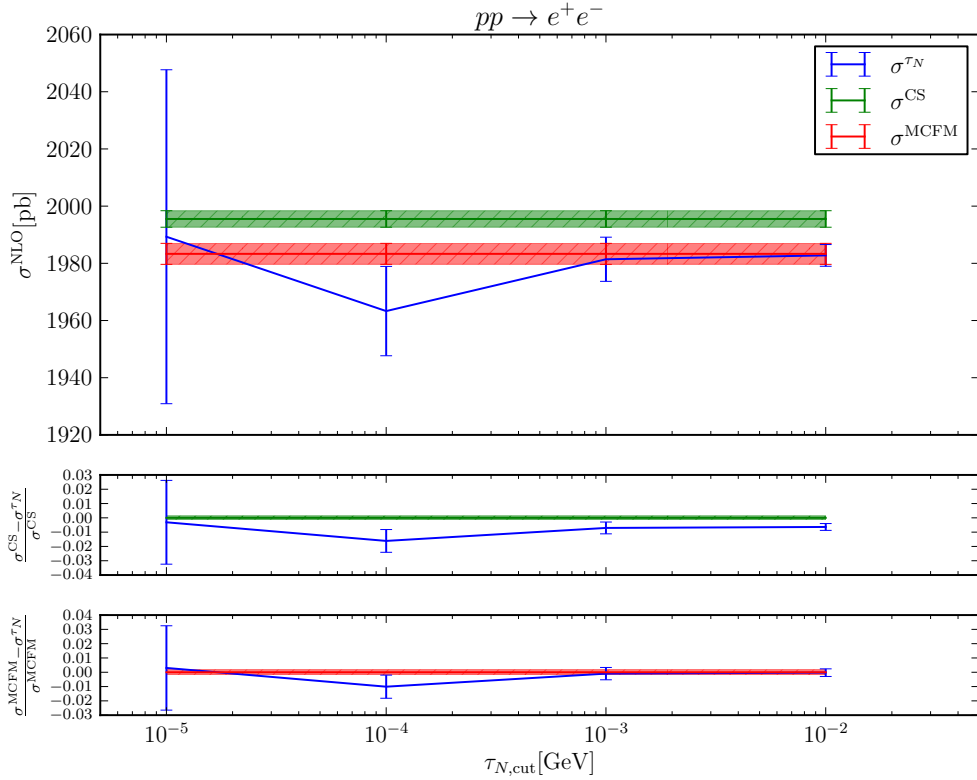
Figure A.8: Close-up of Figure A.7 in the region of the total cross section. The cross sections from the two different methods are found to differ by about 1%. However, the two phase space slicing implementations agree within statistical uncertainties.

A.3.7 Drell-Yan + 1 jet

The production of a weak neutral boson in association with one additional jet is the first non-trivial LHC process we consider in which the soft function cannot be written analytically. In addition, this is the first LHC process that includes contributions from a jet function.

In this section, we consider the process $pp \to e^+e^-j$ at the 13 TeV LHC, requiring as before that the dilepton invariant mass be in the range $m_{ll} \in [50, 150]$ GeV and additionally at least one k_T-jet with radius parameter $dR = 0.4$ and $k_T > 30$ GeV. In Figure A.9, we show the contributions to the sum giving the total cross section shown in red, and Figure A.10 shows a close-up of this result. We find the result to be independent of the cut parameter within the statistical uncertainties of the
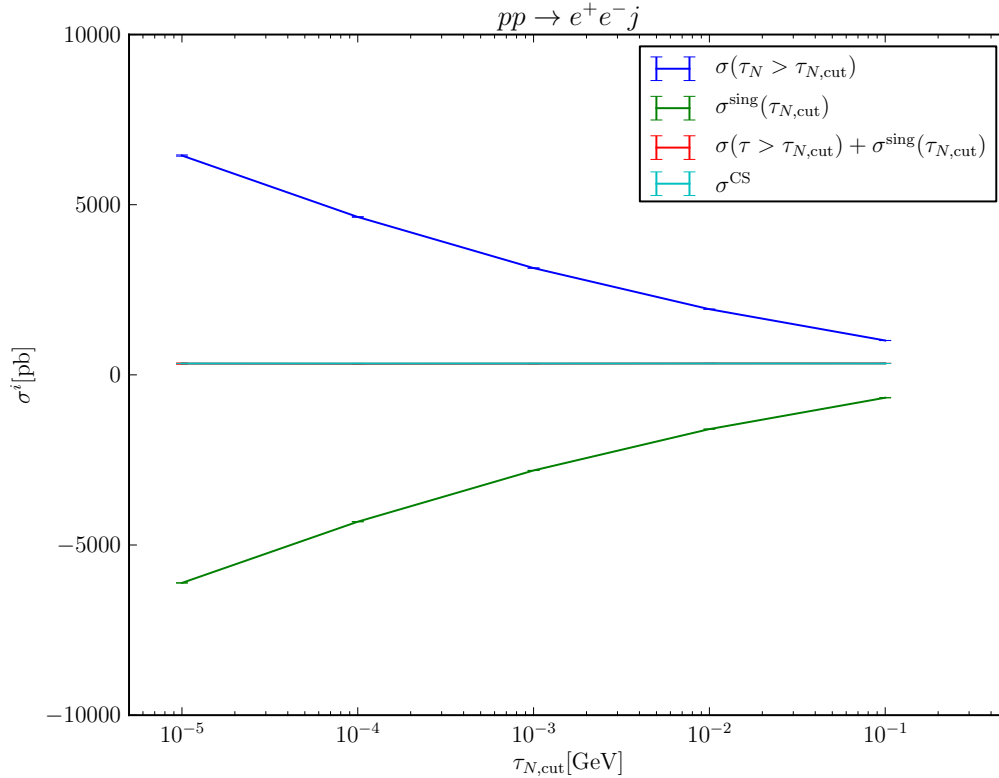
Figure A.9: Plot of the contributions above, in blue, and below, in green, the
N-Jettiness slicing cut in the process $pp \to e^+e^-j$. The red line
denotes their sum, while the cyan band corresponds to the NLO cross
section calculated using Catani-Seymour dipole subtraction. The
two predictions for the total cross section are barely distinguishable.
A close-up of this region can be found in Figure A.10.

integration, without the observable deviation for high values of the cut as we observed
in $e^+e^- \to 3$ jets. This may be due to the fact that in the case of Drell-Yan processes
with additional jets, at least two of the *N*-Jettiness jet directions, the beam directions,
are fixed while in e^+e^- collisions none of the jet directions are fixed. The agreement
with the value obtained from the Catani-Seymour method is good, although the
integration performance of the slicing is significantly worse.

A.3.8   NNLO

In the previous section, we presented an implementation of the *N*-Jettiness phase
space slicing method at NLO QCD accuracy. We found it difficult to establish
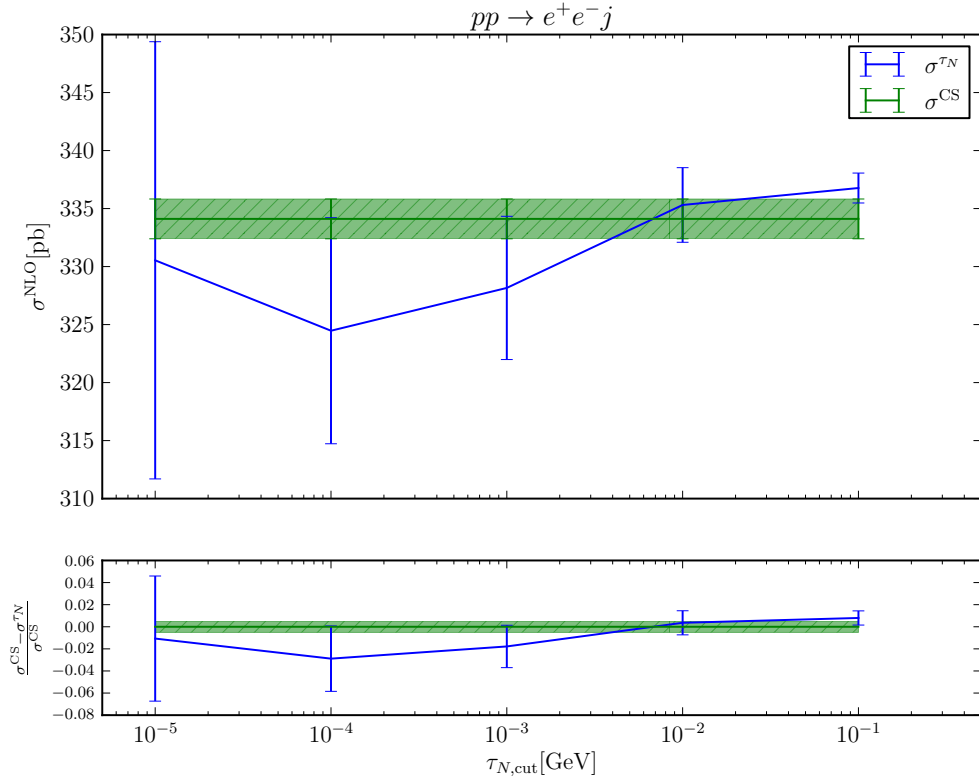
Figure A.10: Close-up of Figure A.9 in the region of the total cross section. The cross sections found from the subtraction and slicing methods agree within the statistical uncertainties of the integration.

the convergence of the integration and thereby also the correctness of the results. In particular, for a relatively simple process such as $e^+e^- \to 3$ jets we cannot be wholly confident that we arrive at a stable result with respect to variations in the cut parameter $\tau_{N,\text{cut}}$.

At NNLO, the components of the calculation become more complex. The above-the-cut contribution is now a NLO calculation of the process with an additional jet, subject to a cut $\tau_N > \tau_{N,\text{cut}}$. This calculation can be performed within the SHERPA framework using Catani-Seymour subtraction and the algorithms described in Section A.1.4 to calculate the value of N-Jettiness both for a single emitted parton and for two additional partons. The cut on N-Jettiness provides the separation between the 0- and 1-jet contributions, and thus no extra jet algorithm is required to define this process.

Below the cut, the contribution takes on the form described in Section A.2.2. This contribution contains hard two-loop contributions, two-loop SCET contributions and the interference of one-loop SCET contributions with both hard one-loop corrections and other one-loop SCET contributions. The latter also require the coefficients $\mathcal{C}_n^{(1)}$ with $n \neq -1$, which were not needed for the pure NLO phase space slicing. All contributions, apart from the hard two-loop corrections, which would have to be taken from an external provider, and the finite parts of the two-loop soft function, have been implemented within SHERPA and are thus in principle ready for testing. The finite parts of the two-loop soft function can be calculated in a similar manner to the NLO soft function, now integrating all soft two-loop currents as described in [236, 237]. Details of this procedure can be found in [225], and a move towards calculating any soft function numerically has recently been proposed in [238]. Since we expect the numerical issues observed at NLO to worsen at NNLO, the implementation in SHERPA was not completed.

A.4 Ingredients for N-Jettiness calculations

In this appendix, we collect all ingredients necessary for the calculation of the contributions below the cut in N-Jettiness phase space slicing.

A.4.1 QCD related functions

In the following, C_A and C_F denote the Casimir operators in the adjoint and fundamental representations, T_R the normalization of the trace of two fundamental operators and n_f the number of light quark flavours. For the case of $SU(3)$, they are $C_A = 3$, $C_F = 4/3$, $T_R = 1/2$, and in this work we work with $n_f = 5$ active flavours. Further, $\zeta_3 = \zeta(3) \approx 1.2020569031595942854$ is the value of the Riemann zeta function $\zeta(z)$ evaluated at $z = 3$.

The running of the coupling constant α_s is governed by the QCD beta function, following

$$\mu \frac{\mathrm{d}}{\mathrm{d}\mu} \alpha_s(\mu) = \beta \left[\alpha_s(\mu) \right], \tag{A.4.1}$$

and the beta function can itself be expanded in terms of α_s as:

$$\beta \left(\alpha_s \right) = -2\alpha_s \sum_{n=0}^{\infty} \beta_n \left(\frac{\alpha_s}{4\pi} \right)^{n+1}. \tag{A.4.2}$$

For the calculations in this work, we require the first two coefficients in this expansion, which read in the $\overline{\mathrm{MS}}$ scheme:

$$\begin{aligned} \beta_0 &= \frac{11}{3} C_A - \frac{4}{3} T_R n_{\mathrm{f}}, \\ \beta_1 &= \frac{34}{3} C_A{}^2 - \left(\frac{20}{3} C_A + 4C_F \right) T_R n_f. \end{aligned} \tag{A.4.3}$$

The cusp and noncusp anomalous dimensions are also expanded in α_s:

$$\Gamma_{\mathrm{cusp}} \left(\alpha_s \right) = \sum_{n=0}^{\infty} \Gamma_n \left(\frac{\alpha_s}{4\pi} \right)^{n+1}, \tag{A.4.4}$$

$$\gamma_F^i \left(\alpha_s \right) = \sum_{n=0}^{\infty} \gamma_{Fn}^i \left(\frac{\alpha_s}{4\pi} \right)^{n+1}. \tag{A.4.5}$$

The coefficients of the cusp anomalous dimension read as follows:

$$\Gamma_n^i = C_i \Gamma_n,$$

$$\Gamma_0 = 4, \tag{A.4.6}$$

$$\Gamma_1 = 4 \left[C_A \left(\frac{67}{9} - \frac{\pi^2}{3} \right) - \frac{20}{9} T_R n_{\mathrm{f}} \right] = \frac{4}{3} \left[C_A \left(4 - \pi^2 \right) + 5\beta_0 \right].$$

The coefficients of the noncusp anomalous dimension in $\overline{\mathrm{MS}}$ read for quark jet and beam functions:

$$\gamma_{J0}^q = \gamma_{B0}^q = 6C_F,$$

$$\gamma_{J1}^q = \gamma_{B1}^q = C_F \left[C_A \left(\frac{146}{9} - 80\zeta_3 \right) + C_F \left(3 - 4\pi^2 + 48\zeta_3 \right) + \beta_0 \left(\frac{121}{9} + \frac{2\pi^2}{3} \right) \right].$$

$$\tag{A.4.7}$$

For the gluon jet and beam functions, we have:

$$\gamma_{J0}^g = \gamma_{B0}^g = 6C_A,$$

$$\gamma_{J1}^g = \gamma_{B1}^g = C_A \left[C_A \left(\frac{182}{9} - 32\zeta_3 \right) + \beta_0 \left(\frac{94}{9} - \frac{2\pi^2}{3} \right) \right] + 2\beta_1. \tag{A.4.8}$$

A.4.2 Jet function

The expansion of the jet functions $i \in \{q, g\}$ is written as:

$$J_i(s, \mu) = \sum_{n=0}^{\infty} \left(\frac{\alpha_s}{4\pi} \right)^n J_i^{(n)}(s, \mu). \tag{A.4.9}$$

The coefficients take the form:

$$J_i^{(m)}(s, \mu) = J_{i,-1}^{(m)} \delta(s) + \sum_{n \geq 0}^{2m-1} J_{i,n}^{(m)} \frac{1}{\mu^2} \mathcal{L}_n \left(\frac{s}{\mu^2} \right), \tag{A.4.10}$$

with the plus distributions $\mathcal{L}_n$. If we rescale these coefficients, we get:

$$J_i^{(m)}(Q_i k_i, \mu) = \frac{1}{Q_i} J_{i,-1}^{(m)} \left(\frac{Q_i \xi}{\mu^2} \right) \delta(k_i) + \frac{1}{Q_i} \sum_{n=0}^{2m-1} J_{i,n}^{(m)} \left(\frac{Q_i \xi}{\mu^2} \right) \frac{1}{\xi} \mathcal{L}_n \left(\frac{k_i}{\xi} \right),$$

$$J_{i,-1}^{(m)}(\lambda) = J_{i,-1}^{(m)} + \sum_{n=0}^{2m-1} J_{i,n}^{(m)} \frac{\ln^{n+1} \lambda}{n+1}, \tag{A.4.11}$$

$$J_{i,n}^{(m)}(\lambda) = J_{i,n}^{(m)} + \sum_{k=1}^{2m-1-n} \frac{(n+k)!}{n!k!} J_{i,n+k}^{(m)} \ln^k \lambda.$$

The dimension-one parameter ξ is arbitrary and can be chosen at our convenience as it cancels between the different coefficients. The coefficients $J_{i,n}^{(m)}(\lambda)$ are the terms that appear in the below the cut contributions in Section A.2.2. For pure slicing, only $J_{i,-1}^{(m)}(\lambda)$ is relevant.

The coefficients needed up to NNLO read:

$$J_{i,1}^{(1)} = \Gamma_0^i,$$

$$J_{i,0}^{(1)} = -\frac{\gamma_{J0}^i}{2},$$

$$J_{i,3}^{(2)} = \frac{(\Gamma_0^i)^2}{2},$$

$$J_{i,2}^{(2)} = -\frac{\Gamma_0^i}{2}\left(\frac{3\gamma_{J0}^i}{2} + \beta_0\right),$$

$$J_{i,1}^{(2)} = \Gamma_1^i - \left(\Gamma_0^i\right)^2\frac{\pi^2}{6} + \frac{\gamma_{J0}^i}{2}\left(\frac{\gamma_{J0}^i}{2} + \beta_0\right) + \Gamma_0^i J_{i,-1}^{(1)},$$

$$J_{i,0}^{(2)} = \left(\Gamma_0^i\right)^2\zeta_3 + \Gamma_0^i\gamma_{J0}^i\frac{\pi^2}{12} - \frac{\gamma_{J1}^i}{2} - \left(\frac{\gamma_{J0}^i}{2} + \beta_0\right)J_{i,-1}^{(1)}. \tag{A.4.12}$$

The coefficients multiplying $\delta(s)$ differ for quark and gluon jet functions. For quarks, we have:

$$J_{q,-1}^{(0)} = 1,$$

$$J_{q,-1}^{(1)} = C_F\left(7 - \pi^2\right),$$

$$J_{q,-1}^{(2)} = C_F\left[C_F\left(\frac{205}{8} - \frac{67\pi^2}{6} + \frac{14\pi^4}{15} - 18\zeta_3\right) + C_A\left(\frac{1417}{108} - \frac{7\pi^2}{9} - \frac{17\pi^4}{180} - 18\zeta_3\right)\right.$$
$$\left. + \beta_0\left(\frac{4057}{216} - \frac{17\pi^2}{9} - \frac{4\zeta_3}{3}\right)\right]. \tag{A.4.13}$$

For gluon jets, the coefficients read:

$$J_{g,-1}^{(0)} = 1,$$

$$J_{g,-1}^{(1)} = C_A\left(\frac{4}{3} - \pi^2\right) + \frac{5}{3}\beta_0,$$

$$J_{g,-1}^{(2)} = C_A^2\left(\frac{4255}{108} - \frac{26\pi^2}{9} + \frac{151\pi^4}{180} - 72\zeta_3\right) + C_A\beta_0\left(-\frac{115}{108} - \frac{65\pi^2}{18} + \frac{56\zeta_3}{3}\right)$$
$$+ \beta_0^2\left(\frac{25}{9} - \frac{\pi^2}{3}\right) + \beta_1\left(\frac{55}{12} - 4\zeta_3\right). \tag{A.4.14}$$

A.4.3   Beam function

The beam function is defined as

$$B_i(t, x, \mu) = \sum_j \int \frac{\mathrm{d}z}{z} \mathcal{I}_{ij}(t, z, \mu, \mu_F) f_j\left(\frac{x}{z}, \mu_F\right), \qquad (A.4.15)$$

containing the usual PDFs $f_j(x, \mu_F)$ and the perturbative matching coefficients $\mathcal{I}_{ij}(t, z, \mu, \mu_F)$. The dependence on the factorization scale μ_F is explicit here, but cancels between the coefficients and the PDFs such that the beam function is independent of this scale[12].

The matching coefficients are expanded as:

$$\mathcal{I}_{ij}(t, z, \mu, \mu_F) = \sum_{n=0}^{\infty} \mathcal{I}_{ij}^{(n)}(t, z, \mu, \mu_F) \left(\frac{\alpha_s}{4\pi}\right)^n. \qquad (A.4.16)$$

These coefficients have the structure

$$\mathcal{I}_{ij}^{(m)}(t, z, \mu, \mu_F) = \mathcal{I}_{ij,-1}^{(m)}\left(z, \frac{\mu^2}{\mu_F^2}\right) \delta(t) + \sum_{n=0}^{2m-1} \mathcal{I}_{ij,n}^{(m)}\left(z, \frac{\mu^2}{\mu_F^2}\right) \frac{1}{\mu^2} \mathcal{L}_n\left(\frac{t}{\mu^2}\right). \quad (A.4.17)$$

Upon rescaling these coefficients, we obtain:

$$\begin{aligned}
\mathcal{I}_{ij}^{(m)}(Qk, z, \mu, \mu_F) =& \frac{1}{Q} \mathcal{I}_{ij,-1}^{(m)}\left(z, \frac{\mu^2}{\mu_F^2}, \frac{Q\xi}{\mu^2}\right) \delta(k) \\
&+ \frac{1}{Q} \sum_{n=0}^{2m-1} \mathcal{I}_{ij,n}^{(m)}\left(z, \frac{\mu^2}{\mu_F^2}, \frac{Q\xi}{\mu^2}\right) \frac{1}{\xi} \mathcal{L}_n\left(\frac{k}{\xi}\right), \\
\mathcal{I}_{ij,-1}^{(m)}(z, \lambda_F, \lambda) =& \mathcal{I}_{ij,-1}^{(m)}(z, \lambda_F) + \sum_{n=0}^{2m-1} \mathcal{I}_{ij,n}^{(m)}(z, \lambda_F) \frac{\ln^{n+1}\lambda}{n+1}, \qquad (A.4.18) \\
\mathcal{I}_{ij,n}^{(m)}(z, \lambda_F, \lambda) =& \mathcal{I}_{ij,n}^{(m)}(z, \lambda_F) + \sum_{k=0}^{2m-1-n} \mathcal{I}_{ij,n+k}^{(m)}(z, \lambda_F) \frac{(n+k)! \ln^k \lambda}{n! k!}.
\end{aligned}$$

Just as in the case of the jet function, the parameter ξ is arbitrary and cancels between the coefficients. Using these coefficients, the beam function coefficients used in Appendix A.2.2 are defined as the convolution with the PDFs:

$$B_{i,n}^{(m)}(x, \mu, \mu_F, \lambda) = \sum_j \int \frac{\mathrm{d}z}{z} \mathcal{I}_{ij,n}^{(m)}\left(z, \frac{\mu^2}{\mu_F^2}, \lambda\right) f_j\left(\frac{x}{z}, \mu_F\right). \qquad (A.4.19)$$

---

[12]Typically, $\mu_F = \mu$ is chosen for lack of formal distinction between the two scales.

The only coefficient present at LO is

$$\mathcal{I}^{(0)}_{ij,-1}(z, \lambda_F) = \delta_{ij}\delta(1-z),\qquad\text{(A.4.20)}$$

a flavour diagonal contribution at the value of z taken by the parton in the LO cross section. At NLO, we have:

$$\mathcal{I}^{(1)}_{ij,1}(z, \lambda_F) = \Gamma^i_0 \delta_{ij}\delta(1-z),$$

$$\mathcal{I}^{(1)}_{ij,0}(z, \lambda_F) = -\frac{\gamma^i_{B0}}{2}\delta_{ij}\delta(1-z) + 2P^{(0)}_{ij}(z),$$

$$\mathcal{I}^{(1)}_{ij,1}(z, \lambda_F) = 2I^{(1)}_{ij}(z) + \ln\lambda_F 2P^{(0)}_{ij}(z),\qquad\text{(A.4.21)}$$

showing the emergence of the splitting functions $P^{(0)}_{ij}(z)$ describing the initial state collinear radiation. The $I^{(1)}_{ij}(z)$ are matching functions. At NNLO, the coefficients read:

$$\mathcal{I}^{(2)}_{ij,3}(z, \lambda_F) = \frac{1}{2}\left(\Gamma^i_0\right)^2 \delta_{ij}\delta(1-z),$$

$$\mathcal{I}^{(2)}_{ij,2}(z, \lambda_F) = \Gamma^i_0\left[-\left(\frac{3}{4}\gamma^i_{B0} + \frac{\beta_0}{2}\right)\delta_{ij}\delta(1-z) + 3P^{(0)}_{ij}(z)\right],$$

$$\mathcal{I}^{(2)}_{ij,1}(z, \lambda_F) = \left[\Gamma^i_1 - \left(\Gamma^i_0\right)^2\frac{\pi^2}{6} + \frac{\gamma^i_{B0}}{2}\left(\frac{\gamma^i_{B0}}{2} + \beta_0\right)\right]\delta_{ij}\delta(1-z) + 2\Gamma^i_0 I^{(1)}_{ij}(z)$$
$$- 2\left(\gamma^i_{B0} + \beta_0\right)P^{(0)}_{ij}(z) + 4\sum_k P^{(0)}_{ik}(z)\otimes_z P^{(0)}_{kj}(z) + \ln\lambda_F 2\Gamma^i_o P^{(0)}_{ij}(z),$$

$$\mathcal{I}^{(2)}_{ij,0}(z, \lambda_F) = \left[\left(\Gamma^i_0\right)^2\zeta_3 + \Gamma^i_0\gamma^i_{B0}\frac{\pi^2}{12} - \frac{\gamma^i_{B1}}{2}\right]\delta_{ij}\delta(1-z)$$
$$- \Gamma^i_0\frac{\pi^2}{3}P^{(0)}_{ij}(z) - \left(\gamma^i_{B0} + 2\beta_0\right)I^{(1)}_{ij}(z)$$
$$+ 4\sum_k I^{(1)}_{ik}(z)\otimes_z P^{(0)}_{kj}(z) + 4P^{(1)}_{ij}(z)$$
$$+ \ln\lambda_F\left[-\gamma^i_{B0}P^{(0)}_{ij}(z) + 4\sum_k P^{(0)}_{ik}(z)\otimes_z P^{(0)}_{kj}(z)\right],$$

$$\mathcal{I}^{(2)}_{ij,-1}(z, \lambda_F) = 4I^{(2)}_{ij}(z) + \ln\lambda_F\left[4\sum_k I^{(1)}_{ik}(z)\otimes_z P^{(0)}_{kj}(z) + 4P^{(1)}_{ij}(z)\right]$$
$$+ \ln^2\lambda_F\left[\beta_0 P^{(0)}_{ij}(z) + 2\sum_k P^{(0)}_{ik}(z)\otimes_z P^{(0)}_{kj}(z)\right].\qquad\text{(A.4.22)}$$

The expressions for the matching coefficients $I^{(m)}_{ij}(z)$ and the splitting functions $P^{(m)}_{ij}(z)$ have been worked out in [239, 240] and can be found there. The notation

$\otimes_z$ denotes a Mellin convolution

$$f(z) \otimes_z g(z) = \int_z^1 \frac{\mathrm{d}w}{w} f(w) g\left(\frac{z}{w}\right), \qquad (A.4.23)$$

the results of which can also be found in those two papers.

A.4.4 Soft function

We defined the single-differential soft function in Appendix A as

$$\hat{S}_\kappa(k, \{\hat{q}_i\}, \mu) = \int \left[\prod_i k_i\right] \hat{S}_\kappa(\{k_i\}, \{\hat{q}_i\}, \mu) \, \delta\left(k - \sum_i k_i\right). \qquad (A.4.24)$$

We expand this as a perturbative series in $\alpha_s(\mu)$

$$\hat{S}_\kappa(k, \{\hat{q}_i\}, \mu) = \sum_n \hat{S}_\kappa^{(n)}(k, \{\hat{q}_i\}, \mu) \left(\frac{\alpha_s}{4\pi}\right)^n, \qquad (A.4.25)$$

where the coefficients take the form

$$\hat{S}_\kappa^{(m)}(k, \{\hat{q}_i\}, \mu) = \hat{S}_{\kappa,-1}^{(m)}(\{\hat{q}_i\}) \, \delta(k) + \sum_{n=0}^{2m-1} \hat{S}_{\kappa,n}^{(m)}(\{\hat{q}_i\}) \frac{1}{\mu} \mathcal{L}_n\left(\frac{k}{\mu}\right). \qquad (A.4.26)$$

Rescaling the arguments to match the expressions in Section A.2.2, we get:

$$\hat{S}_\kappa^{(m)}(k, \{\hat{q}_i\}, \mu) = \hat{S}_{\kappa,-1}^{(m)}\left(\{\hat{q}_i\}, \frac{\xi}{\mu}\right) \delta(k) + \sum_{n=0}^{2m-1} \hat{S}_{\kappa,n}^{(m)}\left(\{\hat{q}_i\}, \frac{\xi}{\mu}\right) \frac{1}{\xi} \mathcal{L}_n\left(\frac{k}{\xi}\right),$$

$$\hat{S}_{\kappa,-1}^{(m)}(\{\hat{q}_i\}, \lambda) = \hat{S}_{\kappa,-1}^{(m)}(\{\hat{q}_i\}) + \sum_{n=0}^{2m-1} \hat{S}_{\kappa,n}^{(m)}(\{\hat{q}_i\}) \frac{\ln^{n+1} \lambda}{n+1}, \qquad (A.4.27)$$

$$\hat{S}_{\kappa,n}^{(m)}(\{\hat{q}_i\}, \lambda) = \hat{S}_{\kappa,n}^{(m)}(\{\hat{q}_i\}) + \sum_{k=0}^{2m-1-n} \hat{S}_{\kappa,n+k}^{(m)}(\{\hat{q}_i\}) \frac{(n+k)! \ln^k \lambda}{n! k!}.$$

The only coefficient at leading order is the colour-diagonal operator

$$\hat{S}_{\kappa,-1}^{(0)}(\{\hat{q}_i\}) = \mathbf{1}_\kappa. \qquad (A.4.28)$$

For the NLO and NNLO coefficients, we will use the following abbreviations:

$$\mathbf{C} \equiv \sum_i \mathbf{T}_i^2 = \mathbf{1}_\kappa \sum_i C_i,$$

$$\mathbf{L}(\{\hat{s}_{ij}\}) \equiv \sum_{i \neq j} \mathbf{T}_i \cdot \mathbf{T}_j \ln \hat{s}_{ij}, \qquad (A.4.29)$$

$$\mathbf{I} \equiv i\pi \sum_{i \neq j} \mathbf{T}_i \cdot \mathbf{T}_j \Delta_{ij} = i\pi \left[2\left(\mathbf{T}_a + \mathbf{T}_b\right)^2 - \mathbf{C} \right],$$

where $\Delta_{ij} = 1$ if both partons are outgoing or incoming and $\Delta_{ij} = 0$ if one parton is incoming, and one outgoing. Using these operators, we can write the NLO soft function coefficients as

$$\hat{S}_{\kappa,1}^{(1)}\left(\{\hat{q}_i\}\right) = -2\Gamma_0\mathbf{C},$$

$$\hat{S}_{\kappa,0}^{(1)}\left(\{\hat{q}_i\}\right) = \Gamma_0\mathbf{L}\left(\{\hat{s}_{ij}\}\right), \tag{A.4.30}$$

$$\hat{S}_{\kappa,-1}^{(1)}\left(\{\hat{q}_i\}\right) = \sum_{i \neq j} \mathbf{T}_i \cdot \mathbf{T}_j \left[\ln^2 \hat{s}_{ij} - \frac{\pi^2}{6} + 4 \sum_{m \neq i,j} I_{ij,m}\left(\{\hat{q}_i\}\right) \right].$$

The functions $I_{ij,m}$ are functions made up of finite phase space integrals, necessary in the case of three or more N-Jettiness axes, and were originally presented in [224]. In Section A.3 we provided a different way of calculating these contributions.

At NNLO, the soft function coefficients are found to be:

$$\hat{S}_{\kappa,3}^{(2)}\left(\{\hat{q}_i\}\right) = 2\Gamma_0^2\mathbf{C}^2,$$

$$\hat{S}_{\kappa,2}^{(2)}\left(\{\hat{q}_i\}\right) = \Gamma_0\mathbf{C}\left[3\Gamma_0\mathbf{L} + 2\beta_0\right],$$

$$\hat{S}_{\kappa,1}^{(2)}\left(\{\hat{q}_i\}\right) = \Gamma_0^2\left(\mathbf{L}^2 + \frac{1}{2}\left[\mathbf{I}, \mathbf{L}\right] - \frac{2\pi^2}{3}\mathbf{C}^2\right) + 2\Gamma_0\left(\beta_0\mathbf{L} - \mathbf{C}\hat{S}_{\kappa,-1}^{(1)}\left(\{\hat{q}_i\}\right)\right) - 2\Gamma_1\mathbf{C},$$

$$\hat{S}_{\kappa,0}^{(2)}\left(\{\hat{q}_i\}\right) = \Gamma_0^2\mathbf{C}\left(4\mathbf{C}\zeta_3 - \frac{\pi^2}{3}\mathbf{L}\right) - \Gamma_1\mathbf{L} - \mathbf{C}\gamma_{S1}$$
$$- \frac{\Gamma_0}{2}\left(\left\{\mathbf{L}, \hat{S}_{\kappa,-1}^{(1)}\left(\{\hat{q}_i\}\right)\right\} + \left[\mathbf{I}, \hat{S}_{\kappa,-1}^{(1)}\left(\{\hat{q}_i\}\right)\right]\right) - 2\beta_0\hat{S}_{\kappa,-1}^{(1)}\left(\{\hat{q}_i\}\right),$$

$$\tag{A.4.31}$$

with

$$\gamma_{S1} = C_A\left(-\frac{64}{9} + 28\zeta_3\right) + \beta_0\left(-\frac{56}{9} + \frac{\pi^2}{3}\right) \tag{A.4.32}$$

the first non-zero term in the noncusp soft anomalous dimension.

The two-loop constants are known analytically only for the channels $\kappa = q\bar{q}$ and $\kappa = gg$ [241–244]. Other channels, in particular those involving more than two N-Jettiness axes have to be calculated numerically. The approach presented in Section A.3 for the calculation of finite contributions in the NLO soft function can also be

used to calculate the contributions to the NNLO soft function.

A.5   Conclusions

In this chapter, we have presented an implementation of a phase space slicing method based on the factorization of the cross section differential in the N-Jettiness variable τ_N. This variable provides a simple and general separation of the cross section into contributions divergent in any possible soft or collinear limit and those free of such divergences. SCET provides a factorization in the soft and collinear limits and thus a framework to analytically cancel the divergent contributions against their counterparts in the virtual corrections. The contributions away from the divergent region can be calculated numerically using a Monte Carlo event generator. Both contributions depend on an arbitrary cutoff that cancels in the limit $\tau_{N,\text{cut}} \to 0$.

The contribution above the phase space slicing cut corresponds to a calculation of the desired cross section with an additional jet in the process, subject to a lower cut on τ_N. Such a calculation can be easily performed using the SHERPA framework, with either of its matrix element generators providing the matrix element. We have presented a simple algorithm to calculate the N-Jettiness value given a particular phase space configuration. In the case of two-jet production in electron-positron collisions, it is possible to directly compare the results from this calculation with SHERPA's native Catani-Seymour method, and we have found good agreement between the two.

The contribution below the cut takes the form of a phase space dependent K-factor, which can also be calculated using the SHERPA framework. While the beam and jet functions correspond to a number of analytically-known expressions, the soft function is calculated numerically. We recalculate it here for our purposes, confirming the results found by other authors.

Implementing these contributions at NLO, we find general agreement of the total cross sections calculated using the phase space slicing with the cross section calculated using a subtraction method. We find the cross sections to be independent of the cut parameter over a wide range of values, although there are significant fluctuations in the results, suggesting the integration to be performing worse than

in the subtraction method. In particular, it is difficult to establish when the cross section is stable with respect to a variation in $\tau_{N,\text{cut}}$. For large values of the slicing cut, power corrections play an important role, and we have observed their effect in the calculations considered in this work. For low values of the cut, the integration performance worsens as the separate contributions can become very large. We observe large fluctuations in the total cross section, as well as fluctuations depending on external parameters of the integration, such as the number of phase space points per iteration of the adaptive integration. We find such behaviour to be particularly visible for the cases in which the kinematics are not fixed at leading order.

The difficulties that arise in the integration of the cross section at different values of the cut parameter require a calculation for several different cut parameters. The total cross section may then be determined through a fit to these values. This requirement, coupled with the large fluctuations observed in our results, means a significant computational overhead for the calculation of a total cross section, even at NLO. While most of the ingredients for an integration at NNLO are implemented, we therefore decided not to pursue the implementation of this method further.

Appendix B

On-shell renormalization

The parameters of the Standard Model Lagrangian are inputs to the model which have to be determined experimentally. However, when taking into account loop corrections, we find, in general, divergent corrections to these quantities. One way to interpret this is that the "bare" parameters in the Lagrangian differ from the physical, experimentally measured, parameters by calculable, but potentially divergent, contributions at each order in perturbation theory. In a renormalizable theory such as the Standard Model, these divergences cancel in physical predictions.

In order for calculations to be performed, physical quantities must then be calculated in terms of bare parameters. For each bare parameter, one can construct a relation to the physical quantity through a renormalization condition. This relation can then be used to set up an associated renormalization constant, and the resulting expression can be used in the calculation of interesty. There is clearly an ambiguity here, as the relationships between bare and physical parameters, and indeed the set of physical parameters to be used as inputs is not fixed. A given choice of independent physical parameters constitutes an *input parameter set*, and the method of separation into renormalized parameters and renormalization constants, together with the choice of renormalization conditions specify a *renormalization scheme*. The differences in predictions between different renormalization schemes are formally of higher order than the calculation performed, and vanish to all orders, but order by order these

differences are nonetheless relevant due to the truncation of the perturbative series.

The on-shell renormalization scheme chooses counterterms in such a way that the finite, renormalized parameters equal physical parameters at all orders. In particular, the masses are renormalized on-shell, such that the residue of the propagator pole at the physical mass is exactly 1. As an independent set of parameters, the full set of masses, the electron charge and the quark mixing matrix are conventionally chosen. For the purpose of the calculations in this work, we set the quark mixing matrix to be the identity matrix such that no mixing between generations occurs. Making this choice has no consequence for leptonic decays, which we focus on here. Renormalizing this set of parameters leaves $\mathcal{S}$-matrix elements finite. In order to also get finite vertex functions and propagators, the fields have to be renormalized, too, which then leaves all Green's functions, and thus all amplitudes, UV-finite.

B.1   The renormalization constants

The parameters in the Lagrangian are renormalized in the on-shell renormalization scheme as follows:

$$e_0 = Z_e e = (1 + \delta Z_e)e \tag{B.1.1}$$

$$M_{W,0}^2 = M_W^2 + \delta M_W^2 \tag{B.1.2}$$

$$M_{Z,0}^2 = M_Z^2 + \delta M_Z^2 \tag{B.1.3}$$

$$M_{H,0}^2 = M_H^2 + \delta M_H^2 \tag{B.1.4}$$

$$m_{f,i,0} = m_{f,i} + \delta m_{f,i} \tag{B.1.5}$$

A further correction to the Higgs potential appears due to tadpoles, with the effect that the minimum of the potential is shifted. This is offset by introducing a counterterm to the vacuum expectation value of the Higgs field.

The field renormalizations are defined as follows:

$$W_0^\pm = Z_W^{1/2} W^\pm = \left(1 + \frac{1}{2}\delta Z_W\right) W^\pm \tag{B.1.6}$$

$$
\begin{pmatrix} Z_0 \\ A_0 \end{pmatrix} = \begin{pmatrix} Z_{ZZ}^{1/2} & Z_{ZA}^{1/2} \\ Z_{AZ}^{1/2} & Z_{AA}^{1/2} \end{pmatrix} \begin{pmatrix} Z \\ A \end{pmatrix} = \begin{pmatrix} 1 + \frac{1}{2}\delta Z_{ZZ} & \frac{1}{2}\delta Z_{ZA} \\ \frac{1}{2}\delta Z_{AZ} & 1 + \frac{1}{2}\delta Z_{AA} \end{pmatrix} \begin{pmatrix} Z \\ A \end{pmatrix} \tag{B.1.7}
$$

$$
H_0 = Z_H^{1/2} H = \left(1 + \frac{1}{2}\delta Z_H\right) H \tag{B.1.8}
$$

$$
f_{i,0}^L = Z_{ij}^{1/2,f,L} f_j^L = \left(\delta_{ij} + \frac{1}{2}\delta Z_{ij}^{f,L}\right) f^L \tag{B.1.9}
$$

$$
f_{i,0}^R = Z_{ij}^{1/2,f,R} f_j^R = \left(\delta_{ij} + \frac{1}{2}\delta Z_{ij}^{f,R}\right) f^R \tag{B.1.10}
$$

In the second equality for each case, the multiplicative renormalization constants are expanded, resulting in the leading expression written exclusively in terms of the physical parameters, and a counterterm part. Only the linear term in the counterterm expansion is required for one-loop corrections. The counterterm pieces can be treated just as any other term in the Lagrangian and give rise to Feynman rules with associated diagrams.

The renormalization conditions in the on-shell scheme are formulated for on-mass shell external fields. All constants are fixed using one-particle irreducible two-point functions; except for the charge renormalization where the $ee\gamma$-vertex is used.

The mass parameters are fixed by the requirement that they are equal to the physical masses. In the case of mass matrices, the conditions are simplified when the external particles are considered on-shell. In this case, the renormalized matrices are diagonal. These elements are chosen such that the fields are properly normalized, such that the mass renormalization involves only the corresponding diagonal self energies. The renormalized electric charge is defined as the full $ee\gamma$-coupling in the limit of zero momentum transfer.

The renormalization constant for the tadpoles is chosen such that it cancels all tadpole contributions at all orders:

$$
\delta t = -T. \tag{B.1.11}
$$

This ensures that the renormalized value of the vacuum expectation value v is the actual minimum of the effective Higgs potential.

The renormalization constants can then be written in terms of the self energies $\Sigma^i(k^2)$. For the gauge fields, we have the following constants:

$$\delta M_W^2 = \mathrm{Re}\Sigma_T^W\left(M_W^2\right), \qquad \delta Z_W = -\mathrm{Re}\frac{\partial \Sigma_T^W(k^2)}{\partial k^2}\bigg|_{k^2=M_W^2}, \qquad \text{(B.1.12)}$$

$$\delta M_Z^2 = \mathrm{Re}\Sigma_T^{ZZ}\left(M_Z^2\right), \qquad \delta Z_{ZZ} = -\mathrm{Re}\frac{\partial \Sigma_T^{ZZ}(k^2)}{\partial k^2}\bigg|_{k^2=M_Z^2}, \qquad \text{(B.1.13)}$$

$$\delta Z_{AZ} = -2\mathrm{Re}\frac{\Sigma_T^{AZ}(M_Z^2)}{M_Z^2}, \qquad \delta Z_{ZA} = 2\frac{\Sigma_T^{AZ}(0)}{M_Z^2}, \qquad \text{(B.1.14)}$$

$$\delta Z_{AA} = -\frac{\partial \Sigma_T^{AA}(k^2)}{\partial k^2}\bigg|_{k^2=0}, \qquad \text{(B.1.15)}$$

$$\delta M_H^2 = \mathrm{Re}\Sigma^H\left(M_H^2\right), \qquad \delta Z_H = -\mathrm{Re}\frac{\partial \Sigma^H(k^2)}{\partial k^2}\bigg|_{k^2=M_H^2}. \qquad \text{(B.1.16)}$$

In the fermion sector, we have:

$$\delta m_{f,i} = \frac{m_{f,i}}{2}\mathrm{Re}\left(\Sigma_{ii}^{f,L}(m_{f,i}^2) + \Sigma_{ii}^{f,R}(m_{f,i}^2) + 2\Sigma_{ii}^{f,S}(m_{f,i}^2)\right), \qquad \text{(B.1.17)}$$

$$\delta Z_{ii}^{f,L} = -\mathrm{Re}\Sigma_{ii}^{f,L}(m_{f,i}^2) - m_{f,i}^2\frac{\partial}{\partial k^2}\mathrm{Re}\left[\Sigma_{ii}^{f,L}(k^2) + \Sigma_{ii}^{f,R}(k^2) + 2\Sigma_{ii}^{f,S}(k^2)\right]\bigg|_{k^2=m_{f,i}^2}, \qquad \text{(B.1.18)}$$

$$\delta Z_{ii}^{f,R} = -\mathrm{Re}\Sigma_{ii}^{f,R}(m_{f,i}^2) - m_{f,i}^2\frac{\partial}{\partial k^2}\mathrm{Re}\left[\Sigma_{ii}^{f,L}(k^2) + \Sigma_{ii}^{f,R}(k^2) + 2\Sigma_{ii}^{f,S}(k^2)\right]\bigg|_{k^2=m_{f,i}^2}. \qquad \text{(B.1.19)}$$

For the charge renormalization constant Z_e, one finds after the application of Ward identities to the general $\gamma \to e^+ e^-$ amplitude:

$$\delta Z_e = -\frac{1}{2}\delta Z_{AA} - \frac{s_W}{2c_W}\delta Z_{ZA}. \qquad \text{(B.1.20)}$$

For convenience, we also define a counterterm for the sine s_W and cosine c_W of the weak mixing angle:

$$\frac{\delta c_W}{c_W} = \frac{1}{2}\left(\frac{\delta M_W^2}{M_W^2} - \frac{\delta M_Z^2}{M_Z^2}\right), \qquad \text{(B.1.21)}$$

$$\frac{\delta s_W}{s_W} = -\frac{c_W^2}{s_W^2}\frac{\delta c_W}{c_W}. \qquad \text{(B.1.22)}$$

Appendix C

NLO EW form factors and counterterms

In this section we collect the electroweak vertex form factors and counterterms required for setting up the NLO electroweak corrections to $\tilde{\beta}_0^1$. We use the vertex form factors found in [142] and the counterterms in the on-shell renormalization scheme, found in [141] and described in the previous appendix. The vertex form factors retain the full dependence on the lepton masses only in the QED corrections, where they are needed to regularize the collinear singularities, while the purely weak contributions are calculated in the massless limit.

In order to find the pure NLO QED corrections, out of the form factors we need to only include the QED form factors. In the counterterms, we only need to include the photonic corrections to the wavefunction renormalization. Such a procedure is not gauge-invariant for W-decays, so this option is only provided for Z- and Higgs boson decays.

We note here, that SHERPA and [141] use $(+,-,-,-)$ as metric signature, whereas [142] use $(-,+,+,+)$. This means that we have to perform the following adjustments:

- Each squared momentum (such as Q^2) receives an additional minus sign in our expression, while invariants such as s and m_i^2 are correct.

- Each γ_5 receives a minus sign.

- The scalar tadpole and triangle functions, A_0 and C_0, also come with an additional minus sign.

- Unrelated to the metric signature, the convention for the left- and right-handed projectors differs by a factor of 2, such that $\gamma_\pm = 2P_{L/R}$ where $\gamma_\pm = 1 \pm \gamma_5$ are the projection operators in [142], and $P_{L/R} = \frac{1 \mp \gamma_5}{2}$ are those used in SHERPA and [141].

These corrections have already been taken into account in the expressions we write down here.

All results are calculated in the Feynman gauge. We call the left- and right-handed tree-level couplings c_L and c_R and introduce $g_L = c_L \frac{s_W c_W}{ie}$, $g_R = c_R \frac{s_W c_W}{ie}$ for convenience. We further use the vector coupling $v_f = (g_L + g_R)$ and the axial coupling $a_f = (g_L - g_R)$. Any quantity denoted as $x_{f'}$ refers to the iso-spin partner of the fermion f.

C.1 $Z \rightarrow f\bar{f}$

The QED corrections to this vertex are given by:

$$
\begin{aligned}
V_\mu^{\mathrm{QED}} =& \frac{\alpha}{4\pi} \frac{e}{2s_W c_W} Q_f^2 \left[i\gamma_\mu \left(v_f - a_f \gamma_5 \right) F_{Aa}(s) - i\gamma_\mu a_f \gamma_5 F_A^{(1)}(s) \right. \\
& \left. + v_f \left(p_f - p_{\bar{f}} \right)_\mu F_V^{(2)}(s) - a_f \gamma_5 \left(p_f + p_{\bar{f}} \right)_\mu F_A^{(3)}(s) \right] \\
=& \frac{\alpha}{4\pi} \frac{1}{s_W c_W} Q_f^2 \left[\gamma_\mu \left(c_L P_L + c_R P_R \right) F_{Aa}(s) - ie \frac{I_f}{2} \gamma_\mu \left(P_R - P_L \right) F_A^{(1)}(s) \right. \\
& + e \frac{I_f - 2s_W^2 Q_f}{2} \left(p_f - p_{\bar{f}} \right)_\mu \left(P_R + P_L \right) F_V^{(2)}(s) \\
& \left. - e \frac{I_f}{2} \left(P_R - P_L \right) \left(p_f + p_{\bar{f}} \right)_\mu F_A^{(3)}(s) \right].
\end{aligned}
\tag{C.1.1}
$$

In the massless limit, only the structure proportional to $\gamma_\mu \left(c_L P_L + c_R P_R\right)$ contributes. The form factor $F_{Aa}(s)$ is given by:

$$F_{Aa}(s) = -2\left(s - 2m_f^2\right) C_0\left(m_f^2, m_f^2, s, m_f^2, 0, m_f^2\right)$$
$$- 3B_0\left(s, m_f^2, m_f^2\right) + 4B_0\left(m_f^2, m_f^2, 0\right) - 2. \tag{C.1.2}$$

The other form factors are all proportional to the fermion mass and are given in the following:

$$F_V^{(2)}(s) = \frac{2m_f}{4m_f^2 - s}\left[B_0\left(s, m_f^2, m_f^2\right) - B_0\left(m_f^2, m_f^2, 0\right)\right], \tag{C.1.3}$$

$$F_A^{(1)}(s) = -\frac{8m_f^2}{4m_f^2 - s}\left[B_0\left(s, m_f^2, 0\right) - B_0\left(m_f^2, m_f^2, 0\right)\right], \tag{C.1.4}$$

$$F_A^{(3)}(s) = \frac{m_f}{s\left(4m_f^2 - s\right)}\left[\frac{4m_f^2 - 3s}{2}\left(B_0\left(s, m_f^2, 0\right) - B_0\left(m_f^2, m_f^2, 0\right)\right) + 4m_f^2 - s\right]. \tag{C.1.5}$$

The effect of abelian Z- and ϕ^0-exchanges is given by:

$$V_\mu^{Za} = \frac{\alpha}{4\pi}\frac{ie}{s_W^3 c_W^3}\gamma_\mu\left(V_f - A_f\gamma_5\right) F_{Za}(s)$$
$$= \frac{\alpha}{4\pi}\frac{ie}{s_W^3 c_W^3}\gamma_\mu\left(g_L^3 P_L + g_R^3 P_R\right) F_{Za}(s), \tag{C.1.6}$$

where $V_f = \left(v_f^2 + a_f^2\right) v_f + 2v_f a_f^2$, $A_f = \left(v_f^2 + a_f^2\right) a_f + 2v_f^2 a_f$ and

$$F_{Za}(s) = -\frac{2M_Z^4}{s}\left(1 + \frac{s}{M_Z^2}\right)^2 C_0\left(0, 0, s, 0, M_Z^2, 0\right)$$
$$+ B_0\left(s, 0, 0\right) - \left(\frac{2M_Z^2}{s} + 4\right)\left[B_0\left(s, 0, 0\right) - B_0\left(0, 0, M_Z^2\right)\right] - 2. \tag{C.1.7}$$

For the diagrams involving W bosons (and the associated ghosts), we introduce:

$$w_f = \frac{m_f^2}{M_W^2}, \qquad\qquad w_{f'} = \frac{m_{f'}^2}{M_W^2}, \tag{C.1.8}$$

$$\beta^2 = 1 - w_{f'}, \qquad\qquad \kappa = -\frac{\beta^2\left(3 - \beta^2\right)}{2}\frac{M_W^2}{s}. \tag{C.1.9}$$

The effect of abelian W- and ϕ-exchanges, i.e. all diagrams not involving a three-boson vertex, is described by:

$$
\begin{aligned}
V_\mu^{Wa} &= \frac{\alpha}{4\pi} \frac{ie}{s_W c_W} \frac{1}{2s_W^2} \gamma_\mu P_L \left[\frac{v_{f'} + a_{f'}}{2} F_{Wa}(s) + a_{f'} \bar{F}_{Wa}(s) \right] \\
&= \frac{\alpha}{4\pi} \frac{1}{2s_W^2} \gamma_\mu P_L \left[g_{L'} F_{Wa}(s) + \frac{I_{f'}}{2} \bar{F}_{Wa}(s) \right].
\end{aligned} \tag{C.1.10}
$$

Note that this is purely a contribution to the left-handed part of the amplitude.

The necessary auxilliary functions are given by:

$$
\begin{aligned}
F_{Wa}(s) = &- \left(-2\beta^2 \kappa + 3 + \beta^4 + 2\frac{s}{M_W^2} \right) M_W^2 C_0 \left(0, 0, s, m_{f'}^2, M_W^2, m_{f'}^2 \right) \\
&+ 2(\kappa - 2) \left[B_0 \left(s, m_{f'}^2, m_{f'}^2 \right) - B_0 \left(0, m_{f'}^2, M_W^2 \right) \right] \\
&+ \frac{(3 - \beta^2)}{2} B_0 \left(s, m_{f'}^2, m_{f'}^2 \right) - \left(2 + \frac{1}{2} w_{f'} \right),
\end{aligned} \tag{C.1.11}
$$

$$
\begin{aligned}
\bar{F}_{Wa}(s) = w_{f'} &\left[\left(\frac{\beta^4 M_W^2}{s} + 2 \right) M_W^2 C_0 \left(0, 0, s, m_{f'}^2, M_W^2, m_{f'}^2 \right) \right. \\
&+ \frac{\beta^2 M_W^2}{s} \left[B_0 \left(s, m_{f'}^2, m_{f'}^2 \right) - B_0 \left(0, m_{f'}^2, M_W^2 \right) \right] \\
&\left. - \frac{1}{2} B_0 \left(s, m_{f'}^2, m_{f'}^2 \right) + \frac{1}{2} \right].
\end{aligned} \tag{C.1.12}
$$

The effect of non-abelian W- and ϕ-exchanges, i.e. all the diagrams containing a three-boson vertex, is described by:

$$
V_\mu^{Wn} = \frac{\alpha}{4\pi} \frac{ie}{s_W c_W} \frac{c_W^2}{s_W^2} (-I_f) \gamma_\mu P_L \left[F_{Wn}(s) + \bar{F}_{Wn}(s) \right]. \tag{C.1.13}
$$

Note that this is again purely a contribution to the left-handed part of the amplitude.

The necessary auxilliary functions are given by:

$$
\begin{aligned}
F_{Wn}(s) = &- \left(-2\beta^2 \kappa + 3 + \beta^4 \right) M_W^2 C_0 \left(0, 0, s, M_W^2, m_{f'}^2, M_W^2 \right) \\
&- 2(\kappa - 2) \left[B_0 \left(s, M_W^2, M_W^2 \right) - B_0 \left(0, m_{f'}^2, M_W^2 \right) \right] \\
&- \left(3 + \frac{1}{2} w_{f'} \right) B_0 \left(s, M_W^2, M_W^2 \right) - \frac{1}{2} w_{f'},
\end{aligned} \tag{C.1.14}
$$

$$
\begin{aligned}
\bar{F}_{Wn}(s) = \frac{1}{2c_W^2} w_{f'} &\left[\left(\frac{\beta^4 M_W^2}{s} - 4 + w_{f'} \right) M_W^2 C_0 \left(0, 0, s, M_W^2, m_{f'}^2, M_W^2 \right) \right. \\
&\left. - \frac{\beta^2 M_W^2}{s} \left[B_0 \left(s, M_W^2, M_W^2 \right) - B_0 \left(0, m_{f'}^2, M_W^2 \right) \right] \right.
\end{aligned}
$$

$$+ \frac{1}{2} \left(B_0 \left(s, M_W^2, M_W^2 \right) + 1 \right) \Bigg]. \tag{C.1.15}$$

The counterterms for this vertex read:

$$\delta_R = c_R \left(1 + \frac{1}{2} \delta Z_{ZZ} + \frac{1}{2} \left(\delta Z_{ii}^{f,R} + \delta Z_{ii}^{f,R,\dagger} \right) \right) + \delta c_R - \frac{1}{2} Q_f \delta Z_{AZ} \tag{C.1.16}$$

$$\delta_L = c_L \left(1 + \frac{1}{2} \delta Z_{ZZ} + \frac{1}{2} \left(\delta Z_{ii}^{f,L} + \delta Z_{ii}^{f,L,\dagger} \right) \right) + \delta c_L - \frac{1}{2} Q_f \delta Z_{AZ}, \tag{C.1.17}$$

where the left- and right-handed, tree-level couplings c_R, c_L and their counterterms δc_R, δc_L are given by:

$$c_R = \frac{ie}{s_W c_W} \left(-s_W^2 Q_f \right), \tag{C.1.18}$$

$$\delta c_R = c_R \left(\delta Z_e + \frac{1}{c_W^2} \frac{\delta s_W}{s_W} \right), \tag{C.1.19}$$

$$c_L = \frac{ie}{s_W c_W} \left(I_f - s_W^2 Q_f \right), \tag{C.1.20}$$

$$\delta c_L = \frac{ie}{s_W c_W} I_f \left(\delta Z_e + \frac{s_W^2 - c_W^2}{c_W^2} \frac{\delta s_W}{s_W} \right) + \delta c_R. \tag{C.1.21}$$

C.2 $W^- \to \ell^- \bar{\nu}_\ell$ and $W^+ \to \ell^+ \nu_\ell$

In the case of $W \to \ell \nu$ decays, there is no diagram for photon exchange between the final state particles.

All the corrections to this decay are purely corrections to the left-handed coupling (since fermion masses are neglected in these subamplitudes).

The effect of non-abelian photon exchange is given by:

$$V_\mu^{An}(s) = \frac{\alpha}{4\pi} \frac{ie}{\sqrt{2} s_W} 2P_L \, \text{sgn}(Q_f) F_{An}(s). \tag{C.2.1}$$

The form factor is given by:

$$F_{An}(s) = Q_f \left[M_W^2 C_0 \left(m_f^2, m_{f'}^2, s, 0, m_f^2, M_W^2 \right) + B_0 \left(m_f^2, m_f^2, 0 \right) \right]$$

$$- Q_{f'} \left[M_W^2 C_0 \left(m_f^2, m_{f'}^2, s, M_W^2, m_{f'}^2, 0 \right) + B_0 \left(m_{f'}^2, m_{f'}^2, 0 \right) \right]$$

$$+ \frac{Q_f - Q_{f'}}{2} \left[- \left(\frac{M_W^2}{s} + 1 \right) B_0 \left(s, M_W^2, 0 \right) + \left(\frac{M_W^2}{s} + 2 \right) B_0 \left(0, 0, M_W^2 \right) \right].$$

$$(C.2.2)$$

The effect of abelian Z-exchange is described by:

$$\begin{aligned} V_\mu^{Za}(s) &= \frac{\alpha}{4\pi} \frac{ie}{\sqrt{2}s_W} \frac{1}{4s_W^2 c_W^2} \gamma_\mu P_L \left(v_f + a_f \right) \left(v_{f'} + a_{f'} \right) F_{Za}(s) \\ &= \frac{\alpha}{4\pi} \frac{ie}{\sqrt{2}s_W} \frac{1}{s_W^2 c_W^2} \gamma_\mu P_L g_L g_{L'} F_{Za}(s). \end{aligned}$$

$$(C.2.3)$$

with the function $F_{Za}(s)$ as in the decay $Z \to f\bar{f}$ (Eq. (C.1.7)).

The effect of non-abelian Z-exchange is given by:

$$\begin{aligned} V_\mu^{Zn}(s) &= \frac{\alpha}{4\pi} \frac{ie}{\sqrt{2}s_W} \frac{2}{s_W^2} \gamma_\mu P_L \mathrm{sgn}\left(Q_f \right) \left(v_f + a_f - v_{f'} - a_{f'} \right) F_{Zn}(s) \\ &= \frac{\alpha}{4\pi} \frac{ie}{\sqrt{2}s_W} \frac{4}{s_W^2} \gamma_\mu P_L \mathrm{sgn}\left(Q_f \right) \left(g_L - g_{L'} \right) F_{Zn}(s). \end{aligned}$$

$$(C.2.4)$$

The form factor reads:

$$\begin{aligned} F_{Zn}(s) = \frac{1}{2} \Bigg\{ & \left[\left(\frac{M_W^2}{s} + 1 \right) \frac{1}{c_W^2} + 1 \right] M_W^2 C_0 \left(0, 0, s, M_W^2, 0, M_Z^2 \right) \\ & - \frac{1}{2} \left(\frac{M_Z^2}{s} + \frac{M_W^2}{s} + 1 \right) B_0 \left(s, M_W^2, M_Z^2 \right) \\ & + \left(\frac{M_Z^2}{2s} + 1 \right) \frac{A_0 \left(M_Z^2 \right)}{M_Z^2} + \left(\frac{M_W^2}{2s} + 1 \right) \frac{A_0 \left(M_W^2 \right)}{M_W^2} \Bigg\}. \end{aligned}$$

$$(C.2.5)$$

The counterterms for this process read:

$$\delta_R = 0, \tag{C.2.6}$$

$$\delta_L = \frac{ie}{\sqrt{2}s_W} \left(\delta Z_e - \frac{\delta s_W}{s_W} + \frac{1}{2} \delta Z_W + \frac{1}{2} \left(\delta Z_{ii}^{\bar{f}, L, \dagger} + \delta Z_{ii}^{f, L} \right) \right). \tag{C.2.7}$$

Here, the conjugated fermion wavefunction counterterm is chosen for the antifermion in the process. The tree level couplings are:

$$c_R = 0, \tag{C.2.8}$$

$$c_L = \frac{ie}{\sqrt{2}s_W}. \tag{C.2.9}$$

C.3 $H \to f\bar{f}$

The vertex corrections to the Higgs decay into fermions are more complex as all masses have to be retained. The amplitude has been fully validated for $H \to b\bar{b}$-decays.

The QED corrections to this vertex read:

$$
\begin{aligned}
V^{\mathrm{QED}} &= \frac{\alpha}{4\pi} \frac{iem_f}{2s_W M_W} 2Q_f^2 s_W^2 F_S^{\mathrm{QED}} \\
&= \frac{\alpha}{4\pi} \frac{iem_f}{2s_W M_W} 2Q_f^2 s_W^2 F_S^{\mathrm{QED}} \left(P_L + P_R\right).
\end{aligned}
\tag{C.3.1}
$$

The form factor is given by:

$$
\begin{aligned}
F_S^{\mathrm{QED}} = \left(s - 2m_f^2\right) C_0 \left(m_f^2, m_f^2, s, m_f^2, 0, m_f^2\right) - 2B_0 \left(m_f^2, m_f^2, 0\right) + 1 \\
- \frac{4m_f^2}{4m_f^2 - s} \left[\left(B_0 \left(s, m_f^2, m_f^2\right) - B_0 \left(m_f^2, m_f^2, 0\right)\right)\right].
\end{aligned}
\tag{C.3.2}
$$

For this amplitude, the weak results will be presented in one go:

$$
\begin{aligned}
V^{\mathrm{weak}} &= \frac{\alpha}{4\pi} \frac{iem_f}{2s_W M_W} 2F_S^{\mathrm{weak}} \\
&= \frac{\alpha}{4\pi} \frac{iem_f}{2s_W M_W} 2F_S^{\mathrm{weak}} \left(P_L + P_R\right).
\end{aligned}
\tag{C.3.3}
$$

The form factor reads:

$$
\begin{aligned}
F_S^{\mathrm{weak}} = -M_W^2 \Big[&f_1 C_0 \left(m_f^2, m_f^2, s, M_W^2, m_{f'}^2, M_W^2\right) + f_2 C_0 \left(m_f^2, m_f^2, s, M_Z^2, m_f^2, M_Z^2\right) \\
&+ f_3 C_0 \left(m_f^2, m_f^2, s, m_{f'}^2, M_W^2, m_{f'}^2\right) + f_4 C_0 \left(m_f^2, m_f^2, s, m_f^2, M_Z^2, m_f^2\right) \\
&+ h_1 C_0 \left(m_f^2, m_f^2, s, M_H^2, m_f^2, M_H^2\right) + h_2 C_0 \left(m_f^2, m_f^2, s, m_f^2, M_H^2, m_f^2\right) \Big] \\
&+ f_5 B_0 \left(s, M_W^2, M_W^2\right) + f_6 B_0 \left(s, M_Z^2, M_Z^2\right) + f_7 B_0 \left(s, m_{f'}^2, m_{f'}^2\right) \\
&+ f_8 B_0 \left(m_f^2, M_W^2, m_{f'}^2\right) + f_9 B_0 \left(m_f^2, M_Z^2, m_f^2\right) + f_{10} \\
&+ h_3 B_0 \left(s, M_H^2, M_H^2\right) + h_4 B_0 \left(s, m_f^2, m_f^2\right) + h_5 B_0 \left(m_f^2, M_H^2, m_f^2\right).
\end{aligned}
\tag{C.3.4}
$$

The coefficients are given by the following expressions:

$$f_1 = \frac{1}{4}\left(\left[\left(4 + w_{f'}\left(2 + w_h\right)\right)\left(1 - w_{f'}\right) - w_f\left(10 - 4w_{f'} - \left(1 - 2w_{f'}\right)w_h\right)\right]\mu_W^2\right.$$

$$\left. + 2 + w_h w_{f'} - 2w_f\right)$$

$$f_2 = \frac{1}{4}\left(\left[\frac{4}{c_W^4}\sigma^{(2)} - w_f\left(\frac{2}{c_W^2} - w_h\right)\right]\left(\frac{1}{c_W^2} - 2w_f\right)\mu_W^2\right.$$

$$\left. + \frac{4}{c_W^4}v_f^2 - \frac{1}{2}w_f\left(\frac{2}{c_W^2} - w_h\right)\right)$$

$$f_3 = \frac{1}{4}w_{f'}\left(\left[2\left(2 + w_{f'}\right)\left(1 - w_{f'}\right) + 2w_f\left(1 + 2w_{f'} - w_f\right)\right]\mu_W^2 - 1\right)$$

$$f_4 = \frac{1}{4c_W^2}\left(\left(\sigma^{(2)} - \frac{1}{2}\right)w + w_f\left[4\sigma^{(2)}\left(\frac{1}{c_W^2}\mu_W^2 + \frac{1}{2}\right) - \frac{3}{2}\right]\right)$$

$$f_5 = \frac{1}{4}\left(\left[4 + w_{f'}\left(2 + w_h\right) - w_f\left(6 - w_h\right)\right]\mu_W^2 + 1\right)$$

$$f_6 = \frac{1}{4}\left(\left[\frac{4}{c_W^4}\sigma^{(2)} - w_f\left(\frac{2}{c_W^2} - w_h\right)\right]\mu_W^2 + \frac{1}{2c_W^2}\right)$$

$$f_7 = -\frac{1}{4}w_{f'}\left(2\left[2 + w_{f'} - w_f\right]\mu_W^2 + 1\right) \tag{C.3.5}$$

$$f_8 = -\frac{1}{4}\left(\left[2\left(2 + w_{f'}\right)\left(1 - w_{f'}\right) + w_{f'}w_h - w_f\left(6 - 2w_{f'} - w_h\right)\right]\mu_W^2 + 2\right)$$

$$f_9 = -\frac{1}{4}\left(\left[\frac{4}{c_W^2}\sigma^{(2)}\left(\frac{1}{c_W^2} - w_f\right) - w_f\left(\frac{2}{c_W^2} - w_h\right)\right]\mu_W^2 + \frac{2}{c_W^2}\sigma^{(2)}\right)$$

$$f_{10} = \frac{1}{4c_W^2}\left(\sigma^{(2)} - \frac{1}{2}\right)$$

$$h_1 = \frac{3}{2}w_f w_h\left[\left(\frac{1}{2}w_h - w_f\right)\mu_W^2 - \frac{1}{4}\right]$$

$$h_2 = -w_f\left[\frac{1}{8}w_h - w_f\left(w_h\mu_W^2 - \frac{1}{2}\right)\right]$$

$$h_3 = \frac{3}{4}w_f w_h\mu_W^2$$

$$h_4 = -w_f\left[\frac{1}{c_W^2}\sigma^{(2)} + w_f\right]\mu_W^2$$

$$h_5 = -w_f\left[\frac{3}{4}w_h - w_f\right]\mu_W^2,$$

where we used the following shorthands:

$$w = -\frac{s}{M_W^2}, \qquad\qquad \mu_W^2 = \frac{M_W^2}{4m_f^2 - s},$$

$$w_{f'} = \frac{m_{f'}^2}{M_W^2}, \qquad\qquad w_f = \frac{m_f^2}{M_W^2},$$

$$w_h = \frac{M_H^2}{M_W^2}. \tag{C.3.6}$$

Note that the corrections as written do not completely agree with Eqs. (5.546)-(5.548) of [142]. [142] provides expressions both with all masses included in Eqs. (5.546)-(5.548), and with terms $\sim m_f^2$ neglected in Eqs. (5.619), (5.621), (5.625). This is an appropriate approximation for the decay $H \to b\bar{b}$ for which $m_f = m_b$, $m_{f'} = m_t$ and $m_b \ll m_t$. For our purposes, we require the exact opposite case, with $m_f = m_\ell$, $m_{f'} = 0$. Nonetheless, the two forms can be used to cross-check terms. In comparison to the expressions including the full mass dependence, there is a factor of 2 in the overall vertex in the approximated form. The latter form appears to be correct as it reproduces the correct divergences. Secondly, the coefficients f_2 and f_6 differ. In f_6, the last term should read $\frac{1}{2c_W^2}$ instead of $\frac{2}{c_W^2}$ in agreement with the limiting expression in Eq. (5.623). Similarly, f_2 has been adapted to match the limiting expression. In particular, the second to last term is multiplied by a factor of $\frac{4}{c_W^2}$, and the last term by w_f. The second to last term can then be cast into a form $\sim \sigma^{(2)}$ as in Eq. (5.623) by adding and subtracting a_f^2. Performing these changes gives a result that agrees with the OPENLOOPS amplitude for $H \to b\bar{b}$.

The counterterms for this process read:

$$\delta_R = \frac{-ie}{2s_W} \frac{m_f}{M_W} \left(\delta Z_e - \frac{\delta s_W}{s_W} + \frac{\delta m_f}{m_f} - \frac{1}{2} \frac{\delta M_W^2}{M_W^2} + \frac{1}{2} \delta Z_H + \frac{1}{2} \left(\delta Z_{ii}^{f,L} + \delta Z_{ii}^{f,R,\dagger} \right) \right), \tag{C.3.7}$$

$$\delta_L = \frac{-ie}{2s_W} \frac{m_f}{M_W} \left(\delta Z_e - \frac{\delta s_W}{s_W} + \frac{\delta m_f}{m_f} - \frac{1}{2} \frac{\delta M_W^2}{M_W^2} + \frac{1}{2} \delta Z_H + \frac{1}{2} \left(\delta Z_{ii}^{f,R} + \delta Z_{ii}^{f,L,\dagger} \right) \right), \tag{C.3.8}$$

with the tree level couplings:

$$c_R = \frac{-ie}{2s_W} \frac{m_f}{M_W}, \tag{C.3.9}$$

$$c_L = \frac{-ie}{2s_W} \frac{m_f}{M_W}. \tag{C.3.10}$$

Appendix D

Infrared form factors

To complete the calculation of the infrared subtracted matrix elements, we need the expression of the infrared factor B_{ij}. This factor, and its real counterpart $\tilde{B}_{ij}(\Omega)$, are defined in Eq. (4.1.15) and Eq. (4.1.16) respectively and have been calculated in [49], where it has also been shown that their sum leads to a finite result as expected from the KLN theorem.

For use with the virtual corrections, we will express the form factor B in terms of the scalar master integrals that are defined in appendix E.

The virtual infrared form factor B can be rewritten in the following form, which will be more useful in expressing it in terms of master integrals:

$$
B_{ij} = -\frac{i}{8\pi^3} Z_i Z_j \theta_i \theta_j \int \mathrm{d}^4k \, \frac{1}{k^2} \left[\left(\frac{2p_i\theta_i}{k^2 - 2\left(k \cdot p_i\right)\theta_i} + \frac{2p_j\theta_j}{k^2 + 2\left(k \cdot p_j\right)\theta_j} \right)^2 \right.
$$
$$
\left. - k^2 \left(\frac{1}{k^2 - 2\left(k \cdot p_i\right)\theta_i} - \frac{1}{k^2 + 2\left(k \cdot p_j\right)\theta_j} \right)^2 \right].
$$

For the purpose of this publication, we have to consider final-final and initial-final dipole combinations. In both cases, the factor $Z_i Z_j \theta_i \theta_j = -1$. Note that the p_i used are the momenta of the external particles. To translate these into the momenta q_i running in the loop, we use $p_1 = q_1$, $p_2 = -q_2$ for the final state particles and $p_3 = -p_1 - p_2 = (q_2 - q_1)$ for the initial state particle.

D.1   Final Final

$$
\begin{aligned}
B_{12} &= \frac{i}{8\pi^3} \int \mathrm{d}^4 k \, \frac{1}{k^2} \Bigg[\left(\frac{2p_1}{k^2 - 2\,(k\cdot p_1)} + \frac{2p_2}{k^2 + 2\,(k\cdot p_2)} \right)^2 \\
&\qquad - k^2 \left(\frac{1}{k^2 - 2\,(k\cdot p_1)} - \frac{1}{k^2 + 2\,(k\cdot p_2)} \right)^2 \Bigg] \\
&= \frac{i}{8\pi^3} \int \mathrm{d}^4 k \, \frac{1}{k^2} \Bigg[\left(\frac{2q_1}{(l-q_1)^2 - q_1^2} - \frac{2q_2}{(l-q_2)^2 - q_2^2} \right)^2 \\
&\qquad - k^2 \left(\frac{1}{(l-q_1)^2 - q_1^2} - \frac{1}{(l-q_2)^2 - q_2^2} \right)^2 \Bigg] \\
&= \frac{i}{8\pi^3} i\pi^2 \Bigg[-8\,(q_1\cdot q_2)\, C_0 \left((-q_1)^2, (-q_2)^2, (-(q_1-q_2))^2, 0, m_1^2, m_2^2 \right) \\
&\qquad + 4 m_1^2 C_0 \left((-q_1)^2, (-q_1)^2, 0, 0, m_1^2, m_1^2 \right) \\
&\qquad + 4 m_2^2 C_0 \left((-q_2)^2, (-q_2)^2, 0, 0, m_2^2, m_2^2 \right) \\
&\qquad + 2 B_0 \left((-(q_1-q_2))^2, m_1^2, m_2^2 \right) - B_0 \left(0, m_1^2, m_1^2 \right) - B_0 \left(0, m_2^2, m_2^2 \right) \Bigg] \\
&= -\frac{1}{4\pi} \Bigg[2 \left(s - m_1^2 - m_2^2 \right) C_0 \left(m_1^2, m_2^2, s, 0, m_1^2, m_2^2 \right) \\
&\qquad + 2 m_1^2 C_0 \left(m_1^2, m_1^2, 0, 0, m_1^2, m_1^2 \right) + 2 m_2^2 C_0 \left(m_2^2, m_2^2, 0, 0, m_2^2, m_2^2 \right) \\
&\qquad + B_0 \left(s, m_1^2, m_2^2 \right) - \frac{1}{2} B_0 \left(0, m_1^2, m_1^2 \right) - \frac{1}{2} B_0 \left(0, m_2^2, m_2^2 \right) \Bigg]. \qquad \text{(D.1.1)}
\end{aligned}
$$

For the double virtual corrections in the decay of the Z-boson in Section 5.3.1, we need the infrared factor B in the limit of $s \gg m_i^2$, regulated with a small photon mass λ. In this case, we have $m_1 = m_2 \equiv m$ and the factor reads:

$$
\begin{aligned}
B &= -\frac{1}{\pi} \Bigg[\left(\frac{1}{2} s - m^2 \right) C_0 \left(m^2, m^2, s, \lambda^2, m^2, m^2 \right) \\
&\qquad + m^2 C_0 \left(m^2, m^2, 0, \lambda^2, m^2, m^2 \right) \\
&\qquad + \frac{1}{4} \left(B_0 \left(s, m^2, m^2 \right) - B_0 \left(0, m^2, m^2 \right) \right) \Bigg] \\
&= -\frac{\alpha}{\pi} \Bigg[-\frac{1}{2} \log \left(\frac{\lambda^2}{m^2} \right) \log \left(\frac{-s}{m^2} \right) + \frac{1}{4} \log^2 \left(\frac{-s}{m^2} \right) - \frac{\pi^2}{12} \\
&\qquad + \frac{1}{2} \log \left(\frac{\lambda^2}{m^2} \right) + \frac{1}{2} - \frac{1}{4} \log \left(\frac{-s}{m^2} \right) \Bigg]. \qquad \text{(D.1.2)}
\end{aligned}
$$

D.2 Initial Final

$$
\begin{aligned}
B_{31} &= \frac{i}{8\pi^3} \int \mathrm{d}^4 k \frac{1}{k^2} \left[\left(\frac{-2p_3}{k^2 + 2\left(k \cdot p_3\right)} + \frac{2p_1}{k^2 + 2\left(k \cdot p_1\right)} \right)^2 \right. \\
&\qquad \left. - k^2 \left(\frac{1}{k^2 + 2\left(k \cdot p_3\right)} - \frac{1}{k^2 + 2\left(k \cdot p_1\right)} \right)^2 \right] \\
&= \frac{i}{8\pi^3} \int \mathrm{d}^4 k \frac{1}{k^2} \left[\left(\frac{2\left(q_1 - q_2\right)}{\left(l - \left(q_1 - q_2\right)\right)^2 - \left(q_1 - q_2\right)^2} - \frac{2q_1}{\left(l + q_1\right)^2 - q_1^2} \right)^2 \right. \\
&\qquad \left. - k^2 \left(\frac{1}{\left(l - \left(q_1 - q_2\right)\right)^2 - \left(q_1 - q_2\right)^2} - \frac{1}{\left(l + q_1\right)^2 - q_1^2} \right)^2 \right] \\
&= \frac{i}{8\pi^3} i\pi^2 \left[-8\left(\left(q_1 - q_2\right) \cdot q_2\right) C_0 \left(\left(-\left(q_1 - q_2\right)\right)^2, \left(-q_1\right)^2, \left(-q_2\right)^2, 0, \left(-\left(q_1 - q_2\right)\right)^2, m_1^2 \right) \right. \\
&\qquad + 4sC_0\left(s, s, 0, 0, s, s\right) \\
&\qquad + 4m_1^2 C_0 \left(\left(-q_1\right)^2, \left(-q_1\right)^2, 0, 0, m_1^2, m_1^2 \right) \\
&\qquad + 2B_0 \left(\left(-q_2\right)^2, \left(-\left(q_1 - q_2\right)\right)^2, q_1^2 \right) \\
&\qquad - B_0 \left(0, m_1^2, m_1^2 \right) \\
&\qquad \left. - B_0 \left(0, \left(-\left(q_1 - q_2\right)\right)^2, \left(-\left(q_1 - q_2\right)\right)^2 \right) \right] \\
&= -\frac{1}{4\pi} \left[2\left(s - m_2^2 + m_1^2\right) C_0 \left(s, m_1^2, m_2^2, 0, s, m_1^2\right) \right. \\
&\qquad + 2sC_0\left(s, s, 0, 0, s, s\right) + 2m_1^2 C_0 \left(m_1^2, m_1^2, 0, 0, m_1^2, m_1^2\right) \\
&\qquad \left. + 2B_0 \left(m_2^2, s, m_1^2\right) - B_0 \left(0, m_1^2, m_1^2\right) - B_0 \left(0, s, s\right) \right].
\end{aligned}
\tag{D.2.1}
$$

Appendix E

Loop integrals

E.1 Preliminaries

Here we list the necessary scalar master integrals for the calculation of the virtual EW and the real-virtual QED corrections. Following the Binoth Les Houches Accord, we factor out an overall constant $C(\epsilon)$ [60]:

$$C(\epsilon) = \frac{(4\pi)^\epsilon}{\Gamma(1-\epsilon)} \left(\frac{\mu^2}{\mu_R^2}\right)^\epsilon = (4\pi)^\epsilon \frac{\Gamma(1+\epsilon)\Gamma(1-\epsilon)^2}{\Gamma(1-2\epsilon)} \left(\frac{\mu^2}{\mu_R^2}\right)^\epsilon . \qquad \text{(E.1.1)}$$

The analytic continuation that is necessary to properly define the integrals can be restored by continuing the arguments as:

$$p_i^2 \to p_i^2 + i\varepsilon,$$

$$s_{ij} \to s_{ij} + i\varepsilon, \qquad \text{(E.1.2)}$$

$$m_i^2 \to m_i^2 - i\varepsilon.$$

The $i\varepsilon$ is followed through each calculation to define the correct continuations of the logarithm and dilogarithm. We comment on this, and the implementation of the complex dilogarithm in Section E.6.

As in the implementation, we will collect results depending on the number of massive propagators, in each case starting with the least complicated expression and working

our way up in complexity.

E.2   Tadpole integrals

There is only one scalar tadpole integral, depending on the mass of the internal propagator m^2:

$$A_0\left(m_0^2\right) = \frac{\mu^{2\epsilon}}{i\pi^2} \int \mathrm{d}^D q \frac{1}{q^2 - m_0^2 + i\varepsilon}. \tag{E.2.1}$$

In D dimensions, this integral is of mass dimension $D - 2$, so if the mass vanishes, the integral is scaleless and vanishes as well. The tadpole integral is UV divergent. For non-vanishing scales, the result is [163]:

$$A_0\left(m_0^2\right) = m_0^2 \left(\frac{1}{\epsilon_{UV}} + \log\left(\frac{\mu^2}{m_0^2}\right) + 1\right). \tag{E.2.2}$$

E.3   Bubble integrals

The bubble integral depends on three potential mass scales in $p_1^2 = s$, m_0^2 and m_1^2, and is in itself of mass dimension $D - 4$:

$$B_0\left(p_1^2, m_0^2, m_1^2\right) = \frac{\mu^{2\epsilon}}{i\pi^2} \int \mathrm{d}^D q \frac{1}{\left(q^2 - m_0^2 + i\varepsilon\right)\left(\left(q + p_1\right)^2 - m_1^2 + i\varepsilon\right)}. \tag{E.3.1}$$

It is invariant under the exchange $m_0 \leftrightarrow m_1$, which can be achieved through a shift of the integration momentum $q' = q + p_1$ to go back to the same form. Thus $B_0\left(s, m_0^2, m_1^2\right) = B_0\left(s, m_1^2, m_0^2\right)$. The bubble integrals are UV divergent.

For later use we define r as the solution of the equation:

$$x^2 + \frac{m_0^2 + m_1^2 - s - i\varepsilon}{m_0 m_1} x + 1 = (x + r)\left(x + \frac{1}{r}\right), \tag{E.3.2}$$

so that:

$$r_+ = \frac{m_0^2 + m_1^2 - s + \sqrt{\left(m_0^2 + m_1^2 - s\right)^2 - 4m_0^2 m_1^2}}{2m_0 m_1},$$

$$r_- = \frac{m_0^2 + m_1^2 - s - \sqrt{\left(m_0^2 + m_1^2 - s\right)^2 - 4m_0^2 m_1^2}}{2m_0 m_1}. \tag{E.3.3}$$

In the results in which this quantity will be used, it does not matter which solution is used (as long as one is used consistently) so we implemented the results using $r \equiv r_+$.

- Two massless internal lines:

    - $s \neq 0$:

        [163], Eq. (4.4)

        $$B_0(s, 0, 0) = \frac{1}{\epsilon_{UV}} + \log\left(\frac{\mu^2}{-s}\right) + 2. \tag{E.3.4}$$

- One massless internal line: define $m^2 = m_0^2 + m_1^2$:

    - $s = 0$:

        $$B_0(0, 0, m^2) = \frac{1}{\epsilon_{UV}} + \log\left(\frac{\mu^2}{m^2}\right) + 1 = \frac{A_0(m^2)}{m^2}, \tag{E.3.5}$$

    - $s = m^2$:

        $$B_0(m^2, 0, m^2) = \frac{1}{\epsilon_{UV}} + \log\left(\frac{\mu^2}{m^2}\right) + 2, \tag{E.3.6}$$

    - $s \neq m^2$:

        [163], Eq. (4.4)

        $$B_0(s, 0, m^2) = \frac{1}{\epsilon_{UV}} + \log\left(\frac{\mu^2}{m^2}\right) + \frac{s - m^2}{s}\log\left(\frac{m^2}{s - m^2}\right) + 2. \tag{E.3.7}$$

- No massless internal line:

    - $s = 0$, $m_0^2 = m_1^2 = m^2$:

        $$B_0(0, m^2, m^2) = \frac{1}{\epsilon_{UV}} + \log\left(\frac{\mu^2}{m^2}\right), \tag{E.3.8}$$

    - $s \neq 0$, $m_0^2 = m_1^2 = m^2$:

        [141], Eq. (4.23) in the limit $m_0 \to m_1$

        $$B_0\left(s, m^2, m^2\right) = \frac{1}{\epsilon_{UV}} + \log\left(\frac{\mu^2}{m^2}\right) - \frac{m^2}{s}\left(\frac{1}{r} - r\right)\log\left(r\right), \tag{E.3.9}$$

− $s = 0$, $m_0^2 \neq m_1^2$:

[141], Eq. (4.23) in the limit $s \to 0$

$$B_0 \left(0, m_0^2, m_1^2 \right) = \frac{1}{\epsilon_{UV}} + 1$$
$$+ \frac{m_0^2}{m_0^2 - m_1^2} \log \left(\frac{\mu^2}{m_0^2} \right) - \frac{m_1^2}{m_0^2 - m_1^2} \log \left(\frac{\mu^2}{m_1^2} \right),$$
$$\text{(E.3.10)}$$

− $s \neq 0$, $m_0^2 \neq m_1^2$:

[141], Eq. (4.23)

$$B_0 \left(s, m_0^2, m_1^2 \right) = \frac{1}{\epsilon_{UV}} + \log \left(\frac{\mu^2}{m_0 m_1} \right)$$
$$+ \frac{m_0^2 - m_1^2}{s} \log \left(\frac{m_1}{m_0} \right) - \frac{m_0 m_1}{s} \left(\frac{1}{r} - r \right) \log (r).$$
$$\text{(E.3.11)}$$

E.4   Triangle integrals

The triangle integrals depend on two internal momenta squared p_1^2, p_2^2, with a further momentum squared $p_3^2 = (p_1 - p_2)^2$ often also given in the argument list. They further depend on the three internal masses m_0^2, m_1^2, m_2^2:

$$C_0 \left(p_1^2, p_2^2, p_3^2, m_0^2, m_1^2, m_2^2 \right) =$$
$$\frac{\mu^{2\epsilon}}{i\pi^2} \int d^D q \frac{1}{(q^2 - m_0^2 + i\varepsilon) \left((q + p_1)^2 - m_1^2 + i\varepsilon \right) \left((q + p_2)^2 - m_2^2 + i\varepsilon \right)} \quad \text{(E.4.1)}$$

These integrals are UV finite, but potentially IR divergent for particular combinations of arguments that include vanishing masses. Different sets of arguments can be related via momentum shifts: The integral is invariant under a simultaneous cyclic shift of both $\{ p_1^2, p_2^2, p_3^2 \}$ and $\{ m_0^2, m_1^2, m_2^2 \}$ (this corresponds to a momentum shift $q' = q + p_2$) as well as under the simultaneous exchange $p_2^2 \leftrightarrow p_3^2$ and $m_0^2 \leftrightarrow m_1^2$ (this corresponds to a shift $q' = q + p_1$). Thus, we can write all analytic results with the non-zero masses shifted to the right, all other results follow from repeated

application of:

$$C_0\left(p_1^2, p_2^2, p_3^2, m_0^2, m_1^2, m_2^2\right) = C_0\left(p_3^2, p_1^2, p_2^2, m_2^2, m_0^2, m_1^2\right), \qquad \text{(E.4.2)}$$

$$C_0\left(p_1^2, p_2^2, p_3^2, m_0^2, m_1^2, m_2^2\right) = C_0\left(p_1^2, p_3^2, p_2^2, m_1^2, m_0^2, m_2^2\right). \qquad \text{(E.4.3)}$$

If there is no specific, simplified formula given for a particular case of arguments, then this will be calculated either through the next general result for that set of vanishing internal masses, if it exists, or through the full finite triangle result.

We will make use of the following definitions:

$$\beta = \sqrt{1 - \frac{4m^2}{p^2}}, \qquad \text{(E.4.4)}$$

$$K\left(z, m, m'\right) = \frac{1 - \sqrt{1 - \frac{4mm'}{z-(m-m')^2}}}{1 + \sqrt{1 - \frac{4mm'}{z-(m-m')^2}}}. \qquad \text{(E.4.5)}$$

- All internal lines massless:

  - $p_1^2 = p_2^2 = 0$, $p_3^2 = s$

    [163], Eq. (4.5)

    $$C_0\left(0, 0, s, 0, 0, 0\right) = \frac{1}{s}\left[\frac{1}{\epsilon_{IR}^2} + \frac{1}{\epsilon_{IR}}\log\left(\frac{\mu^2}{-s}\right) + \frac{1}{2}\log^2\left(\frac{\mu^2}{-s}\right)\right], \quad \text{(E.4.6)}$$

  - $p_1^2 = 0$, $p_2^2 = p_3^2 = p^2$

    [163], Eq. (4.6)

    $$C_0\left(0, p^2, p^2, 0, 0, 0\right) = -\frac{1}{p^2}\left[\frac{1}{\epsilon_{IR}} + \log\left(\frac{\mu^2}{-p^2}\right)\right], \qquad \text{(E.4.7)}$$

  - $p_1^2 = 0$, $p_2^2 \neq p_3^2$

    [163], Eq. (4.7)

    $$C_0\left(0, p_2^2, p_3^2, 0, 0, 0\right) =$$
    $$\frac{1}{p_2^2 - p_3^2}\left[\frac{1}{\epsilon_{IR}}\log\left(\frac{p_3^2}{p_2^2}\right) + \frac{1}{2}\left(\log^2\left(\frac{\mu^2}{-p_2^2}\right) - \log^2\left(\frac{\mu^2}{-p_3^2}\right)\right)\right]. \quad \text{(E.4.8)}$$

- One massive internal line:

$-\ p_1^2 = p_2^2 = 0,\ p_3^2 = m^2$

[163], Eq. (4.8)

$$C_0\left(0, 0, m^2, 0, 0, m^2\right) = -\frac{1}{2m^2}\left[\frac{1}{\epsilon_{IR}^2} + \frac{1}{\epsilon_{IR}}\log\left(\frac{\mu^2}{m^2}\right)\right.$$
$$\left. + \frac{\pi^2}{6} + \frac{1}{2}\log^2\left(\frac{\mu^2}{m^2}\right)\right], \qquad \text{(E.4.9)}$$

$-\ p_1^2 = p_2^2 = 0,\ p_3^2 = p^2 \neq m^2$

$$C_0\left(0, 0, p^2, 0, 0, m^2\right) = -\frac{1}{p^2}\left[\frac{1}{\epsilon_{IR}}\log\left(\frac{m^2 - p^2}{m^2}\right)\right.$$
$$+ \log\left(\frac{\mu^2}{m^2}\right)\log\left(\frac{m^2 - p^2}{m^2}\right)$$
$$\left. - \text{Li}_2\left(\frac{p^2}{m^2}\right) - \log^2\left(\frac{m^2 - p^2}{m^2}\right)\right], \quad \text{(E.4.10)}$$

$-\ p_2^2 = p_3^2 = 0,\ p_1^2 = p^2 \neq 0$

[142], Eq. (5.59)

$$C_0\left(p^2, 0, 0, 0, 0, m^2\right) = \frac{1}{p^2}\left[\text{Li}_2\left(1\right) - \text{Li}_2\left(1 + \frac{p^2}{m^2}\right)\right], \qquad \text{(E.4.11)}$$

$-\ p_1^2 = 0,\ p_2^2 = p_3^2 = m^2$

[163], Eq. (4.12)

$$C_0\left(0, m^2, m^2, 0, 0, m^2\right) = \frac{1}{m^2}\left[-\frac{1}{2\epsilon_{IR}} - \frac{1}{2}\log\left(\frac{\mu^2}{m^2}\right) + 1\right], \quad \text{(E.4.12)}$$

$-\ p_1^2 = 0,\ p_2^2 = p_3^2 = p^2 \neq m^2$

[163], Eq. (4.9)

$$C_0\left(0, p^2, p^2, 0, 0, m^2\right) =$$
$$\frac{1}{m^2 - p^2}\left[\frac{1}{\epsilon_{IR}} + \log\left(\frac{\mu^2}{m^2}\right) + \frac{m^2 + p^2}{p^2}\log\left(\frac{m^2}{m^2 - p^2}\right)\right], \quad \text{(E.4.13)}$$

$-\ p_1^2 = 0,\ p_2^2 = p^2 \neq m^2,\ p_3^2 = m^2$

[163], Eq. (4.11)

$$C_0\left(0, p^2, m^2, 0, 0, m^2\right) = \frac{1}{(p^2 - m^2)}$$

$$\times \left[\frac{1}{2\epsilon_{IR}^2} + \frac{1}{\epsilon_{IR}} \left(\frac{1}{2} \log \left(\frac{\mu^2}{m^2} \right) + \log \left(\frac{m^2}{m^2 - p^2} \right) \right) \right.$$

$$+ \frac{1}{4} \log^2 \left(\frac{\mu^2}{m^2} \right) + \frac{1}{2} \log^2 \left(\frac{m^2}{m^2 - p^2} \right)$$

$$\left. - \text{Li}_2 \left(\frac{-p^2}{m^2 - p^2} \right) + \frac{\pi^2}{12} \right], \quad (E.4.14)$$

$- p_1^2 = 0,\ p_2^2 \neq p_3^2 \neq m^2$

[163], Eq. (4.8)

$$C_0 \left(0, p_2^2, p_3^2, 0, 0, m^2 \right) = \frac{1}{p_2^2 - p_3^2}$$

$$\times \left[\frac{1}{\epsilon_{IR}} \log \left(\frac{m^2 - p_3^2}{m^2 - p_2^2} \right) + \log \left(\frac{\mu^2}{m^2} \right) \log \left(\frac{m^2 - p_3^2}{m^2 - p_2^2} \right) \right.$$

$$+ \text{Li}_2 \left(\frac{p_2^2}{m^2} \right) + \log^2 \left(\frac{m^2 - p_2^2}{m^2} \right)$$

$$\left. - \text{Li}_2 \left(\frac{p_3^2}{m^2} \right) - \log^2 \left(\frac{m^2 - p_3^2}{m^2} \right) \right]. \quad (E.4.15)$$

- Two massive internal lines:

  $- p_1^2 = m_1^2,\ p_3^2 = m_2^2,\ p_2^2 = (m_1 - m_2)^2$

  [163], Eq. (4.16)

  $$C_0 \left(m_1^2, p_2^2, m_2^2, 0, m_1^2, m_2^2 \right) =$$

  $$\frac{1}{2m_1 m_2} \left[\frac{1}{\epsilon_{IR}} + \log \left(\frac{\mu^2}{m_1 m_2} \right) - \frac{m_1 + m_2}{m_2 - m_1} \log \left(\frac{m_1}{m_2} \right) - 2 \right], \quad (E.4.16)$$

  $- p_1^2 = m_1^2,\ p_3^2 = m_2^2,\ p_2^2 \neq (m_2 - m_3)^2$

  [163], Eq. (4.16)

  $$C_0 \left(m_1^2, p_2^2, m_2^2, 0, m_1^2, m_2^2 \right) = \frac{x_s}{m_1 m_2 \left(1 - x_s^2 \right)}$$

  $$\times \left[- \frac{1}{\epsilon_{IR}} \log \left(x_s \right) \right.$$

  $$+ \log \left(x_s \right) \left\{ - \frac{1}{2} \log \left(x_s \right) + 2 \log \left(1 - x_s^2 \right) + \log \left(\frac{m_1 m_2}{\mu^2} \right) \right\}$$

  $$+ \text{Li}_2 \left(x_s^2 \right) + \frac{1}{2} \log^2 \left(\frac{m_1}{m_2} \right) - \frac{\pi^2}{6}$$

  $$\left. + \text{Li}_2 \left(1 - x_s \frac{m_1}{m_2} \right) + \text{Li}_2 \left(1 - x_s \frac{m_2}{m_1} \right) \right], \quad (E.4.17)$$

where $x_s = -K(s, m_2, m_3)$.

- $p_1^2 = p_3^2 = 0$, $p_2^2 = p^2$, $m_1^2 = m_2^2 = m^2 \neq p^2$

  [142], Eq. (5.67)

  $$C_0\left(0, p^2, 0, 0, m^2, m^2\right) = \frac{1}{p^2} \log^2\left(\frac{\beta + 1}{\beta - 1}\right), \tag{E.4.18}$$

- $p_1^2 = p_3^2 = 0$, $p_2^2 = p^2$, $m_1^2 \neq m_2^2 \neq p^2$

  [142], Eq. (5.66)

  $$C_0\left(0, p^2, 0, 0, m_1^2, m_2^2\right) = \frac{1}{p^2} \log\left(\frac{x_2}{x_2 - 1}\right) \log\left(\frac{x_1}{x_1 - 1}\right), \tag{E.4.19}$$

  with
  $$x_{1,2} = \frac{p^2 + m_2^2 - m_1^2 \pm \sqrt{\lambda\left(p^2, m_1^2, m_2^2\right)}}{2p^2}. \tag{E.4.20}$$

- $p_1^2 = p_2^2 = 0$, $p_3^2 = p^2 \neq 0$

  [142], Eq. (5.68)

  $$C_0\left(0, 0, p^2, 0, m_1^2, m_2^2\right) =$$
  $$\frac{1}{p^2}\left[\mathrm{Li}_2\left(1 - \frac{m_2^2}{m_1^3}\right) - \mathrm{Li}_2\left(1 - \frac{m_2^2 - p_2^2}{m_1^2}\right)\right], \tag{E.4.21}$$

- $p_2^2 = 0$, $p_3^2 = m_1^2 = m_2^2 = m^2 \neq p_1^2$, $p_1^2 = p^2$

  $$C_0\left(p^2, 0, m^2, 0, m^2, m^2\right) = -\frac{1}{m^2 - p^2}\left[\frac{\pi^2}{6} - \mathrm{Li}_2\left(\frac{p^2}{m^2}\right)\right], \tag{E.4.22}$$

- $p_1^2 = p_2^2 = m_1^2 = m_2^2 = m^2$, $p_3^2 = 0$

  [163], Eq. (4.16) in the limit $m_2 \to m_3$

  $$C_0\left(m^2, m^2, 0, 0, m^2, m^2\right) = \frac{1}{2m^2}\left[\frac{1}{\epsilon_{IR}} + \log\left(\frac{\mu^2}{m^2}\right) - 4\right]. \tag{E.4.23}$$

- All massive internal lines:

  - $p_1^2 = p_2^2 = m^2$, $p_3^2 = s$, $m_2^2 = m_3^2 = m^2$, $m_1^2 = \lambda^2$

    This is the infrared divergent triangle with two massive internal lines, regulated through a small photon mass λ. It can be found from the

version in dimensional regularization Eq. (E.4.17) by replacing

$$\frac{C(\epsilon)}{\epsilon_{IR}} + \log \mu^2 \to \log \lambda^2 + \mathcal{O}(\epsilon), \tag{E.4.24}$$

a replacement which is valid in the case of a single soft singularity. The integral then reads:

$$C_0\left(m^2, m^2, s, \lambda^2, m^2, m^2\right) =$$
$$\frac{1}{s}\left[-\log\left(\frac{\lambda^2}{m^2}\right)\log\left(\frac{-s}{m^2}\right) + \frac{1}{2}\log^2\left(\frac{-s}{m^2}\right) - \frac{\pi^2}{6}\right]. \tag{E.4.25}$$

$- \ p_1^2 = p_2^2 = m^2, \ p_3^2 = 0, \ m_2^2 = m_3^2 = m^2, \ m_1^2 = \lambda^2$

This is the infrared divergent triangle with two massive internal lines and vanishing p_3^2, regulated through a small photon mass λ. It reads:

$$C_0\left(m^2, m^2, 0, \lambda^2, m^2, m^2\right) = \frac{1}{2m^2}\left[\log\left(\frac{\lambda^2}{m^2}\right) - 4\right]. \tag{E.4.26}$$

$- \ p_1^2 = p_2^2 = 0, \ p_3^2 = p^2, \ m_1^2 = m_2^2 = m_3^2 = m^2$

[245], Finite Triangle 3

$$C_0\left(0, 0, p^2, m^2, m^2, m^2\right) = \frac{1}{2p^2}\log^2\left(\frac{\beta - 1}{\beta + 1}\right), \tag{E.4.27}$$

$- \ p_1^2 = 0, \ p_2^2 \neq p_3^2, \ m_1^2 = m_2^2 = m_3^2 = m^2$

[245], Finite Triangle 4

$$C_0\left(0, p_2^2, p_3^2, m^2, m^2, m^2\right) =$$
$$\frac{1}{p_2^2 - p_3^2}\left[p_2^2 C_0\left(0, 0, p_2^2, m^2, m^2, m^2\right) - p_3^2 C_0\left(0, 0, p_3^2, m^2, m^2, m^2\right)\right].$$
$$\tag{E.4.28}$$

$- \ p_1^2 \neq p_2^2 \neq p_3^2$

The general result for the triangle result was derived in [246] for complex masses. Some parts of the calculation only contribute for complex masses. The expression as written here follows [141]. In the following, we introduce

the η-function:

$$\eta(a,b) = 2\pi i \Big[\theta\left(-\mathrm{Im}(a)\right) \theta\left(-\mathrm{Im}(b)\right) \theta\left(\mathrm{Im}(ab)\right)$$

$$- \theta\left(\mathrm{Im}(a)\right) \theta\left(\mathrm{Im}(b)\right) \theta\left(-\mathrm{Im}(ab)\right) \Big]. \qquad \text{(E.4.29)}$$

This function compensates for cut crossings in the logarithms and dilog-aritms. In particular, we have

$$\log(ab) = \log(a) + \log(b) + \eta(a,b). \qquad \text{(E.4.30)}$$

η vanishes if a and b have differing signs in their imaginary parts.

We define the following quantities where $i,j,k = \{1,2,3\}/\{0,1,2\}$ for momenta and masses respectively and the indices are taken to be cyclic:

$$\alpha = \sqrt{\lambda\left(p_1^2, p_2^2, p_3^2\right)}, \qquad \text{(E.4.31)}$$

$$\alpha_i = \sqrt{\lambda\left(p_j^2, m_j^2, m_k^2\right)\left(1 + i\varepsilon p_j^2\right)}, \qquad \text{(E.4.32)}$$

$$x_{i\pm} = \frac{1}{2p_j^2}\left(p_j^2 - m_j^2 + m_k^2 \pm \alpha_i\right), \qquad \text{(E.4.33)}$$

$$y_{0i} = \frac{1}{2\alpha p_j^2}\Big[p_j^2\left(p_j^2 - p_i^2 - p_k^2 + 2m_i^2 - m_j^2 - m_k^2\right), \qquad \text{(E.4.34)}$$

$$- \left(p_k^2 - p_i^2\right)\left(m_j^2 - m_k^2\right) + \alpha\left(p_j^2 - m_j^2 + m_k^2\right)\Big], \qquad \text{(E.4.35)}$$

$$y_{i\pm} = y_{0i} - x_{i\pm}. \qquad \text{(E.4.36)}$$

The result for the triangle integral is then given by:

$$C_0\left(p_1^2, p_2^2, p_3^2, m_0^2, m_1^2, m_2^2\right) =$$

$$\frac{1}{\alpha}\sum_{i=1}^{2}\Bigg\{\sum_{\sigma=\pm}\Bigg[\mathrm{Li}_2\left(\frac{y_{0i}-1}{y_{i\sigma}}\right) - \mathrm{Li}_2\left(\frac{y_{0i}}{y_{i\sigma}}\right)$$

$$+ \eta\left(1 - x_{i\sigma}, \frac{1}{y_{i\sigma}}\right)\log\left(\frac{y_{0i}-1}{y_{i\sigma}}\right) - \eta\left(-x_{i\sigma}, \frac{1}{y_{i\sigma}}\right)\log\left(\frac{y_{0i}}{y_{i\sigma}}\right)\Bigg]$$

$$- \Bigg[\eta\left(-x_{i+}, -x_{i-}\right) - \eta\left(y_{i+}, y_{i-}\right)$$

$$- 2\pi i\theta\left(-p_j^2\right)\theta\left(-\mathrm{Im}\left(y_{i+}y_{i-}\right)\right)\Bigg]\log\left(\frac{1 - y_{0i}}{-y_{0i}}\right)\Bigg\}. \qquad \text{(E.4.37)}$$

Note that all the η-functions vanish if all masses are real and α is real as

well. This is the case for all on-shell decay and scattering processes.

E.5   Box integrals

The box integrals depend on four internal momenta squared, $p_1^2, p_2^2, p_3^2, p_4^2$, four internal masses, $m_0^2, m_1^2, m_2^2, m_3^2$ as well as two independent momentum invariants between two external particles, usually chosen as s_{12}, s_{23}. The latter are necessary to completely determine the external kinematics of the process, which was not necessary before. We then have:

$$D_0\left(p_1^2, p_2^2, p_3^2, p_4^2; s_{12}, s_{23}; m_0^2, m_1^2, m_2^2, m_3^2\right) = \frac{\mu^{2\epsilon}}{i\pi^2}$$
$$\int \mathrm{d}^D q \frac{1}{\left(q^2 - m_0^2 + i\varepsilon\right)\left((q+p_1)^2 - m_1^2 + i\varepsilon\right)\left((q+p_2)^2 - m_2^2 + i\varepsilon\right)\left((q+p_3)^2 - m_3^2 + i\varepsilon\right)}.$$
$$(\text{E.5.1})$$

As in the case of the triangle integrals, different orderings of the parameters are related to each other through a redefinition of the loop momentum. The identities for the boxes are:

$$D_0\left(p_1^2, p_2^2, p_3^2, p_4^2; s_{12}, s_{23}; m_0^2, m_1^2, m_2^2, m_3^2\right) = D_0\left(p_2^2, p_3^2, p_4^2, p_1^2; s_{23}, s_{12}; m_1^2, m_2^2, m_3^2, m_0^2\right),$$
$$(\text{E.5.2})$$

$$D_0\left(p_1^2, p_2^2, p_3^2, p_4^2; s_{12}, s_{23}; m_0^2, m_1^2, m_2^2, m_3^2\right) = D_0\left(p_4^2, p_3^2, p_2^2, p_1^2; s_{12}, s_{23}; m_0^2, m_3^2, m_2^2, m_1^2\right).$$
$$(\text{E.5.3})$$

There are in general 16 infrared divergent boxes, and the full finite box has been worked out as well. Here, we will only list the one box integral that will be necessary for the evaluation of the real virtual corrections to particle decays into two fermions, namely the box integral with three non-vanishing internal masses. The result for $s_{23} \neq (m_1 - m_3)^2$ is:

$$D_0\left(p_1^2, p_2^2, p_3^2, p_4^2; s_{12}, s_{23}; 0, m_1^2, m_2^2, m_3^2\right) = \frac{x_{23}}{m_1 m_3 \left(s_{12} - m_2^2\right)\left(1 - x_{23}^2\right)}$$
$$\times \left\{ -\frac{\log x_{23}}{\epsilon_{IR}} - 2\log x_{23} \log\left(\frac{m_2\mu}{m_2^2 - s_{12}}\right) + \log^2 x_2 + \log^2 x_3 - \mathrm{Li}_2\left(1 - x_{23}^2\right) \right.$$

$$\text{Li}_2\left(1 - x_{23}x_2 x_3\right) + \text{Li}_2\left(1 - \frac{x_{23}}{x_2 x_3}\right) + \text{Li}_2\left(1 - \frac{x_{23}x_2}{x_3}\right) + \text{Li}_2\left(1 - \frac{x_{23}x_3}{x_2}\right)\Bigg\},$$

$$(\text{E.5.4})$$

where $x_{23} = -K\left(s_{23}, m_1, m_3\right)$, $x_2 = -K\left(p_2^2, m_1, m_2\right)$ and $x_3 = -K\left(p_3^2, m_2, m_3\right)$.

When $x_{23} \to 1$ (equivalent to $s_{23} = (m_1 - m_3)^2$), we have:

$$D_0\left(p_1^2, p_2^2, p_3^2, p_4^2; s_{12}, s_{23}; 0, m_1^2, m_2^2, m_3^2\right) = \frac{1}{2m_1 m_3\left(s_{12} - m_2^2\right)}$$
$$\times \Bigg\{ \frac{1}{\epsilon_{IR}} + 2\log\left(\frac{m_2 \mu}{m_2^2 - s_{12}}\right) - \frac{1 + x_2 x_3}{1 - x_2 x_3}\left[\log x_2 + \log x_3\right]$$
$$- \frac{x_3 + x_2}{x_3 - x_2}\left[\log x_2 - \log x_3\right] - 2\Bigg\}.$$

$$(\text{E.5.5})$$

E.6 Note on logarithms, dilogarithms and the $i\varepsilon$-prescription

As seen in the original definition of the master integrals, the denominator functions contain small imaginary parts $i\varepsilon$. These are introduced in order to make sense of the integral and define the correct time ordering.

The $i\varepsilon$ propagate through into the results to define the proper analytic continuation of functions containing branch cuts. These are for example the complex logarithm and the dilogarithm, both for negative real values of the argument. The $i\varepsilon$-description then determines on which side of the branch cut the argument sits, and thus determines the sign of the imaginary part of the result.

Logarithm

For the logarithm the $i\varepsilon$-description leads to the following identities (where $\text{Re}(z) < 0$ and $\text{Im}(z) = 0$):

$$\log(z + i\varepsilon) = \log(|z|) + i\pi,$$

$$(\text{E.6.1})$$

$$\log(z - i\varepsilon) = \log(|z|) - i\pi.$$

$$(\text{E.6.2})$$

In the case in which z has a non-vanishing imaginary part, this prescription is inconsequential as the imaginary part dominates. However, for negative real arguments, one has to keep track of this small imaginary part in order to get the results correct.

C++ natively implements a complex logarithm function `log(std::complex<double>)`. Let us denote a `std::complex<double>` as `Complex`. This native complex logarithm function determines the imaginary part in the case of $\text{Re}(z) < 0$ and $\text{Im}(z) = 0$ by keeping the sign of the imaginary part. Then, `z = Complex(z,0.0)` will be treated using Eq. (E.6.1) whereas `z = Complex(z,-0.0)` will be treated using Eq. (E.6.2). A logarithm of a negative `double` will instead return `nan`. With this functionality alone, it quickly becomes tricky keeping track of each of the signs across additions and multiplications, in particular if in use z can be either real or complex.

It is thus prudent to implement a separate, overloaded, function, which we call `CLog`. It takes as its input either a `double` or `Complex` z and an `int` *ieps*, which is the sign attached to $i\varepsilon$, and returns a `Complex`. For a `double` z as input, this function returns the normal logarithm for any $z > 0$ in the form `Complex(log(z),0.)`. For $z < 0$, it returns `Complex(log(-z),0.)+Complex(0.,ieps*`π`)`. For a `Complex` z as input, the function returns the normal logarithm unless $\text{Im}(z) = 0$ and $\text{Re}(z) < 0$ in which case it returns `Complex(log(-Re(z)),0.)+Complex(0.,ieps*`π`)`.

Dilogarithm

The dilogarithm is not natively implemented in C++. We require an implementation for potentially complex arguments of the dilogarithm, which can occur even if all masses are real.

Here, we follow the example of [164], who base their implementation on [247] and [248]. The (Euler) dilogarithm is defined as

$$\text{Li}_2(x) = -\int_0^x dy \frac{\log(1-y)}{y} = -\int_0^1 dy \frac{\log(1-xy)}{y} = \int_0^{-\log(1-x)} du \frac{u}{e^u - 1}. \quad \text{(E.6.3)}$$

Integrating term by term in a series expansion of the logarithm, we find the following

series expansion:

$$\text{Li}_2(x) = \sum_{j=1}^{\infty} \frac{x^j}{j^2}, \tag{E.6.4}$$

which is valid for $|x| < 1$. For $|x| > 1$, one can use an inversion relation to map the argument back into the convergent region. For the dilogarithm, this inversion relation reads:

$$\text{Li}_2(x) = -\text{Li}_2\left(\frac{1}{x}\right) - \frac{1}{2}\log^2(-x) - \frac{\pi^2}{6}. \tag{E.6.5}$$

The convergence of the series Eq. (E.6.4) is poor close to $|x| = 1$. This can however be circumvented by an expansion instead in the logarithm of the argument, as proposed by [247]:

$$\text{Li}_2\left(e^{-\alpha}\right) = \frac{\pi^2}{6} - \alpha - \frac{1}{4}\alpha^2 + \alpha\log(\alpha) + \sum_{n=1}^{\infty} \frac{B_{2n}}{2n(2n+1)!}\alpha^{2n+1}, \tag{E.6.6}$$

where the B_i are the Bernoulli numbers. The factorial decay of the terms in the sum means a fast convergence even for $|x| \approx 1$. Based on similar considerations, one can find an expression that involves a factorial decay within the region $|x| < \frac{1}{2}$:

$$\text{Li}_2\left(1 - e^{-\alpha}\right) = \alpha - \frac{1}{4}\alpha^2 + \sum_{n=1}^{\infty} \frac{B_{2n}}{(2n+1)!}\alpha^{2n+1}. \tag{E.6.7}$$

We calculate the dilogarithm for any value x by Eq. (E.6.7) for $\text{Re}(x) \leq \frac{1}{2}$ and $|x| \leq 1$, by Eq. (E.6.6) for $\text{Re}(x) > \frac{1}{2}$ and $|x - 1| \leq 1$, and use the inversion relation Eq. (E.6.5) to map any other value into one of the aforementioned regions.

Appendix F

Real corrections in the YFS formalism

In this appendix we will describe our approach to implementing real corrections for the decays considered in Part I, focussing on the procedure for the decays of the vector bosons. We define the shorthand $\Gamma^\mu \equiv \gamma^\mu (c_L P_L + c_R P_R)$, with the couplings $c_{L/R}$ given in C. For the decays of a scalar boson, this reduces instead to $\Gamma = (c_L P_L + c_R P_R)$ and the polarization vector is removed from the amplitude.

In the following, we will make use of two functions X and Y that describe the helicity amplitudes. The calculation of these functions has been outlined in [49, 54], and is based on the work in [153–155]. The functions are defined as:

$$X (p_1, s_1; p; p_2, s_2; c_R, c_L) = \bar{u} (p_1, s_1) \not{p} [c_R P_R + c_L P_L] u (p_2, s_2), \qquad \text{(F.0.1)}$$

where the u may be particle or anti-particle spinors. The latter case will be denoted through a bar over the spin index s_i. Similarly, we can define another function Y:

$$Y (p_1, s_1; p; p_2, s_2; c_R, c_L) = \bar{u} (p_1, s_1) [c_R P_R + c_L P_L] u (p_2, s_2), \qquad \text{(F.0.2)}$$

which would be used in the decay of a Higgs boson.

F.1   Single Real

The real matrix element for the process $Z \to f\bar{f}\gamma$ reads:

$$
\mathcal{M}_1^{\frac{1}{2}} = ie^2 \bar{u}\left(p_1, s_1\right)\left[\gamma^\nu \frac{\not{p}_1 + \not{k} + m}{\left(p_1 + k\right)^2 - m^2}\Gamma^\mu\right.
$$
$$
\left. - \Gamma^\mu \frac{\not{p}_2 + \not{k} - m}{\left(p_2 + k\right)^2 - m^2}\gamma^\nu\right]v\left(p_2, s_2\right)\epsilon_\mu^Z(p, \lambda)\epsilon_\nu^{\gamma*}\left(k, \kappa\right). \quad \text{(F.1.1)}
$$

We can express a fermion propagator as a sum over spins of an intermediate particle:

$$
\not{p} \pm m = \frac{1}{2}\sum_s \left[\left(1 \pm \frac{m}{\sqrt{p^2}}\right)u(p, s)\bar{u}(p, s) + \left(1 \mp \frac{m}{\sqrt{p^2}}\right)v(p, s)\bar{v}(p, s)\right], \quad \text{(F.1.2)}
$$

where $u[v](p, s)$ are [anti-]spinors of a fictitious fermion with mass $m = \sqrt{p^2}$.

We can then write the full amplitude in terms of helicity amplitudes:

$$
\mathcal{M}_1^{\frac{1}{2}} = \frac{ie^2}{2}\left[\frac{1}{\left(p_a\right)^2 - m^2}\sum_s\left\{\left(1 + \frac{m}{\sqrt{\left(p_a\right)^2}}\right) X\left(s_1, \epsilon^{\gamma*}, p_a, s\right) X\left(p_a, s, \epsilon^Z, \bar{s}_2\right)\right.\right.
$$
$$
\left. + \left(1 - \frac{m}{\sqrt{\left(p_a\right)^2}}\right) X\left(s_1, \epsilon^{\gamma*}, p_a, \bar{s}\right) X\left(p_a, \bar{s}, \epsilon^Z, \bar{s}_2\right)\right\}
$$
$$
- \frac{1}{\left(p_b\right)^2 - m^2}\sum_s\left\{\left(1 - \frac{m}{\sqrt{\left(p_b\right)^2}}\right) X\left(s_1, \epsilon^Z, p_b, s\right) X\left(p_b, s, \epsilon^{\gamma*}, \bar{s}_2\right)\right.
$$
$$
\left.\left. + \left(1 + \frac{m}{\sqrt{\left(p_b\right)^2}}\right) X\left(s_1, \epsilon^Z, p_b, \bar{s}\right) X\left(p_b, \bar{s}, \epsilon^{\gamma*}, \bar{s}_2\right)\right\}\right], \quad \text{(F.1.3)}
$$

with

$$
p_a = p_1 + k \qquad\qquad p_b = p_2 + k. \qquad\qquad \text{(F.1.4)}
$$

To reduce the size of the expressions, we have only written the spin labels, the intermediate momenta and the respective internal vector. It is understood that the spin label $s_{1,2}$ corresponds to the momentum $p_{1,2}$. It is further understood that the left- and right-handed couplings are $(-ie, -ie)$ when contracted with a photon polarization and (c_L, c_R) when contracted with the Z-polarization.

For the decay of a W-boson, we have the following real matrix element:

$$
\mathcal{M}_1^{\frac{1}{2}} = ie^2 \epsilon_\tau^W(p, \lambda)\epsilon_\nu^{\gamma*}\left(k, \kappa\right)\bar{u}\left(p_1, s_1\right)
$$

$$\times \left[\gamma^\nu \frac{\not{p}_1 + \not{k} + m}{(p_1 + k)^2 - m^2} \Gamma^\tau \right. \tag{F.1.5}$$

$$\left. + \Gamma^\mu \frac{g_{\mu\rho} - \frac{(p-k)_\mu (p-k)_\rho}{p^2}}{(p - k)^2 - p^2} V_{\tau\rho\nu} (p, -p + k, -k) \right] v (p_2, s_2),$$

where we introduced the triple boson vertex $V_{\tau\rho\nu} = g_{\tau\rho} (p_2 - p_1)_\nu + g_{\rho\nu} (p_3 - p_2)_\tau + g_{\nu\tau} (p_1 - p_3)_\rho$. The first term can be treated as in the case of the Z-decay, while the second term, upon contraction of all indices, is already in the form of an X-function.

F.2 Double Real

For the process $Z \to f\bar{f}\gamma\gamma$, the double real matrix element reads:

$$\mathcal{M}_2^1 = ie^3 \epsilon_\mu^Z(p, \lambda) \epsilon_\nu^{\gamma*} (k_1, \kappa_1) \epsilon_\rho^{\gamma*} (k_2, \kappa_2) \bar{u} (p_1, s_1)$$

$$\left[\gamma^\nu \frac{\not{p}_1 + \not{k}_1 + m}{(p_1 + k_1)^2 - m^2} \gamma^\rho \frac{\not{p}_1 + \not{k}_1 + \not{k}_2 + m}{(p_1 + k_1 + k_2)^2 - m^2} \Gamma^\mu \right.$$

$$- \gamma^\nu \frac{\not{p}_1 + \not{k}_1 + m}{(p_1 + k_1)^2 - m^2} \Gamma^\mu \frac{\not{p}_2 + \not{k}_2 - m}{(p_2 + k_2)^2 - m^2} \gamma^\rho \tag{F.2.1}$$

$$+ \Gamma^\mu \frac{\not{p}_2 + \not{k}_1 + \not{k}_2 - m}{(p_2 + k_1 + k_2)^2 - m^2} \gamma^\nu \frac{\not{p}_2 + \not{k}_2 - m}{(p_2 + k_2)^2 - m^2} \gamma^\rho$$

$$\left. + (k_1 \leftrightarrow k_2) \right] v (p_2, s_2).$$

Replacing the propagators, we can rewrite the matrix element as follows:

$$\mathcal{M}_2^1 = \frac{ie^3}{4} \left[\frac{1}{(p_{b,1})^2 - m^2} \frac{1}{(p_{a,1})^2 - m^2} \sum_{s_a, s_b} \right.$$

$$\left\{ \left(1 + \frac{m}{\sqrt{(p_{a,1})^2}} \right) \left(1 + \frac{m}{\sqrt{(p_{b,1})^2}} \right) X \left(s_1, \epsilon_1^{\gamma*}, p_{a,1}, s_a \right) X \left(p_{a,1}, s_a, \epsilon_2^{\gamma*}, p_{b,1}, s_b \right) X \left(p_{b,1}, s_b, \epsilon^Z, \bar{s}_2 \right) \right.$$

$$+ \left(1 + \frac{m}{\sqrt{(p_{a,1})^2}} \right) \left(1 - \frac{m}{\sqrt{(p_{b,1})^2}} \right) X \left(s_1, \epsilon_1^{\gamma*}, p_{a,1}, s_a \right) X \left(p_{a,1}, s_a, \epsilon_2^{\gamma*}, p_{b,1}, \bar{s}_b \right) X \left(p_{b,1}, \bar{s}_b, \epsilon^Z, \bar{s}_2 \right)$$

$$+ \left(1 - \frac{m}{\sqrt{(p_{a,1})^2}} \right) \left(1 + \frac{m}{\sqrt{(p_{b,1})^2}} \right) X \left(s_1, \epsilon_1^{\gamma*}, p_{a,1}, \bar{s}_a \right) X \left(p_{a,1}, \bar{s}_a, \epsilon_2^{\gamma*}, p_{b,1}, s_b \right) X \left(p_{b,1}, s_b, \epsilon^Z, \bar{s}_2 \right)$$

$$\left. + \left(1 - \frac{m}{\sqrt{(p_{a,1})^2}} \right) \left(1 - \frac{m}{\sqrt{(p_{b,1})^2}} \right) X \left(s_1, \epsilon_1^{\gamma*}, p_{a,1}, \bar{s}_a \right) X \left(p_{a,1}, \bar{s}_a, \epsilon_2^{\gamma*}, p_{b,1}, \bar{s}_b \right) X \left(p_{b,1}, \bar{s}_b, \epsilon^Z, \bar{s}_2 \right) \right\}$$

$$- \frac{1}{(p_{a,2})^2 - m^2} \frac{1}{(p_{b,2})^2 - m^2} \sum_{s_a, s_b}$$

$$\Bigg\{\left(1+\frac{m}{\sqrt{\left(p_{a,2}\right)^2}}\right)\left(1-\frac{m}{\sqrt{\left(p_{b,2}\right)^2}}\right) X\left(s_1,\epsilon_1^{\gamma*},p_{a,2},s_a\right) X\left(p_{a,2},s_a,\epsilon^Z,p_{b,2},s_b\right) X\left(p_{b,2},s_b,\epsilon_2^{\gamma*},\bar{s}_2\right)$$

$$+\left(1+\frac{m}{\sqrt{\left(p_{a,2}\right)^2}}\right)\left(1+\frac{m}{\sqrt{\left(p_{b,2}\right)^2}}\right) X\left(s_1,\epsilon_1^{\gamma*},p_{a,2},s_a\right) X\left(p_{a,2},s_a,\epsilon^Z,p_{b,2},\bar{s}_b\right) X\left(p_{b,2},\bar{s}_b,\epsilon_2^{\gamma*},\bar{s}_2\right)$$

$$+\left(1-\frac{m}{\sqrt{\left(p_{a,2}\right)^2}}\right)\left(1-\frac{m}{\sqrt{\left(p_{b,2}\right)^2}}\right) X\left(s_1,\epsilon_1^{\gamma*},p_{a,2},\bar{s}_a\right) X\left(p_{a,2},\bar{s}_a,\epsilon^Z,p_{b,2},s_b\right) X\left(p_{b,2},s_b,\epsilon_2^{\gamma*},\bar{s}_2\right)$$

$$+\left(1-\frac{m}{\sqrt{\left(p_{a,2}\right)^2}}\right)\left(1+\frac{m}{\sqrt{\left(p_{b,2}\right)^2}}\right) X\left(s_1,\epsilon_1^{\gamma*},p_{a,2},\bar{s}_a\right) X\left(p_{a,2},\bar{s}_a,\epsilon^Z,p_{b,2},\bar{s}_b\right) X\left(p_{b,2},\bar{s}_b,\epsilon_2^{\gamma*},\bar{s}_2\right)\Bigg\}$$

$$+\frac{1}{\left(p_{a,3}\right)^2-m^2}\frac{1}{\left(p_{b,3}\right)^2-m^2}\sum_{s_a,s_b}$$

$$\Bigg\{\left(1-\frac{m}{\sqrt{\left(p_{a,3}\right)^2}}\right)\left(1-\frac{m}{\sqrt{\left(p_{b,3}\right)^2}}\right) X\left(s_1,\epsilon^Z,p_{a,3},s_a\right) X\left(p_{a,3},s_a,\epsilon_1^{\gamma*},p_{b,3},s_b\right) X\left(p_{b,3},s_b,\epsilon_2^{\gamma*},\bar{s}_2\right)$$

$$+\left(1-\frac{m}{\sqrt{\left(p_{a,3}\right)^2}}\right)\left(1+\frac{m}{\sqrt{\left(p_{b,3}\right)^2}}\right) X\left(s_1,\epsilon^Z,p_{a,3},s_a\right) X\left(p_{a,3},s_a,\epsilon_1^{\gamma*},p_{b,3},\bar{s}_b\right) X\left(p_{b,3},\bar{s}_b,\epsilon_2^{\gamma*},\bar{s}_2\right)$$

$$+\left(1+\frac{m}{\sqrt{\left(p_{a,3}\right)^2}}\right)\left(1-\frac{m}{\sqrt{\left(p_{b,3}\right)^2}}\right) X\left(s_1,\epsilon^Z,p_{a,3},\bar{s}_a\right) X\left(p_{a,3},\bar{s}_a,\epsilon_1^{\gamma*},p_{b,3},s_b\right) X\left(p_{b,3},s_b,\epsilon_2^{\gamma*},\bar{s}_2\right)$$

$$+\left(1+\frac{m}{\sqrt{\left(p_{a,3}\right)^2}}\right)\left(1+\frac{m}{\sqrt{\left(p_{b,3}\right)^2}}\right) X\left(s_1,\epsilon^Z,p_{a,3},\bar{s}_a\right) X\left(p_{a,3},\bar{s}_a,\epsilon_1^{\gamma*},p_{b,3},\bar{s}_b\right) X\left(p_{b,3},\bar{s}_b,\epsilon_2^{\gamma*},\bar{s}_2\right)\Bigg\}$$

$$+\ (k_1\leftrightarrow k_2)\Bigg]. \tag{F.2.2}$$

In this equation, we abbreviated the intermediate momenta as:

$$p_{a,1}=p_1+k_1, \qquad\qquad p_{b,1}=p_1+k_1+k_2,$$

$$p_{a,2}=p_1+k_1, \qquad\qquad p_{b,2}=p_2+k_2, \tag{F.2.3}$$

$$p_{a,3}=p_2+k_1+k_2, \qquad\qquad p_{b,3}=p_2+k_2.$$

Appendix G

Validation of EW corrections

G.1 Internal consistency of the implementation

G.1.1 Matrix elements

Given the complexity and the modular setup of the expressions for the real matrix elements, the fulfillment of the QED Ward identity is a good check on the validity of the expressions. We verified that the matrix elements obey the Ward identity within machine precision, with the double real expressions obeying the identity also separately for $\epsilon_i \to k_i$.

Similarly, in the virtual corrections, the cancellation of both UV and IR divergences has been confirmed analytically, as well as numerically at machine precision.

The matrix elements have been point-checked against implementations in OPENLOOPS [39,40] for the virtual corrections, and against both WZGRAD [24–26] and AMEGIC [54] for the fully massive real matrix elements.

We also checked that the subtraction outlined in Chapters 4 and 5 becomes exact in the limit of soft photon emission. In the Tables G.1 - G.3 we collect the largest order of magnitude observed for the deviation $\Delta = \frac{ME - \tilde{S} \otimes B}{ME}$ for photons with $E < 2E_{\gamma,\text{cut}}$ in 10^4 decays to electrons, muons and τ's respectively. For the double

$E_{\gamma,\text{cut}}$		$Z \to e^+e^-$	$W \to e\nu$
100 MeV	R	10^{-3}	10^{-3}
	RV	10^{-2}	-
	RR, 1	10^{-2}	-
	RR, 2	10^{-4}	-
10 MeV	R	10^{-5}	10^{-5}
	RV	10^{-4}	-
	RR, 1	10^{-3}	-
	RR, 2	10^{-4}	-
1 MeV	R	10^{-6}	10^{-5}
	RV	10^{-5}	-
	RR, 1	10^{-1}	-
	RR, 2	10^{-1}	-
100 keV	R	10^{-2}	10^{-2}
	RV	10^{-2}	-
	RR, 1	10^{-1}	-
	RR, 2	10^{-1}	-

Table G.1: Magnitude of maximal difference $\Delta = \frac{ME - \tilde{S} \otimes B}{ME}$ observed for 10^4 decays into electrons and varying infrared cutoffs. In the real (R) and real-virtual (RV) cases, we require the photon to have an energy $E < 2E_{\gamma,\text{cut}}$. For the real-real, we consider two cases: 1. One photon has energy $E < 2E_{\gamma,\text{cut}}$, the other one $E > 1\,\text{GeV}$; 2. both photons have $E < 2E_{\gamma,\text{cut}}$.

$E_{\gamma,\mathrm{cut}}$		$Z \to \mu^+\mu^-$	$H \to \mu^+\mu^-$	$W \to \mu\nu$
100 MeV	R	10^{-6}	10^{-5}	10^{-4}
	RV	10^{-5}	10^{-5}	-
	RR, 1	10^{-2}	10^{-2}	-
	RR, 2	10^{-5}	10^{-4}	-
10 MeV	R	10^{-7}	10^{-7}	10^{-6}
	RV	10^{-6}	10^{-6}	-
	RR, 1	10^{-3}	10^{-3}	-
	RR, 2	10^{-5}	10^{-6}	-
1 MeV	R	10^{-7}	10^{-7}	10^{-7}
	RV	10^{-6}	10^{-6}	-
	RR, 1	10^{-4}	10^{-4}	-
	RR, 2	10^{-6}	10^{-6}	-
100 keV	R	10^{-6}	10^{-7}	10^{-6}
	RV	10^{-6}	10^{-6}	-
	RR, 1	10^{-5}	10^{-5}	-
	RR, 2	10^{-6}	10^{-7}	-

Table G.2: Magnitude of maximal difference $\Delta = \frac{ME - \tilde{S} \otimes B}{ME}$ observed for 10^4 decays into muons and varying infrared cutoffs. The cases are defined as in Table G.1.

$E_{\gamma,\mathrm{cut}}$		$Z \to \tau^+\tau^-$	$H \to \tau^+\tau^-$	$W \to \tau\nu$
100 MeV	R	10^{-5}	10^{-6}	10^{-5}
	RV	10^{-3}	10^{-4}	-
	RR, 1	10^{-2}	10^{-3}	-
	RR, 2	10^{-4}	10^{-5}	-
10 MeV	R	10^{-7}	10^{-7}	10^{-7}
	RV	10^{-4}	10^{-4}	-
	RR, 1	10^{-4}	10^{-5}	-
	RR, 2	10^{-5}	10^{-6}	-
1 MeV	R	10^{-9}	10^{-9}	10^{-8}
	RV	10^{-4}	10^{-4}	-
	RR, 1	10^{-4}	10^{-5}	-
	RR, 2	10^{-6}	10^{-6}	-
100 keV	R	10^{-8}	10^{-10}	10^{-8}
	RV	10^{-4}	10^{-4}	-
	RR, 1	10^{-5}	10^{-5}	-
	RR, 2	10^{-6}	10^{-7}	-

Table G.3: Magnitude of maximal difference $\Delta = \frac{ME - \tilde{S} \otimes B}{ME}$ observed for 10^4 decays into τ's and varying infrared cutoffs. The cases are defined as in Table G.1.
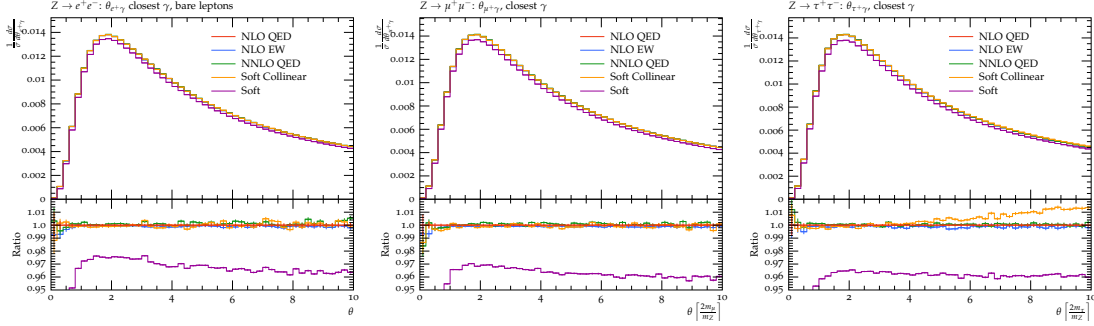
Figure G.1: The extent of the dead cone in Z-boson decays into bare electrons on the left, muons in the middle and τ's on the right. The angle $\theta_{\ell^+\gamma}$ between the positively charged lepton and the photon in the center of mass frame of the lepton system is plotted in units of $2m_\ell/m_Z$, which puts all the leptons on the same footing. Note the peak position denoting the extent of the dead cone does not change upon the inclusion of higher order corrections.

real matrix elements, we provide two cases in which either both photons have an energy $E < 2E_{\gamma,\text{cut}}$ or one photon fulfills this condition, while the other has an energy $E > 1\,\text{GeV}$.

Generally, the cancellation improves for decreasing values of the infrared cutoff as the soft approximation becomes more justified. In the case of decays into electrons, we start to see the performance worsen again for values of the cutoff of $E_{\gamma,\text{cut}} < 1\,\text{MeV}$ in the single real matrix elements, and for cutoffs as high as $10\,\text{MeV}$ in the double real matrix elements. This marks the region in which the two terms reach the limits of `double` precision. In the real-virtual, the performance plateaus when most of the events are described by the soft-collinear approximation, and many of the other points are not stable enough. In the double real matrix elements, the approximation does not work as well if one of the photons is fairly hard. This can be traced to configurations in which this photon is quasi-collinear to the emitting lepton, a configuration which is not well described by the soft approximation.

G.1.2 Parameter dependence

At a distributional level, our implementation of higher order corrections allows for a number of further cross checks. Due to the mass of the leptons, the collinear
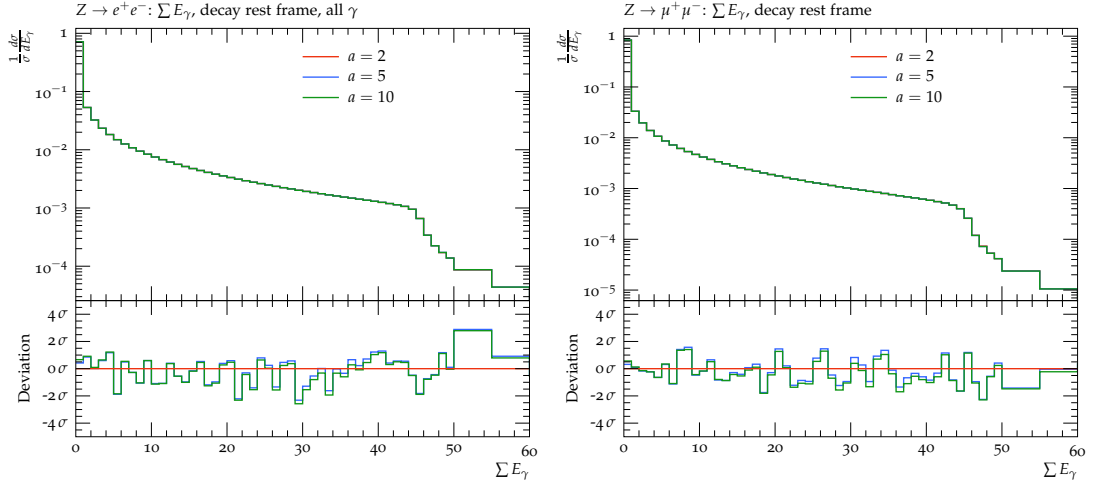
Figure G.2: The effect of varying the cut a in the RV terms. This cut was introduced in 5.3.2 in order to prevent numerical instabilities in highly collinear regions of phase space. Z-boson decays into bare electrons on the left, muons on the right.

singularity is screened and very collinear radiation is suppressed. This results in a "dead cone", depleted in photon radiation, at angles close to the lepton. The extent of this region is about $\theta \sim 2m_\ell/m_Z$ for any species of massive lepton ℓ, and should not be affected by higher order corrections. We plot the angle of the closest photon with respect to the positively charged lepton in units of $2m_\ell/m_Z$ in Fig. G.1. We observe that the peak of this distribution, which determines the extent of the dead cone, is indeed not affected by the inclusion of higher order corrections. We also note that in the decay into τ's, we can begin to see a pronounced deviation in the soft-collinear approximation, brought about by neglecting the interference contributions and hard wide-angle radiation corrections.

The NNLO corrections require further checks owing to the choices made in our implementation. The choice of the parameter below which we choose to use the collinear approximation in the real virtual approximation is one such choice. We show in Fig. G.2 the radiative energy loss for $a = \{2, 5, 10\}\ m_\ell^2$. We find that this variation does not make a significant systematic difference and are thus encouraged to use a value in this range. We performed a similar test for the parameter c that determines the allowed scaling violation in the real-virtual matrix elements, but found that the quality of the calculation quickly deteriorates. Thus we keep this

Program	LO	NLO EW μ	NLO EW e
Wzgrad	431.03(3)	437.98(03)	419.7(1.1)
Sherpa	431.38(6)	438.8(1.8)	418.8(2.1)

Table G.4: Like Table 7 in [50]. Total cross section for $pp \to Z/\gamma^* \to \ell^+\ell^-$ in pb, at the 8 TeV LHC using ATLAS/CMS like cuts as defined in the text, and in Section 2 of [50]. Cross sections for bare leptons are compared.

parameter fixed at $c = 0.1$.

G.2   External validation of NLO EW cross section

Corrections at the NLO EW level have been implemented in a number of programs, as outlined in the introduction. Most of these programs implement corrections to the neutral-current (NC) and charged-current (CC) Drell-Yan cross sections in hadron collisions. The corrections to these $2 \to 2$ processes contain the corrections implemented in this work as a subset.

For the validation of the total cross sections, we choose to compare against the implementations in Wzgrad. Wzgrad is an amalgamation of the two programs Wgrad2 and Zgrad2 for the calculation of electroweak corrections to the NC and CC Drell-Yan process, respectively. It allows for a simple separation of contributions originating from the initial state, the final state or the interference between the two. It further provides the separation of the virtual correction into purely QED and purely weak pieces in the case of the NC process, which allows for dedicated comparisons.

For the validation of the generated cross section, we choose to compare against the setup outlined in section 2 of [50]. We use the version of Wzgrad as used in that report[13]. We refer to that publication for the input parameters, and the choice of EW schemes. We note here that the cross sections are calculated using the

[13]The installations are available from the website of the LPCC *Electroweak Precision Measurements at the LHC WG*, at https://twiki.cern.ch/twiki/bin/view/Main/DrellYanComparison. The installations used in this work were retrieved on the 04.06.2018.
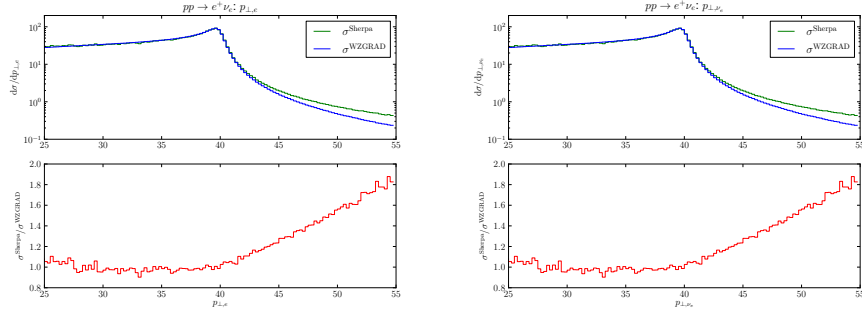
Figure G.3: Plots of the charged lepton transverse momentum, $p_{\perp,e}$, on the left and the neutrino transverse momentum, $p_{\perp,\nu_e}$, on the right in the process $pp \to e^+\nu_e$ at LO. Results from SHERPA and WZGRAD are compared, and found to disagree in the tail of the distribution.

MSTW2008 PDF set interfaced to SHERPA through LHAPDF 6.1.6 whereas in the review, LHAPDF 5.9.1 was used. This may lead to mild differences.

We compare the results for one of the setups described in the review, corresponding to cuts that approximate the acceptances of either the ATLAS or CMS detector. We require $p_{\perp}^{\ell} > 25\,\mathrm{GeV}$, $p_{\perp}^{\nu} > 25\,\mathrm{GeV}$ and $|\eta(\ell)| < 2.5$. In addition, for the NC process we ask for the invariant mass of the lepton pair to be $m_{\ell\ell} > 50\,\mathrm{GeV}$ and for the CC process, we ask for the invariant mass between lepton and neutrino to be $m_{\ell\nu} > 1\,\mathrm{GeV}$. We only provide results for the bare setup which does not put further restrictions on the fermions.

At LO, we find good agreement between our implementation and WZGRAD.

At NLO, we compare results only containing FSR corrections, hence the results from WZGRAD shown here are not the same as the ones quoted in [50].

In both the NC and CC processes, we find good agreement between our implementation and the calculation in WZGRAD for the contribution below the infrared cutoff, which includes the virtual corrections and the YFS form factor contribution.

In the NC process, we also find good agreement in the real contribution. The total cross section for this process is also in agreement, and we show the results in Table G.4.

In the CC process, we find the real contributions disagree by a ratio depending on
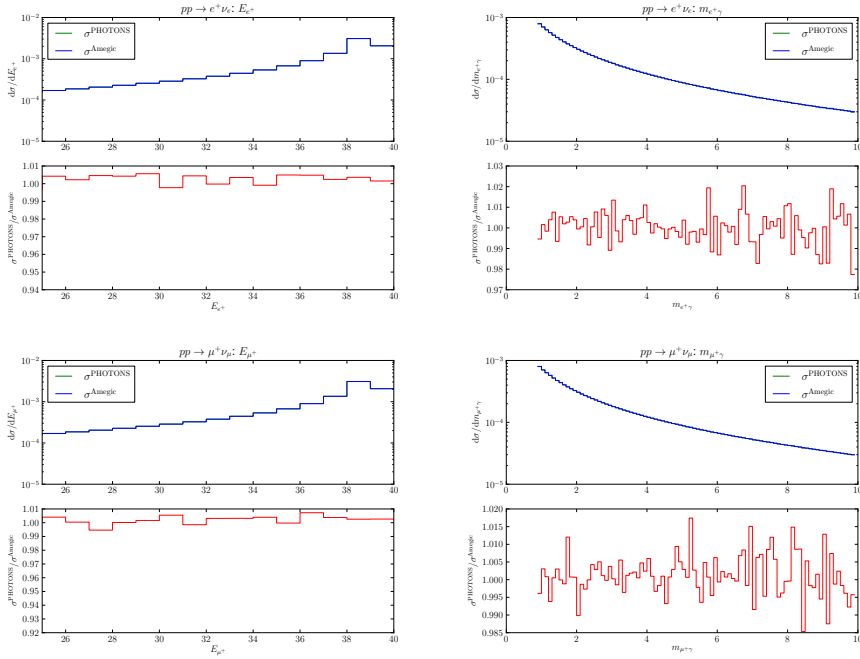
Figure G.4: Plots of the charged lepton energy, E_l, on the left and the invariant mass of the charged lepton and the photon, $m_{\ell\gamma}$, on the right for the decays $W^+ \to e^+\nu_e\gamma$ on the top and $W^+ \to \mu^+\nu_\mu\gamma$ on the bottom. Results from the implementation presented in this work, σ^{PHOTONS}, and from AMEGIC integrated with the RAMBO phase space generator, σ^{Amegic}, are compared and found to agree within statistical uncertainties.

phase space constraints. Further investigation showed that the transverse momentum distributions of either lepton, $p_{\perp,\ell}$, disagree already at the LO. This behaviour is illustrated in Figure G.3, where a clear difference in the tail of the distribution is observed. We excluded the possibility that this difference might be caused by the PDFs by running SHERPA with the same PDF data set as used in WZGRAD, interfaced directly instead of via LHAPDF. This latter run showed only marginal differences that cannot explain the factor 2 difference found in the tail of these distributions. Despite help from the authors, this difference could not be resolved to date.

The behaviour in the transverse momenta is found to be exacerbated in the real contribution, thus making a direct comparison of our results and the ones calculated with WZGRAD unfeasible. We therefore fall back on several consistency checks. Having confirmed the value of the matrix element to machine precision before, we confirm the correctness of the phase space generation by comparing to decay events
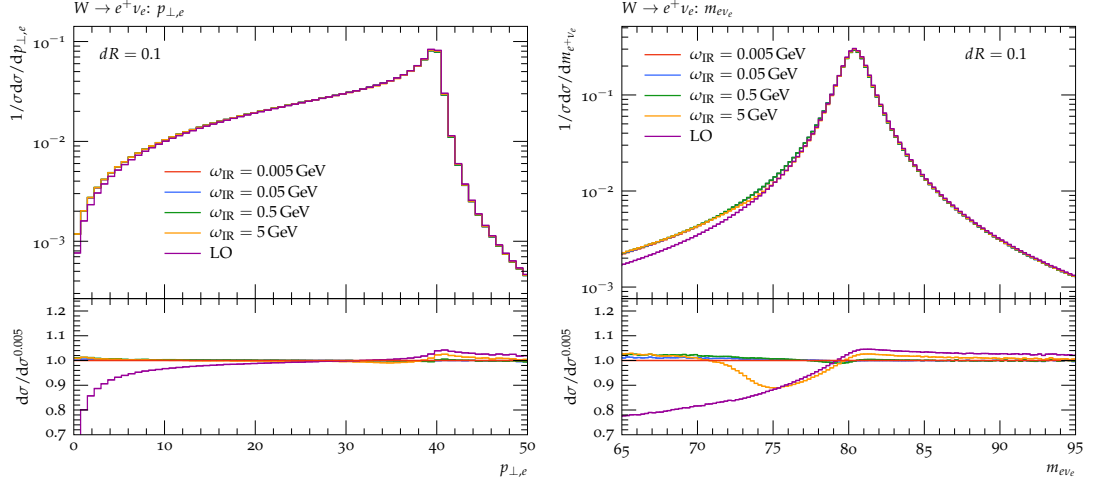
Figure G.5: Plots of the charged lepton transverse momentum, $p_{\perp,e}$, on the left and the invariant mass of the charged lepton and the neutrino, $m_{e\nu_e}$, on the right for the decay $W^+ \to e^+\nu_e(\gamma)$. Results for different values of the infrared cutoff in the YFS formalism are exhibited, with the results converging to a common result.

generated using AMEGIC and integrated using an implementation of the phase space generator RAMBO [249]. RAMBO generates the phase space isotropically, and is thus entirely independent of the approach chosen in the YFS formalism presented in this work. In Figure G.4, we show results for the invariant mass of the charged lepton and the photon, $m_{\ell\gamma}$, as well as the energy of the charged lepton, E_ℓ, for a run with a phase space cut $m_{\ell\gamma} > 1\,\mathrm{GeV}$, finding perfect agreement between the two approaches. This gives us confidence that our phase space generation is indeed correct.

As a final check of our implementation, we check the independence of our results from the infrared cutoff used to define the small infrared region Ω. To this end, we run the setup outlined in Section 6, restricting the number of real emissions to at most one, for cutoffs $\omega_{\mathrm{IR}} = 5, 0.5, 0.05, 0.005\,\mathrm{GeV}$, and exhibit some of the results in Figure G.5. We observe that the distributions converge to a common result.

We can further confirm the independence of our result from the infrared cutoff by plotting the dependence of a single bin against the cutoff parameter. In Figure G.6, we show the normalized cross section in the single bin from 75 to 76.5 GeV of the invariant mass between charged lepton and neutrino. We observe a flattening of the distribution for lower cutoffs, while at large cutoffs the values are significantly further
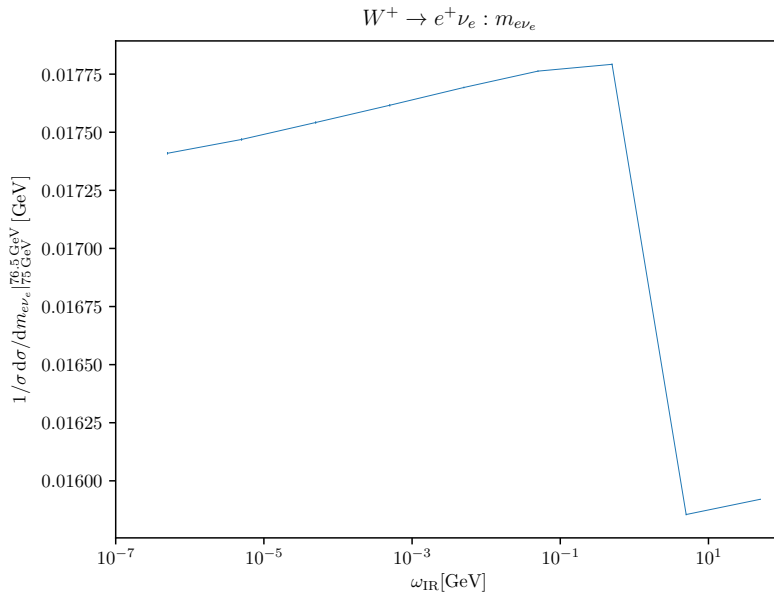
Figure G.6: Plot of the normalized cross section in the invariant mass of the charged lepton and the neutrino binned in the range from 75 to 76.5 GeV, $m_{e\nu_e}|_{75\,\mathrm{GeV}}^{76.5\,\mathrm{GeV}}$, for the decay $W^+ \to e^+\nu_e(\gamma)$. Results are plotted against the infrared cutoff parameter ω_{IR} used to define the small infrared region Ω in the YFS formalism.

away. It should be noted that these results were produced under the assumption that at most one photon was radiated. For very low cutoffs, it is expected that a significantly larger number of photons is emitted. The interplay between the YFS form factor and the requirement that only one photon be radiated is the reason that we do not observe a full flattening of the distribution.

Bibliography

[1] F. Krauss, J. M. Lindert, R. Linten and M. Schönherr, *Accurate simulation of W, Z and Higgs boson decays in Sherpa*, `1809.10650`.

[2] D. Goncalves, F. Krauss and R. Linten, *Distinguishing b-quark and gluon jets with a tagged b-hadron, Phys. Rev.* **D93** (2016) 053013, [`1512.05265`].

[3] ATLAS Collaboration collaboration, G. Aad et al., *Observation of a new particle in the search for the Standard Model Higgs boson with the ATLAS detector at the LHC, Phys.Lett.* **B716** (2012) 1–29, [`1207.7214`].

[4] CMS collaboration, S. Chatrchyan et al., *Observation of a new boson at a mass of 125 GeV with the CMS experiment at the LHC, Phys. Lett.* **B716** (2012) 30–61, [`1207.7235`].

[5] ATLAS, CMS collaboration, G. Aad et al., *Combined Measurement of the Higgs Boson Mass in pp Collisions at $\sqrt{s} = 7$ and 8 TeV with the ATLAS and CMS Experiments, Phys. Rev. Lett.* **114** (2015) 191803, [`1503.07589`].

[6] S. D. Drell and T.-M. Yan, *Massive Lepton Pair Production in Hadron-Hadron Collisions at High-Energies, Phys. Rev. Lett.* **25** (1970) 316–320.

[7] CMS collaboration, V. Khachatryan et al., *Measurements of differential and double-differential Drell-Yan cross sections in proton-proton collisions at 8 TeV, Eur. Phys. J.* **C75** (2015) 147, [`1412.1115`].

[8] CMS collaboration, C. Collaboration, *Measurement of inclusive W and Z boson production cross sections in pp collisions at sqrt(s)=13 TeV*, .

[9] ATLAS collaboration, M. Aaboud et al., *Measurement of the Drell-Yan triple-differential cross section in pp collisions at $\sqrt{s} = 8$ TeV, JHEP* **12** (2017) 059, [1710.05167].

[10] ATLAS collaboration, G. Aad et al., *Measurement of $W^{\pm}$ and Z-boson production cross sections in pp collisions at $\sqrt{s} = 13$ TeV with the ATLAS detector, Phys. Lett.* **B759** (2016) 601–621, [1603.09222].

[11] W. T. Giele and E. W. N. Glover, *Higher-order corrections to jet cross sections in e^+e^- annihilation, Phys. Rev.* **D46** (1992) 1980–2010.

[12] W. Giele, E. N. Glover and D. A. Kosower, *Higher order corrections to jet cross-sections in hadron colliders, Nucl.Phys.* **B403** (1993) 633–670, [hep-ph/9302225].

[13] S. Catani and M. H. Seymour, *A general algorithm for calculating jet cross sections in NLO QCD, Nucl. Phys.* **B485** (1997) 291–419, [hep-ph/9605323].

[14] D. A. Kosower, *Antenna factorization of gauge-theory amplitudes, Phys. Rev.* **D57** (1998) 5410–5416, [hep-ph/9710213].

[15] S. Frixione, Z. Kunszt and A. Signer, *Three-jet cross-sections to next-to-leading order, Nucl. Phys.* **B467** (1996) 399–442, [hep-ph/9512328].

[16] Z. Nagy and D. E. Soper, *General subtraction method for numerical calculation of one loop QCD matrix elements, JHEP* **09** (2003) 055, [hep-ph/0308127].

[17] A. Buckley et al., *General-purpose event generators for LHC physics, Phys. Rept.* **504** (2011) 145–233, [1101.2599].

[18] A. Gehrmann-De Ridder, T. Gehrmann and E. W. N. Glover, *Antenna subtraction at NNLO, JHEP* **09** (2005) 056, [hep-ph/0505111].

[19] G. Somogyi, Z. Trocsanyi and V. Del Duca, *Matching of singly- and doubly-unresolved limits of tree-level QCD squared matrix elements*, *JHEP* **06** (2005) 024, [hep-ph/0502226].

[20] S. Catani and M. Grazzini, *An NNLO subtraction formalism in hadron collisions and its application to Higgs boson production at the LHC*, *Phys.Rev.Lett.* **98** (2007) 222002, [hep-ph/0703012].

[21] J. Gaunt, M. Stahlhofen, F. J. Tackmann and J. R. Walsh, *N-jettiness Subtractions for NNLO QCD Calculations*, *JHEP* **09** (2015) 058, [1505.04794].

[22] M. Czakon, *A novel subtraction scheme for double-real radiation at NNLO*, *Phys.Lett.* **B693** (2010) 259–268, [1005.0274].

[23] M. Cacciari, F. A. Dreyer, A. Karlberg, G. P. Salam and G. Zanderighi, *Fully Differential Vector-Boson-Fusion Higgs Production at Next-to-Next-to-Leading Order*, *Phys. Rev. Lett.* **115** (2015) 082002, [1506.02660].

[24] U. Baur, S. Keller and D. Wackeroth, *Electroweak radiative corrections to W boson production in hadronic collisions*, *Phys. Rev.* **D59** (1999) 013002, [hep-ph/9807417].

[25] U. Baur, O. Brein, W. Hollik, C. Schappacher and D. Wackeroth, *Electroweak radiative corrections to neutral current Drell-Yan processes at hadron colliders*, *Phys.Rev.* **D65** (2002) 033007, [hep-ph/0108274].

[26] U. Baur and D. Wackeroth, *Electroweak radiative corrections to $p\bar{p} \to W^{\pm} \to \ell^{\pm}\nu$ beyond the pole approximation*, *Phys. Rev.* **D70** (2004) 073015, [hep-ph/0405191].

[27] C. M. Carloni Calame, G. Montagna, O. Nicrosini and A. Vicini, *Precision electroweak calculation of the charged current Drell-Yan process*, *JHEP* **12** (2006) 016, [hep-ph/0609170].

[28] C. M. Carloni Calame, G. Montagna, O. Nicrosini and A. Vicini, *Precision electroweak calculation of the production of a high transverse-momentum lepton pair at hadron colliders*, *JHEP* **10** (2007) 109, [`0710.1722`].

[29] A. Andonov, A. Arbuzov, D. Bardin, S. Bondarenko, P. Christova, L. Kalinovskaya et al., *SANCscope - v.1.00*, *Comput. Phys. Commun.* **174** (2006) 481–517, [`hep-ph/0411186`].

[30] S. Dittmaier and M. Krämer, *Electroweak radiative corrections to W boson production at hadron colliders*, *Phys. Rev.* **D65** (2002) 073007, [`hep-ph/0109062`].

[31] S. Dittmaier and M. Huber, *Radiative corrections to the neutral-current Drell-Yan process in the Standard Model and its minimal supersymmetric extension*, *JHEP* **01** (2010) 060, [`0911.2329`].

[32] S. Alioli, P. Nason, C. Oleari and E. Re, *NLO vector-boson production matched with shower in POWHEG*, *JHEP* **07** (2008) 060, [`0805.4802`].

[33] L. Barze, G. Montagna, P. Nason, O. Nicrosini and F. Piccinini, *Implementation of electroweak corrections in the POWHEG BOX: single W production*, *JHEP* **04** (2012) 037, [`1202.0465`].

[34] L. Barze, G. Montagna, P. Nason, O. Nicrosini, F. Piccinini and A. Vicini, *Neutral current Drell-Yan with combined QCD and electroweak corrections in the POWHEG BOX*, *Eur. Phys. J.* **C73** (2013) 2474, [`1302.4606`].

[35] Y. Li and F. Petriello, *Combining QCD and electroweak corrections to dilepton production in FEWZ*, *Phys.Rev.* **D86** (2012) 094034, [`1208.5967`].

[36] S. Dittmaier, A. Huss and C. Schwinn, *Dominant mixed QCD-electroweak $O(\alpha_s\alpha)$ corrections to Drell–Yan processes in the resonance region*, *Nucl. Phys.* **B904** (2016) 216–252, [`1511.08016`].

[37] J. Alwall, R. Frederix, S. Frixione, V. Hirschi, F. Maltoni, O. Mattelaer et al., *The automated computation of tree-level and next-to-leading order differential cross sections, and their matching to parton shower simulations*, *JHEP* **07** (2014) 079, [1405.0301].

[38] R. Frederix, S. Frixione, V. Hirschi, D. Pagani, H. S. Shao and M. Zaro, *The automation of next-to-leading order electroweak calculations*, *JHEP* **07** (2018) 185, [1804.10017].

[39] F. Cascioli, P. Maierhöfer and S. Pozzorini, *Scattering Amplitudes with Open Loops*, *Phys.Rev.Lett.* **108** (2012) 111601, [1111.5206].

[40] S. Kallweit, J. M. Lindert, P. Maierhöfer, S. Pozzorini and M. Schönherr, *NLO electroweak automation and precise predictions for W+multijet production at the LHC*, 1412.5157.

[41] S. Actis, A. Denner, L. Hofer, A. Scharf and S. Uccirati, *Recursive generation of one-loop amplitudes in the Standard Model*, *JHEP* **1304** (2013) 037, [1211.6316].

[42] S. Actis, A. Denner, L. Hofer, J.-N. Lang, A. Scharf and S. Uccirati, *RECOLA: REcursive Computation of One-Loop Amplitudes*, *Comput. Phys. Commun.* **214** (2017) 140–173, [1605.01090].

[43] C. Carloni Calame, G. Montagna, O. Nicrosini and M. Treccani, *Higher order QED corrections to W boson mass determination at hadron colliders*, *Phys.Rev.* **D69** (2004) 037301, [hep-ph/0303102].

[44] C. M. Carloni Calame, G. Montagna, O. Nicrosini and M. Treccani, *Multiple photon corrections to the neutral-current Drell-Yan process*, *JHEP* **05** (2005) 019, [hep-ph/0502218].

[45] D. R. Yennie, S. C. Frautschi and H. Suura, *The Infrared Divergence Phenomena and High-Energy Processes*, *Ann. Phys.* **13** (1961) 379–452.

[46] E. Barberio and Z. Wąs, *PHOTOS - a universal monte carlo for QED radiative corrections: version 2.0, Comput. Phys. Commun.* **79** (1994) 291–308.

[47] W. Placzek and S. Jadach, *Multiphoton radiation in leptonic W boson decays, Eur.Phys.J.* **C29** (2003) 325–339, [hep-ph/0302065].

[48] K. Hamilton and P. Richardson, *Simulation of QED radiation in particle decays using the YFS formalism, JHEP* **07** (2006) 010, [hep-ph/0603034].

[49] M. Schönherr and F. Krauss, *Soft photon radiation in particle decays in sherpa, JHEP* **12** (2008) 018, [0810.5071].

[50] S. Alioli et al., *Precision studies of observables in* $pp \to W \to l\nu_l$ *and* $pp \to \gamma, Z \to l^+l^-$ *processes at the LHC, Eur. Phys. J.* **C77** (2017) 280, [1606.02330].

[51] T. Gleisberg, S. Höche, F. Krauss, M. Schönherr, S. Schumann, F. Siegert et al., *Event generation with* SHERPA *1.1, JHEP* **02** (2009) 007, [0811.4622].

[52] C. Degrande, C. Duhr, B. Fuks, D. Grellscheid, O. Mattelaer and T. Reiter, *UFO - The Universal FeynRules Output, Comput.Phys.Commun.* **183** (2012) 1201–1214, [1108.2040].

[53] S. Höche, S. Kuttimalai, S. Schumann and F. Siegert, *Beyond Standard Model calculations with Sherpa, Eur. Phys. J.* **C75** (2015) 135, [1412.6478].

[54] F. Krauss, R. Kuhn and G. Soff, *AMEGIC++ 1.0: A Matrix Element Generator In C++, JHEP* **02** (2002) 044, [hep-ph/0109036].

[55] T. Gleisberg, F. Krauss, K. T. Matchev, A. Schälicke, S. Schumann and G. Soff, *Helicity formalism for spin-2 particles, JHEP* **09** (2003) 001, [hep-ph/0306182].

[56] T. Gleisberg and S. Höche, *Comix, a new matrix element generator, JHEP* **12** (2008) 039, [0808.3674].

[57] S. Catani, S. Dittmaier, M. H. Seymour and Z. Trocsanyi, *The dipole formalism for next-to-leading order QCD calculations with massive partons*, *Nucl. Phys.* **B627** (2002) 189–265, [hep-ph/0201036].

[58] T. Gleisberg and F. Krauss, *Automating dipole subtraction for QCD NLO calculations*, *Eur. Phys. J.* **C53** (2008) 501–523, [0709.2881].

[59] C. F. Berger, Z. Bern, L. J. Dixon, F. Febres-Cordero, D. Forde, H. Ita et al., *Automated implementation of on-shell methods for one-loop amplitudes*, *Phys. Rev.* **D78** (2008) 036003, [0803.4180].

[60] T. Binoth et al., *A proposal for a standard interface between Monte Carlo tools and one-loop programs*, *Comput. Phys. Commun.* **181** (2010) 1612–1622, [1001.1307].

[61] S. Alioli, S. Badger, J. Bellm, B. Biedermann, F. Boudjema et al., *Update of the Binoth Les Houches Accord for a standard interface between Monte Carlo tools and one-loop programs*, *Comput.Phys.Commun.* **185** (2014) 560–571, [1308.3462].

[62] S. Schumann and F. Krauss, *A parton shower algorithm based on Catani-Seymour dipole factorisation*, *JHEP* **03** (2008) 038, [0709.1027].

[63] S. Höche and S. Prestel, *The midpoint between dipole and parton showers*, *Eur. Phys. J.* **C75** (2015) 461, [1506.05057].

[64] S. Höche, F. Krauss and S. Prestel, *Implementing NLO DGLAP evolution in Parton Showers*, *JHEP* **10** (2017) 093, [1705.00982].

[65] S. Höche and S. Prestel, *Triple collinear emissions in parton showers*, *Phys. Rev.* **D96** (2017) 074017, [1705.00742].

[66] S. Catani, F. Krauss, R. Kuhn and B. R. Webber, *QCD matrix elements + parton showers*, *JHEP* **11** (2001) 063, [hep-ph/0109231].

[67] S. Höche et al., *Matching Parton Showers and Matrix Elements*, `hep-ph/0602031`.

[68] S. Höche, F. Krauss, S. Schumann and F. Siegert, *QCD matrix elements and truncated showers*, *JHEP* **05** (2009) 053, [`0903.1219`].

[69] S. Höche, F. Krauss, M. Schönherr and F. Siegert, *A critical appraisal of NLO+PS matching methods*, *JHEP* **09** (2012) 049, [`1111.1220`].

[70] T. Gehrmann, S. Höche, F. Krauss, M. Schönherr and F. Siegert, *NLO QCD matrix elements + parton showers in $e^+e^- \rightarrow$ hadrons*, *JHEP* **01** (2013) 144, [`1207.5031`].

[71] S. Höche, F. Krauss, M. Schönherr and F. Siegert, *QCD matrix elements + parton showers: The NLO case*, *JHEP* **04** (2013) 027, [`1207.5030`].

[72] J.-C. Winter, F. Krauss and G. Soff, *A modified cluster-hadronisation model*, *Eur. Phys. J.* **C36** (2004) 381–395, [`hep-ph/0311085`].

[73] B. Andersson, G. Gustafson, G. Ingelman and T. Sjöstrand, *Parton Fragmentation and String Dynamics*, *Phys. Rept.* **97** (1983) 31–145.

[74] B. Andersson, G. Gustafson and T. Sjöstrand, *A Model for Baryon Production in Quark and Gluon Jets*, *Nucl. Phys.* **B197** (1982) 45.

[75] B. Andersson, *The Lund model*, vol. 7. Camb. Monogr. Part. Phys. Nucl. Phys. Cosmol., 1997.

[76] C. W. Bauer, S. Fleming and M. E. Luke, *Summing Sudakov logarithms in B —> X(s gamma) in effective field theory*, *Phys. Rev.* **D63** (2000) 014006, [`hep-ph/0005275`].

[77] C. W. Bauer, S. Fleming, D. Pirjol and I. W. Stewart, *An Effective field theory for collinear and soft gluons: Heavy to light decays*, *Phys.Rev.* **D63** (2001) 114020, [`hep-ph/0011336`].

[78] C. W. Bauer and I. W. Stewart, *Invariant operators in collinear effective theory, Phys.Lett.* **B516** (2001) 134–142, [`hep-ph/0107001`].

[79] C. W. Bauer, D. Pirjol and I. W. Stewart, *Soft collinear factorization in effective field theory, Phys.Rev.* **D65** (2002) 054022, [`hep-ph/0109045`].

[80] C. W. Bauer, S. Fleming, D. Pirjol, I. Z. Rothstein and I. W. Stewart, *Hard scattering factorization from effective field theory, Phys.Rev.* **D66** (2002) 014017, [`hep-ph/0202088`].

[81] M. Beneke, A. P. Chapovsky, M. Diehl and T. Feldmann, *Soft collinear effective theory and heavy to light currents beyond leading power, Nucl. Phys.* **B643** (2002) 431–476, [`hep-ph/0206152`].

[82] R. Boughezal, J. M. Campbell, R. K. Ellis, C. Focke, W. Giele, X. Liu et al., *Color singlet production at NNLO in MCFM, Eur. Phys. J.* **C77** (2017) 7, [`1605.08011`].

[83] J. M. Campbell, R. K. Ellis and C. Williams, *Associated production of a Higgs boson at NNLO, JHEP* **06** (2016) 179, [`1601.00658`].

[84] J. M. Campbell, R. K. Ellis and C. Williams, *Driving missing data at the LHC: NNLO predictions for the ratio of $\gamma + j$ and $Z + j$, Phys. Rev.* **D96** (2017) 014037, [`1703.10109`].

[85] R. Boughezal, J. M. Campbell, R. K. Ellis, C. Focke, W. T. Giele, X. Liu et al., *Z-boson production in association with a jet at next-to-next-to-leading order in perturbative QCD, Phys. Rev. Lett.* **116** (2016) 152001, [`1512.01291`].

[86] R. Boughezal, X. Liu and F. Petriello, *Phenomenology of the Z-boson plus jet process at NNLO, Phys. Rev.* **D94** (2016) 074015, [`1602.08140`].

[87] R. Boughezal, C. Focke, X. Liu and F. Petriello, *W-boson production in association with a jet at next-to-next-to-leading order in perturbative QCD, Phys. Rev. Lett.* **115** (2015) 062002, [`1504.02131`].

[88] R. Boughezal, X. Liu and F. Petriello, *W-boson plus jet differential distributions at NNLO in QCD, Phys. Rev.* **D94** (2016) 113009, [`1602.06965`].

[89] R. Boughezal, F. Caola, K. Melnikov, F. Petriello and M. Schulze, *Higgs boson production in association with a jet at next-to-next-to-leading order, Phys. Rev. Lett.* **115** (2015) 082003, [`1504.07922`].

[90] R. Boughezal, C. Focke, W. Giele, X. Liu and F. Petriello, *Higgs boson production in association with a jet at NNLO using jettiness subtraction, Phys. Lett.* **B748** (2015) 5–8, [`1505.03893`].

[91] J. M. Campbell, R. K. Ellis and C. Williams, *Direct Photon Production at Next-to–Next-to-Leading Order, Phys. Rev. Lett.* **118** (2017) 222001, [`1612.04333`].

[92] J. M. Campbell, R. K. Ellis, Y. Li and C. Williams, *Predictions for diphoton production at the LHC through NNLO in QCD, JHEP* **07** (2016) 148, [`1603.02663`].

[93] V. S. Fadin, L. N. Lipatov, A. D. Martin and M. Melles, *Resummation of double logarithms in electroweak high-energy processes, Phys. Rev.* **D61** (2000) 094002, [`hep-ph/9910338`].

[94] J. H. Kuhn, A. A. Penin and V. A. Smirnov, *Summing up subleading Sudakov logarithms, Eur. Phys. J.* **C17** (2000) 97–105, [`hep-ph/9912503`].

[95] A. Denner and S. Pozzorini, *One loop leading logarithms in electroweak radiative corrections. 1. Results, Eur.Phys.J.* **C18** (2001) 461–480, [`hep-ph/0010201`].

[96] A. Denner and S. Pozzorini, *One loop leading logarithms in electroweak radiative corrections. 2. Factorization of collinear singularities, Eur.Phys.J.* **C21** (2001) 63–79, [`hep-ph/0104127`].

[97] M. Ciafaloni, P. Ciafaloni and D. Comelli, *Bloch-Nordsieck violating electroweak corrections to inclusive TeV scale hard processes*, *Phys. Rev. Lett.* **84** (2000) 4810–4813, [hep-ph/0001142].

[98] U. Baur, *Weak Boson Emission in Hadron Collider Processes*, *Phys.Rev.* **D75** (2007) 013005, [hep-ph/0611241].

[99] G. Altarelli and G. Parisi, *Asymptotic freedom in parton language*, *Nucl. Phys.* **B126** (1977) 298–318.

[100] J. C. Collins, D. E. Soper and G. F. Sterman, *Factorization for Short Distance Hadron - Hadron Scattering*, *Nucl.Phys.* **B261** (1985) 104.

[101] J. C. Collins, D. E. Soper and G. F. Sterman, *Transverse Momentum Distribution in Drell-Yan Pair and W and Z Boson Production*, *Nucl.Phys.* **B250** (1985) 199.

[102] S. Catani, D. de Florian and G. Rodrigo, *Space-like (versus time-like) collinear limits in QCD: Is factorization violated?*, *JHEP* **07** (2012) 026, [1112.4405].

[103] F. Bloch and A. Nordsieck, *Note on the Radiation Field of the electron*, *Phys. Rev.* **52** (1937) 54–59.

[104] T. Kinoshita, *Mass Singularities of Feynman Amplitudes*, *J.Math.Phys.* **3** (1962) 650–677.

[105] T. Lee and M. Nauenberg, *Degenerate Systems and Mass Singularities*, *Phys. Rev.* **133** (1964) B1549–B1562.

[106] J. M. Campbell, M. A. Cullen and E. W. N. Glover, *Four jet event shapes in electron - positron annihilation*, *Eur. Phys. J.* **C9** (1999) 245–265, [hep-ph/9809429].

[107] D. A. Kosower, *Antenna factorization in strongly-ordered limits*, *Phys. Rev.* **D71** (2005) 045016, [hep-ph/0311272].

[108] ATLAS collaboration, M. Aaboud et al., *Measurement of the W-boson mass in pp collisions at $\sqrt{s} = 7$ TeV with the ATLAS detector*, Eur. Phys. J. **C78** (2018) 110, [`1701.07240`].

[109] CMS collaboration, V. Khachatryan et al., *Measurement of the Z boson differential cross section in transverse momentum and rapidity in proton–proton collisions at 8 TeV*, Phys. Lett. **B749** (2015) 187–209, [`1504.03511`].

[110] ATLAS collaboration, G. Aad et al., *Measurement of the transverse momentum and ϕ_η^* distributions of Drell–Yan lepton pairs in proton–proton collisions at $\sqrt{s} = 8$ TeV with the ATLAS detector*, Eur. Phys. J. **C76** (2016) 291, [`1512.02192`].

[111] R. Boughezal, A. Guffanti, F. Petriello and M. Ubiali, *The impact of the LHC Z-boson transverse momentum data on PDF determinations*, JHEP **07** (2017) 130, [`1705.00343`].

[112] J. R. Andersen et al., *Les Houches 2015: Physics at TeV Colliders Standard Model Working Group Report*, in *9th Les Houches Workshop on Physics at TeV Colliders (PhysTeV 2015) Les Houches, France, June 1-19, 2015*, 2016, `1605.04692`, http://lss.fnal.gov/archive/2016/conf/fermilab-conf-16-175-ppd-t.pdf.

[113] C. M. Carloni Calame, M. Chiesa, H. Martinez, G. Montagna, O. Nicrosini, F. Piccinini et al., *Precision Measurement of the W-Boson Mass: Theoretical Contributions and Uncertainties*, Phys. Rev. **D96** (2017) 093005, [`1612.02841`].

[114] C. Anastasiou, L. J. Dixon, K. Melnikov and F. Petriello, *High precision QCD at hadron colliders: Electroweak gauge boson rapidity distributions at NNLO*, Phys.Rev. **D69** (2004) 094008, [`hep-ph/0312266`].

[115] C. Anastasiou, L. J. Dixon, K. Melnikov and F. Petriello, *Dilepton rapidity distribution in the Drell-Yan process at NNLO in QCD*, *Phys.Rev.Lett.* **91** (2003) 182002, [`hep-ph/0306192`].

[116] K. Melnikov and F. Petriello, *Electroweak gauge boson production at hadron colliders through O(alpha(s)**2)*, *Phys.Rev.* **D74** (2006) 114017, [`hep-ph/0609070`].

[117] S. Catani, L. Cieri, G. Ferrera, D. de Florian and M. Grazzini, *Vector boson production at hadron colliders: a fully exclusive QCD calculation at NNLO*, *Phys.Rev.Lett.* **103** (2009) 082001, [`0903.2120`].

[118] R. Gavin, Y. Li, F. Petriello and S. Quackenbush, *FEWZ 2.0: A code for hadronic Z production at next-to-next-to-leading order*, *Comput.Phys.Commun.* **182** (2011) 2388–2403, [`1011.3540`].

[119] M. Grazzini, S. Kallweit and M. Wiesemann, *Fully differential NNLO computations with MATRIX*, *Eur. Phys. J.* **C78** (2018) 537, [`1711.06631`].

[120] S. Höche, Y. Li and S. Prestel, *Drell-Yan lepton pair production at NNLO QCD with parton showers*, `1405.3607`.

[121] A. Karlberg, E. Re and G. Zanderighi, *NNLOPS accurate Drell-Yan production*, *JHEP* **09** (2014) 134, [`1407.2940`].

[122] A. Gehrmann-De Ridder, T. Gehrmann, E. W. N. Glover, A. Huss and T. A. Morgan, *Precise QCD predictions for the production of a Z boson in association with a hadronic jet*, *Phys. Rev. Lett.* **117** (2016) 022001, [`1507.02850`].

[123] A. Gehrmann-De Ridder, T. Gehrmann, E. W. N. Glover, A. Huss and T. A. Morgan, *The NNLO QCD corrections to Z boson production at large transverse momentum*, *JHEP* **07** (2016) 133, [`1605.04295`].

[124] A. Gehrmann-De Ridder, T. Gehrmann, E. W. N. Glover, A. Huss and T. A. Morgan, *NNLO QCD corrections for Drell-Yan p_T^Z and ϕ^* observables at the LHC*, *JHEP* **11** (2016) 094, [1610.01843].

[125] A. Gehrmann-De Ridder, T. Gehrmann, E. W. N. Glover, A. Huss and D. M. Walker, *Next-to-Next-to-Leading-Order QCD Corrections to the Transverse Momentum Distribution of Weak Gauge Bosons*, *Phys. Rev. Lett.* **120** (2018) 122001, [1712.07543].

[126] D. Wackeroth and W. Hollik, *Electroweak radiative corrections to resonant charged gauge boson production*, *Phys. Rev.* **D55** (1997) 6788–6818, [hep-ph/9606398].

[127] U. Baur, S. Keller and W. K. Sakumoto, *QED radiative corrections to Z boson production and the forward backward asymmetry at hadron colliders*, *Phys. Rev.* **D57** (1998) 199–215, [hep-ph/9707301].

[128] A. Denner, S. Dittmaier, T. Kasprzik and A. Muck, *Electroweak corrections to W + jet hadroproduction including leptonic W-boson decays*, *JHEP* **08** (2009) 075, [0906.1656].

[129] A. Denner, S. Dittmaier, T. Kasprzik and A. Muck, *Electroweak corrections to dilepton + jet production at hadron colliders*, *JHEP* **06** (2011) 069, [1103.0914].

[130] A. Denner, S. Dittmaier, T. Kasprzik and A. Mück, *Electroweak corrections to monojet production at the LHC*, *Eur. Phys. J.* **C73** (2013) 2297, [1211.5078].

[131] S. Kallweit, J. M. Lindert, P. Maierhofer, S. Pozzorini and M. Schönherr, *NLO QCD+EW predictions for V + jets including off-shell vector-boson decays and multijet merging*, *JHEP* **04** (2016) 021, [1511.08692].

[132] C. Bernaciak and D. Wackeroth, *Combining NLO QCD and Electroweak Radiative Corrections to W boson Production at Hadron Colliders in the POWHEG Framework, Phys.Rev.* **D85** (2012) 093003, [`1201.4804`].

[133] A. Mück and L. Oymanns, *Resonace-improved parton-shower matching for the Drell-Yan process including electroweak corrections, JHEP* **05** (2017) 090, [`1612.04292`].

[134] R. Bonciani, F. Buccioni, R. Mondini and A. Vicini, *Double-real corrections at $\mathcal{O}(\alpha\alpha_s)$ to single gauge boson production, Eur. Phys. J.* **C77** (2017) 187, [`1611.00645`].

[135] R. Bonciani, S. Di Vita, P. Mastrolia and U. Schubert, *Two-Loop Master Integrals for the mixed EW-QCD virtual corrections to Drell-Yan scattering, JHEP* **09** (2016) 091, [`1604.08581`].

[136] A. von Manteuffel and R. M. Schabinger, *Numerical Multi-Loop Calculations via Finite Integrals and One-Mass EW-QCD Drell-Yan Master Integrals, JHEP* **04** (2017) 129, [`1701.06583`].

[137] D. de Florian, M. Der and I. Fabre, *QCD⊕QED NNLO corrections to Drell Yan production,* `1805.12214`.

[138] S. Dittmaier, A. Huss and C. Schwinn, *Mixed QCD-electroweak $O(\alpha_s\alpha)$ corrections to Drell-Yan processes in the resonance region: pole approximation and non-factorizable corrections, Nucl. Phys.* **B885** (2014) 318–372, [`1403.3216`].

[139] S. Dittmaier, *A general approach to photon radiation off fermions, Nucl. Phys.* **B565** (2000) 69–122, [`hep-ph/9904440`].

[140] F. U. Bernlochner and M. Schonherr, *Comparing different ansatzes to describe electroweak radiative corrections to exclusive semileptonic B meson*

decays into (pseudo)scalar final state mesons using Monte-Carlo techniques, 1010.5997.

[141] A. Denner, *Techniques for calculation of electroweak radiative corrections at the one loop level and results for W physics at LEP-200, Fortsch. Phys.* **41** (1993) 307–420, [0709.1075].

[142] D. Yu. Bardin and G. Passarino, *The standard model in the making: Precision study of the electroweak interactions.* 1999.

[143] F. A. Berends, W. L. van Neerven and G. J. H. Burgers, *Higher Order Radiative Corrections at LEP Energies, Nucl. Phys.* **B297** (1988) 429.

[144] W. F. L. Hollik, *Radiative Corrections in the Standard Model and their Role for Precision Tests of the Electroweak Theory, Fortsch. Phys.* **38** (1990) 165–260.

[145] R. Mertig, M. Bohm and A. Denner, *FEYN CALC: Computer algebraic calculation of Feynman amplitudes, Comput. Phys. Commun.* **64** (1991) 345–359.

[146] V. Shtabovenko, R. Mertig and F. Orellana, *New Developments in FeynCalc 9.0, Comput. Phys. Commun.* **207** (2016) 432–444, [1601.01167].

[147] T. Hahn and M. Perez-Victoria, *Automatized one loop calculations in four-dimensions and D-dimensions, Comput. Phys. Commun.* **118** (1999) 153–165, [hep-ph/9807565].

[148] H. H. Patel, *Package-X: A Mathematica package for the analytic calculation of one-loop integrals, Comput. Phys. Commun.* **197** (2015) 276–290, [1503.01469].

[149] M. Chiesa, N. Greiner and F. Tramontano, *Automation of electroweak corrections for LHC processes, J. Phys.* **G43** (2016) 013002, [1507.08579].

[150] M. Chiesa, N. Greiner, M. Schönherr and F. Tramontano, *Electroweak corrections to diphoton plus jets*, *JHEP* **10** (2017) 181, [`1706.09022`].

[151] I. Dubovyk, A. Freitas, J. Gluza, T. Riemann and J. Usovitsch, *The two-loop electroweak bosonic corrections to* $\sin^2 \theta_{\mathrm{eff}}^{\mathrm{b}}$, *Phys. Lett.* **B762** (2016) 184–189, [`1607.08375`].

[152] I. Dubovyk, A. Freitas, J. Gluza, T. Riemann and J. Usovitsch, *Complete electroweak two-loop corrections to Z boson production and decay*, *Phys. Lett.* **B783** (2018) 86–94, [`1804.10236`].

[153] R. Kleiss and W. J. Stirling, *Spinor Techniques for Calculating p anti-p –> W+- / Z0 + Jets*, *Nucl.Phys.* **B262** (1985) 235–262.

[154] A. Ballestrero, E. Maina and S. Moretti, *Heavy quarks and leptons at* $e^+ e^-$ *colliders*, *Nucl. Phys.* **B415** (1994) 265–292, [`hep-ph/9212246`].

[155] A. Ballestrero and E. Maina, *A new method for helicity calculations*, *Phys. Lett.* **B350** (1995) 225–233, [`hep-ph/9403244`].

[156] G. J. H. Burgers, *On the Two Loop QED Vertex Correction in the High-energy Limit*, *Phys. Lett.* **164B** (1985) 167–169.

[157] R. Bonciani, P. Mastrolia and E. Remiddi, *QED vertex form-factors at two loops*, *Nucl. Phys.* **B676** (2004) 399–452, [`hep-ph/0307295`].

[158] W. Bernreuther, R. Bonciani, T. Gehrmann, R. Heinesch, T. Leineweber, P. Mastrolia et al., *Two-loop QCD corrections to the heavy quark form-factors: The Vector contributions*, *Nucl. Phys.* **B706** (2005) 245–324, [`hep-ph/0406046`].

[159] W. Bernreuther, R. Bonciani, T. Gehrmann, R. Heinesch, T. Leineweber, P. Mastrolia et al., *Two-loop QCD corrections to the heavy quark form-factors: Axial vector contributions*, *Nucl. Phys.* **B712** (2005) 229–286, [`hep-ph/0412259`].

[160] W. Bernreuther, R. Bonciani, T. Gehrmann, R. Heinesch, T. Leineweber and E. Remiddi, *Two-loop QCD corrections to the heavy quark form-factors: Anomaly contributions, Nucl. Phys.* **B723** (2005) 91–116, [`hep-ph/0504190`].

[161] W. Bernreuther, R. Bonciani, T. Gehrmann, R. Heinesch, P. Mastrolia and E. Remiddi, *Decays of scalar and pseudoscalar Higgs bosons into fermions: Two-loop QCD corrections to the Higgs-quark-antiquark amplitude, Phys. Rev.* **D72** (2005) 096002, [`hep-ph/0508254`].

[162] J. Ablinger, A. Behring, J. Blümlein, G. Falcioni, A. De Freitas, P. Marquard et al., *Heavy quark form factors at two loops, Phys. Rev.* **D97** (2018) 094022, [`1712.09889`].

[163] R. K. Ellis and G. Zanderighi, *Scalar one-loop integrals for QCD, JHEP* **0802** (2008) 002, [`0712.1851`].

[164] H. Frellesvig, D. Tommasini and C. Wever, *On the reduction of generalized polylogarithms to Li_n and $Li_{2,2}$ and on the evaluation thereof, JHEP* **03** (2016) 189, [`1601.02649`].

[165] A. Denner, S. Dittmaier and L. Hofer, *Collier: a fortran-based Complex One-Loop LIbrary in Extended Regularizations, Comput. Phys. Commun.* **212** (2017) 220–238, [`1604.06792`].

[166] A. Buckley, J. Butterworth, L. Lönnblad, D. Grellscheid, H. Hoeth et al., *Rivet user manual, Comput.Phys.Commun.* **184** (2013) 2803–2819, [`1003.0694`].

[167] A. Banfi, S. Redford, M. Vesterinen, P. Waller and T. R. Wyatt, *Optimisation of variables for studying dilepton transverse momentum distributions at hadron colliders, Eur. Phys. J.* **C71** (2011) 1600, [`1009.1580`].

[168] ATLAS collaboration, M. Aaboud et al., *Observation of Higgs boson production in association with a top quark pair at the LHC with the ATLAS detector*, *Phys. Lett.* **B784** (2018) 173–191, [`1806.00425`].

[169] CMS collaboration, A. M. Sirunyan et al., *Observation of $t\bar{t}H$ production*, *Phys. Rev. Lett.* **120** (2018) 231801, [`1804.02610`].

[170] W. Beenakker, S. Dittmaier, M. Kramer, B. Plumper, M. Spira and P. M. Zerwas, *Higgs radiation off top quarks at the Tevatron and the LHC*, *Phys. Rev. Lett.* **87** (2001) 201805, [`hep-ph/0107081`].

[171] W. Beenakker, S. Dittmaier, M. Kramer, B. Plumper, M. Spira and P. M. Zerwas, *NLO QCD corrections to t anti-t H production in hadron collisions*, *Nucl. Phys.* **B653** (2003) 151–203, [`hep-ph/0211352`].

[172] S. Dawson, L. Orr, L. Reina and D. Wackeroth, *Associated top quark Higgs boson production at the LHC*, *Phys.Rev.* **D67** (2003) 071503, [`hep-ph/0211438`].

[173] S. Dawson, C. Jackson, L. Orr, L. Reina and D. Wackeroth, *Associated Higgs production with top quarks at the large hadron collider: NLO QCD corrections*, *Phys.Rev.* **D68** (2003) 034022, [`hep-ph/0305087`].

[174] A. Bredenstein, A. Denner, S. Dittmaier and S. Pozzorini, *NLO QCD corrections to pp —> t anti-t b anti-b + X at the LHC*, *Phys. Rev. Lett.* **103** (2009) 012002, [`0905.0110`].

[175] A. Bredenstein, A. Denner, S. Dittmaier and S. Pozzorini, *NLO QCD corrections to top anti-top bottom anti-bottom production at the LHC: 2. full hadronic results*, *JHEP* **03** (2010) 021, [`1001.4006`].

[176] T. Gleisberg, S. Höche, F. Krauss, A. Schälicke, S. Schumann and J. Winter, *Sherpa 1.α, a proof-of-concept version*, *JHEP* **02** (2004) 056, [`hep-ph/0311263`].

[177] J. Alwall, M. Herquet, F. Maltoni, O. Mattelaer and T. Stelzer, *MadGraph 5 : Going Beyond*, *JHEP* **06** (2011) 128, [1106.0522].

[178] S. Frixione and B. R. Webber, *Matching NLO QCD computations and parton shower simulations*, *JHEP* **06** (2002) 029, [hep-ph/0204244].

[179] R. Frederix, S. Frixione, V. Hirschi, F. Maltoni, R. Pittau et al., *Scalar and pseudoscalar Higgs production in association with a top-antitop pair*, *Phys.Lett.* **B701** (2011) 427–433, [1104.5613].

[180] F. Cascioli, P. Maierhoefer, N. Moretti, S. Pozzorini and F. Siegert, *NLO matching for $t\bar{t}b\bar{b}$ production with massive b-quarks*, 1309.5912.

[181] R. Frederix and S. Frixione, *Merging meets matching in MC@NLO*, *JHEP* **12** (2012) 061, [1209.6215].

[182] L. Lönnblad and S. Prestel, *Unitarising Matrix Element + Parton Shower merging*, *JHEP* **02** (2013) 094, [1211.4827].

[183] S. Plätzer, *Controlling inclusive cross sections in parton shower + matrix element merging*, *JHEP* **08** (2013) 114, [1211.5467].

[184] S. Höche, J. Huang, G. Luisoni, M. Schönherr and J. Winter, *Zero and one jet combined NLO analysis of the top quark forward-backward asymmetry*, *Phys.Rev.* **D88** (2013) 014040, [1306.2703].

[185] S. Höche, F. Krauss, P. Maierhöfer, S. Pozzorini, M. Schönherr and F. Siegert, *Next-to-leading order QCD predictions for top-quark pair production with up to two jets merged with a parton shower*, *Phys. Lett.* **B748** (2015) 74–78, [1402.6293].

[186] CMS collaboration, V. Khachatryan et al., *Search for a Standard Model Higgs Boson Produced in Association with a Top-Quark Pair and Decaying to Bottom Quarks Using a Matrix Element Method*, *Eur. Phys. J.* **C75** (2015) 251, [1502.02485].

[187] ATLAS collaboration, G. Aad et al., *Search for the Standard Model Higgs boson produced in association with top quarks and decaying into $b\bar{b}$ in pp collisions at $\sqrt{s}$ = 8 TeV with the ATLAS detector, Eur. Phys. J.* **C75** (2015) 349, [1503.05066].

[188] N. Moretti, P. Petrov, S. Pozzorini and M. Spannowsky, *Measuring the signal strength in ttH with H->bb*, 1510.08468.

[189] M. R. Buckley and D. Goncalves, *Boosting the Direct CP Measurement of the Higgs-Top Coupling*, 1507.07926.

[190] ATLAS collaboration, M. Aaboud et al., *Observation of $H \rightarrow b\bar{b}$ decays and VH production with the ATLAS detector*, 1808.08238.

[191] CMS collaboration, A. M. Sirunyan et al., *Observation of Higgs boson decay to bottom quarks*, 1808.08242.

[192] ATLAS collaboration, G. Aad et al., *Performance of b-Jet Identification in the ATLAS Experiment*, 1512.01094.

[193] ATLAS COLLABORATION collaboration, *Commissioning of the ATLAS high-performance b-tagging algorithms in the 7 TeV collision data*, Tech. Rep. ATLAS-CONF-2011-102, CERN, Geneva, Jul, 2011.

[194] T. C. collaboration, *Identification of b-quark jets with the cms experiment, Journal of Instrumentation* **8** (2013) P04013.

[195] CMS collaboration, A. M. Sirunyan et al., *Identification of heavy-flavour jets with the CMS detector in pp collisions at 13 TeV, JINST* **13** (2018) P05011, [1712.07158].

[196] G. Piacquadio and C. Weiser, *A new inclusive secondary vertex algorithm for b-jet tagging in atlas, Journal of Physics: Conference Series* **119** (2008) 032032.

[197] ATLAS COLLABORATION collaboration, *Optimisation of the ATLAS b-tagging performance for the 2016 LHC Run*, Tech. Rep. ATL-PHYS-PUB-2016-012, CERN, Geneva, Jun, 2016.

[198] ATLAS COLLABORATION collaboration, *Optimisation and performance studies of the ATLAS b-tagging algorithms for the 2017-18 LHC run*, Tech. Rep. ATL-PHYS-PUB-2017-013, CERN, Geneva, Jul, 2017.

[199] ATLAS COLLABORATION collaboration, *Identification of Jets Containing b-Hadrons with Recurrent Neural Networks at the ATLAS Experiment*, Tech. Rep. ATL-PHYS-PUB-2017-003, CERN, Geneva, Mar, 2017.

[200] CMS COLLABORATION collaboration, *Performance of Deep Tagging Algorithms for Boosted Double Quark Jet Topology in Proton-Proton Collisions at 13 TeV with the Phase-0 CMS Detector*, .

[201] CMS COLLABORATION collaboration, *Performance of b tagging algorithms in proton-proton collisions at 13 TeV with Phase 1 CMS detector*, .

[202] CMS COLLABORATION collaboration, *Heavy flavor identification at CMS with deep neural networks*, .

[203] DELPHI collaboration, P. Abreu et al., *Measurement of the multiplicity of gluons splitting to bottom quark pairs in hadronic Z0 decays, Phys. Lett.* **B405** (1997) 202–214.

[204] ALEPH collaboration, R. Barate et al., *A Measurement of the gluon splitting rate into b anti-b pairs in hadronic Z decays, Phys. Lett.* **B434** (1998) 437–450.

[205] DELPHI collaboration, P. Abreu et al., *Measurement of the rate of b anti-b b anti-b events in hadronic Z decays and the extraction of the gluon splitting into b anti-b, Phys. Lett.* **B462** (1999) 425–439.

[206] OPAL collaboration, G. Abbiendi et al., *Production rates of b anti-b quark pairs from gluons and b anti-b b anti-b events in hadronic Z0 decays*, *Eur. Phys. J.* **C18** (2001) 447–460, [`hep-ex/0010029`].

[207] CDF collaboration, D. Acosta et al., *Measurements of $b\bar{b}$ azimuthal production correlations in $p\bar{p}$ collisions at $\sqrt{s} = 1.8$ TeV*, *Phys. Rev.* **D71** (2005) 092001, [`hep-ex/0412006`].

[208] ATLAS COLLABORATION collaboration, *Identification and Tagging of Double b-hadron jets with the ATLAS Detector*, Tech. Rep. ATLAS-CONF-2012-100, CERN, Geneva, Jul, 2012.

[209] CMS COLLABORATION collaboration, *b-tagging in boosted topologies*, .

[210] M. Bähr et al., *Herwig++ Physics and Manual*, *Eur. Phys. J.* **C58** (2008) 639–707, [`0803.0883`].

[211] T. Sjöstrand, S. Ask, J. R. Christiansen, R. Corke, N. Desai, P. Ilten et al., *An Introduction to PYTHIA 8.2*, `1410.3012`.

[212] J. Gallicchio and M. D. Schwartz, *Quark and Gluon Tagging at the LHC*, *Phys. Rev. Lett.* **107** (2011) 172001, [`1106.3076`].

[213] J. Gallicchio and M. D. Schwartz, *Quark and Gluon Jet Substructure*, *JHEP* **04** (2013) 090, [`1211.7038`].

[214] A. Buckley, J. Butterworth, L. Lonnblad, D. Grellscheid, H. Hoeth, J. Monk et al., *Rivet user manual*, *Comput. Phys. Commun.* **184** (2013) 2803–2819, [`1003.0694`].

[215] M. Cacciari, G. P. Salam and G. Soyez, *The Anti-k(t) jet clustering algorithm*, *JHEP* **04** (2008) 063, [`0802.1189`].

[216] I. W. Stewart, F. J. Tackmann and W. J. Waalewijn, *N-Jettiness: An Inclusive Event Shape to Veto Jets*, *Phys. Rev. Lett.* **105** (2010) 092002, [`1004.2489`].

[217] J. Thaler and K. Van Tilburg, *Identifying Boosted Objects with N-subjettiness*, *JHEP* **03** (2011) 015, [1011.2268].

[218] I. W. Stewart, F. J. Tackmann, J. Thaler, C. K. Vermilion and T. F. Wilkason, *XCone: N-jettiness as an Exclusive Cone Jet Algorithm*, *JHEP* **11** (2015) 072, [1508.01516].

[219] E. Farhi, *A QCD Test for Jets*, *Phys. Rev. Lett.* **39** (1977) 1587–1588.

[220] S. Catani, G. Turnock, B. Webber and L. Trentadue, *Thrust distribution in e+ e- annihilation*, *Phys.Lett.* **B263** (1991) 491–497.

[221] S. Catani, L. Trentadue, G. Turnock and B. R. Webber, *Resummation of large logarithms in e^+e^- event shape distributions*, *Nucl. Phys.* **B407** (1993) 3–42.

[222] JADE collaboration, W. Bartel et al., *Experimental Studies on Multijet Production in e^+ e^- Annihilation at PETRA Energies*, *Z. Phys.* **C33** (1986) 23.

[223] I. W. Stewart, F. J. Tackmann and W. J. Waalewijn, *Factorization at the LHC: From PDFs to Initial State Jets*, *Phys. Rev.* **D81** (2010) 094035, [0910.0467].

[224] T. T. Jouttenus, I. W. Stewart, F. J. Tackmann and W. J. Waalewijn, *The Soft Function for Exclusive N-Jet Production at Hadron Colliders*, *Phys. Rev.* **D83** (2011) 114030, [1102.4344].

[225] J. M. Campbell, R. K. Ellis, R. Mondini and C. Williams, *The NNLO QCD soft function for 1-jettiness*, *Eur. Phys. J.* **C78** (2018) 234, [1711.09984].

[226] Z. Ligeti, I. W. Stewart and F. J. Tackmann, *Treating the b quark distribution function with reliable uncertainties*, *Phys. Rev.* **D78** (2008) 114014, [0807.1926].

[227] I. Moult, L. Rothen, I. W. Stewart, F. J. Tackmann and H. X. Zhu, *Subleading Power Corrections for N-Jettiness Subtractions*, *Phys. Rev.* **D95** (2017) 074023, [`1612.00450`].

[228] R. Boughezal, X. Liu and F. Petriello, *Power Corrections in the N-jettiness Subtraction Scheme*, *JHEP* **03** (2017) 160, [`1612.02911`].

[229] I. Moult, L. Rothen, I. W. Stewart, F. J. Tackmann and H. X. Zhu, *N-jettiness subtractions for gg → H at subleading power*, *Phys. Rev.* **D97** (2018) 014013, [`1710.03227`].

[230] R. Boughezal, A. Isgrò and F. Petriello, *Next-to-leading-logarithmic power corrections for N-jettiness subtraction in color-singlet production*, *Phys. Rev.* **D97** (2018) 076006, [`1802.00456`].

[231] M. A. Ebert, I. Moult, I. W. Stewart, F. J. Tackmann, G. Vita and H. X. Zhu, *Power Corrections for N-Jettiness Subtractions at $\mathcal{O}(\alpha_s)$*, `1807.10764`.

[232] T. T. Jouttenus, I. W. Stewart, F. J. Tackmann and W. J. Waalewijn, *The soft function for exclusive N-jet production at hadron colliders*, *AIP Conf. Proc.* **1441** (2012) 803–805, [`1109.3184`].

[233] R. Boughezal, X. Liu and F. Petriello, *N-jettiness soft function at next-to-next-to-leading order*, *Phys. Rev.* **D91** (2015) 094035, [`1504.02540`].

[234] T. Becher, G. Bell, C. Lorentzen and S. Marti, *Transverse-momentum spectra of electroweak bosons near threshold at NNLO*, *JHEP* **02** (2014) 004, [`1309.3245`].

[235] G. P. Lepage, *A New Algorithm for Adaptive Multidimensional Integration*, *J. Comput. Phys.* **27** (1978) 192.

[236] S. Catani and M. Grazzini, *Infrared factorization of tree level QCD amplitudes at the next-to-next-to-leading order and beyond*, *Nucl. Phys.* **B570** (2000) 287–325, [`hep-ph/9908523`].

[237] S. Catani and M. Grazzini, *The soft gluon current at one loop order, Nucl. Phys.* **B591** (2000) 435–454, [`hep-ph/0007142`].

[238] G. Bell, B. Dehnadi, T. Mohrmann and R. Rahn, *Automated Calculation of **N**-jet Soft Functions*, in *14th DESY Workshop on Elementary Particle Physics: Loops and Legs in Quantum Field Theory 2018 (LL2018) St Goar, Germany, April 29-May 4, 2018*, 2018, `1808.07427`.

[239] J. Gaunt, M. Stahlhofen and F. J. Tackmann, *The Gluon Beam Function at Two Loops, JHEP* **08** (2014) 020, [`1405.1044`].

[240] J. R. Gaunt, M. Stahlhofen and F. J. Tackmann, *The Quark Beam Function at Two Loops, JHEP* **04** (2014) 113, [`1401.5478`].

[241] R. Kelley, M. D. Schwartz, R. M. Schabinger and H. X. Zhu, *The two-loop hemisphere soft function, Phys. Rev.* **D84** (2011) 045022, [`1105.3676`].

[242] P. F. Monni, T. Gehrmann and G. Luisoni, *Two-Loop Soft Corrections and Resummation of the Thrust Distribution in the Dijet Region, JHEP* **08** (2011) 010, [`1105.4560`].

[243] A. Hornig, C. Lee, I. W. Stewart, J. R. Walsh and S. Zuberi, *Non-global Structure of the $\mathcal{O}(\alpha_s^2)$ Dijet Soft Function, JHEP* **08** (2011) 054, [`1105.4628`].

[244] D. Kang, O. Z. Labun and C. Lee, *Equality of hemisphere soft functions for e^+e^-, DIS and pp collisions at $\mathcal{O}(\alpha_s^2)$, Phys. Lett.* **B748** (2015) 45–54, [`1504.04006`].

[245] R. K. Ellis, "QCDloop: A repository for one-loop scalar integrals." `http://qcdloop.fnal.gov/`.

[246] G. 't Hooft and M. J. G. Veltman, *Scalar One Loop Integrals, Nucl. Phys.* **B153** (1979) 365–401.

[247] R. E. Crandall, "Note on fast polylogarithm computation." January, 2006.

[248] J. Vollinga and S. Weinzierl, *Numerical evaluation of multiple polylogarithms*, *Comput. Phys. Commun.* **167** (2005) 177, [`hep-ph/0410259`].

[249] R. Kleiss, W. J. Stirling and S. D. Ellis, *A new Monte Carlo treatment of multiparticle phase space at high energies*, *Comput. Phys. Commun.* **40** (1986) 359.